DTU

Technical
University of
Denmark

Optimisation of Propellers Using the Vortex-Lattice Method

Anders Smærup Olsen
PhD thesis
December 2001

Department of
Mechanical
Engineering

MEK

Maritime
Engineering

Optimisation of Propellers Using the Vortex-Lattice Method

Anders Smærup Olsen

TECHNICAL UNIVERSITY OF DENMARK
DEPARTMENT OF MECHANICAL ENGINEERING
MARITIME ENGINEERING
DECEMBER 2001

Published in Denmark by
Technical University of Denmark

Maritime Engineering
Department of Mechanical Engineering
Technical University of Denmark
Studentertorvet, Building 101E, DK-2800 Kgs. Lyngby, Denmark
Phone +45 4525 1360, Telefax +45 4588 4325
E-mail: maritime.engineering@mek.dtu.dk
WWW: http://www.mek.dtu.dk/

Publication Reference Data
Olsen, A. S.
Optimisation of Propellers Using the Vortex-Lattice Method
PhD Thesis
Technical University of Denmark, Maritime Engineering.
December, 2001
ISBN 87-89502-58-2
Keywords: Optimum Distribution of Circulation, Vortex-Lattice Method, Propeller Efficiency, Energy Coefficients, Actuator Disk Model Including Radially Applied Force

Preface

This thesis is submitted as a partial fulfilment of the requirements for the Danish PhD defence. The work was performed at the Section of Maritime Engineering (MT), Department of Mechanical Engineering (MEK), Technical University of Denmark (DTU), during the period of June 1998 to December 2001. The project was supervised by Associate Professor Poul Andersen, whose help and encouragement during the project are highly appreciated.

The work was done as part of the KAPRICCIO project under the Industrial and Materials Technologies research and technological development programme of the European Community, Contract no. BRPR-CT97-0458(DG12-GZMM) of Brite Euram III. The financial support is gratefully acknowledged.

Many thanks to my colleagues at MT, friends and family for their encouragement and invaluable support. Last but not least, special thanks to Vicky for her support and patience during my entire study.

Anders S. Olsen

Lyngby, December 21, 2001

This page is intentionally left blank.

Executive Summary

This study has two main objectives. One is to extend the classic theory for determination of the optimum distribution of circulation along a propeller blade for the purpose of achieving the highest efficiency for a given thrust. The other objective is a comparison of different propellers by use of energy coefficients. These coefficients are related to an axial loss, a rotational loss, a frictional loss and a loss due to the finite blade number of the propeller. If the propeller is located in a radially varying wake, this will be related to an axial gain.

The optimum distribution of circulation can be found by solving a variational problem where the propeller torque is minimised for a given propeller thrust. In classic theory this problem is solved in an integral formulation where the propeller is modelled as a lifting line with a continuous distribution of circulation. Betz (1927) and Lerbs (1952) solve this problem for a propeller in open water and in a radially varying wake, respectively, and find two optimum criteria. In order to solve the problem it is necessary to use Munk's displacement theorem (von Kármán and Burgers, 1963) and linearise the problem. The method used in this thesis for solution of the problem is based on the method described by Kerwin et al. (1986). In this method the continuous distribution of circulation is discretised and thus it is possible to solve the problem directly without the assumptions from classic theory. Kerwin et al. (1986) use a lifting-line model of the propeller but in this thesis the propeller is modelled by the vortex-lattice method and thus the effect of the entire blade can be included in the optimisation. In the vortex-lattice method the propeller blade is replaced by a lattice of quadrilateral panels with constant circulation and the shed horseshoe vortices follow regular helices. According to Munk's displacement theorem it is necessary to specify the chordwise distribution of circulation in order to reach a solution to the variational problem. It is shown that the largest contribution to the forces on the propeller blade comes from the vortex along the trailing edge, which combines the two shed vortices in a horseshoe vortex. This is in accordance with Munk's displacement theorem and due to this the form of the chordwise distribution of circulation has only a small influence on the results. As the entire blade is used in the optimisation it is possible to examine the influence of the propeller geometry on the optimum distribution of circulation. Results from five propellers from the David W. Taylor Naval Ship Research and Development Center (DTNSRDC) propeller series with systematic varying skew and skew-induced rake show that the radial distribution of thrust is almost identical for all the propellers, whereas the distributions of circulation and torque differ. This results in increased efficiency with increasing skew, which is also noted by Mishima and Kinnas (1997). If the skew-induced rake is removed the efficiency is further increased.

The reasons for this are not known in detail and should be further investigated. But an examination of the total velocities at the trailing edge shows that skew has a favourable influence on these velocities. It is interesting that the distributions of thrust are identical for all the propellers. Hence, the propeller geometry has no influence on the optimum distribution of thrust but the geometry influences the efficiency. It is possible to include a radially varying axi-symmetric onset flow including all three velocity components in the optimisation. Furthermore, it is possible to include a simple alignment of the grid and the trailers during the optimisation. This method is similar to that used for moderately loaded propellers. The present method has been used to optimise a Kappel propeller in a wake with specification of both axial and radial velocity components and with inclusion of the wake alignment procedure. The results from the present method are compared to results obtained by the method described in Andersen (1997). This comparison shows a good agreement for the torque coefficient and a reasonable agreement for the distribution of circulation and the pitch of the shed vortices.

The energy coefficients proposed by Dyne (1993) have been extended to include a radially varying axial onset flow. Thus, it is possible to calculate the efficiency for a propeller as a sum of five energy coefficients related to the axial loss, the rotational loss, the frictional loss and a finite blade number loss. If the propeller is located in a wake the fifth coefficient is included, which is an axial gain. The axial and rotational losses have been compared to the two corresponding coefficients derived by Glauert (1963) for a simple propeller with satisfactory agreement.

In order to calculate the energy coefficients it is necessary to know the averaged axially induced velocity at the propeller plane and the averaged axial and tangential velocities far downstream of it. These velocities are found either by the optimisation computer program or by a modified linear actuator disk model of the propeller. By this model the induced velocities are found as a weighted sum of the induced velocities from a normal linear disk and a duct. By use of the modified actuator disk it is possible to make fast calculations of the induced velocities from propellers with skew, skew-induced rake and unconventional geometry. Examinations of the induced velocities from the five DTNSRDC propellers calculated by the two methods indicate that they may be too simple, but this should be further investigated. The open water energy coefficients for the five propellers have been calculated. Unfortunately, the efficiency for a propeller with an infinite number of blades calculated by the energy coefficients does not agree with the efficiency found in the optimisation. In the optimisation the efficiency is increasing with increasing skew, whereas the efficiency based on the coefficients is decreasing with increasing skew. The reason is that the averaged induced axial velocity at the propeller plane is increasing with increasing skew, whereas the axial velocities far downstream are almost identical for all five propellers. This results in an increased axial loss and thus a decrease in the efficiency. If this is a real effect or caused by the methods used in the calculation of the induced velocities is not known and should be further investigated. The open water energy coefficients for three Kappel propellers have been calculated by the actuator disk model. Unfortunately, again with questionable results, which should be further examined but it is probably due to the actuator disk model.

Synopsis

Dette studium har to formål: Dels at udvide den klassiske måde at finde den optimale belastningsfordeling på et propellerblad, så virkningsgraden for propelleren bliver størst mulig. Dels at sammenligne forskellige propellere ved hjælp af energikoefficienter. Disse koefficienter relaterer sig til et aksialt tab, et rotationstab, et friktionstab og et tab på grund af endeligt bladantal. Hvis propelleren arbejder i et radialt varierende medstrømsfelt, vil dette dog være forbundet med en aksial gevinst.

Den optimale belastningsfordeling på propellerbladet kan findes ved at løse et varationsproblem, hvor propellermomentet minimeres for et givet propellertryk. I den klassiske teori bliver dette problem løst i en integral formulering, hvor propelleren er modelleret som en løftende linje med en kontinuert fordeling af cirkulation. Betz (1927) og Lerbs (1952) løser dette problem for en propeller i henholdsvis åbenvand og i et radialt varierende medstrømsfelt. For at løse problemet er det nødvendigt at bruge Munks teorem (von Kármán and Burgers, 1963) og linearisere problemet. Metoden til at løse variationsproblemet i dette studium bygger på en diskretisering af den kontinuerte cirkulationsfordeling foreslået af Kerwin et al. (1986). Ved at diskretisere fordelingen kan variationsproblemet løses direkte, og antagelserne fra den klassiske teori undgås. Metoden i Kerwin et al. (1986) bygger på en løftende linje model for propelleren, men i dette studium er propelleren beskrevet med en hvirvelmetode, så hele bladets indflydelse kan inkluderes i optimeringen. I hvirvelmetoden er bladet inddelt i firkantede paneler med konstant cirkulation, og de afløste hvirvler er hesteskohvirvler, der følger regulære skruelinjer. Ifølge Munks teorem er det nødvendigt at specificere den kordevise trykfordeling for at opnå en løsning på variationsproblemet. Med den benyttede hvirvelmetode er det påvist, at det største bidrag til kræfterne på propellerbladet stammer fra kraften på den agterste hvirvel, der følger agterkanten af bladet og forbinder de to afløste hvivler til hesteskohvirvelen. Dette er i overensstemmelse med Munks teorem og er årsagen til, at den angivne kordevise trykfordeling kun har en mindre indflydelse på resultaterne. Ved at inkludere indflydelsen fra hele bladet er det muligt at undersøge propellergeometriens effekt på den optimale belastningsfordeling. Resultater for fem propellere med varierende skew og skew induceret rake fra David W. Taylor Naval Ship Research and Development Center's (DTNSRDC) propellerserie viser, at den radiale trykkraftfordeling er næsten ens for alle propellerne, mens cirkulations- og momentfordelingerne er forskellige. Dette resulterer i en øget virkningsgrad, hvis skew øges, dette er også påvist i Mishima and Kinnas (1997). Fjernes den skew inducerede rake vil virkningsgraden øges yderligere. Hvad denne forøgelse af virkningsgraden skyldes vides ikke med sikkerhed og skal underøges nærmere. Men en undersøgelse

af de totale hastigheder på agterkanten af bladet viser, at skew har en gunstig indvirkning på disse. Det er bemærkelsesværdigt, at trykkraftfordelingen er ens for alle propellerne, dermed har propellergeometrien ingen indflydelse på den optimale trykkraftfordeling, men kun på virkningsgraden. Det er muligt at inkludere et radialt varierende aksesymmetrisk medstrømsfelt, hvor alle tre hastighedskomposanter kan angives. Endvidere kan en simpel opdatering af de afløste hvirvler og nettets placering inkluderes under optimeringen. Metoden er magen til den, der bliver benyttet for moderat belastede propellere. Den nye optimeringsmetode er brugt til at optimere en Kappel propeller i et medstrømsfelt, hvor både den aksiale og den radiale hastighedskomposant er specificeret. Opdateringen af nettet og de afløste hvirvler er også indkluderet. Resultaterne fra den nye metode er sammenlignet med resultaterne fra metoden, der er beskrevet i Andersen (1997). Denne sammenligning viser en god overensstemmelse for momentkoefficienten og en rimelig overensstemmelse for cirkulationsfordelingen og for stigningen af de afløste hvirvler.

Energikoefficienterne foreslået i Dyne (1993) er udvidet til at inkludere et radialt varierende medstrømsfelt i den aksiale komposant. Ved hjælp af koefficienterne kan virkningsgraden for propelleren beregnes som en sum af fem energikoefficienter, der relaterer sig til et aksialt, et rotations- og et friktionstab samt et tab på grund af endeligt bladantal. Hvis propelleren befinder sig i et medstrømsfelt, resulterer dette i en aksial gevinst. For en simpel propeller sammenlignes det aksiale tab og rotationstabet med tilsvarede koefficienter foreslået af Glauert (1963) med tilfredsstillende overensstemmelse.

For at beregne energikoefficienterne er det nødvendigt at kende de midlede aksialt inducerede hastigheder i propellerplanet og de midlede aksialt og tangentielt inducerede hastigheder langt nedstrøms for propelleren. Disse hastigheder er enten fundet ved hjælp af computerprogrammet, der bruges til optimeringen, eller ved hjælp af en modificeret lineær impulsskivemodel for propelleren. I denne model findes hastighederne som en vægtet sum af hastighederne fra den normale impulsskive og en dyse. Ved hjælp af den modificerede impulsskive er det muligt hurtigt at beregne hastighederne fra propellere med skew, rake og ukonventionel geometri. Undersøgelser af de inducerede hastigheder fra de fem DTNSRDC propellere indikerer, at de to metoder måske er for simple, men dette skal undersøges nærmere. Energikoefficienterne i åbenvand er beregnet for de fem propellere. Desværre er der uoverensstemmelser mellem virkningsgraden for en propeller med et uendeligt antal blade fundet med energikoefficienterne og virkningsgraden fundet ved optimeringen. I optimeringen stiger virkningsgraden, hvis skew øges, mens den derimod er faldende ifølge energikoefficienterne. Grunden til dette er, at de midlede akisialt inducerede hastigheder i propellerplanet stiger med øget skew, mens hastighederne langt nedstrøms næsten er identiske for de fem propellere. Dette giver et øget aksialt tab og dermed en faldende virkningsgrad. Om dette virkelig er tilfældet eller skyldes metoderne brugt til at beregne hastighederne vides ikke og skal undersøges nærmere. Energikoefficienterne i åbenvand for tre Kappel propellere er beregnet med impulsskivemodellen. Desværre igen med tvivlsomme resultater, som skal undersøges nærmere, men dette skyldes formentlig den brugte impulsskivemodel.

Contents

Symbols

The symbols used in this thesis are generally explained when they are first introduced. The following list contains the main symbols used.

Roman Symbols

A	Area
AXG	Energy coefficient for the axial gain
AXL	Energy coefficient for the axial loss
A_e/A_0	Expanded blade area
$\mathbf{a}$	NACA mean line constant
b	Semispan of hydrofoil
C_D	Sectional drag coefficient $= D(y)/(\frac{1}{2}\rho U_0^2 c(y))$
C_D^{tot}	Total drag coefficient $= D/(\frac{1}{2}\rho U_0^2 A)$
C_L	Sectional lift coefficient $= L(y)/(\frac{1}{2}\rho U_0^2 c(y))$
$C_{L,i}$	Ideal lift coefficient
$C_{L,r}$	Required lift coefficient $= L_r/(\frac{1}{2}\rho U_0^2 A)$
C_{Th}	Thrust loading $= T/(\frac{1}{2}\rho U_A^2 \pi R^2)$
ΔC_p	Pressure jump coefficient $= (p - p_0)/(\frac{1}{2}\rho U_0^2)$
ΔC_{prot}	Pressure reduction coefficient in the slipstream due to rotation
c	Chord length
c_0	Maximum chord length for the elliptic planform
D	Drag / propeller diameter
$FBNL$	Energy coefficient for the finite blade number loss
FRL	Energy coefficient for the frictional loss
$H(x)$	Heaviside's step function
ΔH	Jump in total head across the propeller disk
J	Advance number $J = U_a/(nD)$
K_Q	Torque coefficient $= Q/(\rho n^2 D^5)$

$K_{Q,\infty}$	Torque coefficient for a propeller with infinite number of blades
K_T	Thrust coefficient $= T/(\rho n^2 D^4)$
$K_{T,\infty}$	Thrust coefficient for a propeller with infinite number of blades
L	Lift
L_r	Required lift
$\vec{l}$	Vector for the panel side $= (l_x, l_y, l_z)$
M_{sp}	Number of spanwise panels
N_{ch}	Number of chordwise panels
n	Rate of revolutions
(n_a, n_r, n_t)	Unit normal of a surface
P	Pitch of the trailers
p	Pressure in the fluid
p_0	Free-stream pressure
Δp	Pressure jump across the propeller disk
Q	Propeller torque
Q_Z	Torque for a propeller with a finite number of blades
$Q_{n-\frac{1}{2}}(Z)$	Legendre functions of the second kind and the order $n - \frac{1}{2}$
$Q'_{n-\frac{1}{2}}(Z)$	Derivative of $Q_{n-\frac{1}{2}}(Z)$ with respect to Z
Q_∞	Torque for a propeller with an infinite number of blades
ΔQ_{fr}	Additional torque due to viscosity
$\vec{q}_i^*$	Induced velocity from an entire panel with unit circulation
R	Propeller radius
$ROTL$	Energy coefficient for the rotational loss
s	Arc length parameter/non-dimensional spanwise parameter
T	Propeller thrust
T_∞	Thrust for a propeller with infinite number of blades
ΔT_{fr}	Additional thrust due to viscosity
t	Non-dimensional chordwise parameter
(t_a, t_r, t_t)	Tangent vector
U_0	Axial onset flow
$U_{0,x}, U_{0,r}, U_{0,t}$	Onset flow in cylindrical coordinates
$U_{0,x}, U_{0,y}, U_{0,z}$	Onset flow in Cartesian coordinates
U_A	Advance speed $= (1 - w)U_s$
U_s	Ship speed
U_x, U_y, U_z	Total velocity in Cartesian coordinates
u_x, u_r, u_t	Induced velocity in cylindrical coordinates
u_x, u_y, u_z	Induced velocity in Cartesian coordinates

$u_{a,0}$	Induced axial velocity at the propeller plane
$u_{a,-\infty}, u_{t,-\infty}$	Induced axial and tangential velocity far downstream
w	Wake fraction
x, r, ϕ	Cylindrical coordinates
x, y, z	Cartesian coordinates
x_m	Propeller rake
Z	Number of blades / parameter for the Legendre functions

Greek Symbols

α	Angle of attack
β	Pitch angle
β_0	Pitch angle for the onset flow $= \tan^{-1}(U_0/\omega r)$
β_h	Horizontal pitch angle
β_i	Pitch angle for the total inflow $= \tan^{-1}((U_0 - u_a)/(\omega r - u_t))$
β_v	Vertical pitch angle
$\delta(x)$	Dirac's delta function
η	Propeller efficiency $= J/(2\pi)K_T/K_Q$
η_{ideal}	Ideal efficiency $= 2/(1 + \sqrt{1 + C_{Th}})$
η_∞	Efficiency for a propeller with infinite number of blades $= J/(2\pi)K_{T,\infty}/K_{Q,\infty}$
Γ	Circulation
Γ_0	Maximum circulation for the elliptic distribution
γ	Chordwise circulation
κ	Weight function
λ	Lagrange multiplier
ν	Ratio of the flat plate pressure distribution
ω	Angular velocity $= 2\pi n$
$\phi_{T.E.}$	Phase angle for the trailers
ϕ_m	Skew angle
ρ	Density of sea water $= 1025\,^{\mathrm{kg}}/_{\mathrm{m}^3}$

Superscripts

$\hat{}$	Non-dimensional parameter
FP	Flat plate pressure distribution
RT	Rooftop pressure distribution

Subscripts

cp	Control point
gp	Grid point
h	Hub
t	Tip

Abbreviations

$DTNSRDC$ or DC	David W. Taylor Naval Ship Research and Development Center
LL	Lifting line
LS	Lifting surface
$L.E.$	Leading edge
$NACA$	National Advisory Committee for Aeronautics
$T.E.$	Trailing edge
xdisk	Actuator disk computer program
xlift	Lifting-surface optimisation program

Chapter 1

Introduction

Even though propellers have been used to drive ships for over a century investigations of the action and the design of the propellers are as important as ever. Both because the size of ships continues to increase and because of increased focus on the limited fuel resources and the impact on the environment from the burning of fuel. This forces the propeller manufacturers to think of new alternative solutions of ship propulsion systems which are capable of fulfilling the requirements of developing higher thrust with higher efficiency.

The action of the propeller will inevitably involve a loss of energy. This loss can be divided into three, i.e. an axial loss, a rotational loss and a loss due to the friction. An example of the magnitude of the losses as a function of the thrust loading for a propeller in open water is shown in Table 1.1. From the table it is seen that the axial loss is highest, followed by the frictional loss and finally the rotational loss. As the axial loss comes from the acceleration of the fluid through the propeller disk, which is necessary in order to develop the thrust, it is impossible to remove this loss. Hence, if the efficiency of the propeller should be increased, it is necessary to focus on lowering the rotational and the frictional losses.

The frictional loss depends on the surface roughness and the blade area. The cavitation on the blades is dependent on these parameters as well. Therefore, the blade area cannot be based solely on frictional considerations but the cavitation has to be considered too. As both the friction and the cavitation inception are lowered when the surface is smooth, the propeller is manufactured with a smooth surface.

This leaves the rotational loss as the part which should be minimised in order to improve the efficiency. This has also been the task of many research projects during the past decades, resulting in new systems of propulsion such as propeller and vane wheel, contra-rotating propellers and propeller and stators. The ITTC (1990) made a comparison of the efficiencies for a number of these unconventional propulsion systems, which in full-scale tests showed improvements of 6–16% achieved by these systems.

A simpler way to improve the efficiency is by modifying the tip geometry of the propeller. By this method the more complicated construction of a two-device propulsion system is

Table 1.1: *Energy coefficients for a propeller in open water. From Glover (1987).*

C_{Th}	Axial loss (%)	Rotational loss (%)	Frictional loss (%)	Total efficiency
0.56	15.5	6.7	16.4	61.4
1.43	22.7	5.6	13.9	57.8
3.44	32.1	4.8	14.3	48.8
5.98	40.6	6.9	10.7	41.8

avoided. This modification is inspired by the results obtained in the aircraft industry. For aeroplane wings it is possible to improve the lift to drag ratio by fitting winglets to the wings, see Andersen (1999) for an overview of the improvements. The idea is that a similar modification to the tip of the propeller blade will result in an improved efficiency by increased thrust-torque ratio. During the past two decades many results for the tip modified propellers have been published, see e.g. Sparenberg (1984), de Jong (1991) or Andersen et al. (2000). Numerical results and model experiments show that improvements in the efficiency of 1–4% are possible with a tip modified propeller (Andersen, 1999).

Another way of improving the overall propulsive efficiency is by improving the propeller-hull interaction. This may be done by placing a duct around the propeller or fitting the hull with other flow straightening devices. ITTC (1990) shows that in full-scale tests, propulsive efficiency improvements of 5–10% can be achieved.

The focus of this thesis will be on the development of a new optimisation method for propellers, including the tip modified ones. From the above it is seen that the improvements in efficiency for the tip modified propellers are in the range of 1–4%, which is in fact the lowest gain of the mentioned systems. Despite this, the tip modified propellers are an interesting alternative to the other propulsive systems, as the construction of the propellers is less complicated and the maintenance costs are lower. The one to four per cent increase in efficiency may seem small, but as the total fuel consumption of the merchant fleet today is approximately 275 million tons per year (Andersen et al., 2000), even a small improvement of the ship's propulsive efficiency will reduce the consumption with millions of tons per year for the benefit of the shipowner and the environment. The new method will, unlike the classic approach, make it possible to include more details about the propeller geometry.

1.1 Background

Before the new method is described a review of the classic design cycle will be given. Apart from the fact that a ship propeller has to deliver the necessary thrust to maintain the cruising speed, it is necessary that the blades have sufficient strength to avoid deflection during operation. These two basic requirements should be fulfilled with the highest possible

efficiency for the propeller and with the lowest possible levels of induced vibrations and cavitation. As all this cannot be fulfilled at the same time, the best compromise between high efficiency and low induced vibrations and cavitation is regarded as the optimum propeller.

In order to find this best compromise, the propeller is normally designed in a number of steps, which are described in the following. Before the design cycle is initiated the following input data should be determined:

- Main dimensions, i.e. radius of the propeller and the hub, number of blades, submergence of the shaft ggg
- Design point, i.e the required thrust or available power, the number of rotations and the advance speed of the propeller
- Sectional profile data, i.e. the thickness distribution and the mean line
- Blade outline, i.e. chord length, skew and rake distributions based on cavitation and vibration considerations and maximum thickness distribution based on strength requirements
- Wake in the propeller plane

Figure 1.1: *Design steps.*

As in any other design process iterations through the steps can be necessary before the optimum solution is found. Through the design cycle, which consists of three steps as depicted in Figure 1.1, the blade pitch and camber distributions are determined. In the first step the radial distribution of loading, which gives the highest efficiency for the propeller, is found. Commonly used optimum criteria are the Betz (1927) criterion for propellers in uniform inflow and the Lerbs (1952) criterion for wake adapted propellers. By use of this distribution as input to the second step the corresponding pitch and camber distributions are found. For that purpose either a vortex-lattice method, see e.g. Greely and Kerwin (1982), or a panel method is used, see e.g. Su and Ikehata (1999). These methods include the effects of the entire blade and it is possible to include a better description of the trailing vortices than in the optimisation. In step three the cavitation and the induced vibrations are examined in unsteady and off-design conditions. These investigations can either be performed numerically, by an unsteady vortex-lattice method, see e.g. Kerwin and Lee (1978), or a panel method, see e.g. Kinnas and Fine (1994), or experimentally.

During the years the above method has proved to be very useful for the design of conventional propellers, but the focus in recent years on unconventional propulsion systems has made it necessary to review the design method in order to treat these devices. Kerwin et al. (1986) developed a method by which the optimum distribution of circulation could be found for a multiple device system, such as contra-rotating propellers or a propeller and a stator. The method is based on a vortex-lattice description of the lifting line for which the optimum distribution is found by solving a variational problem where the propeller torque is minimised for a given thrust. The same approach is used by Andersen (1997) to find the optimum distribution of circulation for a propeller with tip modified geometry. Unlike the classic lifting-line theory the geometry of the lifting line can be curved as it corresponds to the midchord line of the propeller. The calculations of the forces on the blades are confined to the lifting line, while the circulation is distributed over the entire blade. Another way of designing tip modified propellers is described by de Jong (1991). Here the optimum distribution of circulation is found by minimising the lost energy in the slipstream infinitely abaft the propeller. In this method it is furthermore possible to include an optimisation of the thickness and chord length distributions in order to minimise the frictional loss.

Modifications to the second step, see Figure 1.1, in the design cycle have been applied continuously during the years. In recent years the focus has been on the determination of the effective wake, which is normally found by empirical corrections to the nominal wake. Kerwin et al. (1994) overcome this problem by coupling a vortex-lattice method and an axi-symmetric Navier-Stokes solver. The vortex-lattice method is used to determine the blade shape and the Navier-Stokes solver finds the corresponding effective wake.

In recent years several attempts have been made to integrate the three design steps. One attempt is that of Kinnas et al. (1998), which couples a vortex-lattice analysis method for cavitating flows, an Euler solver and a numerical optimisation method in order to develop an automated, systematic design of cavitating blades. The method is capable of finding the blade shape which has the highest efficiency for a given thrust, with given constraints on the cavitation extent and the induced hull pressure pulses. Generic algorithms have also been used to integrate the three steps, see e.g. Caponnetto (2000), who uses a generic algorithm to find the optimum design of contra-rotating propellers, and Karim et al. (2001), who use a micro generic algorithm in the design of conventional propellers.

1.2 Objective of the Thesis

The aim of the present work is to extend the method by which the optimum distribution of loading is found, hence the present work is confined to step one in the design cycle, see Figure 1.1. As in Kerwin et al. (1986), the optimum distribution will be found by solving a variational problem in which the torque is minimised for a required thrust. The essential fact of the present method is that the effect of the entire blade is included in the optimisation. To calculate the thrust and torque for the propeller the vortex-lattice method is used. By this

method the geometry of the propeller can be chosen almost arbitrarily so the present method can be applied to both conventional and tip modified propellers. A simple wake and blade alignment procedure is included similar to the wake alignment procedure for the moderately loaded lifting line. For simplicity the effects of the thickness and the hub have been omitted. The vortex-lattice method is used as it is fast compared to boundary element methods and Navier-Stokes solvers and at the same time has a sufficient accuracy. Therefore, the computational time can be reduced at the design stage, where iterations will be necessary in order to find the optimum propeller, without loss of accuracy, using the vortex-lattice method. As the present method is restricted to step one in the design cycle, it is necessary to give the same input data as in the classic design method.

As shown in Table 1.1 it is possible to decompose the propeller efficiency into different losses. This is used to compare different propellers as a supplement to the propeller efficiency. In the present work the energy coefficients of Dyne (1993) will be used. Dyne (1993) suggests that the efficiency for a propeller in open water can be calculated as a sum of four energy coefficients. These coefficients are connected with the axial loss, the rotational loss, the frictional loss and finally a loss due to the finite number of blades. The work of Dyne (1993) has been extended to include a radially varying axial onset flow. Thus, an axial gain is introduced.

1.3 Outline of the Thesis

The contents of the thesis are presented in seven chapters. Chapter 2 is an outline of the potential flow theory and the linearised thin wing theory.

Chapter 3 gives an outline of the lifting-surface optimisation method for a planar hydrofoil in uniform inflow. The chapter describes the grid generation and the calculation of induced velocities for the used vortex-lattice method. The chapter ends with a grid study for the present method.

Chapter 4 contains the derivation of the lifting-surface optimisation method for propellers. The chapter also contains the results for the optimisations of five DTNSRDC propellers in open water and of a Kappel propeller in a wake.

Chapter 5 describes the derivation of the expressions for the induced velocities and the pressure for the modified actuator disk theory. The removal of the singular terms in the derived expressions is outlined. A validation of the method is also included.

Chapter 6 contains the derivation of the energy coefficients and the validations of the coefficients. The chapter presents the obtained energy coefficients for the DTNSRDC propellers series and the Kappel propellers.

Chapter 7 contains the conclusions.

This page is intentionally left blank.

Chapter 2

Equations of Motion

The basic equations for any fluid motion are the equation for conservation of mass, i.e. the continuity equation, and the equations for conservation of momentum. In the present study the equations of motion are used in a simplified form which will be outlined in the following. A thorough derivation of the complete equations of motion and their simplifications can be found in e.g. Breslin and Andersen (1994) or Newman (1978).

All flows considered concern deeply submerged bodies. The fluid will in all cases be water, which can be considered to be incompressible. Furthermore, the water is assumed to be inviscid. This assumption is valid as the propeller is working at a relatively high Reynolds number so that the viscose effects are restricted to a thin boundary layer on the body, whose influence on the overall flow can be ignored. During the design phase the both spatially and time-varying wake behind the hull is assumed to be steady and axi-symmetric. Thus, the equations of motion are not functions of the time but only of the three Cartesian coordinates (x, y, z).

The continuity equation for a steady incompressible and inviscid fluid is given by

$$\frac{\partial u_x}{\partial x} + \frac{\partial u_y}{\partial y} + \frac{\partial u_z}{\partial z} = 0 \tag{2.1}$$

and the conservation of momentum is given by the steady Euler equations

$$\nabla \left[\frac{p}{\rho} + \tfrac{1}{2}|\vec{u}|^2 \right] - \vec{u} \times \vec{\xi} = \frac{\vec{F}}{\rho} \tag{2.2}$$

where

$\nabla = (\frac{\partial}{\partial x}, \frac{\partial}{\partial y}, \frac{\partial}{\partial z})$ is the gradient operator,

$\vec{u} = (u_x, u_y, u_z)$ is the velocity vector,

$\vec{\xi} = \nabla \times \vec{u}$ is the vorticity,

ρ is the density,

p is the pressure and

$\vec{F}$ are the external forces per unit volume acting on the fluid.

As gravitational forces are ignored the external forces are only due to the lifting surfaces in the fluid. The forces from the fluid on these surfaces will be opposite and equal the forces from the surfaces on the fluid.

2.1 Irrotational Flow

By use of Lord Kelvin's theorem it is possible to simplify the equations of motion further. This theorem states that for an ideal fluid acted upon by conservative forces the circulation is constant about any closed material contour moving with the fluid. The circulation, Γ, is defined as the integral of the tangential velocity along a closed contour

$$\Gamma = \int_C \vec{u} \cdot d\vec{x}.$$

where C is any closed contour in the fluid.

Thus, any motion which started from a state of rest at some initial time will remain irrotational for all subsequent times, and the circulation about any material contour will vanish (Newman, 1978). That this holds can be seen by applying Stokes' theorem to the circulation. Then the circulation can be related to the vorticity vector by

$$\int_S (\nabla \times \vec{u}) dS = \int_C \vec{u} \cdot d\vec{x}$$

where the integral on the left-hand side is a surface integral and S is the surface bounded by the contour C. As the flow started from a state of rest where the circulation is zero the circulation should remain zero, therefore it is necessary that the integrand of the surface integral is zero:

$$\nabla \times \vec{u} = 0 \tag{2.3}$$

This means that the motion of the fluid is irrotational.

As shown in e.g. Newman (1978) this is a sufficient condition for the existence of a scalar velocity potential, ϕ, which can describe the flow.

2.2 The Velocity Potential

By introducing the velocity potential the equations of motion are further simplified as the velocities and the velocity potential are related through

$$u_x = \frac{\partial \phi}{\partial x}\,; \quad u_y = \frac{\partial \phi}{\partial y}\,; \quad u_z = \frac{\partial \phi}{\partial z} \tag{2.4}$$

Thus, the velocity is now expressed by just one scalar instead of the three components of $\vec{u}$.

By inserting Equation (2.4) in the continuity equation, Equation (2.1), a Laplace equation for the velocity potential follows:

$$\frac{\partial^2 \phi}{\partial x^2} + \frac{\partial^2 \phi}{\partial y^2} + \frac{\partial^2 \phi}{\partial z^2} = \nabla^2 \phi = 0 \tag{2.5}$$

By solving the Laplace equation with additional boundary conditions, which are described later, the motion of the fluid is found. In order to obtain a complete description of the motion, it is necessary to have an expression for the pressure in the fluid. This expression can be found from the Euler equations.

2.3 The Bernoulli Equation

In Lord Kelvin's theorem the external force was assumed to be conservative, hence it is possible to express the force as the negative gradient of a scalar function, Ω:

$$\vec{F} = -\nabla \Omega \tag{2.6}$$

By inserting Equation (2.6) together with the assumption of irrotational flow, Equation (2.3), in the Euler equations, Equation (2.2), these are reduced to

$$\nabla \left[\frac{p + \Omega}{\rho} + \tfrac{1}{2} |\vec{u}|^2 \right] = 0$$

In order to fulfil this, the term in the brackets should be constant:

$$\frac{p + \Omega}{\rho} + \tfrac{1}{2} |\vec{u}|^2 = C \tag{2.7}$$

This is the Bernoulli equation, which gives a relation between the velocity and the pressure in the fluid. For an irrotational flow it can be applied between any to points in the fluid.

If the disturbance velocity from the body is small compared to the onset flow, the Bernoulli equation can be linearised (Breslin and Andersen, 1994):

$$p = p_\infty + \rho U_0 u_x \tag{2.8}$$

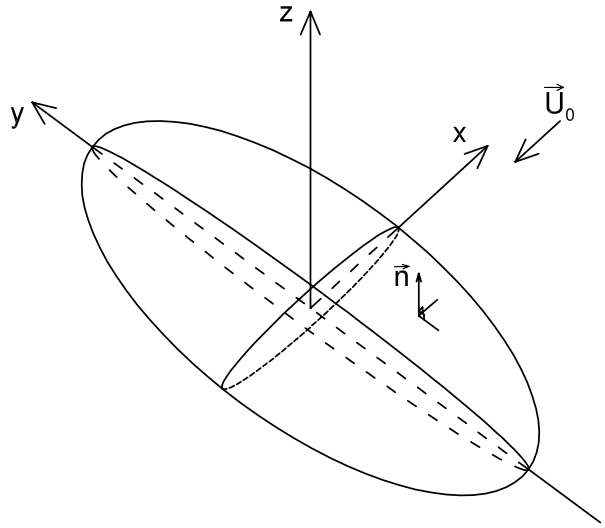

Figure 2.1: *Deeply submerged lifting surface.*

where u_x is the axial component of the disturbance velocity from the body. Rewriting the above equation gives the relation between the pressure coefficient ΔC_p and the disturbance velocity, which will be used in a following section

$$\Delta C_p = \frac{p - p_\infty}{\frac{1}{2}\rho U_0^2} \approx 2\frac{u_x}{U_0} \tag{2.9}$$

2.4 Boundary Conditions

The derived boundary conditions are for the deeply submerged planar hydrofoil in Figure 2.1, which is a lifting surface subject to an onset flow $\vec{U_0}$. The boundary conditions are the same for a propeller.

As the Laplace equation is linear it is possible to separate the boundary value problem into a problem for the undisturbed onset flow, with the potential ϕ_{onset}, and a problem for the perturbation flow caused by the lifting surface, with the potential ϕ. The final solution will then be the sum of these two potentials.

The velocity potential for the onset flow is derived from the definition of the velocity potential, see Equation (2.4), hence

$$\phi_{onset} = \vec{U_0} \cdot \vec{x} = U_{0,x}x + U_{0,y}y + U_{0,z}z \tag{2.10}$$

As there is no flow through the surface of the body the flow has to be tangential to it:

$$\frac{\partial \phi}{\partial n} = -\vec{U_0} \cdot \vec{n} \quad \text{on the surface} \tag{2.11}$$

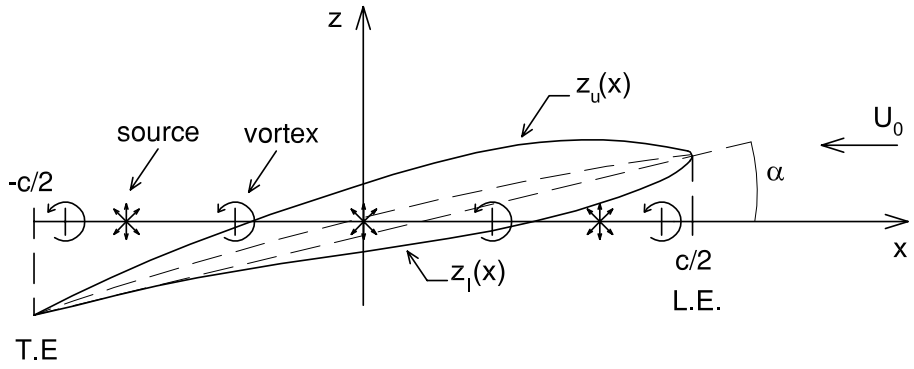

Figure 2.2: *Example of a thin wing section. The proportions are exaggerated.*

where $\vec{n}$ is the unit normal of the surface with direction from the surface into the fluid, see Figure 2.1. The flow has to leave the trailing edge smoothly. This is secured by applying the Kutta condition at the trailing edge, this means that the velocity induced by the body has to be finite at the trailing edge:

$$\nabla\phi < \infty \quad \text{at the trailing edge} \tag{2.12}$$

As the influence from the body should vanish far from it, the perturbation potential has to fulfil the radiation condition:

$$\nabla\phi(r) \to 0 \quad \text{for} \quad r \to \infty \tag{2.13}$$

These are the boundary conditions which the perturbation potential should fulfil in the general case, but by restricting the bodies to be thin and with a small angle of attack the thin wing theory can be used.

2.5 Linearised Thin Wing Theory

The thin wing theory was originally developed for flow about two-dimensional wing sections, hence the flow in this section will be assumed to be two-dimensional only. The flow will be in the x-z-plane of Figure 2.1. A thorough description of the theory can be found in Abbott and von Doenhoff (1959), Newman (1978) or Breslin and Andersen (1994). As the name suggests the theory is applied to thin profiles with the additional restriction that the angle of attack is small. An example of a profile is shown in Figure 2.2, where $z_u(x)$ defines the upper side of the profile and $z_l(x)$ the lower side and c the chord length. If the thin wing assumption is to be valid the $z_u(x)$ and $z_l(x)$ should be small compared to the chord length, furthermore, the slope of the profile, $z'_u(x)$ and $z'_l(x)$, should be small compared to one. If these requirements are fulfilled the velocity boundary condition in Equation (2.11) can be

linearised (Newman, 1978), hence

$$\begin{aligned}\frac{\partial\phi}{\partial z} &= -Uz'_u(x) \quad \text{on } z = 0_+,\ -c/2 \le x \le c/2\\ \frac{\partial\phi}{\partial z} &= -Uz'_l(x) \quad \text{on } z = 0_-,\ -c/2 \le x \le c/2\end{aligned} \tag{2.14}$$

Thus for the linearised theory the singularities describing the foil are located on the x-axis between $-c/2 \le x \le c/2$ as illustrated in Figure 2.2.

The question is which singularities should be used to describe the profile. This can be seen by dividing the disturbance potential into an even and an odd potential (Newman, 1978):

$$\begin{aligned}\phi(x,z) &= \phi_e(x,z) + \phi_o(x,z)\\ \phi_e(x,z) &= \phi_e(x,-z) = \tfrac{1}{2}\big[\phi(x,z) + \phi(x,-z)\big]\\ \phi_o(x,z) &= -\phi_o(x,-z) = \tfrac{1}{2}\big[\phi(x,z) - \phi(x,-z)\big]\end{aligned} \tag{2.15}$$

so that the boundary condition, Equation (2.14), becomes (Newman, 1978):

$$\frac{\partial\phi_e}{\partial z} = \mp\tfrac{1}{2}U(z'_u(x) - z'_l(x)) \quad \text{on } z = 0_\pm,\ -c/2 \le x \le c/2 \tag{2.16}$$

$$\frac{\partial\phi_o}{\partial z} = -\tfrac{1}{2}U(z'_u(x) + z'_l(x)) \quad \text{on } z = 0_\pm,\ -c/2 \le x \le c/2 \tag{2.17}$$

Since $\partial/\partial z$ is an odd operator, $\partial\phi_e/\partial z$ is odd and $\partial\phi_o/\partial z$ is even. Then the physical interpretation of the even potential is a flow past a symmetric profile, with no angle of attack and with the thickness $\tau = z_u(x) - z_l(x)$. The physical interpretation of the odd potential is an asymmetric flow past an arc with zero thickness defined by the profile camber line $z = \frac{1}{2}(z_u(x) + z_l(x))$. The two profiles are shown in Figure 2.3.

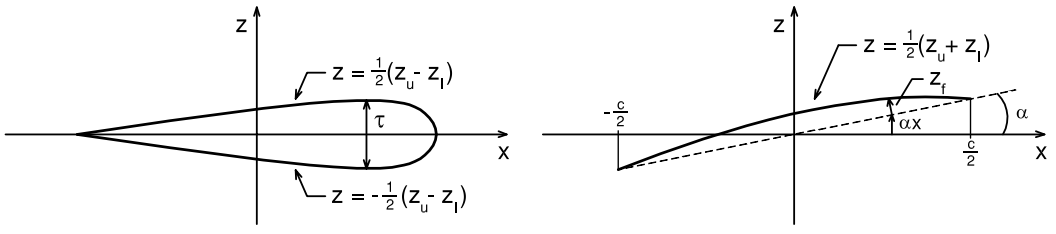

Figure 2.3: *Left: Symmetric section with thickness τ. Right: Camber line with angle of attack α.*

This means that the problem is now separated into a thickness problem, represented by the even potential, and a problem for the camber and angle of attack, represented by the odd potential. As the flow is symmetric about the profile with thickness there is no lift related to this flow, hence the lift of a profile is only related to the angle of attack and its camber.

The thickness is important to the distribution of pressure along the chord and thus it can influence the inception of separation and cavitation.

From the boundary condition for the even potential, Equation (2.16), it is seen that the potential has an asymmetric vertical velocity along the projection of the profile on the x-axis. A distribution of sources along the projection results in such a velocity, see e.g. Breslin and Andersen (1994). The boundary condition for the odd potential, Equation (2.17), requires that the vertical velocity along the projection is symmetric. A distribution of vortices gives a symmetric velocity, see e.g. Breslin and Andersen (1994).

Thus, the flow about a sufficiently thin and horizontal profile can be modelled by a distribution of sources and vortices along the projection of the profile on the x-axis as illustrated in Figure 2.2. As mentioned previously, the effects from the thickness will be omitted in this work, hence the foil is replaced by a distribution of circulation.

2.6 Distribution of Circulation

The mean line of a cambered section can be written as

$$z = \tfrac{1}{2}(z_u(x) + z_l(x)) = \alpha x + z_f(x) \tag{2.18}$$

where $z_f(x)$ is the camber line function and α is the angle of attack, see Figure 2.3, right. Hence, the boundary condition for the odd potential, Equation (2.17) is

$$\frac{\partial \phi_o}{\partial z} = -Uz'(x) = -U(\alpha + z_f'(x)) \quad \text{on } z = 0_{\pm},\ -c/2 \leq x \leq c/2 \tag{2.19}$$

It is seen that the boundary condition can be divided into a contribution from the angle of attack and another from the camber line. For the present study it is necessary to know the distribution of circulation along the chord. Therefore, two very useful distributions will be reviewed in the following.

The distribution of circulation related to the angle of attack corresponds to the distribution for a flat plate with an angle of attack. Hence, the distribution is given by (Breslin and Andersen, 1994):

$$\gamma_{FP}(x) = 2U_0\alpha\sqrt{\frac{c/2 + x}{c/2 - x}} \quad \text{for } -c/2 \leq x \leq c/2 \tag{2.20}$$

It is seen that the distribution is square-root singular at the leading edge, therefore the solution close to the leading edge will not be accurate but for the rest of the profile the solution will be usable.

The distribution of circulation related to the camber line is found from a prescribed pressure distribution $\Delta C_p(x)$ across the line and the linearised Bernoulli equation, Equation

(2.9). Furthermore, it is used that the tangential velocity $u_x(x,z)$ on either side of a planar distribution of circulation along the x-axis is given by (Breslin and Andersen, 1994):

$$u_x(x,0_\pm) = \mp\frac{\gamma(x)}{2} \quad \text{for } -c/2 \leq x \leq c/2 \tag{2.21}$$

Insertion of this in Equation (2.9) gives

$$\gamma(x) = \tfrac{1}{2}U_0\Delta C_p(x) \tag{2.22}$$

thus, when $\Delta C_p(x)$ is specified along the mean line the circulation is known.

The pressure distribution should of course be suitable with respect to separation and cavitation. The NACA **a** mean line series represents such distributions. The factor **a** is the fraction of the chord, from the leading edge, over which the pressure is constant. Over the last part of the mean line the pressure is linearly decreased to zero at the trailing edge. Hence, these mean lines are often referred to as having a rooftop pressure distribution. The distribution of circulation for these mean lines is

$$\gamma_{RT}(x) = \begin{cases} \frac{(c/2+x)U_0}{c(1-\mathbf{a}^2)}C_{L,i} & \text{for } -c/2 \leq x \leq c/2(1-2\mathbf{a}) \\ \frac{U_0}{1+\mathbf{a}}C_{L,i} & \text{for } c/2(1-2\mathbf{a}) \leq x \leq c/2 \end{cases} \tag{2.23}$$

where $C_{L,i}$ is a specified ideal lift coefficient. A more thorough description of the NACA **a** mean lines is given in Abbott and von Doenhoff (1959).

By adding the distributions from Equation (2.20) and Equation (2.23) the chordwise distribution of circulation is known for a profile with rooftop pressure distribution and arbitrary angle of attack, provided that the limits of the linear theory are not exceeded.

After this description of the linearised thin wing theory in two dimensions it is simple to extend the theory to three dimensions.

2.7 Three-Dimensional Flow

Unlike the flow past a body in two dimensions the flow in three dimensions will have a variation in the spanwise direction also. Thus, the circulation is a function of both the chordwise and spanwise coordinates, where the chordwise variation is given by the two-dimensional expressions. The linearised thin wing theory can also be applied in three dimensions provided that the two-dimensional assumptions are also valid spanwise.

In two-dimensional steady flow the requirement for irrotational flow is fulfilled by applying a vortex infinitely downstream of the foil, i.e. the shed starting vortex. This vortex has the same circulation as the total chordwise circulation at the foil but in the opposite direction,

hence the net circulation will be zero as required. For three dimensions the requirement is fulfilled if the vortices are closed curves and the circulation is constant along the curve (Newman, 1978). Thus, for a body in steady flow with a varying circulation in the spanwise direction, there will be a vortex sheet behind it combining the shed starting vortices and the trailing edge. The circulation of the vortex sheet is $d\Gamma(y)/dy$, where $\Gamma(y)$ is the total chordwise circulation at the spanwise coordinate y. As the vortex sheet is force-free it has to move with the fluid according to Helmholtz's theorem.

On the basis of the reviewed theory the examined lifting surfaces, i.e. hydrofoils or propellers, will in the following be modelled by a distribution of vortices on the planform of the surface and a sheet of trailing vortices in the wake of the surface. Even though the theory may seem to include many restrictions on the fluid and the flow, the potential flow theory has been used extensively over the years and has given reliable results.

This page is intentionally left blank.

Chapter 3

Optimisation of a Planar Hydrofoil

3.1 Introduction

In the following chapter the optimisation of a planar hydrofoil with elliptic planform is shown. The aim of the optimisation is to find the spanwise distribution of circulation which gives the highest lift to drag ratio for the hydrofoil. The elliptic planform is interesting as Prandtl derived analytically the optimum distribution of circulation for this planform. Therefore, it is possible to see how the new optimisation routine performs compared to the analytical solution. The term hydrofoil is used for a wing deeply submerged in water.

3.2 The Vortex-Lattice Method

The optimisation problem is solved by the numerical vortex-lattice method. In this method the continuous distribution of circulation over the planform of the foil is replaced by a discrete distribution, and the planform of the foil is replaced by a lattice of straight line vortices.

3.2.1 Grid Generation

The geometry of the hydrofoil is described in a body fixed Cartesian coordinate system, see Figure 3.1, with the x-axis pointing upstream, the y-axis pointing left and finally the z-axis completes the right-hand system, the onset flow is in the negative x-direction.

As the continuous distribution of circulation is replaced with a discrete distribution, the planform of the foil is divided into a number of panels, as depicted in Figure 3.1. Each panel consists of four straight lines forming a quadrilateral. Consistent with linear theory

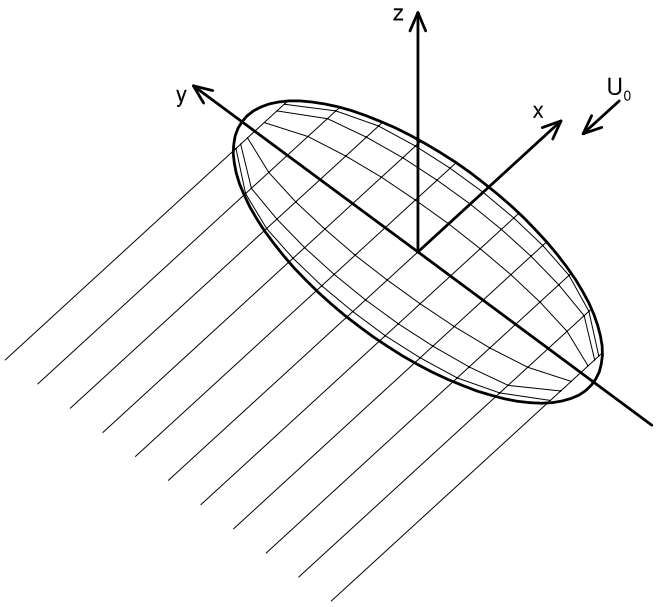

Figure 3.1: *The coordinate system for the hydrofoil.*

the panels are placed on the x-y-plane and not directly on the surface of the foil. The circulation is positive counterclockwise along the sides of the panel and in order to fulfil Lord Kelvin's theorem the circulation along the sides is constant. The corners of the panels, the grid points, are numbered from $P1$ to $P4$ in the direction of the circulation and the vectors along the sides are designated as $\vec{l}_1$ to $\vec{l}_4$ so that the vector along side 1 $\vec{l}_1$ is from $P1$ to $P2$, and so on, an example of a panel is shown in Figure 3.2.

The spanwise location of the grid points follows James (1972):

$$s_{gp,m} = -1 + \frac{8m-6}{4M_{sp}+2} \quad \text{for } m = 1, 2, \ldots, M_{sp}+1 \tag{3.1}$$

where $s = y/b$ is a non-dimensional spanwise parameter, b is the semispan of the hydrofoil and M_{sp} is the number of panels along the span. This discretisation has equidistance between the grid points and the outermost points at the tips are moved one quarter interval inward.

In the chordwise direction a cosine discretisation, according to Lan (1974), is used:

$$\begin{aligned} t_{gp,1} &= -\tfrac{1}{2} \\ t_{gp,n} &= -\tfrac{1}{2}\cos\left(\frac{(n-\frac{3}{2})\pi}{N_{ch}}\right) \quad \text{for } n = 2, 3, \ldots, N_{ch}+1 \end{aligned} \tag{3.2}$$

where $t = x/c$ is a non-dimensional chordwise parameter and N_{ch} is the number of panels along the chord. $t = -\frac{1}{2}$ at the trailing edge and $t = \frac{1}{2}$ at the leading. This discretisation provides finer spacing at the leading and trailing edges.

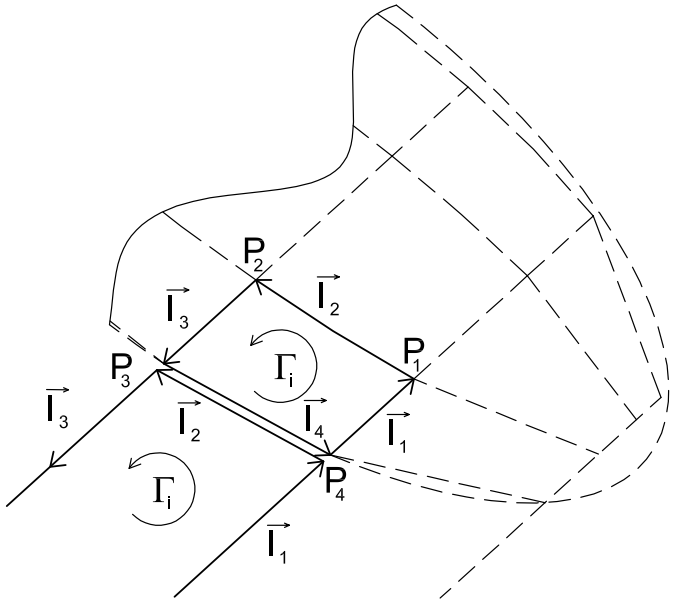

Figure 3.2: *Description of a panel and a trailer for a fictive discretisation.*

3.2.2 The Trailers

The trailing vortex sheet is due to the discretisation reduced to a finite number of horseshoe vortices, see Figure 3.1. A horseshoe vortex consists of three straight line vortices, i.e. two vortices from the trailing edge to infinity downstream and a vortex at the trailing edge combining these two, see Figure 3.2. In order to fulfil the Kutta condition the circulation of the shed horseshoe vortex is equal to the circulation of the adjacent trailing edge panel. The trailers are according to linear theory aligned with the onset flow. Thus, they are parallel to the x-axis, and the geometry is not changed during the calculations.

3.3 Lift and Drag Calculations

The force on the panel sides is found by the Kutta-Joukowsky theorem:

$$\vec{F}_{side} = \rho \vec{U}(\vec{x}) \times \vec{\Gamma}_{side}$$

where $\vec{\Gamma}_{side}$ is the total circulation of the panel side, which is the difference in circulation for the two adjacent panels, see Figure 3.3. $\vec{U}(\vec{x})$ is the total velocity at the midpoint of the panel side given by

$$\vec{U}(\vec{x}) = \vec{U_0}(\vec{x}) + \vec{u}(\vec{x})$$

where $\vec{U_0}(\vec{x})$ is the onset flow and $\vec{u}(\vec{x})$ is the induced velocities from the entire vortex distribution. The induced velocity is found by the law of Biot-Savart, hence the velocity

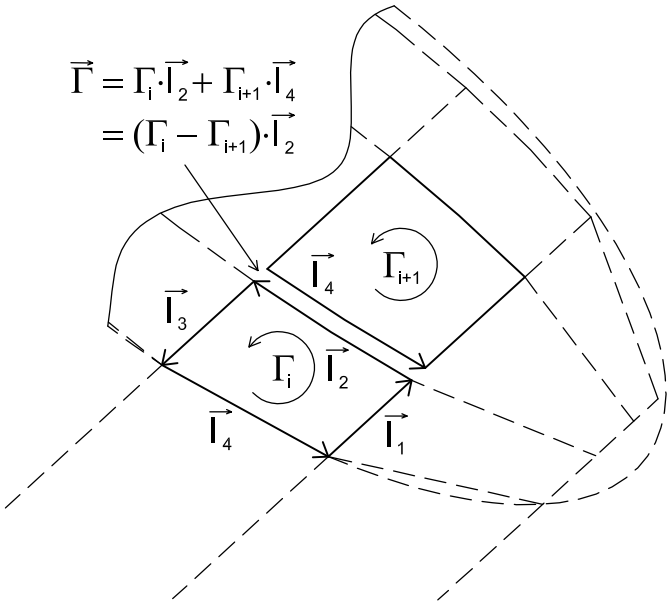

Figure 3.3: *Description of the total circulation at a panel side.*

from one panel in the point $\vec{x}$ is

$$\vec{u}_i^*(\vec{x}) = \frac{\Gamma_i}{4\pi} \sum_{k=1}^{4} \int_0^{s_k} \frac{d\vec{\xi} \times \vec{R}}{|\vec{R}|^3} = \Gamma_i \vec{q}_i^*(\vec{x}) \tag{3.3}$$

where Γ_i is the circulation of the panel, $d\vec{\xi}$ is a length element along the panel side of the length s_k. $\vec{R}$ is the vector from the vortex line element, $d\vec{\xi}$, to the point $\vec{x}$, see Figure 3.4. $\vec{q}_i^*$ is defined as the velocity induced by the entire panel with an unit circulation. The numerical evaluation of the integral is given in Appendix B.

For the optimisation of the planar hydrofoil the two used forces are the lift force, the force in the z-direction, and the drag force, the force in the negative x-direction. The total forces on the hydrofoil are the sum of the forces on each panel, hence the total lift on the hydrofoil is

$$\begin{aligned} L = \vec{F}_z = \rho \sum_{m=1}^{M_{sp}} \Gamma_{1+(m-1)N_{ch}} \Bigg\{ & \sum_{n=1}^{N_{ch}} \kappa_n \sum_{k=1}^{4} \big[l_{y,n+(m-1)N_{ch},k} U_x(\vec{x}_{n+(m-1)N_{ch},k}) \\ & - l_{x,n+(m-1)N_{ch},k} U_y(\vec{x}_{n+(m-1)N_{ch},k}) \big] - l_{y,1+(m-1)N_{ch},4} U_x(\vec{x}_{1+(m-1)N_{ch},4}) \\ & + l_{x,1+(m-1)N_{ch},4} U_y(\vec{x}_{1+(m-1)N_{ch},4}) \Bigg\} \end{aligned} \tag{3.4}$$

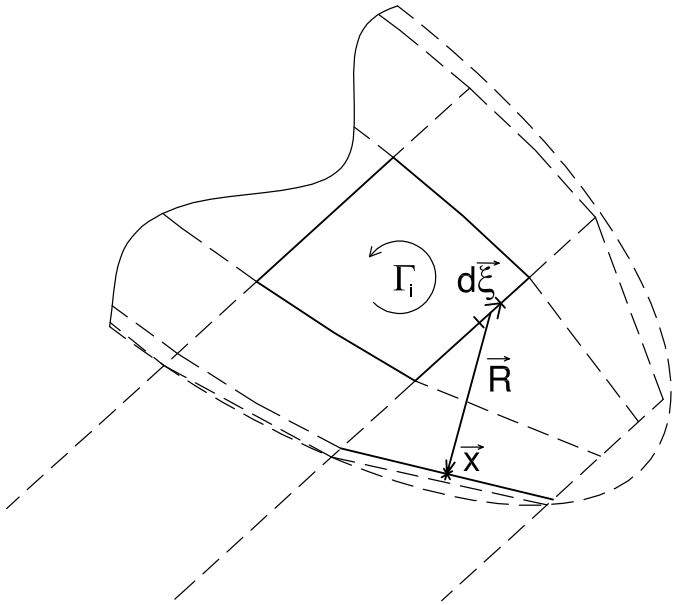

Figure 3.4: *Description of the parameters used in the Biot-Savart law.*

and the total drag for the hydrofoil is

$$D = -\vec{F}_x = -\rho \sum_{m=1}^{M_{sp}} \Gamma_{1+(m-1)N_{ch}} \left\{ \sum_{n=1}^{N_{ch}} \kappa_n \sum_{k=1}^{4} \left[l_{z,n+(m-1)N_{ch},k} U_y(\vec{x}_{n+(m-1)N_{ch},k}) \right.\right. \\ \left. - l_{y,n+(m-1)N_{ch},k} U_z(\vec{x}_{n+(m-1)N_{ch},k}) \right] - l_{z,1+(m-1)N_{ch},4} U_y(\vec{x}_{1+(m-1)N_{ch},4}) \\ \left. + l_{y,1+(m-1)N_{ch},4} U_z(\vec{x}_{1+(m-1)N_{ch},4}) \right\} \quad (3.5)$$

where $\vec{x}_{i,k}$ is the coordinate of the midpoint of side k of panel i, $U_{x,y,z}(\vec{x})$ is the $x-, y-, z-$component, respectively, of the total velocity in position $\vec{x}$ and $l_{x,y,z,i,k}$ is the $x-, y-, z-$component, respectively, of the vector $\vec{l}_k$ for panel i and side k. The circulation $\Gamma_{1+(m-1)N_{ch}}$ in the above expressions corresponds to the circulation of the trailing vortices. The chordwise distribution of circulation is given by the weight function κ_n.

3.4 The Weight Function

According to Munk's displacement theorem, which states that the induced drag for a lifting surface only depends on the total chordwise circulation and not on the chordwise distribution of the circulation, see von Kármán and Burgers (1963), it is necessary to specify the chordwise distribution of circulation in order to achieve convergence of the optimisation. Therefore, the optimisation problem is reduced to finding the optimum distribution of the total circulation

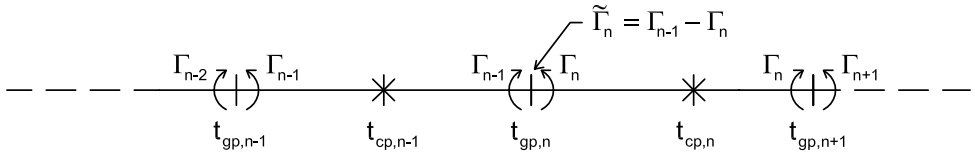

Figure 3.5: *Description of the total circulation at a panel side.*

for each chordwise strip, which corresponds to the circulation of the shed vortex. The chordwise distribution of circulation is specified through a weight function.

For a two-dimensional section with a discrete distribution of vortices, as depicted in Figure 3.5, the weight function is defined as

$$\tilde{\kappa}_n \equiv \frac{\tilde{\Gamma}_n}{\Gamma_{tot}} \tag{3.6}$$

where $\tilde{\Gamma}_n$ is the total circulation at grid point n. This is equal to the difference in circulation for two adjacent panels, see Figure 3.5. Γ_{tot} is the total circulation for the chordwise strip, which is given by

$$\Gamma_{tot} = \int_{-c/2}^{c/2} \gamma(x)dx \tag{3.7}$$

where $\gamma(x)$ is the given continuous distribution of circulation. This is a combination of the flat plate distribution, see Equation (2.20), and the rooftop distribution, see Equation (2.23).

The circulation for the discrete vortex can be approximated by

$$\tilde{\Gamma}_n = c \int_{t_{cp,n-1}}^{t_{cp,n}} \gamma(t')dt' \approx \gamma(t_{gp,n})\big(t_{cp,n} - t_{cp,n-1)}\big) \tag{3.8}$$

where $t_{cp,n}$ is the location of the control point, which is (Lan, 1974):

$$t_{cp,n} = -\tfrac{1}{2}\cos\left(\frac{(n-1)\pi}{N_{ch}}\right) \quad \text{for } n = 1, 2, \ldots, N_{ch} \tag{3.9}$$

for the discretisation given in Equation (3.2). By inserting Equation (3.9) in Equation (3.8) the discrete circulation can be approximated by

$$\tilde{\Gamma}_n \approx \gamma(t_{gp,n})C\sqrt{\big(\tfrac{1}{2} - t_{gp,n}\big)\big(\tfrac{1}{2} + t_{gp,n}\big)} \tag{3.10}$$

where C is a constant and the grid point $t_{gp,n}$ is given by Equation (3.2), hence the weight function is

$$\tilde{\kappa}_n = \frac{\gamma(t_{gp,n})\sqrt{\big(\tfrac{1}{2} - t_{gp,n}\big)\big(\tfrac{1}{2} + t_{gp,n}\big)}}{\sum_{i=1}^{N_{ch}+1} \gamma(t_{gp,i})\sqrt{\big(\tfrac{1}{2} - t_{gp,i}\big)\big(\tfrac{1}{2} + t_{gp,i}\big)}} \quad \text{for } n = 1, 2, \ldots, N_{ch}+1 \tag{3.11}$$

Table 3.1: *Induced vertical velocity at the grid points with the cosine and equidistant discretisations. The flat plate distribution of circulation is used. The theoretical value is* $u_z/U_0 = -0.318$*. It should be noted that the t-coordinate for the same grid point number is different for the two discretisations.*

	Cosine	Equidistant
Grid point	u_z/U_0	u_z/U_0
1	-0.318	-0.274
2	-0.288	-0.290
3	-0.288	-0.296
4	-0.286	-0.297
5	-0.282	-0.297
6	-0.274	-0.295
7	-0.254	-0.288
8	-0.180	-0.261
9	0.737	0.389

As the circulation in the vortex-lattice method is applied to the panels the weight function is changed so the weight function gives the circulation of the panels. The relation between the weight function, $\tilde{\kappa}$, and the circulation of the panels is

$$\begin{aligned} \tilde{\kappa}_1 &= 0 \\ \tilde{\kappa}_n &= \frac{\Gamma_{n-1} - \Gamma_n}{\Gamma_{tot}} \quad \text{for } n = 2, 3, \ldots, N_{ch} \\ \tilde{\kappa}_{N_{ch}+1} &= \frac{\Gamma_{N_{ch}}}{\Gamma_{tot}} \end{aligned} \tag{3.12}$$

From this the weight function for the circulation of the panels, κ, becomes

$$\kappa_n = \sum_{i=n+1}^{N_{ch}+1} \left((1-\nu)\tilde{\kappa}_i^{RT} + \nu\tilde{\kappa}_i^{FP} \right), \quad \text{for } n = 1, 2, \ldots, N_{ch} \tag{3.13}$$

where $\tilde{\kappa}_i^{FP}$ is the weight function for the flat plate distribution and $\tilde{\kappa}_i^{RT}$ is for the rooftop distribution. ν is the ratio of the flat plate distribution.

3.4.1 Validation of the Weight Function

The weight function has been validated for a two-dimensional section with either the flat plate distribution of circulation, see Equation (2.20) or the rooftop distribution with $\mathbf{a} = 0.8$, see Equation (2.23). The validation is made for two different discretisations, both with the

Table 3.2: *Induced vertical velocity at the control points with the cosine and equidistant discretisations. The flat plate distribution of circulation is used. The theoretical value is* $u_z/U_0 = -0.318$*. It should be noted that the t-coordinate for the same control point number is different for the two discretisations.*

	Cosine	Equidistant
Control point	u_z/U_0	u_z/U_0
1	-0.318	-0.310
2	-0.318	-0.313
3	-0.318	-0.315
4	-0.318	-0.318
5	-0.318	-0.322
6	-0.318	-0.329
7	-0.318	-0.347
8	-0.318	-0.421

cosine discretisation given by Lan (1974), see Equation (3.2) and Equation (3.9), and with an equidistant discretisation given by James (1972). For this discretisation the grid points and control points are located at

$$\begin{aligned} t_{gp,1} &= -\tfrac{1}{2} \\ t_{gp,n} &= \frac{i-5/4}{N_{ch}} - \frac{1}{2} \quad \text{for } n = 2, 3, \ldots, N_{ch}+1 \\ t_{cp,n} &= \frac{i-3/4}{N_{ch}} - \frac{1}{2} \quad \text{for } n = 1, 2, \ldots, N_{ch} \end{aligned} \tag{3.14}$$

The weight function has been modified for the equidistant distribution.

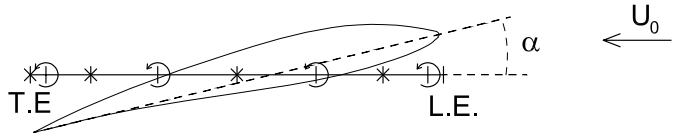

Figure 3.6: *The location of the vortices and the control points, for the cosine discretisation, for the two-dimensional calculations.*

In accordance with linear theory the vortices are distributed along the x-axis, see Figure 3.6. The vertically induced velocity from the discrete distribution should, as the velocity from the continuous distribution, fulfil the boundary condition in Equation (2.19). The boundary condition requires that the induced velocity for the flat plate distribution is constant along the chord and for the rooftop distribution the velocity should equal the slope of the mean line.

Table 3.3: *Induced vertical velocity at the grid points with the cosine and equidistant discretisations. The NACA* $\mathbf{a} = 0.8$ *rooftop distribution of circulation is used. The ratio between the slope of the mean line and the calculated velocities is also shown. The theoretical value for this ratio is* $z'_f/(u_z/U_0) = 0.5$*. It should be noted that the t-coordinate for the same grid point number is different for the two discretisations.*

	Cosine		Equidistant	
Grid point	u_z/U_0	$z'_f/(u_z/U_0)$	u_z/U_0	$z'_f/(u_z/U_0)$
1	-0.463	0.498	-0.424	0.544
2	-0.452	0.547	-0.442	0.641
3	-0.447	0.633	-0.338	0.535
4	-0.306	0.578	-0.179	0.504
5	-0.113	0.547	-0.073	0.459
6	0.030	0.613	0.020	0.833
7	0.171	0.576	0.115	0.601
8	0.341	0.588	0.232	0.593
9	0.581	0.689	0.429	0.685

The equation for the NACA rooftop mean lines is given in e.g. Abbott and von Doenhoff (1959) and is reproduced in Appendix C.

The vertically induced velocity for the discrete vortex distribution is

$$u_{z,j} = \frac{1}{2\pi c} \sum_{i=1}^{N_{ch}} \frac{\tilde{\Gamma}_i}{t_{gp,i} - t_j} \tag{3.15}$$

where t_j is the point where the velocity is calculated and $t_{gp,i}$ is the location of the vortex with the circulation $\tilde{\Gamma}_i$, which will be numerically negative.

The vertically induced velocity has been calculated at the grid points and at the control points for both distributions of circulation and both discretisations. Table 3.1 shows the induced velocity at the grid points for the flat plate with both discretisations. It is seen that the velocity is varying and that the velocity at the grid point nearest to the leading edge even has an opposite sign relative to the others. Table 3.2 shows the induced velocity at the control points for the flat plate with both discretisations. These results show that the cosine discretisation gives the exact constant velocity at all control points, unlike the equidistant discretisation, which has a small variation.

Table 3.3 shows the induced velocity at the grid points and Table 3.4 shows the velocity at the control points for the NACA $\mathbf{a} = 0.8$ rooftop distribution with both discretisations. The ratio between the induced velocity and the mean line slope is also shown in the tables. This ratio should be constant if the boundary condition is fulfilled. From the tables it is seen that

Table 3.4: *Induced vertical velocity at the control points with the cosine and equidistant discretisations. The NACA* $\mathbf{a} = 0.8$ *rooftop distribution of circulation is used. The ratio between the slope of the mean line and the calculated velocities is also shown. The theoretical value for this ratio is* $z'_f/(u_z/U_0) = 0.5$*. It should be noted that the t-coordinate for the same control point number is different for the two discretisations.*

	Cosine		Equidistant	
Control point	u_z/U_0	$z'_f/(u_z/U_0)$	u_z/U_0	$z'_f/(u_z/U_0)$
1	-0.463	0.498	-0.508	0.524
2	-0.540	0.501	-0.507	0.517
3	-0.531	0.505	-0.246	0.515
4	-0.211	0.519	-0.123	0.490
5	-0.040	0.521	-0.026	0.316
6	0.113	0.505	0.067	0.633
7	0.284	0.509	0.169	0.591
8	0.535	0.515	0.312	0.610

this ratio is varying both at the grid points and at the control points, but the variation at the control points is smaller and again the cosine discretisation is superior to the equidistant discretisation.

Another important aspect is the calculation of the drag of the profile, which should be zero for a two-dimensional section. The total drag of a section with a discrete distribution of vortices is as follows, see Equation (3.5):

$$D = \rho \sum_{i=1}^{N_{ch}} u_{z,i} \tilde{\Gamma}_i \tag{3.16}$$

where $u_{z,i}$ is the vertically induced velocity at the grid point i. The velocity can be calculated either directly at the grid points, so the velocity corresponds to the results in Tables 3.1 and 3.3, or as an interpolation of the velocities at the control points, which are given in Tables 3.2 and 3.4. The calculations show that the drag for both the flat plate and the rooftop distribution is zero only if the velocities are calculated directly at the grid points. This is the case for both discretisations. For the flat plate this is because the velocity at the grid point nearest to the leading edge has an opposite sign, hence the force calculated here is opposite the drag on the remaining part of the profile. This force corresponds to the leading edge suction force.

From the above validation it is seen that the continuous distribution of circulation can be discretised by use of the weight function from Equation (3.13). The validation shows furthermore that the cosine discretisation is the most accurate of the two discretisations, for the flat plate it is even exact. And finally the validation shows it is important that the

velocities, used for the force calculations, are calculated directly at the points where the discrete vortices are placed.

3.5 Optimisation

In the optimisation for the hydrofoil the aim is to find the distribution of circulation which gives the minimum drag for a specified lift. The distribution is found by solving a variational problem.

3.5.1 Optimisation Procedure

As the optimisation procedure is identical for the hydrofoil and for the propeller the main results will only be given here and a more thorough description of the procedure is postponed until the propeller is treated, see Chapter 4.

The functional to be minimised is

$$H(\vec{\Gamma}, \lambda) = D(\vec{\Gamma}) + \lambda(L(\vec{\Gamma}) - L_r) \tag{3.17}$$

where $\vec{\Gamma}$ is the sought distribution of circulation for the trailers, L_r is the required lift, and λ is the Lagrange multiplier.

The optimum distribution is found by setting the partial derivatives with respect to $\vec{\Gamma}$ and λ of the functional equal to zero. This gives a non-linear system of equations for the unknown circulations and the Lagrange multiplier. The system is linearised and therefore iterations are necessary in order to obtain the solution.

The linear system of equations is

$$\begin{aligned} &\frac{\partial D(\vec{\Gamma})}{\partial \Gamma_{1+(m-1)M_{sp}}} + \lambda^{t-1}\frac{\partial L(\vec{\Gamma})}{\partial \Gamma_{1+(m-1)M_{sp}}} + \lambda^{t}\frac{\partial L(\vec{U_0})}{\partial \Gamma_{1+(m-1)M_{sp}}} = -\frac{\partial D(\vec{U_0})}{\partial \Gamma_{1+(m-1)M_{sp}}} \\ &L(\vec{\Gamma}) = L_r - L(\vec{U_0}) \end{aligned} \tag{3.18}$$

for $m = 1, 2, ..., M_{sp}$. $\partial L(\vec{U_0})/\partial \Gamma_{1+(m-1)M_{sp}}$ is the part of $\partial L/\partial \Gamma_{1+(m-1)M_{sp}}$ which is independent of the circulation and $\partial D(\vec{U_0})/\partial \Gamma_{1+(m-1)M_{sp}}$ is the similar part for the drag. $L(\vec{U_0})$ is the part of the lift which is independent of the circulation. The superscript $t-1$ refers to the value from the previous step in the iteration. The partial derivative for the drag is

found by differentiating Equation (3.5), thus

$$\begin{aligned}
\frac{\partial D}{\partial \Gamma_{1+(m-1)N_{ch}}} = -\rho\Bigg\{ & \sum_{n=1}^{N_{ch}} \kappa_n \sum_{k=1}^{4} \big\{ l_{z,n+(m-1)N_{ch},k} U_{0,y}(\vec{x}_{n+(m-1)N_{ch},k}) \\
& - l_{y,n+(m-1)N_{ch},k} U_{0,z}(\vec{x}_{n+(m-1)N_{ch},k}) \big\} \\
& - l_{z,1+(m-1)N_{ch},4} U_{0,y}(\vec{x}_{1+(m-1)N_{ch},4}) \\
& + l_{y,1+(m-1)N_{ch},4} U_{0,z}(\vec{x}_{1+(m-1)N_{ch},4}) \\
& + \sum_{j=1}^{M_{sp}} \Gamma_{1+(j-1)N_{ch}} \Bigg[\sum_{n=1}^{N_{ch}} \kappa_n \sum_{i=1}^{N_{ch}} \kappa_i \sum_{k=1}^{4} \\
& \big\{ l_{z,n+(m-1)N_{ch},k} q^*_{y,i+(j-1)N_{ch}}(\vec{x}_{n+(m-1)N_{ch},k}) \\
& - l_{y,n+(m-1)N_{ch},k} q^*_{z,i+(j-1)N_{ch}}(\vec{x}_{n+(m-1)N_{ch},k}) \\
& + l_{z,i+(j-1)N_{ch},k} q^*_{y,n+(m-1)N_{ch}}(\vec{x}_{i+(j-1)N_{ch},k}) \\
& - l_{y,i+(j-1)N_{ch},k} q^*_{z,n+(m-1)N_{ch}}(\vec{x}_{i+(j-1)N_{ch},k}) \big\} \\
& + \sum_{i=1}^{N_{ch}} \kappa_i \big\{ -l_{z,1+(m-1)N_{ch},4} q^*_{y,i+(j-1)N_{ch}}(\vec{x}_{1+(m-1)N_{ch},4}) \\
& + l_{y,1+(m-1)N_{ch},4} q^*_{z,i+(j-1)N_{ch}}(\vec{x}_{1+(m-1)N_{ch},4}) \big\} \\
& + \sum_{n=1}^{N_{ch}} \kappa_n \big\{ -l_{z,1+(j-1)N_{ch},4} q^*_{y,n+(m-1)N_{ch}}(\vec{x}_{1+(j-1)N_{ch},4}) \\
& + l_{y,1+(j-1)N_{ch},4} q^*_{z,n+(m-1)N_{ch}}(\vec{x}_{1+(j-1)N_{ch},4}) \big\} \Bigg] \Bigg\}
\end{aligned} \tag{3.19}$$

for $m = 1, 2, \ldots, M_{sp}$

and the partial derivative for the lift is found by differentiating Equation (3.4):

$$\begin{aligned}
\frac{\partial L}{\partial \Gamma_{1+(m-1)N_{ch}}} = \rho\Bigg\{ & \sum_{n=1}^{N_{ch}} \kappa_n \sum_{k=1}^{4} \big\{ l_{y,n+(m-1)N_{ch},k} U_{0,x}(\vec{x}_{n+(m-1)N_{ch},k}) \\
& - l_{x,n+(m-1)N_{ch},k} U_{0,y}(\vec{x}_{n+(m-1)N_{ch},k}) \big\} \\
& - l_{y,1+(m-1)N_{ch},4} U_{0,x}(\vec{x}_{1+(m-1)N_{ch},4}) \\
& + l_{x,1+(m-1)N_{ch},4} U_{0,y}(\vec{x}_{1+(m-1)N_{ch},4}) \\
& + \sum_{j=1}^{M_{sp}} \Gamma_{1+(j-1)N_{ch}} \Bigg[\sum_{n=1}^{N_{ch}} \kappa_n \sum_{i=1}^{N_{ch}} \kappa_i \sum_{k=1}^{4} \\
& \big\{ l_{y,n+(m-1)N_{ch},k} q^*_{x,i+(j-1)N_{ch}}(\vec{x}_{n+(m-1)N_{ch},k}) \\
& - l_{x,n+(m-1)N_{ch},k} q^*_{y,i+(j-1)N_{ch}}(\vec{x}_{n+(m-1)N_{ch},k}) \\
& + l_{y,i+(j-1)N_{ch},k} q^*_{x,n+(m-1)N_{ch}}(\vec{x}_{i+(j-1)N_{ch},k}) \\
& - l_{x,i+(j-1)N_{ch},k} q^*_{y,n+(m-1)N_{ch}}(\vec{x}_{i+(j-1)N_{ch},k}) \big\}
\end{aligned}$$

$$
\begin{aligned}
&+ \sum_{i=1}^{N_{ch}} \kappa_i \big\{ -l_{y,1+(m-1)N_{ch},4} q^*_{x,i+(j-1)N_{ch}}(\vec{x}_{1+(m-1)N_{ch},4}) \\
&+ l_{x,1+(m-1)N_{ch},4} q^*_{y,i+(j-1)N_{ch}}(\vec{x}_{1+(m-1)N_{ch},4}) \big\} \\
&+ \sum_{n=1}^{N_{ch}} \kappa_n \big\{ -l_{y,1+(j-1)N_{ch},4} q^*_{x,n+(m-1)N_{ch}}(\vec{x}_{1+(j-1)N_{ch},4}) \\
&+ l_{x,1+(j-1)N_{ch},4} q^*_{y,n+(m-1)N_{ch}}(\vec{x}_{1+(j-1)N_{ch},4}) \big\} \Bigg] \Bigg\}
\end{aligned}
\tag{3.20}
$$

for $m = 1, 2, \ldots, M_{sp}$

where $U_{0,x,y,z}$ is the $x-, y-, z$-component, respectively, of the onset flow, and $q^*_{x,y,z,i}(\vec{x}_{j,k})$ is the $x-, y-, z$-component, respectively, of the induced velocity from panel i in point $\vec{x}_{j,k}$, which is the midpoint of side k of panel j.

The optimum distribution of circulation is obtained by inserting the above derivatives in Equation (3.18) and iterating until convergence.

3.5.2 Results for the Optimisation of an Elliptic Hydrofoil

As previously mentioned, Prandtl found analytically the spanwise distribution of circulation for a planar wing with elliptic planform and high aspect ratio, see e.g. Breslin and Andersen (1994). Prandtl used a lifting-line model for the wing, which is a valid assumption for the high aspect ratios, and found that the distribution was elliptic, thus the spanwise circulation is

$$\Gamma(y) = -\Gamma_0 \sqrt{1 - \left(\frac{y}{b}\right)^2} \tag{3.21}$$

where Γ_0 is the maximum circulation and b is the semispan of the wing.

This distribution corresponds to the optimum distribution of circulation for the planar wing, which can be seen from the following considerations.

For the elliptic distribution of circulation the vertically induced velocity along the lifting line has the constant value

$$u_z(y) = -\frac{\Gamma_0}{4b} \tag{3.22}$$

As the induced drag is

$$D(y) = \rho u_z(y) \Gamma(y) \tag{3.23}$$

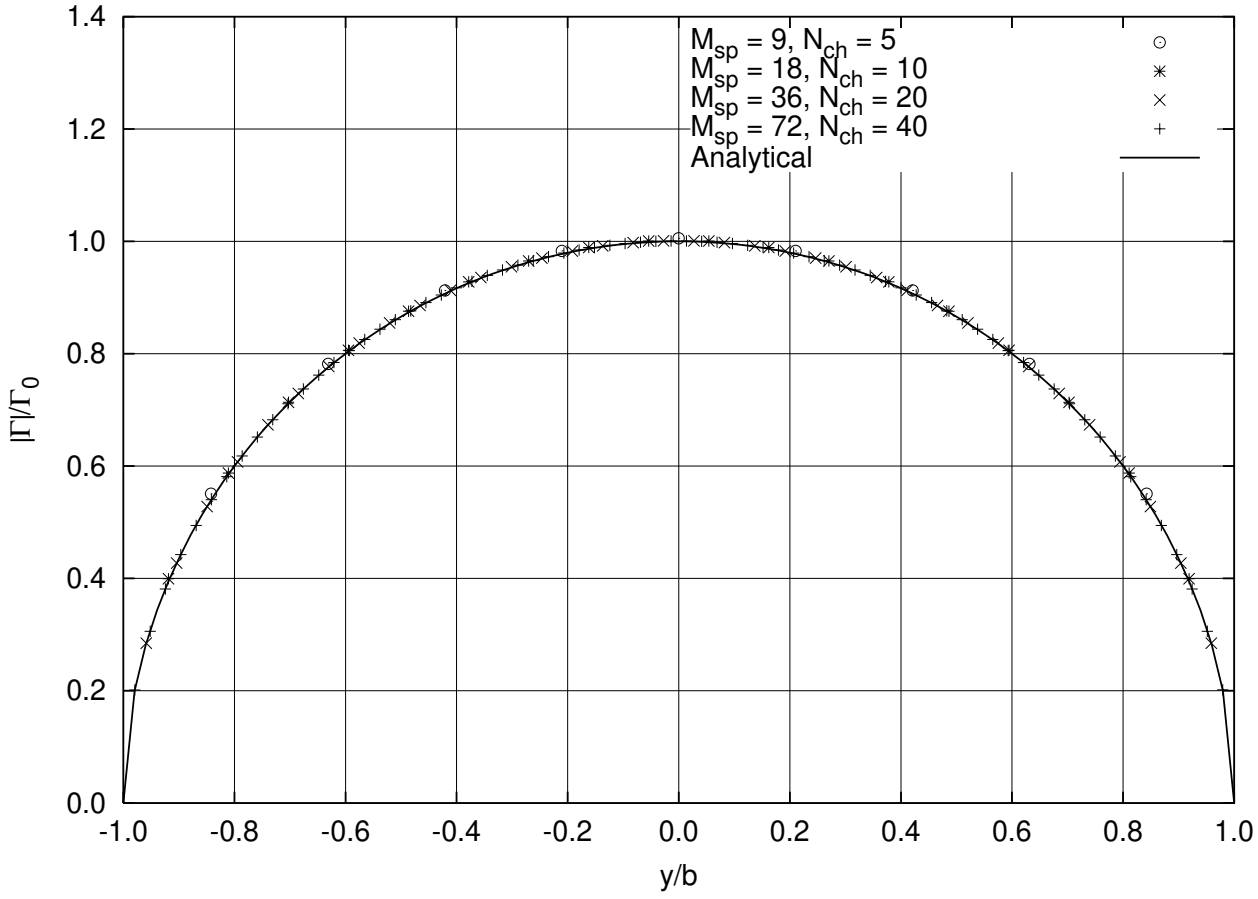

Figure 3.7: *Optimum distribution of circulation for an elliptic hydrofoil, with* $b = 6.0\,m$, $c_0 = 3.0\,m$, $U_0 = 10.0\,{}^{m}/_{s}$, *and* $C_{L,r} = 0.345$.

and the sectional drag coefficient is

$$C_D(y) = \frac{D(y)}{\frac{1}{2}\rho U_0^2 c(y)} = \frac{\Gamma_0^2}{2U_0^2 b c_0} \tag{3.24}$$

it is seen that the sectional drag coefficient is constant. It has been used that the chord length is

$$c(y) = c_0\sqrt{1 - \left(\frac{y}{b}\right)^2} \tag{3.25}$$

where c_0 is the maximum chord length. The sectional lift coefficient is constant also, as the lift is given by

$$L(y) = -\rho U_0 \Gamma(y) \tag{3.26}$$

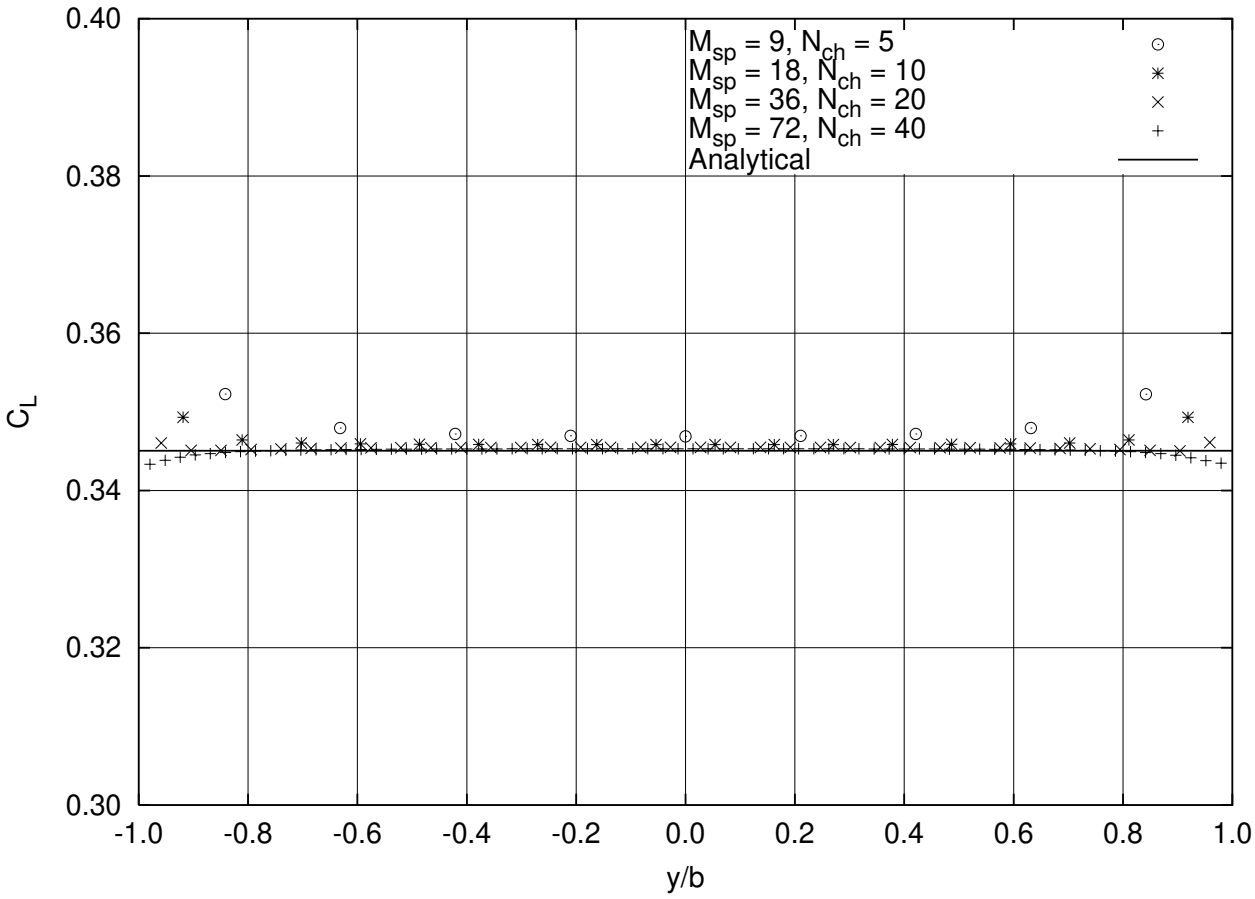

Figure 3.8: *Sectional lift coefficient for an elliptic hydrofoil, with* $b = 6.0\ m$, $c_0 = 3.0\ m$, $U_0 = 10.0\ {}^{m}/_{s}$, *and* $C_{L,r} = 0.345$.

and the sectional lift coefficient is

$$C_L(y) = \frac{L(y)}{\frac{1}{2}\rho U_0^2 c(y)} = \frac{\Gamma_0}{\frac{1}{2}U_0 c_0} \tag{3.27}$$

Therefore, the sectional lift to drag ratio will be constant along the entire span of the wing. If this ratio is varying the overall ratio could be increased by moving the load to the point with the highest lift to drag ratio. Thus, the elliptic distribution of circulation corresponds to the optimum distribution for a wing with elliptic planform.

For a wing with elliptic planform and elliptic distribution of circulation the maximum circulation is found from the required lift coefficient, $C_{L,r}$:

$$\Gamma_0 = \tfrac{1}{2}U_0 c_0 C_{L,r} \tag{3.28}$$

and the corresponding angle of attack is (Breslin and Andersen, 1994):

$$\alpha = \frac{\Gamma_0(4b + \pi c_0)}{4\pi U_0 b c_0} \tag{3.29}$$

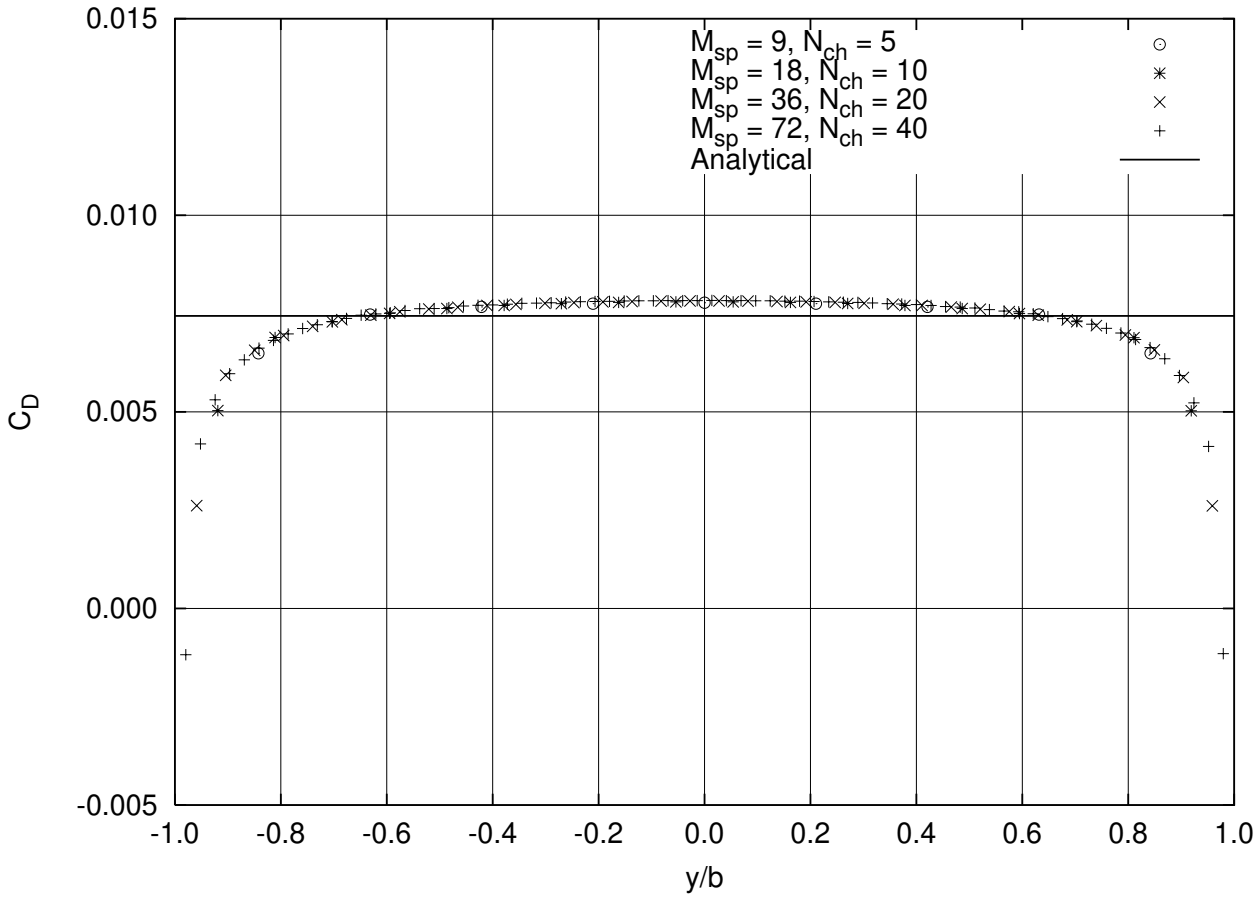

Figure 3.9: *Sectional drag coefficient for an elliptic hydrofoil, with* $b = 6.0\,m$, $c_0 = 3.0\,m$, $U_0 = 10.0\,{}^{m}/_{s}$, *and* $C_{L,r} = 0.345$.

The surface optimisation has been tested on an elliptic hydrofoil with the following input data:

$$b = 6.0\,m, \quad c_0 = 3.0\,m, \quad U_0 = 10.0\,{}^{\mathrm{m}}/_{\mathrm{s}}, \quad C_{L,r} = 0.345, \quad \text{and } 10^3 C^{tot}_{D,ana} = 7.441.$$

The chordwise distribution of circulation corresponds to half a flat plate and half a NACA **a** = 0.8 rooftop distribution ($\nu = 0.5$). The discretisation is equidistant spanwise, see Equation (3.1), and cosine chordwise, see Equation (3.2). The specified lift corresponds to a 4.4° angle of attack, which is within the limits of the linear theory.

The optimisation has been performed with four different grid sizes from $M_{sp} \times N_{ch} = 9 \times 5$ to 72×40. Table 3.5 shows the minimised drag as a function of the number of panels. It is seen that the agreement with the analytical solution is very good already for nine spanwise and five chordwise panels. Furthermore, it is seen that the difference between the analytical and the numerical solution is decreasing for increasing number of panels.

Table 3.5: *Minimised total drag coefficient, C_D^{tot}, as a function of the number of panels for an elliptic planform, with $b = 6.0\,m$, $c_0 = 3.0\,m$, $U_0 = 10.0\,{}^{m}/_{s}$, $C_{L,r} = 0.345$, and $10^3 C_{D,ana}^{tot} = 7.441$.*

M_{sp}	N_{ch}	$10^3 C_D^{tot}$	$C_{D,ana}^{tot}/C_D^{tot}$
9	5	7.430	1.0015
18	10	7.428	1.0018
36	20	7.435	1.0008
72	40	7.438	1.0004

Figure 3.7 shows the distribution of circulation for the trailers. It is seen that the distributions for all four calculations fit the analytical solution very well.

Figure 3.8 shows the sectional lift coefficient. It is seen that the distribution is almost constant along the span. The 9×5 grid is only constant over 50% of the span but already from 18×10 the C_L is constant over approximately 80% of the span. Close to the tips all the grids deviate from the constant value. This is due to the rapid decrease of the chord length at the tips, which is not captured by the discretisation. Furthermore, it is seen that the sectional lift coefficient is higher than the analytical for all the grids. It is most pronounced for the 9×5 grid in Figure 3.8. This is because the lift coefficient, due to the discretisation, is actually based on a planform area which is smaller than the area of the ellipse, while the total lift has the required value, thus the lift coefficient for the discretised hydrofoil will be higher.

Figure 3.9 shows the sectional drag coefficient. It is observed that even though the total drag coefficient is well predicted there is a difference between the analytical and numerical sectional drag coefficient, as the numerical C_D is only constant on a small part of the span and tends to zero at the tips. This variation is due to the discretisation and the relatively small chord length at the tips.

For the above optimisation the only induced velocity is the vertical velocity u_z and the onset flow is parallel to the x-axis. Furthermore, the length of the panel sides in the y-direction l_y is equal for all the panels. By using this it is seen that the calculations of the lift and the drag can be reduced. For the lift, see Equation (3.4), it is observed that the lifts of the individual panels cancel each other and that the lift comes from the spanwise vortex at the trailing edge, which combines the trailers into a horseshoe vortex. For the drag, see Equation (3.5), it is seen that the drag from the individual panels depends on the difference in induced velocity at the sides 2 and 4, which will be small.

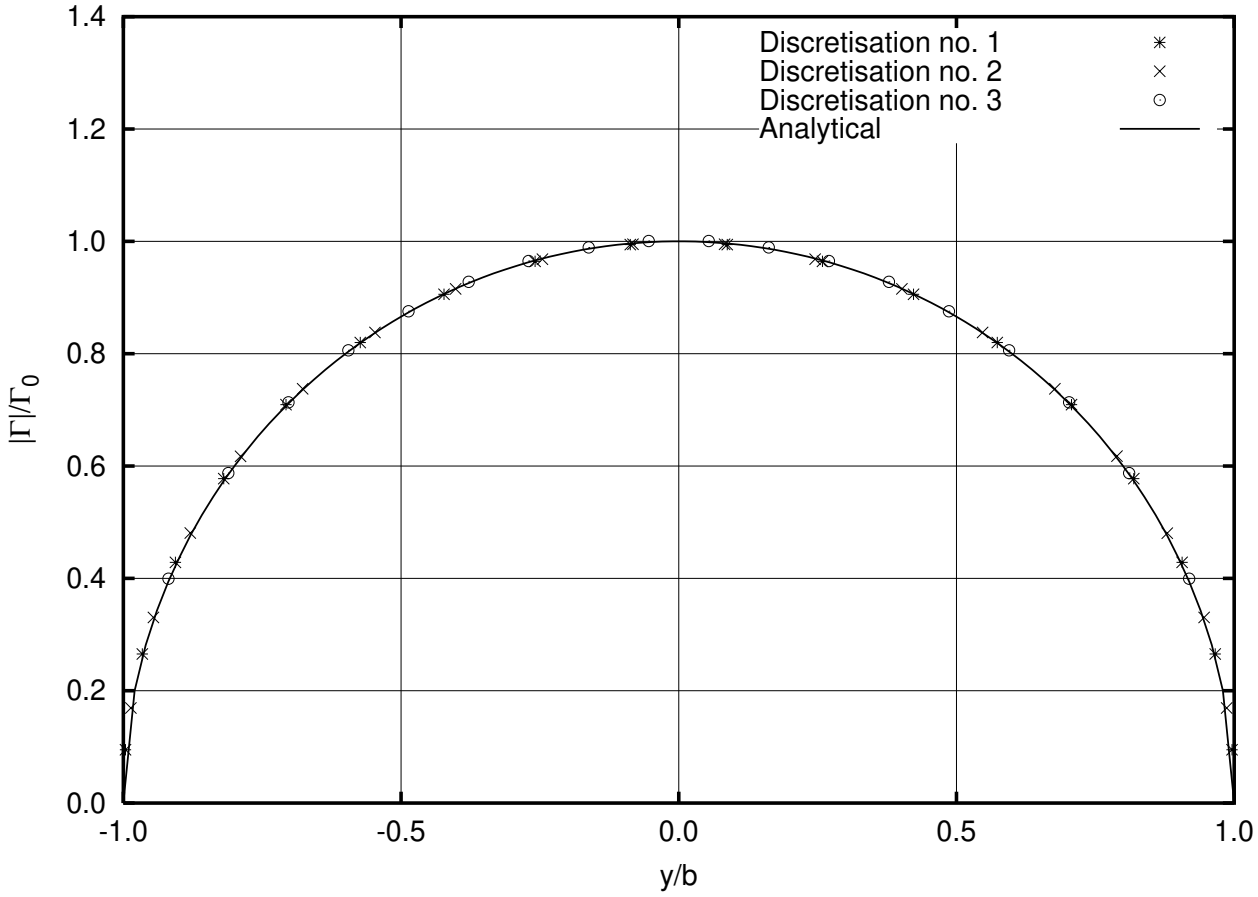

Figure 3.10: *Optimum distribution of circulation for an elliptic planform with different spanwise discretisations for* $M_{sp} \times N_{ch} = 18 \times 10$, $b = 6.0\,m$, $c_0 = 3.0\,m$, $U_0 = 10.0\,{}^{m}/_{s}$, *and* $C_{L,r} = 0.345$.

3.6 Spanwise Discretisation

To determine the most suitable spanwise discretisation three different discretisations have been tested for the optimisation of the hydrofoil.

Discretisation no. 1 (Streckwall, 1994):

$$s_{gp,i} = -\cos\left(\frac{(i-1)\pi}{M_{sp}}\right), \quad i = 1, 2, \ldots, M_{sp}+1$$

$$s_{cp,i} = -\cos\left(\frac{(i-\frac{1}{2})\pi}{M_{sp}}\right), \quad i = 1, 2, \ldots, M_{sp}$$

Here the outermost vortices are placed at the tips of the wing and due to the cosine function the spacing is finer in the tip regions. Because the number of chordwise panels is constant,

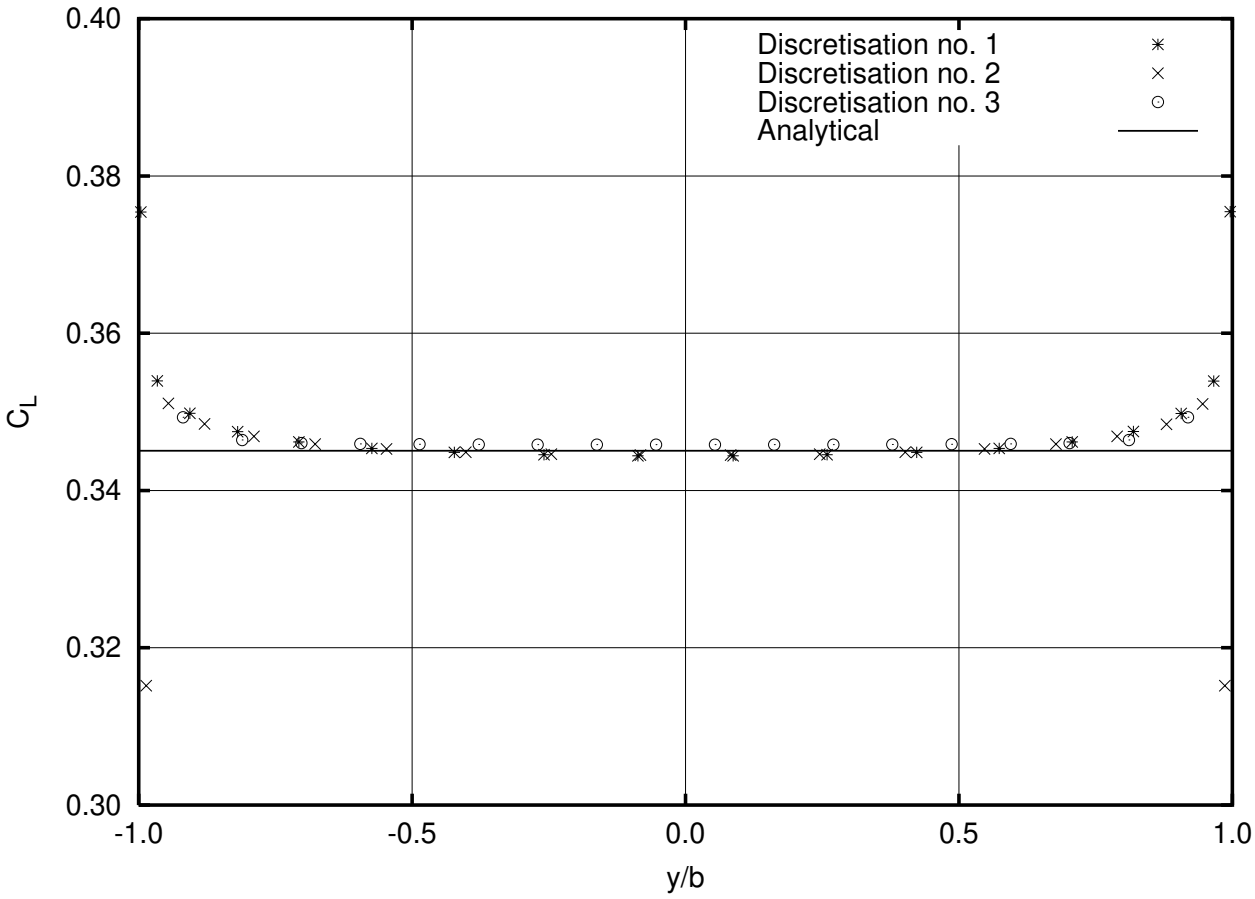

Figure 3.11: *Sectional lift coefficient for an elliptic planform with different spanwise discretisations for* $M_{sp} \times N_{ch} = 18 \times 10$, $b = 6.0\,m$, $c_0 = 3.0\,m$, $U_0 = 10.0\,{}^{m}/_{s}$, *and* $C_{L,r} = 0.345$.

it is necessary to have a finite chord length at the tip, in order to avoid numerical problems.

Discretisation no. 2 (Kerwin and Lee, 1978):

$$s_{gp,i} = -\cos\left(\frac{(i-\frac{1}{2})\pi}{M_{sp}+1}\right), \quad i = 1, 2, \ldots, M_{sp}+1$$

$$s_{cp,i} = -\cos\left(\frac{i\pi}{M_{sp}+1}\right), \quad i = 1, 2, \ldots, M_{sp}$$

This is also a cosine discretisation but unlike no. 1 the vortices are moved a little inward from the tips. This discretisation corresponds to the Lan (1974) discretisation transformed to the spanwise direction.

Discretisation no. 3 is the equidistant discretisation from Equation (3.1), where the control points are located at

$$s_{cp,i} = \tfrac{1}{2}(s_{gp,i} + s_{gp,i+1}), \quad i = 1, 2, \ldots, M_{sp}$$

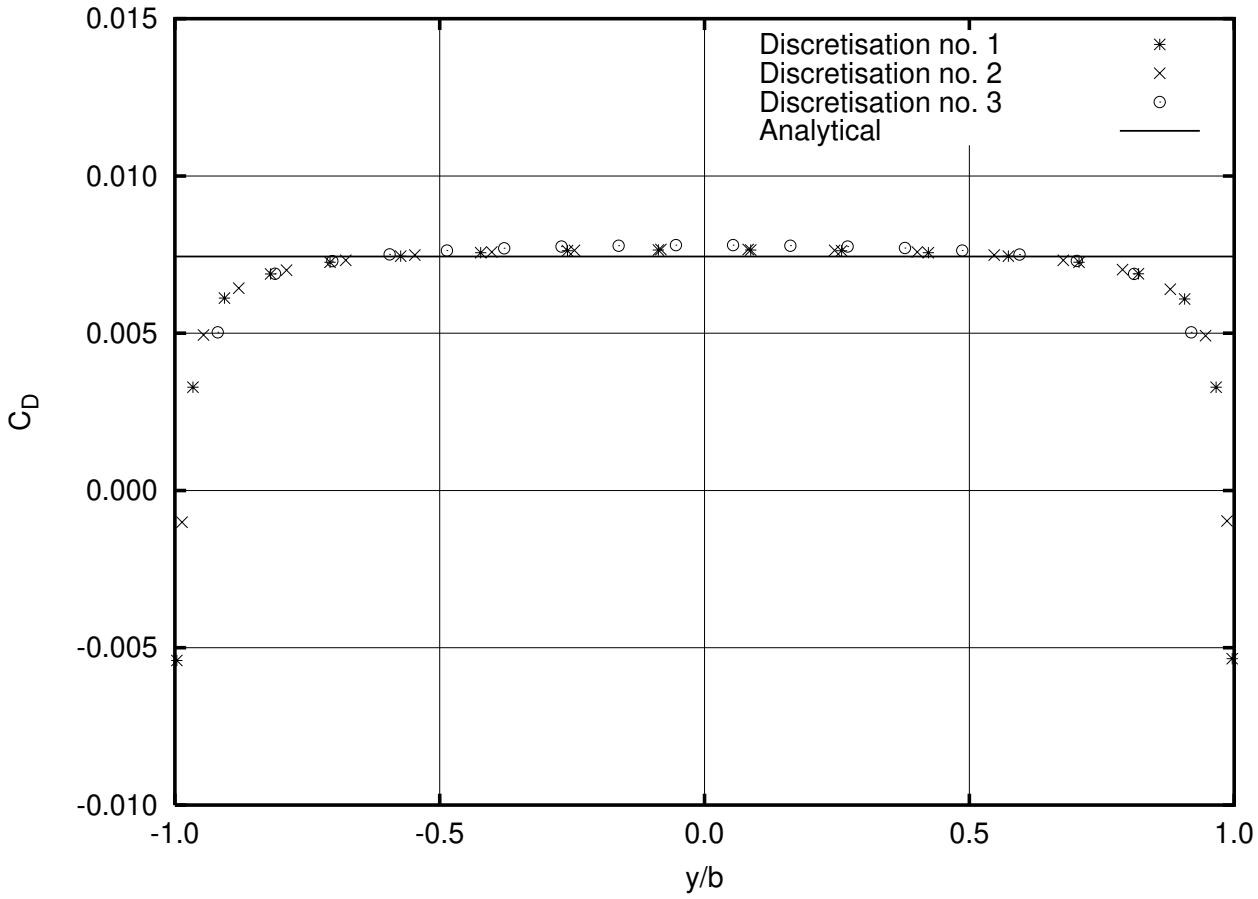

Figure 3.12: *Sectional drag coefficient for an elliptic planform with different spanwise discretisations for* $M_{sp} \times N_{ch} = 18 \times 10$, $b = 6.0\,m$, $c_0 = 3.0\,m$, $U_0 = 10.0\,{}^{m}/_{s}$, *and* $C_{L,r} = 0.345$.

This corresponds to the James (1972) discretisation transformed to the spanwise direction.

Optimisation for a lifting line shows that the two cosine discretisations (no. 1 and no. 2) give the exact induced drag for a very low number of panels, when the induced velocity is calculated at the control points. The equidistant discretisation (no. 3) gives reasonable results for nine or more panels. For all three discretisations the optimum distribution of circulation is elliptic.

A hydrofoil with the same input parameter as before is optimised with the three discretisations. For all calculations the grid contains 18 panels spanwise and 9 chordwise. Table 3.6 shows the minimised total drag coefficient for the different discretisations. From the table it is seen that, unlike the lifting-line calculations, the equidistant discretisation, i.e. discretisation no. 3, is closest to the analytical solution when the planform is included in the optimisation.

The optimum distribution of circulation is shown in Figure 3.10. It is seen that all three

Table 3.6: *Minimised total drag coefficient for an elliptic planform with different discretisations for* $M_{sp} \times N_{ch} = 18 \times 10$, $b = 6.0\,m$, $c_0 = 3.0\,m$, $U_0 = 10.0\,{}^{m}/_{s}$, *and* $C_{L,r} = 0.345$.

Discretisation	$10^3 C_D^{tot}$	$C_{D,ana}^{tot}/C_D^{tot}$
Cosine no. 1 (grid points at the tip)	7.340	1.0138
Cosine no. 2	7.348	1.0127
Equidistant no. 3	7.428	1.0018

distributions fit the analytical distribution well. The sectional lift coefficient is shown in Figure 3.11. Again the differences between the results from the different discretisations are small. The largest discrepancies are observed at the tips, where the cosine discretisation no. 1 (Streckwall, 1994) increases rapidly and the cosine discretisation no. 2 (Lan, 1974) decreases abruptly. For the equidistant discretisation the sectional lift coefficient is constant over a larger part of the span than the coefficients from the cosine discretisations.

Figure 3.12 shows the spanwise variation of the sectional drag coefficient. It is seen that the sectional drag coefficients from the cosine discretisations are lower and closer to the analytical solution than the coefficients from the equidistant discretisation. But for the cosine discretisations the C_D is decreasing rapidly close to the tip and the point nearest to the tip has even a negative C_D. This results in the lower total drag coefficient for the cosine discretisations compared to the coefficient for the equidistant discretisation. This shows why the total drag coefficient from the equidistant discretisation is closest to the analytical value.

Even though the negative drag coefficients at the tips have only a small influence on the overall drag coefficient, it indicates that there might be problems with the cosine discretisations at the tips. Therefore, the equidistant discretisation has been chosen as the most suitable spanwise discretisation. The same conclusions were drawn in Kerwin and Lee (1978), also due to problems in the tip region for the cosine discretisation. But from the above comparison it is evident that the differences between the discretisations are small.

3.7 Summary

In this chapter the lifting-surface optimisation procedure is outlined and tested with a planar hydrofoil with elliptic planform. The results are in good agreement with the analytical results obtained by Prandtl. For the used vortex-lattice method for the planar hydrofoil it is shown that the lift is restricted to the vortex at the trailing edge, whereas the drag depends on the difference in induced velocity at the sides of the panel which are perpendicular to the onset flow, i.e. side 2 and 4. According to Munk's displacement theorem (von Kármán and Burgers, 1963), it is necessary to use a weight function for the chordwise distribution of circulation. The hydrofoil is optimised with different types of discretisations and the results

show that the cosine discretisation should be used chordwise and the equidistant should be used spanwise.

Chapter 4

Optimisation of Propellers

4.1 Introduction

The aim of the optimisation procedure is to find the radial distribution of circulation, which results in the highest efficiency for the propeller. The problem can be formulated as a variational problem where the applied torque is minimised for a specified thrust. Betz (1927) solved this problem for a propeller in open water by the assumption of linear theory and the lifting-line model. He used the integral formulation of the problem and it was necessary to use Munk's displacement theorem, see e.g. Yim (1976), in order to solve the problem. Betz (1927) found that the criterion for the optimum distribution of circulation is

$$\frac{\tan\beta_0(r)}{\tan\beta_i(r)} = c \tag{4.1}$$

where $\beta_0(r)$ is the pitch angle of the onset flow and $\beta_i(r)$ is the pitch angle for the total inflow. Lerbs (1952) extended the problem to include a radially varying axial onset flow and found an optimum criterion similar to Betz's criterion:

$$\frac{\tan\beta_0(r)}{\tan\beta_i(r)} = c\sqrt{\frac{1-w(r)}{1-t(r)}} \tag{4.2}$$

where $\beta_0(r)$ is the pitch angle of the onset flow, $\beta_i(r)$ is the pitch angle of the total inflow, $w(r)$ is the radially varying wake fraction, and $t(r)$ is the radially varying thrust deduction fraction. For a propeller in open water Lerbs' criterion is identical to that of Betz. For the calculation of the induced velocities from the trailing vortices, which are assumed to have a regular helix shape, Lerbs used induction factors. The shed vortices are in Lerbs' method aligned with the total flow at the lifting line, which is known as the method for moderately loaded propellers. Betz's and Lerbs' criteria have for decades been used extensively to optimise single conventional propellers. The need for an optimisation method for multi-component propulsors caused Kerwin et al. (1986) to introduce another method for solving

the variational problem. The propeller is still modelled by a lifting line but the continuous distribution of circulation along the line is discretised. This makes it possible to solve the variational problem directly. Kerwin et al. (1986) showed that the obtained distributions of circulation were identical for the discrete model and for the Betz optimisation. Coney (1992) continued the work on the discrete method and showed that the discrete distribution of circulation for a lightly loaded propeller fulfilled Betz's criterion. The distribution of circulation obtained by the discrete method was compared to the distribution obtained by Lerbs' criterion for a propeller in a radial varying wake. The obtained distributions were identical. From Kerwin et al. (1986) and Coney (1992), it can be concluded that it is possible to find the optimum distribution of circulation for a discrete distribution of circulation and that the results for sufficiently low loading resemble the results from the Betz and the Lerbs criteria. The advantage of the discrete model is that Munk's displacement theorem and the linearisation which were necessary in the integral approach adopted by Betz and Lerbs are avoided by the direct solution of the variational problem. Other advantages of the discrete model are, as concluded by Coney (1992), that the geometry of the propeller can be of theoretically unlimited complexity and that the propeller model is not restricted to the lifting-line model. The observation about the geometry is important to the present work, as one of the aims is to optimise the distribution of circulation for the Kappel propellers. The Kappel propellers are propellers with an integrated tip fin, for details of the Kappel propellers see e.g. Andersen et al. (2000). As a further modification to the optimisation procedure the lifting-line model is replaced by a lifting-surface model for the propeller. The model used has some similarities, but it is not completely identical to the vortex-lattice model described by Kerwin and Lee (1978) and Greely and Kerwin (1982). By using the lifting-surface method it is possible to include the effects of the entire blade in the optimisation.

4.2 Propeller Geometry

The propeller is described in a Cartesian coordinate system which rotates with the propeller. The x-axis is positive upstream, the y-axis is positive to the port side and the z-axis completes the right-hand coordinate system, see Figure 4.1. The origin of the coordinate system is at the centre of the hub. The angular velocity of the propeller, ω, is positive when the propeller, viewed in the positive x-direction, is rotating clockwise. For the cylindrical coordinate system the radius, r, is positive away from the origin and the angle, ϕ, is positive in the same direction as ω. ϕ is measured from the z-axis. The x-coordinate for the cylindrical coordinate system is the same as for the Cartesian system. The cylindrical coordinate system is also shown in Figure 4.1.

4.2.1 Description of the Blade Surface

The geometry of the Kappel propeller is given in e.g. Andersen (1988) and is described briefly in the following. Figure 4.1 shows the geometry of a Kappel propeller. The reference

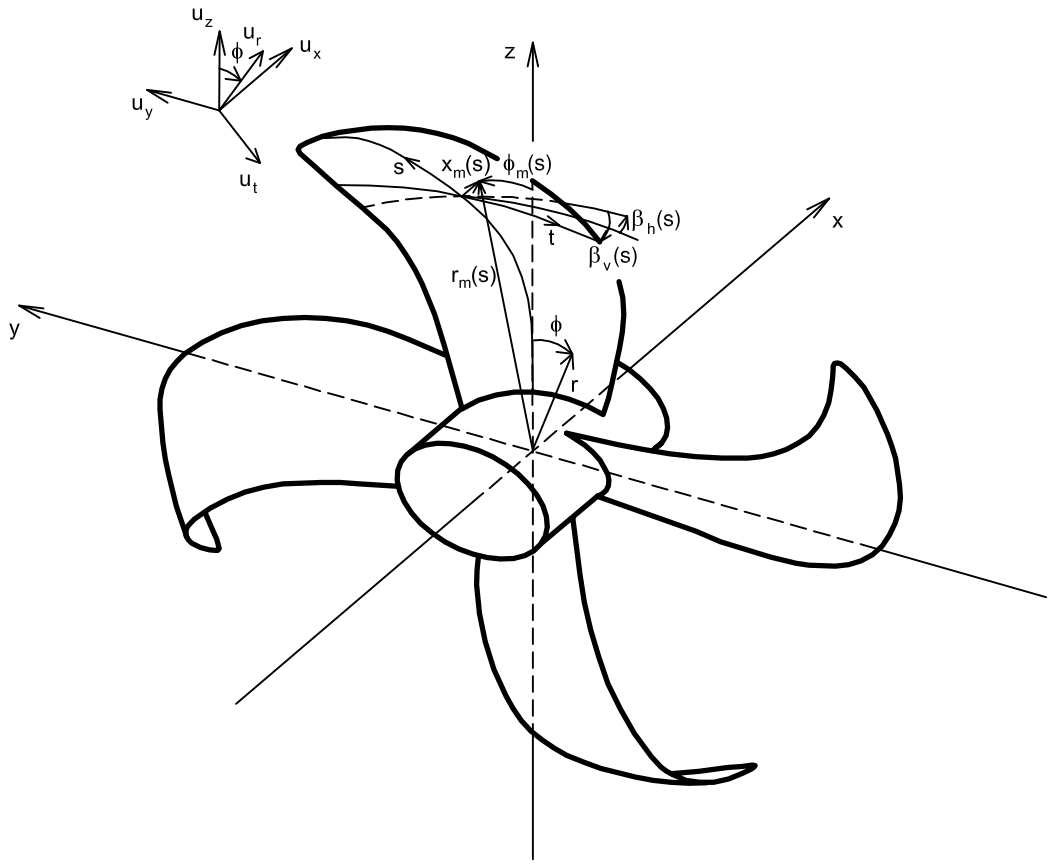

Figure 4.1: *Coordinate system for the propeller.*

surface of the propeller blade is described by the vector $\vec{\mathcal{R}}(s,t)$, where s is an arc length parameter along the midchord line and t is the dimensionless chordwise parameter, which is $t = \frac{1}{2}$ at the leading edge (L.E.) and $t = -\frac{1}{2}$ at the trailing edge (T.E.). In a rolled off coordinate system, $(x, r, r\phi)$, the reference surface is

$$\vec{\mathcal{R}}(s,t) = \begin{Bmatrix} x_m(s) + c(s)\cos(\beta_v(s))\sin(\beta_h(s))t \\ r_m(s) + c(s)\sin(\beta_v(s))t \\ -r_m(s)\phi_m(s) + c(s)\cos(\beta_v(s))\cos(\beta_h(s))t \end{Bmatrix} \tag{4.3}$$

where $x_m(s)$ is the rake, $r_m(s)$ is the radius and $\phi_m(s)$ is the skew of the midchord line. ϕ_m is positive in the opposite direction of ϕ, thus skew back is positive. $\beta_h(s)$ is the horizontal pitch angle of the nose-tail line, which corresponds to the pitch angle of a conventional propeller. For the Kappel propeller an additional pitch angle, $\beta_v(s)$, is introduced. This angle allows the profiles to be inclined with respect to a cylinder with the radius $r_m(s)$ and the axis parallel to the x-axis. Finally, $c(s)$ is the chord length. The Cartesian coordinates for the blade surface are

$$(x, y, z) = (x, -r\sin(\phi), r\cos(\phi)) \tag{4.4}$$

At the outset of the optimisation the pitch angles β_h and β_v are not known. Therefore β_v is set equal to zero, consistently with linear theory, and β_h is equal to the fluid pitch angle β_i of the reference flow. Section 4.4 describes how this angle is found. Hence, the description of the blade in the Cartesian coordinate system is

$$\begin{aligned}
\phi(s,t) &= -\phi_m(s) + \frac{c(s)}{r_m(s)}\cos(\beta_i(s))t \\
x(s,t) &= x_m(s) + c(s)\sin(\beta_i(s))t \\
y(s,t) &= -r_m(s)\sin(\phi(s,t)) \\
z(s,t) &= r_m(s)\cos(\phi(s,t)), \quad \text{for } -\tfrac{1}{2} \le t \le \tfrac{1}{2} \text{ and } s_{hub} \le s \le s_{tip}
\end{aligned}$$

For a conventional propeller the s-parameter is equal to the radius r.

4.2.2 Grid Generation

The blade surface is divided into a number of quadrilateral panels and the trailing vortex sheet is thus reduced to a number of trailing horseshoe vortices. An example of a propeller grid is shown in Figure 4.2. The description of the panels is similar to the description of the panels on the hydrofoil, which was given in Section 3.2.1.

The grid study of the hydrofoil, see Section 3.6, showed that the discretisation should be equidistant spanwise and cosine chordwise. For the propeller this means that the radial discretisation should be equidistant and the chordwise discretisation should be cosine. Hence, the radial discretisation is

$$\begin{aligned}
s_{gp,i} &= \frac{4i-3}{4M_{sp}+2}(s_{tip}-s_{hub}) + s_{hub} \quad \text{for } i = 1,2,\ldots,M_{sp}+1 \\
s_{cp,i} &= \tfrac{1}{2}(s_{gp,i} + s_{gp,i+1}) \quad \text{for } i = 1,2,\ldots,M_{sp}
\end{aligned} \tag{4.5}$$

where M_{sp} is the number of spanwise panels and gp refers to grid points and cp refers to control points. The chordwise discretisation is

$$\begin{aligned}
t_{gp,1} &= -\frac{1}{2} \quad \text{located at T.E.} \\
t_{gp,i} &= -\frac{1}{2}\cos\left(\frac{(i-\frac{3}{2})\pi}{N_{ch}}\right) \quad \text{for } i = 2,3,\ldots,N_{ch}+1 \\
t_{cp,i} &= -\frac{1}{2}\cos\left(\frac{(i-1)\pi}{N_{ch}}\right) \quad \text{for } i = 1,2,\ldots,N_{ch}
\end{aligned} \tag{4.6}$$

where N_{ch} is the number of chordwise panels.

As for the hydrofoil, the shed vortices are horseshoe vortices consisting of two sides which are moved infinitely downstream with the fluid and a straight line at the trailing edge combining

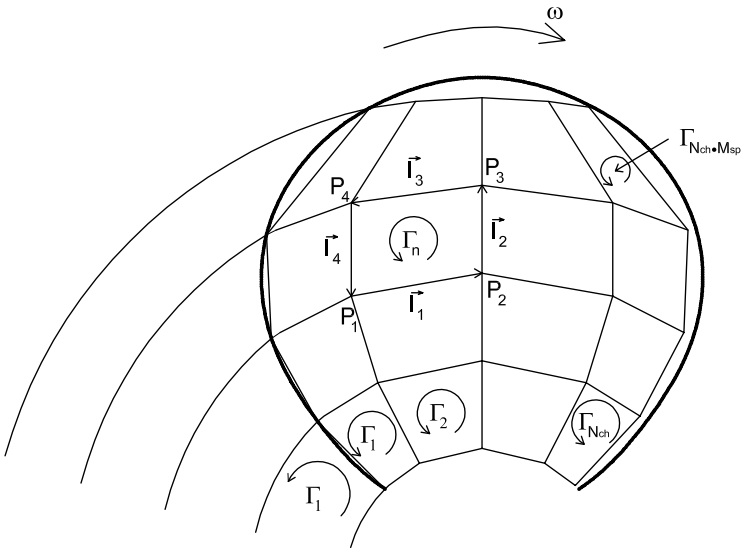

Figure 4.2: *Example of a grid, the trailers and the direction of the circulation for the propeller.*

the sides in the horseshoe. The sides of the horseshoes are assumed to follow regular helices with constant pitch and radius, see Figure 4.2. Hence, the shed vortex is described by

$$\vec{x} = \left\{ x, -r\sin\left(\frac{2\pi}{P}(x - x_{T.E.}) + \phi_{T.E.}\right), r\cos\left(\frac{2\pi}{P}(x - x_{T.E.}) + \phi_{T.E.}\right) \right\} \tag{4.7}$$

where r is the radius, corresponding to the radius of the grid point at the trailing edge from which the vortex is shed. P is the pitch of the helix, which is equal to the pitch of the reference flow, see Section 4.4. $\phi_{T.E.}$ is the phase angle of the helix.

From Equation (4.6) it is seen that the first grid point is at the trailing edge in order to fulfil the Kutta condition. This condition is fulfilled as the net circulation at the trailing edge is zero because the circulations of the trailer and the first panel are identical.

4.3 Onset Flow and Induced Velocities

The onset flow is given in the cylindrical coordinate system and it is possible to specify all three components. The onset flow is assumed to be axi-symmetric and independent of the longitudinal position, so that the onset flow has only a radial variation. The Cartesian components of the onset flow are

$$\begin{aligned} \vec{U}_0(\vec{x}) = (&-U_{0,x}(s),\ -U_{0,r}(s)\sin\phi - (U_{0,t}(s) - \omega r(s))\cos\phi, \\ &U_{0,r}(s)\cos\phi - (U_{0,t}(s) - \omega r(s))\sin\phi) \end{aligned} \tag{4.8}$$

where $(U_{0,x}(s),\ U_{0,r}(s),\ U_{0,t}(s))$ are the wake velocities given in cylindrical coordinates and ωr, which is the tangential velocity caused by the rotation of the propeller, is included, as the coordinate system is fixed to the blade.

The induced velocities from the panels at the propeller blade are calculated in the same way as for the hydrofoil, see Equation (3.3) and Appendix B.

In order to calculate the induced velocities from the shed vortices the wake of the propeller is divided into two parts. The first part, which is designated the transition wake, covers the helix from the trailing edge of the propeller and four radii downstream. The second part, designated the ultimate wake, covers the part from the end of the transition wake and infinitely downstream. The regular helix is in the transition wake replaced by a number of straight line vortices so that the induced velocity can be found in the same way as for a panel side, see Equation (B.2). The induced velocity from the ultimate wake is found by the method developed by de Jong (1991). The expressions are derived in Appendix B for Cartesian coordinates.

The total velocity at point $\vec{x}$ is the sum of the onset flow and the vortex induced velocities:

$$\vec{U}(\vec{x}) = \sum_{j=1}^{M_{sp}} \vec{\Gamma}_{1+(j-1)N_{ch}} \sum_{i=1}^{N_{ch}} \kappa_i \vec{q}^*_{i+(j-1)N_{ch}}(\vec{x}) + \vec{U}_0(\vec{x}) \tag{4.9}$$

where κ_i is the weight function, which was defined in Section 3.4. $\vec{q}^*_{i+(j-1)N_{ch}}$ is the induced velocity from panel number $i + (j-1)N_{ch}$ for all the blades. The induced velocities from the trailing horseshoe vortices are included in the $\vec{q}^*_{i+(j-1)N_{ch}}$ function for $i = 1$, which corresponds to the trailing edge panels.

4.4 Grid and Wake Alignment

The applied grid and wake alignment procedure assumes that the pitch of the shed vortices is constant and neglects the contraction of the slipstream. Furthermore, it is assumed that the blade and the shed vortices have the same pitch. The pitch is based on the total velocity at the midchord line of the blade, hence the pitch angle of the grid and the shed vortices is

$$\beta_i(s) = \tan^{-1}\left(\frac{U_{0,x}(s) - u_x(s)}{\omega r(s) - u_t(s) - U_{0,t}(s)}\right) \tag{4.10}$$

where $u_x(s)$ and $u_t(s)$ are the total axial and tangential components, respectively, of the induced velocities from the vortex system at the midchord line. The midchord line is located at $t = 0$.

The applied alignment procedure corresponds to the wake alignment used in the moderately loaded lifting-line theory. But unlike the lifting-line theory the induced velocity from the bound vortices is included in the total induced velocity for the lifting-surface optimisation. The effects of these vortices are assumed to be small, which they will be for a propeller without skew and rake, but for a skewed propeller the assumption is more questionable.

4.5 Thrust and Torque Calculations

The forces on the propeller blade are found in the same manner as for the hydrofoil. Thus, the forces from the circulation are found by the law of Kutta–Joukowsky and the force on one side of the panel is

$$\vec{F}_{side} = \rho\vec{U}(\vec{x}) \times \vec{\Gamma}_{side} = \rho\Gamma_{side}\left(\vec{U}(\vec{x}) \times \vec{l}_{side}\right) \tag{4.11}$$

where the total velocity $\vec{U}(\vec{x})$ is calculated at the midpoint of the panel side, $\vec{l}_{side}$ is the vector for this side, see Figure 3.2, and Γ_{side} is the total circulation on the side.

The moment from one side of the panel is

$$\vec{M}_{side} = \vec{r}(\vec{x}) \times \vec{F}_{side} \tag{4.12}$$

where $\vec{r}(\vec{x})$ is the vector from the origin of the coordinate system to the midpoint of the side. It is assumed that there is no local moment on the side.

The total force on the propeller blade is found by adding the contributions from all the panel sides on the blade. As the propeller is working in a steady state condition the forces on all the blades are the same. Hence, the force on the entire propeller is found by multiplying the force on one blade by the number of blades, Z. The thrust of the propeller is the x-component of the total force, so that the total thrust for the propeller is

$$\begin{aligned} T = F_x = \rho Z \sum_{m=1}^{M_{sp}} \Gamma_{1+(m-1)N_{ch}} \Bigg\{ \sum_{n=1}^{N_{ch}} \kappa_n \sum_{k=1}^{4} \big[& l_{z,n+(m-1)N_{ch},k} U_y(\vec{x}_{n+(m-1)N_{ch},k}) \\ & - l_{y,n+(m-1)N_{ch},k} U_z(\vec{x}_{n+(m-1)N_{ch},k}) \big] - l_{z,1+(m-1)N_{ch},4} U_y(\vec{x}_{1+(m-1)N_{ch},4}) \\ & + l_{y,1+(m-1)N_{ch},4} U_z(\vec{x}_{1+(m-1)N_{ch},4}) \Bigg\} \end{aligned} \tag{4.13}$$

where l_y and l_z are the y- and z-components of $\vec{l}$, respectively, and U_y and U_z are the y- and z-components of the total velocity, respectively. $\vec{x}_{n+(m-1)N_{ch},k}$ is the coordinate for the midpoint of side k of the panel number $n + (m-1)N_{ch}$.

The torque, Q, which should be applied to the propeller axis is the negative x-component of the total moment, hence

$$\begin{aligned} Q = -M_x &= -\sum_{i=1}^{sides} (yF_z - zF_y)_i \\ &= Q_2 - Q_1 \end{aligned} \tag{4.14}$$

where F_y and F_z are the $y-$ and $z-$components of the force on side i, respectively, and y, z are the coordinates for the midpoint of the panel side. Q_1 and Q_2 are introduced in order to make the expression more readable.

The two components of the torque are

$$\begin{aligned} Q_1 = \rho Z \sum_{m=1}^{M_{sp}} \Gamma_{1+(m-1)N_{ch}} \Bigg\{ \sum_{n=1}^{N_{ch}} \kappa_n \sum_{k=1}^{4} y_{n+(m-1)N_{ch},k} \big[l_{y,n+(m-1)N_{ch},k} U_x(\vec{x}_{n+(m-1)N_{ch},k}) \\ - l_{x,n+(m-1)N_{ch},k} U_y(\vec{x}_{n+(m-1)N_{ch},k}) \big] \\ + y_{1+(m-1)N_{ch},4} \big[-l_{y,1+(m-1)N_{ch},4} U_x(\vec{x}_{1+(m-1)N_{ch},4}) \\ + l_{x,1+(m-1)N_{ch},4} U_y(\vec{x}_{1+(m-1)N_{ch},4}) \big] \Bigg\} \end{aligned} \tag{4.15}$$

$$\begin{aligned} Q_2 = \rho Z \sum_{m=1}^{M_{sp}} \Gamma_{1+(m-1)N_{ch}} \Bigg\{ \sum_{n=1}^{N_{ch}} \kappa_n \sum_{k=1}^{4} z_{n+(m-1)N_{ch},k} \big[l_{x,n+(m-1)N_{ch},k} U_z(\vec{x}_{n+(m-1)N_{ch},k}) \\ - l_{z,n+(m-1)N_{ch},k} U_x(\vec{x}_{n+(m-1)N_{ch},k}) \big] \\ + z_{1+(m-1)N_{ch},4} \big[-l_{x,1+(m-1)N_{ch},4} U_z(\vec{x}_{1+(m-1)N_{ch},4}) \\ + l_{z,1+(m-1)N_{ch},4} U_x(\vec{x}_{1+(m-1)N_{ch},4}) \big] \Bigg\} \end{aligned} \tag{4.16}$$

4.6 The Variational Problem

The aim of the optimisation procedure is to find the distribution of circulation which enables the propeller to develop a specified thrust with a minimum use of energy. Therefore, the torque applied to the propeller should be as low as possible. This distribution is found by solving a discrete variational problem as described in Kerwin et al. (1986).

The functional for the problem is

$$H(\vec{\Gamma}, \lambda) = Q(\vec{\Gamma}) + \lambda(T(\vec{\Gamma}) - T_r) \tag{4.17}$$

where $\vec{\Gamma}$ is the sought distribution of circulation, λ is the Lagrange multiplier, and T_r is the required thrust. As the circulation on the blade is given by the weight function and the circulation of the trailing vortices the number of unknown circulations corresponds to the number of radial panels M_{sp}.

The optimum distribution is that which minimises the functional, H. Thus, the distribution can be found by setting the partial derivatives of $H(\vec{\Gamma}, \lambda)$ with respect to $\vec{\Gamma}$ and λ equal to zero.

This gives the following system of equations:

$$\begin{aligned} \frac{\partial H}{\partial \Gamma_{1+(m-1)N_{ch}}} = \frac{\partial Q}{\partial \Gamma_{1+(m-1)N_{ch}}} + \lambda \frac{\partial T}{\partial \Gamma_{1+(m-1)N_{ch}}} = 0 \quad \text{for } m = 1, 2, \cdots M_{sp} \\ \frac{\partial H}{\partial \lambda} = T - T_r = 0 \end{aligned} \tag{4.18}$$

which has $M_{sp}+1$ equations with $M_{sp}+1$ unknowns. The unknowns are the circulation of the M_{sp} trailing vortices and the Lagrange multiplier.

The derivative of the thrust is found by differentiating Equation (4.13):

$$\begin{aligned}
\frac{\partial T}{\partial \Gamma_{1+(m-1)N_{ch}}} = \rho Z \Bigg\{ & \sum_{n=1}^{N_{ch}} \kappa_n \sum_{k=1}^{4} \big\{ l_{z,n+(m-1)N_{ch},k} U_{0,y}(\vec{x}_{n+(m-1)N_{ch},k}) \\
& - l_{y,n+(m-1)N_{ch},k} U_{0,z}(\vec{x}_{n+(m-1)N_{ch},k}) \big\} \\
& - l_{z,1+(m-1)N_{ch},4} U_{0,y}(\vec{x}_{1+(m-1)N_{ch},4}) \\
& + l_{y,1+(m-1)N_{ch},4} U_{0,z}(\vec{x}_{1+(m-1)N_{ch},4}) \\
& + \sum_{j=1}^{M_{sp}} \Gamma_{1+(j-1)N_{ch}} \Bigg[\sum_{n=1}^{N_{ch}} \kappa_n \sum_{i=1}^{N_{ch}} \kappa_i \sum_{k=1}^{4} \\
& \quad \big\{ l_{z,n+(m-1)N_{ch},k} q^*_{y,i+(j-1)N_{ch}}(\vec{x}_{n+(m-1)N_{ch},k}) \\
& - l_{y,n+(m-1)N_{ch},k} q^*_{z,i+(j-1)N_{ch}}(\vec{x}_{n+(m-1)N_{ch},k}) \\
& + l_{z,i+(j-1)N_{ch},k} q^*_{y,n+(m-1)N_{ch}}(\vec{x}_{i+(j-1)N_{ch},k}) \\
& - l_{y,i+(j-1)N_{ch},k} q^*_{z,n+(m-1)N_{ch}}(\vec{x}_{i+(j-1)N_{ch},k}) \big\} \\
& + \sum_{i=1}^{N_{ch}} \kappa_i \big\{ -l_{z,1+(m-1)N_{ch},4} q^*_{y,i+(j-1)N_{ch}}(\vec{x}_{1+(m-1)N_{ch},4}) \\
& + l_{y,1+(m-1)N_{ch},4} q^*_{z,i+(j-1)N_{ch}}(\vec{x}_{1+(m-1)N_{ch},4}) \big\} \\
& + \sum_{n=1}^{N_{ch}} \kappa_n \big\{ -l_{z,1+(j-1)N_{ch},4} q^*_{y,n+(m-1)N_{ch}}(\vec{x}_{1+(j-1)N_{ch},4}) \\
& + l_{y,1+(j-1)N_{ch},4} q^*_{z,n+(m-1)N_{ch}}(\vec{x}_{1+(j-1)N_{ch},4}) \big\} \Bigg] \Bigg\}
\end{aligned} \tag{4.19}$$

for $m = 1, 2, \ldots, M_{sp}$

From Equation (4.15) the derivative of Q_1 is found:

$$\begin{aligned}
\frac{\partial Q_1}{\partial \Gamma_{1+(m-1)N_{ch}}} = \rho Z \Bigg\{ & \sum_{n=1}^{N_{ch}} \kappa_n \sum_{k=1}^{4} y_{n+(m-1)N_{ch},k} \\
& \big\{ l_{y,n+(m-1)N_{ch},k} U_{0,x}(\vec{x}_{n+(m-1)N_{ch},k}) \\
& - l_{x,n+(m-1)N_{ch},k} U_{0,y}(\vec{x}_{n+(m-1)N_{ch},k}) \big\} \\
& + y_{1+(m-1)N_{ch},4} \big\{ -l_{y,1+(m-1)N_{ch},4} U_{0,x}(\vec{x}_{1+(m-1)N_{ch},4}) \\
& + l_{x,1+(m-1)N_{ch},4} U_{0,y}(\vec{x}_{1+(m-1)N_{ch},4}) \big\}
\end{aligned}$$

$$
\begin{aligned}
&+ \sum_{j=1}^{M_{sp}} \Gamma_{1+(j-1)N_{ch}} \Bigg[\sum_{n=1}^{N_{ch}} \kappa_n \sum_{i=1}^{N_{ch}} \kappa_i \sum_{k=1}^{4} \Big[y_{n+(m-1)N_{ch},k} \\
&\quad \big\{ l_{y,n+(m-1)N_{ch},k} q^*_{x,i+(j-1)N_{ch}}(\vec{x}_{n+(m-1)N_{ch},k}) \\
&\quad - l_{x,n+(m-1)N_{ch},k} q^*_{y,i+(j-1)N_{ch}}(\vec{x}_{n+(m-1)N_{ch},k}) \big\} \\
&\quad + y_{i+(j-1)N_{ch},k} \big\{ l_{y,i+(j-1)N_{ch},k} q^*_{x,n+(m-1)N_{ch}}(\vec{x}_{i+(j-1)N_{ch},k}) \\
&\quad - l_{x,i+(j-1)N_{ch},k} q^*_{y,n+(m-1)N_{ch}}(\vec{x}_{i+(j-1)N_{ch},k}) \big\} \Big] \\
&\quad + \sum_{i=1}^{N_{ch}} \kappa_i y_{1+(m-1)N_{ch},4} \\
&\quad \big\{ -l_{y,1+(m-1)N_{ch},4} q^*_{x,i+(j-1)N_{ch}}(\vec{x}_{1+(m-1)N_{ch},4}) \\
&\quad + l_{x,1+(m-1)N_{ch},4} q^*_{y,i+(j-1)N_{ch}}(\vec{x}_{1+(m-1)N_{ch},4}) \big\} \\
&\quad + \sum_{n=1}^{N_{ch}} \kappa_n y_{1+(j-1)N_{ch},4} \\
&\quad \big\{ -l_{y,1+(j-1)N_{ch},4} q^*_{x,n+(m-1)N_{ch}}(\vec{x}_{1+(j-1)N_{ch},4}) \\
&\quad + l_{x,1+(j-1)N_{ch},4} q^*_{y,n+(m-1)N_{ch}}(\vec{x}_{1+(j-1)N_{ch},4}) \big\} \Big] \Bigg\}
\end{aligned}
\tag{4.20}
$$

for $m = 1, 2, \ldots, M_{sp}$

Finally, the derivative of Q_2 is found from Equation (4.16):

$$
\begin{aligned}
\frac{\partial Q_2}{\partial \Gamma_{1+(m-1)N_{ch}}} &= \rho Z \Bigg\{ \sum_{n=1}^{N_{ch}} \kappa_n \sum_{k=1}^{4} z_{n+(m-1)N_{ch},k} \\
&\quad \big\{ l_{x,n+(m-1)N_{ch},k} U_{0,z}(\vec{x}_{n+(m-1)N_{ch},k}) \\
&\quad - l_{z,n+(m-1)N_{ch},k} U_{0,x}(\vec{x}_{n+(m-1)N_{ch},k}) \big\} \\
&\quad + z_{1+(m-1)N_{ch},4} \big\{ -l_{x,1+(m-1)N_{ch},4} U_{0,z}(\vec{x}_{1+(m-1)N_{ch},4}) \\
&\quad + l_{z,1+(m-1)N_{ch},4} U_{0,x}(\vec{x}_{1+(m-1)N_{ch},4}) \big\} \\
&\quad + \sum_{j=1}^{M_{sp}} \Gamma_{1+(j-1)N_{ch}} \Bigg[\sum_{n=1}^{N_{ch}} \kappa_n \sum_{i=1}^{N_{ch}} \kappa_i \sum_{k=1}^{4} \Big[z_{n+(m-1)N_{ch},k} \\
&\quad \big\{ l_{x,n+(m-1)N_{ch},k} q^*_{z,i+(j-1)N_{ch}}(\vec{x}_{n+(m-1)N_{ch},k}) \\
&\quad - l_{z,n+(m-1)N_{ch},k} q^*_{x,i+(j-1)N_{ch}}(\vec{x}_{n+(m-1)N_{ch},k}) \big\} \\
&\quad + z_{i+(j-1)N_{ch},k} \big\{ l_{x,i+(j-1)N_{ch},k} q^*_{z,n+(m-1)N_{ch}}(\vec{x}_{i+(j-1)N_{ch},k}) \\
&\quad - l_{z,i+(j-1)N_{ch},k} q^*_{x,n+(m-1)N_{ch}}(\vec{x}_{i+(j-1)N_{ch},k}) \big\} \Big]
\end{aligned}
$$

$$
\begin{aligned}
&+\sum_{i=1}^{N_{ch}} \kappa_i z_{1+(m-1)N_{ch},4} \\
&\quad \left\{-l_{x,1+(m-1)N_{ch},4} q^*_{z,i+(j-1)N_{ch}}(\vec{x}_{1+(m-1)N_{ch},4})\right. \\
&\quad \left.+\, l_{z,1+(m-1)N_{ch},4} q^*_{x,i+(j-1)N_{ch}}(\vec{x}_{1+(m-1)N_{ch},4})\right\} \\
&+\sum_{n=1}^{N_{ch}} \kappa_n z_{1+(j-1)N_{ch},4} \\
&\quad \left\{-l_{x,1+(j-1)N_{ch},4} q^*_{z,n+(m-1)N_{ch}}(\vec{x}_{1+(j-1)N_{ch},4})\right. \\
&\quad \left.+\, l_{z,1+(j-1)N_{ch},4} q^*_{x,n+(m-1)N_{ch}}(\vec{x}_{1+(j-1)N_{ch},4})\right\}\Bigg]\Bigg\}
\end{aligned}
\tag{4.21}
$$

for $m = 1, 2, \ldots, M_{sp}$

From Equation (4.18) it is seen that the optimisation procedure is non-linear. The non-linearity occurs because there are products of λ and Γ and because the induced velocities, which are used to calculate the thrust, depend on the circulation.

The non-linear variational problem is linearised, which results in the following system of equations:

$$
\frac{\partial Q(\vec{\Gamma})}{\partial \Gamma_{1+(m-1)M_{sp}}} + \lambda^{t-1}\frac{\partial T(\vec{\Gamma})}{\partial \Gamma_{1+(m-1)M_{sp}}} + \lambda^{t}\frac{\partial T(\vec{U_0})}{\partial \Gamma_{1+(m-1)M_{sp}}} = -\frac{\partial Q(\vec{U_0})}{\partial \Gamma_{1+(m-1)M_{sp}}} \tag{4.22}
$$

for $m = 1, 2, ..., M_{sp}$, and

$$
T(\vec{\Gamma}) = T_r - T(\vec{U_0}) \tag{4.23}
$$

where $Q(\vec{\Gamma})$ and $T(\vec{\Gamma})$ refer to the parts of Q and T which are functions of the circulation and $Q(\vec{U_0})$ and $T(\vec{U_0})$ refer to the parts of Q and T which are functions of the onset flow. $t-1$ is the value from the previous iteration. Due to the linearisation, iterations are necessary to achieve a solution to the problem. The iterations are carried out until the residual defined as

$$
\mathrm{R}^t = \max_{m=1,2,\ldots,M_{sp}} \left(\left| 1 - \frac{\Gamma^t_{1+(m-1)M_{sp}}}{\Gamma^{t-1}_{1+(m-1)M_{sp}}} \right| \right) \tag{4.24}
$$

is below a certain small limit.

4.7 Optimisation Procedure

The solution to the variational problem is found by the computer code xlift . The flow chart of the program is shown in Figure 4.3.

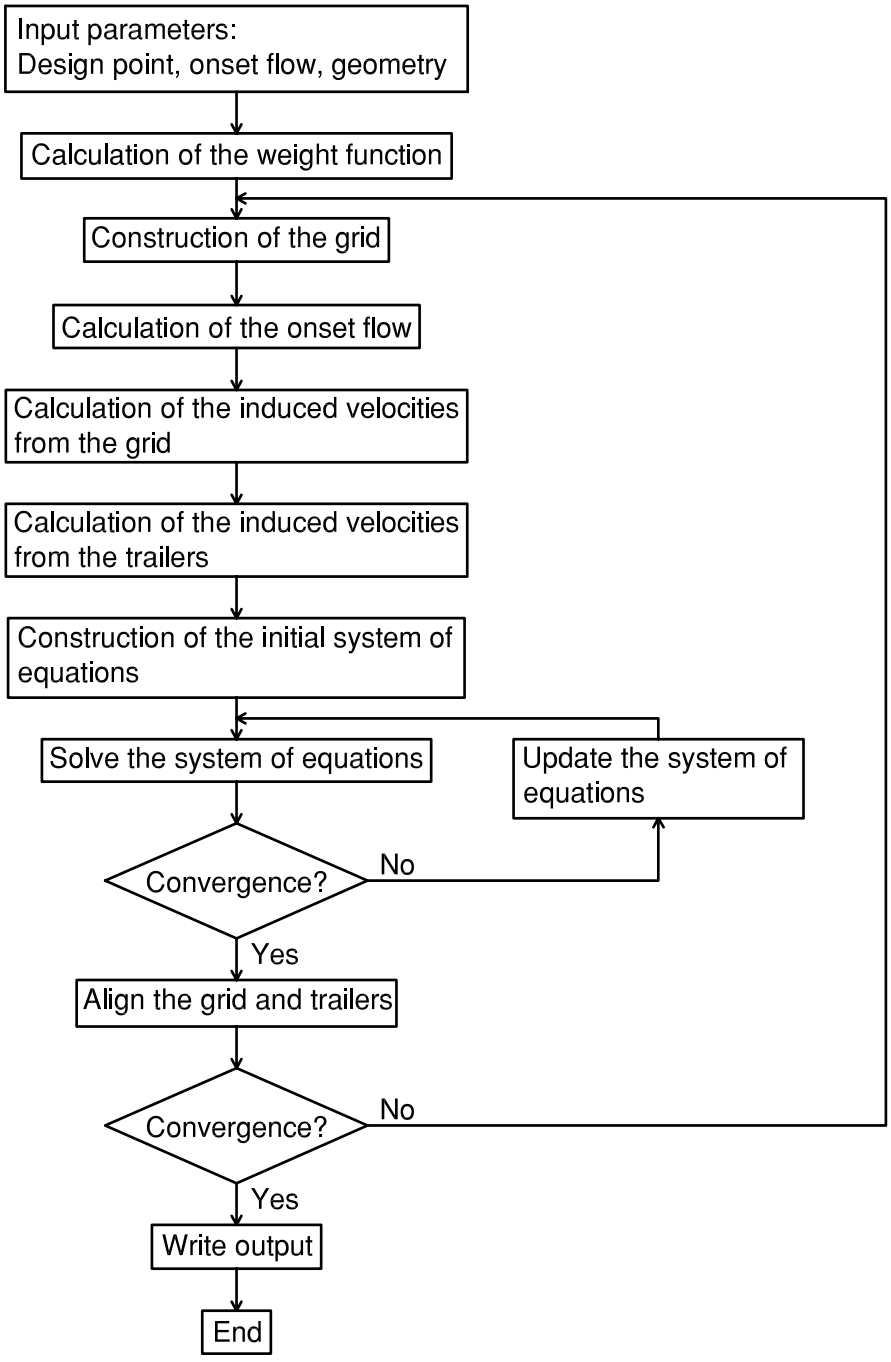

Figure 4.3: *Flow chart for the optimisation program xlift.*

At the outset of the optimisation a list of input parameters should be specified. These include the main dimensions of the propeller, i.e. the radius of the propeller and of the hub, and the number of blades. The size of the grid should be specified, i.e. the number of radial and chordwise panels. The geometry of the midchord line is specified through the distributions of radius, rake, and skew, which are all functions of the arc length parameter.

The chord length distribution is given in order to construct the grid. The design point, i.e. the advance number and the required thrust, and the onset flow are specified and finally the ratio between the flat plate and the rooftop distributions should be given.

With the given input the initial system of equations for the variational problem is constructed according to Equation (4.22). The distribution of circulation is initially set to zero and the Lagrange multiplier is -1 (Coney, 1992). The iteration for the variational problem is continued until the residual, see Equation (4.24), is below 10^{-5}, which is normally reached by less than ten iterations. When the variational problem has converged, the grid and the trailers are aligned according to Equation (4.10). Then the system of equations for the variational problem is updated with the new grid and wake geometry and the variational problem is solved again. The alignment of the grid and the wake is continued until the residual for the pitch distribution of the wake is less than 10^{-5}. The number of iterations required for the wake alignment to converge depends on the propeller geometry and the loading of the propeller, but in general the convergence is slower than for the variational problem. When the wake alignment has converged the distribution of circulation is written to a file and the program stops.

It is necessary to obtain the optimum distribution of circulation without changing the wake or grid, as Kerwin et al. (1986) showed that the solution to the variational problem is a heavily tip-loaded propeller if the wake is aligned for each iteration of the optimisation procedure. The heavy tip loading results in a high pitch of the tip vortex, which contradicts experimental results for the pitch of the tip vortex, see e.g. Hoshino (1989). The conclusion in Kerwin et al. (1986) is that as long as the problems of aligning the wake cannot be solved satisfactorily the optimisation is done better by the linear theory. This conclusion is later modified by Coney (1992), who obtained usable results if the wake is aligned for each solution of the optimisation problem.

4.8 Results

The performance of the optimisation routine has been tested on the DTNSRDC propeller series, see e.g. Kerwin and Lee (1978). For these calculations five of the propellers from the series are used. The propellers are designed for the same radial distribution of circulation with the same expanded blade area and thickness distribution, whereas the skew and the skew-induced rake are varied. Therefore, the pitch and camber distributions are different for the propellers. The main dimensions and the design point for the propellers are

$$Z = 5,\ R = 3.0\,m,\ \hat{r}_h = 0.2,\ A_E/A_0 = 0.725,\ J = 0.889,\ K_{T,D} = 0.2055,\ C_{Th} = 0.662$$

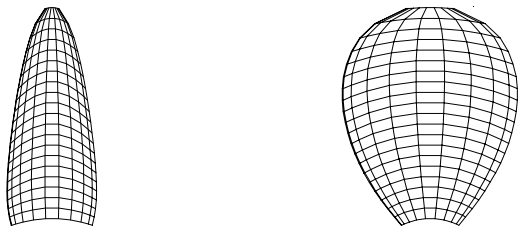

DC4381, no skew or rake.

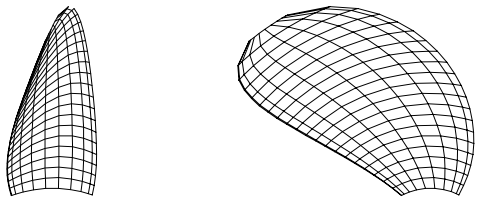

DC4497, 36° skew and no skew-induced rake.

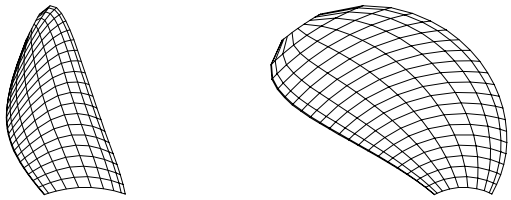

DC4382, 36° skew and skew-induced rake.

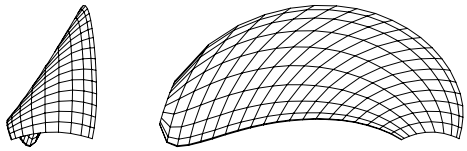

DC4498, 72° skew and no skew-induced rake.

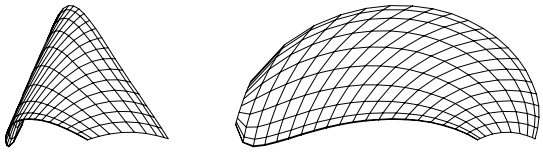

DC4383, 72° skew and skew-induced rake.

Figure 4.4: *Grids for the five DTNSRDC propellers for* $J = 0.889$ *and* $M_{sp} \times N_{ch} = 20 \times 10$.

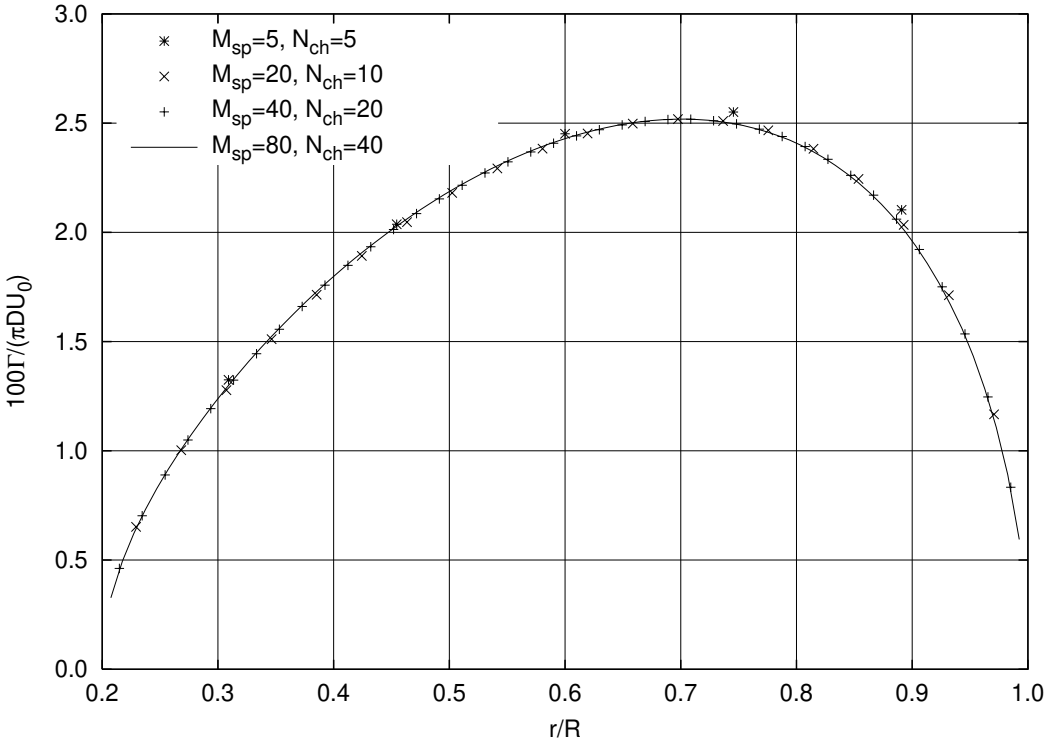

Figure 4.5: *Grid study for the reference propeller, DC4381.* $C_{Th} = 0.662$, $J = 0.889$ *and* $U_0 = 10.0\ ^m/_s$.

The design thrust coefficient, $K_{T,D}$, is approximated from Kerwin and Lee (1978), which also contains the detailed geometry of the propellers. The radius is chosen for this project. The five propellers are one reference propeller, which has no skew or rake, and the other four are connected two and two so that they both have the same skew, but only one of them has skew-induced rake. The skew is either 36° or 72°. An outline of the propellers with their designations is seen in Figure 4.4.

At first a grid study is performed in order to verify that the optimisation routine is at all useful. The grid study is done with the reference propeller, DC4381, and the propeller with 72° skew and skew-induced rake, DC4383. For the grid study the linear theory is used. Hence, the grids of the propellers are aligned with the onset flow and the grid is not changed

Table 4.1: *Parameters for the grid study.*

C_{Th}	0.662	2.0	4.0
K_T	0.2055	0.2055	0.2055
J	0.889	0.512	0.362
U_0	10.0 $^m/_s$	5.754 $^m/_s$	4.070 $^m/_s$

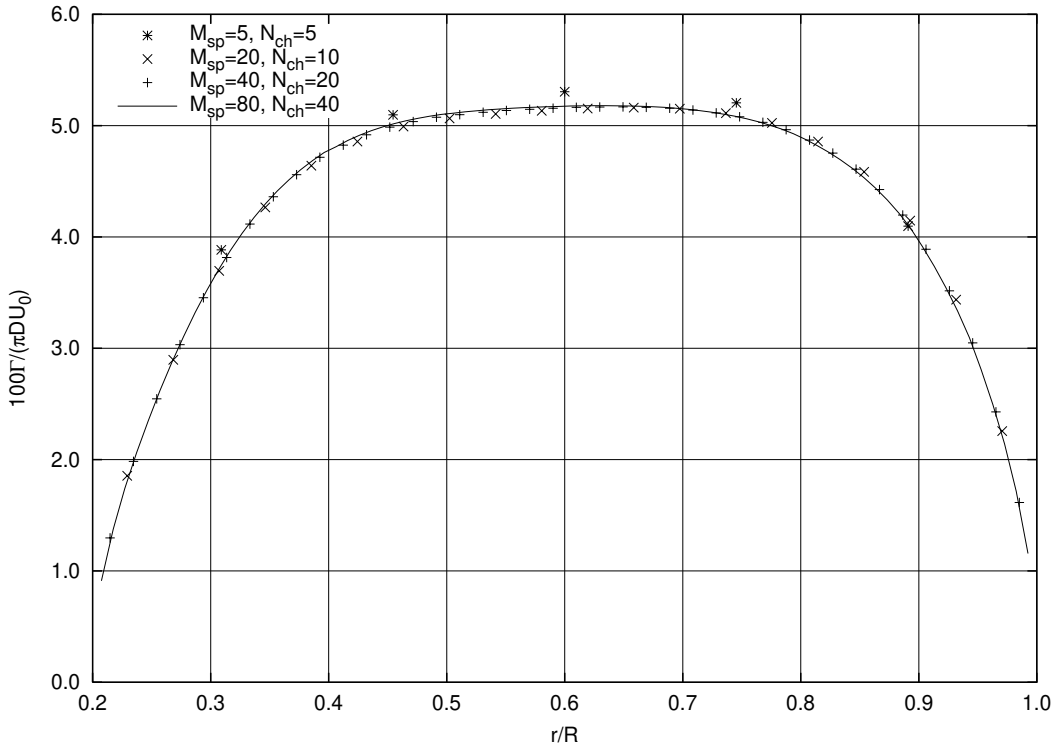

Figure 4.6: *Grid study for propeller with 72^o skew and skew-induced rake, DC4383.* $C_{Th} = 4.0$, $J = 0.362$ *and* $U_0 = 4.070\ ^m/_s$.

during the calculations. The grid study is performed in the open water condition for three thrust loadings, $C_{Th} = 0.662$, $C_{Th} = 2.0$ and $C_{Th} = 4.0$. Table 4.1 shows the input data. As the linear theory is used the results from the high thrust loadings, $C_{Th} = 2.0$ and $C_{Th} = 4.0$, are not correct due to the missing alignment of the trailers, but the results indicate how the method performs for high thrust loadings. The lowest thrust loading, $C_{Th} = 0.662$, is low enough to justify the use of linear theory. There will of course be a difference between results with and without wake alignment, but it is assumed to be small for this thrust loading. The size of the grid is varied from $M_{sp} \times N_{ch} = 5 \times 5$ to 80×40. Tables 4.2 and 4.3 show the results from the grid study. It is seen from the tables that the relative difference between the lowest

Table 4.2: *Optimised torque coefficient* ($10K_Q$) *for the reference propeller, DC4381, and varying number of grid points.*

	C_{Th}		
$M_{sp} \times N_{ch}$	0.662	2.0	4.0
5×5	0.3701	0.2725	0.2490
20×10	0.3695	0.2715	0.2477
40×20	0.3697	0.2717	0.2478
80×40	0.3698	0.2718	0.2479

Table 4.3: *Optimised torque coefficient ($10K_Q$) for the propeller with 72° skew and skew-induced rake, DC4383, and varying number of grid points.*

	C_{Th}		
$M_{sp} \times N_{ch}$	0.662	2.0	4.0
5×5	0.3639	0.2615	0.2328
20×10	0.3640	0.2612	0.2316
40×20	0.3645	0.2616	0.2319
80×40	0.3649	0.2620	0.2322

and the highest value is below 0.5% for all thrust loadings. Furthermore, it is seen that the absolute difference between the results is decreasing for increasing number of panels, except for DC4383 for the two highest thrust loadings where the absolute difference is constant. Figure 4.5 presents the distribution of circulation for the different grids for propeller DC4381 with $C_{Th} = 0.662$. It should be noted that the differences between the distributions are small. Figure 4.6 shows the circulation for propeller DC4383 with $C_{Th} = 4.0$. Again the differences between the results are negligible. Thus, it is concluded from the grid study that the number of grid points is not so important to the final result, but only concerns the desired resolution of the solution. Furthermore, the results are converging for increasing number of panels.

The effect of the chordwise pressure distribution has also been investigated. Table 4.4 shows the torque coefficient for an optimisation for propeller DC4381 and DC4383 with $C_{Th} = 0.662$ and varying chordwise pressure distribution. The pressure distribution is either pure rooftop ($\nu = 0.0$ and $\mathbf{a} = 0.8$), half rooftop and half flat plate ($\nu = 0.5$) or pure flat plate ($\nu = 1.0$). It is seen from the table that the pressure distribution has only a small effect on the results. The relative differences in K_Q for the different distributions are below one percent, with the lowest K_Q for the pure flat plate distribution. This is in agreement with the Munk theorem, which states that the thrust and energy loss is only a function of the radial distribution of integrated chordwise pressures and does not depend upon the modes of chordwise distribution as long as the integrated lift is the same (von Kármán and Burgers, 1963).

In order to compare the lifting-surface optimisation and the lifting-line optimisation the reference propeller, DC4381, has been optimised for a constant thrust loading and a range

Table 4.4: *Torque coefficient ($10K_Q$) for the reference propeller with no skew or rake, DC4381, and for the propeller with 72° skew and skew-induced rake, DC4383, for different chordwise pressure distributions.* $C_{Th} = 0.662$, $J = 0.889$, $U_0 = 10.0$ $^m/_s$ *and* $M_{sp} \times N_{ch} = 40 \times 20$.

ν	DC4381	DC4383
0.0	0.3709	0.3658
0.5	0.3697	0.3645
1.0	0.3684	0.3628

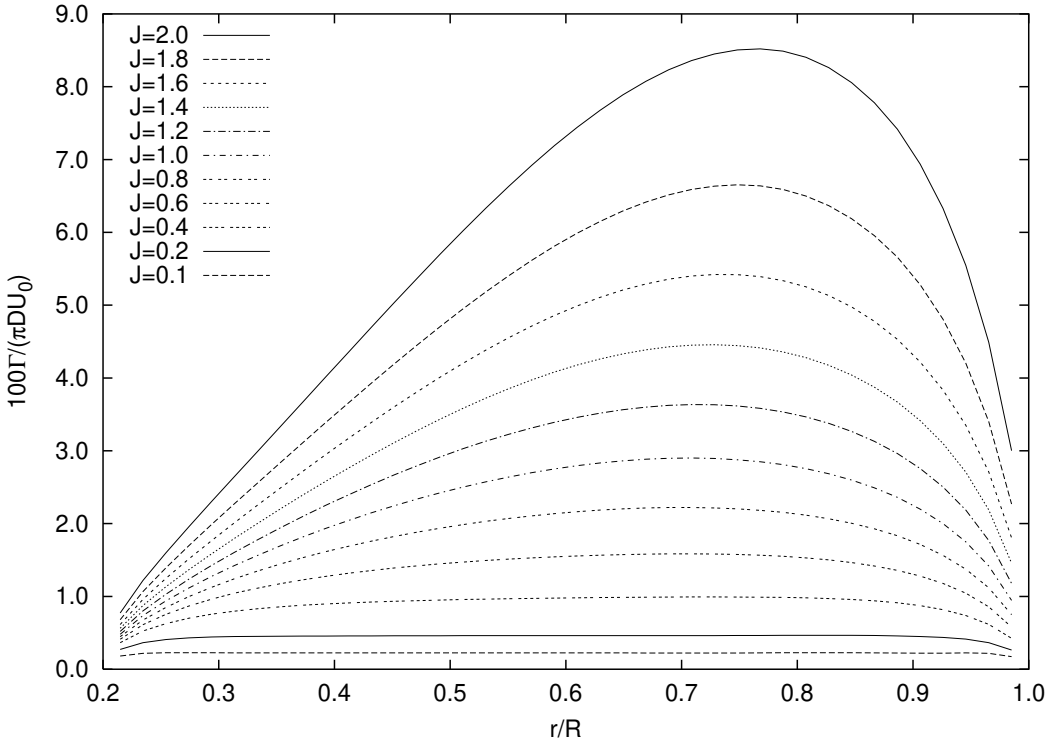

Figure 4.7: *Optimum distributions of circulation for the reference propeller, DC4381, with lifting-surface calculations.* $C_{Th} = 0.662$ *and* $U_0 = 10.0^{m}/_{s}$ *with varying number of rotations.*

of advance numbers. The calculations are similar to those presented in Coney (1992) for a lifting line with a discrete distribution of circulation. The calculations are made for a thrust loading of 0.662 and the uniform onset flow has a velocity of $10.0\,^{\mathrm{m}}/_{\mathrm{s}}$. The advance number is varied by changing the rotational speed of the propeller. The chordwise loading is half flat plate and half rooftop ($\nu = 0.5$). The grid size is 40 panels spanwise and 20 panels chordwise and the linear theory is used. The results of the optimisation are given in Table 4.5. In the table the corresponding results from a lifting-line optimisation are given as well. For the lifting-line calculations the same procedure as for the lifting-surface optimisation has been used, but the grid of the propeller blade is replaced by a straight line. Figure 4.7 shows the optimum distribution of circulation from the lifting-surface optimisation for the different advance numbers. The outline of the figure is similar to the one in Coney (1992).

First it should be noted that all distributions fall off to zero at the root and the tip of the blade. This is as expected since the pressure difference between the suction and the pressure side must vanish there. For the low advance numbers the high rotational speed will tend to eliminate the influence from the individual blades and the propeller will appear as a propeller with an infinite number of blades or an actuator disk. The optimum distribution for an actuator disk without slipstream rotation is a constant distribution, see e.g. Glauert (1963). Figure 4.7 shows that the distribution found by the lifting-surface optimisation approaches a constant distribution for decreasing advance number.

Table 4.5: *Results for the optimisation for the reference propeller, DC4381, with different advance numbers.* $C_{Th} = 0.662$, $U_0 = 10.0\ ^{m}/_{s}$, $\nu = 0.5$ *and* $M_{sp} \times N_{ch} = 40 \times 20$. *LL references to lifting line and LS to lifting surface.*

J	0.1	0.2	0.4	0.6	0.8	1.0	1.2
n (rps)	16.667	8.333	4.167	2.778	2.083	1.667	1.389
ω (rad/sec)	104.7198	52.3599	26.1799	17.4533	13.090	10.4720	8.7266
K_T	0.00260	0.01040	0.04161	0.09363	0.16645	0.26008	0.37453
K_Q LS	0.00005	0.00039	0.00317	0.01091	0.02655	0.05371	0.09709
K_Q LL	0.00005	0.00039	0.00319	0.01099	0.02681	0.05438	0.09866
η_{LS}	0.85211	0.84795	0.83585	0.81961	0.79810	0.77074	0.73673
η_{LL}	0.84914	0.84455	0.83166	0.81373	0.79043	0.76118	0.72501

J	1.4	1.6	1.8	2.0
n (rps)	1.190	1.042	0.926	0.833
ω (rad/sec)	7.4800	6.5450	5.8178	5.2360
K_T	0.50976	0.66581	0.84266	1.04033
K_Q LS	0.16348	0.26390	0.41989	0.69325
K_Q LL	0.16695	0.27160	0.43882	0.76304
η_{LS}	0.69477	0.64248	0.57493	0.47768
η_{LL}	0.68036	0.62426	0.55013	0.43399

For increasing advance numbers the circulation is observed to increase. This is as expected as the force on the blade is a function of the velocity and the circulation, see Equation (4.11). Hence, if the thrust should be the same it is necessary that the circulation increases for decreasing rotational velocity.

Furthermore, it is seen that the position of the maximum circulation is moved toward the tip of the blade for increasing advance number. The same is observed for the lifting line in Coney (1992). For the straight lifting-line this effect can be explained by the expressions for the thrust and the torque given by

$$\begin{aligned} T &= \rho \sum_{i=1}^{M_{sp}} \Gamma_i(\omega r_i - u_t(r_i))\Delta r \\ Q &= -\rho \sum_{i=1}^{M_{sp}} \Gamma_i r_i(U_{0,x} + u_x(r_i))\Delta r \end{aligned} \tag{4.25}$$

where M_{sp} is the number of discrete vortex elements along the line. They are of the length Δr and have the circulation Γ_i. r_i is the radius to the midpoint of the element. u_x and u_t are the induced velocities at the midpoint and $U_{0,x}$ is the axial onset flow.

The above proves that the thrust is a function of the circulation and the total tangential velocity and the torque is a function of the circulation, the moment arm and the total axial

velocity. Thus, at the tip, more thrust is available with an increment of the circulation due to the higher rotational speed, ωr, but at the same time the moment arm is increased and thereby the torque. The optimum distribution of circulation is therefore a balance between the prescribed thrust and the minimum torque (Coney, 1992). For the lifting surface the explanation is similar but due to the more complicated description of the blade some remarks will be given. Equation (4.13) shows that the thrust is a function of the transverse velocities (U_y, U_z) and the y- and z-components of the vector $\vec{l}$ for the panel side. From the equation it is seen that the contribution from each panel is added to get the total thrust. As the grid will be almost tangential to the resulting flow, the contribution to the thrust from the panel sides 1 and 3 will be small whereas sides 2 and 4 will give the highest contribution to the thrust, see Figure 4.2 for an example of a panel. Calculations show that the contribution to the thrust and torque from sides 1 and 3 is below 5% of the total values. From Equation (4.13) it is seen that the thrust is dependent on the term $(l_z U_y - l_y U_z)$. This term can be rearranged in the following way:

$$\begin{aligned}
l_z U_y - l_y U_z &= l_z(U_{0,r}(r_i)y_i/r_i - U_{0,t}(r_i)z_i/r_i + \omega z_i + u_y(r_i)) \\
&\quad - l_y(U_{0,r}(r_i)z_i/r_i + U_{0,t}(r_i)y_i/r_i - \omega y_i + u_z(r_i)) \\
&= \omega(l_z z_i + l_y y_i) + U_{0,r}(r_i)/r_i(l_z y_i - l_y z_i) - U_{0,t}(r_i)/r_i(l_z z_i + l_y y_i) \\
&\quad + l_z u_y(r_i) - l_y u_z(r_i) \\
&= (\omega - U_{0,t}(r_i)/r_i)(l_z z_i + l_y y_i) + U_{0,r}(r_i)/r_i(l_z y_i - l_y z_i) \\
&\quad + l_z u_y(r_i) - l_y u_z(r_i) \\
&= (\omega - U_{0,t}(r_i)/r_i)\vec{r} \cdot \vec{l} + U_{0,r}(r_i)(l_z y_i - l_y z_i)/r_i \\
&\quad + l_z u_y(r_i) - l_y u_z(r_i)
\end{aligned} \tag{4.26}$$

where all three components of the onset flow are included and u_y, u_z are the $y-$ and z-components of the induced velocities. $\vec{r} = (0, y_i, z_i)$ where y_i and z_i are the coordinates of the midpoint of the panel side, $r_i = |\vec{r}|$ and $\vec{l} = (l_x, l_y, l_z)$. By use of vector calculus the first term on the right-hand side is observed to correspond to $(\omega - U_{0,t}(r_i)/r_i)r_i\Delta r$. As r_i is the same and Δr has an opposite sign for sides 2 and 4, the contributions from the tangential onset flow on these sides will cancel for each panel. The term which contains the radial onset flow will not necessarily disappear, only if $\vec{r}$ and $\vec{l}$ are parallel. By this derivation it becomes clear that the net contribution from each panel is due to the difference in the term $l_z u_y(r_i) - l_y u_z(r_i)$ on sides 2 and 4. This difference will be small and therefore the contributions from the panels will generally be small. The largest contribution to the thrust is due to the side at the trailing edge which combines the two trailers in the horseshoe vortex, i.e. the term $-l_{z,1+(m-1)N_{ch},4}U_y(\vec{x}_{1+(m-1)N_{ch},4}) + l_{y,1+(m-1)N_{ch},4}U_z(\vec{x}_{1+(m-1)N_{ch},4})$ of Equation (4.13), because the contribution from the tangential onset flow does not vanish here and the induced velocities are fully included. A similar derivation can be made for the torque, where the contributions from sides 1 and 3 are again negligible. From Equations (4.14), (4.15) and (4.16) it is seen that the torque depends on the term $y(l_y U_x - l_x U_y) - z(l_x U_z - l_z U_x)$. This

can be expressed in the following form:

$$
\begin{aligned}
&y(l_yU_x - l_xU_y) - z(l_xU_z - l_zU_x) = \\
&= (-U_{0,x}(r_i) + u_x(r_i))(y_il_y + z_il_z) - l_x(y_i(U_{0,y}(r_i) + u_y(r_i)) \\
&+ z_i(U_{0,z}(r_i) + u_z(r_i))) \\
&= (-U_{0,x}(r_i) + u_x(r_i))(\vec{r}\cdot\vec{l}) - l_x(y_i(U_{0,r}(r_i)y_i/r_i - U_{0,t}(r_i)z_i/r_i + \omega z_i + u_y(r_i)) \\
&+ z_i(U_{0,r}(r_i)z_i/r_i + U_{0,t}(r_i)y_i/r_i - \omega y_i + u_z(r_i))) \\
&= (-U_{0,x}(r_i) + u_x(r_i))r_i\Delta r_i - l_x(U_{0,r}(r_i)r_i + y_iu_y(r_i) + z_iu_z(r_i)) \\
&\qquad = (-U_{0,x}(r_i) + u_x(r_i))r_i\Delta r_i - l_xr_i(U_{0,r}(r_i) + u_r(r_i)) \quad (4.27)
\end{aligned}
$$

As for the thrust, the net contribution from the axial onset flow is observed to vanish for the panels. Hence, from the first term in the above expression the net contribution will be the difference in induced axial velocity on sides 2 and 4, which will be small. The last term will also be small as l_x is small for sides 2 and 4. Therefore, the largest contribution to the torque is again from the side at the trailing edge where the onset flow contribution does not vanish and the induced velocities are fully included. This is in accordance with Munk's displacement theorem. From the above derivations it is clear that also the circulation for the lifting-surface optimisation should be increasingly tip-loaded for decreasing advance number, because of the same arguments as for the lifting line.

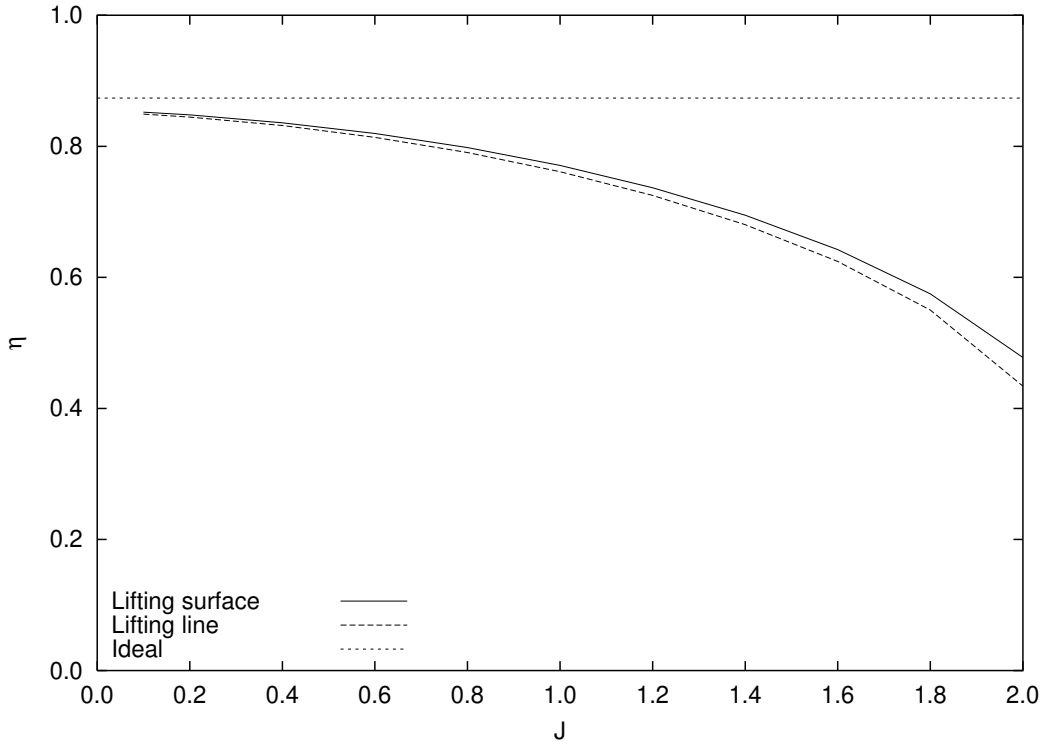

Figure 4.8: *Efficiency for the reference propeller, DC4381, from lifting-surface and lifting-line calculations compared with the ideal efficiency.* $C_{Th} = 0.662$.

Figure 4.8 shows the efficiency as a function of the advance number for the above optimisations. The propeller efficiency is given by

$$\eta = \frac{J}{2\pi}\frac{K_T}{K_Q} \tag{4.28}$$

Together with the efficiencies from the lifting-surface and the lifting-line calculations the ideal efficiency is also shown. The ideal efficiency is

$$\eta_{ideal} = \frac{2}{1+\sqrt{1+C_{Th}}} \tag{4.29}$$

From the figure it is seen that the efficiencies are approaching the ideal efficiency for decreasing advance numbers. This is again an indication of the high rotational velocities eliminating the individual blades and the results therefore approach the actuator disk results. For increasing advance numbers the efficiency is observed to decrease. This is because the relative magnitude of the axial velocity to the rotational velocity is increased for increasing advance numbers. Thus the torque is also increased relative to the thrust (Coney, 1992). For the entire range of advance numbers the efficiency for the lifting line is lower than for the lifting surface. This is also noted by Greely and Kerwin (1982).

As a further comparison between lifting-surface and lifting-line optimisations the optimum distribution of circulation and the corresponding distributions of thrust and torque are considered. Figure 4.9 shows the optimum distribution of circulation and the radial distributions of thrust and torque for two different advance numbers, $J = 0.8$ and $J = 1.0$.

The figure reveals that the circulation for the lifting-line optimisation is higher than the lifting-surface distribution at the hub and at the tip, but from approximately $r/R = 0.5$ to $r/R = 0.7$ the lifting-surface distribution is highest.

The differences in the shape of the distributions of circulation are not seen for the distribution of thrust. They are almost identical for the two methods, but the lifting-surface optimisation tends to be slightly more loaded at the tip than the lifting-line optimisation.

For the distributions of torque the lifting-surface distribution is lower on the entire blade, except from approximately $r/R = 0.5$ to $r/R = 0.7$, resulting in the higher efficiency for the lifting-surface optimisation. The difference between the two methods is largest at the tip.

For the classic optimisation theory the blade outline has no influence on the optimum distribution of circulation, as the Munk theorem is applied and the optimum distribution is found for a straight lifting line. In order to see if this is also the case for the lifting-surface optimisation procedure, the five DTNSRDC propellers are optimised for four different advance numbers. The parameters are the same as listed in Table 4.5 and the advance numbers are from $J = 0.6$ to $J = 1.2$. The results from the optimisation are given in Table 4.6, which shows that the efficiency is increasing with increasing skew. This effect was also noted by Mishima and Kinnas (1997), though for a design for a non-uniform wake. From the table it

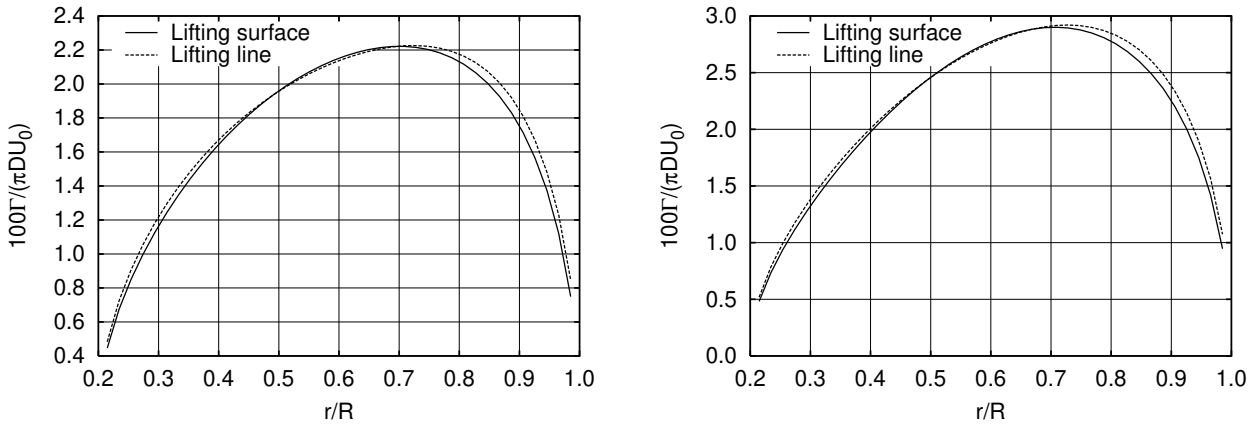

Radial distribution of circulation.

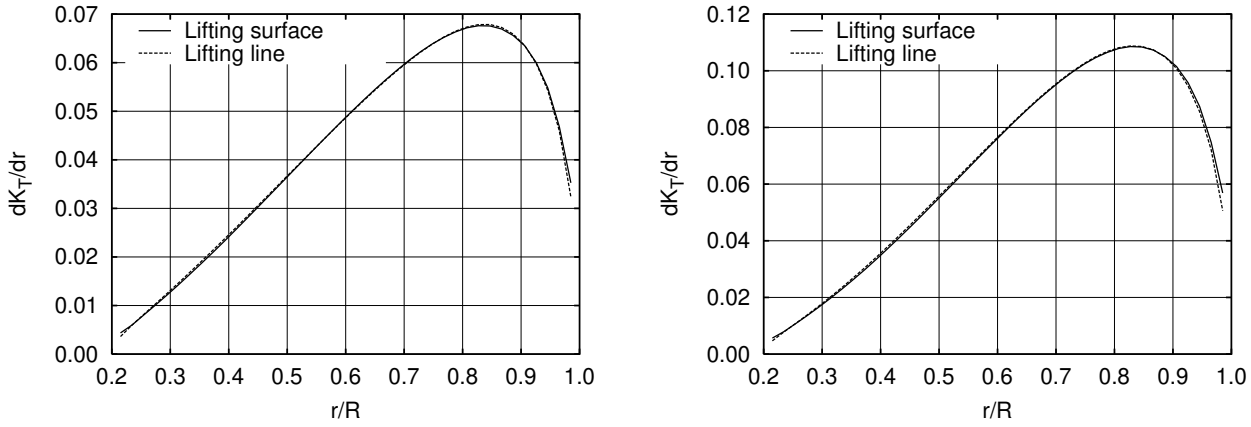

Radial distribution of thrust.

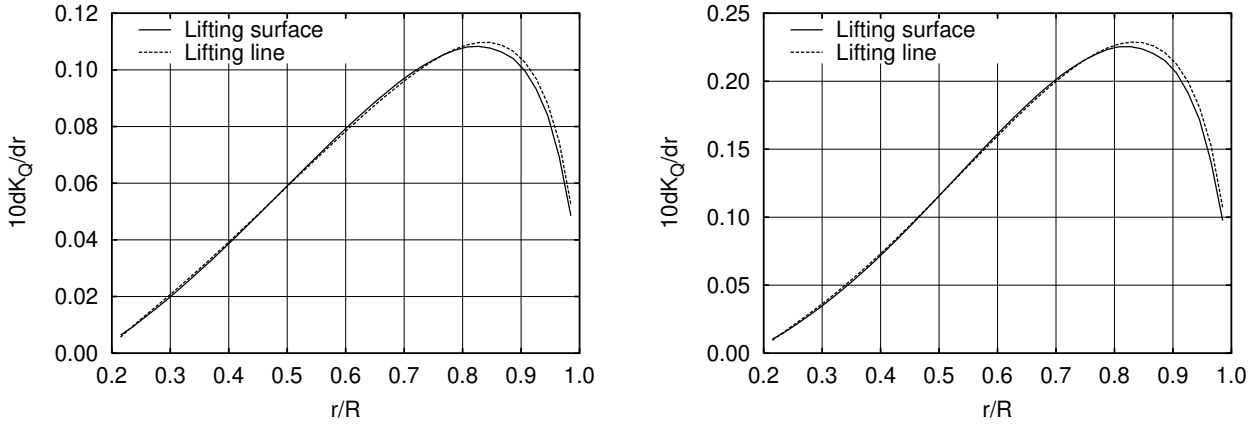

Radial distribution of torque.

Figure 4.9: *Comparison between lifting-surface results and lifting-line results for the reference propeller, DC4381. Left* $J = 0.8$*, right* $J = 1.0$.

is seen that skew has a major influence on the results while rake has only a minor influence. The differences are increasing with increasing advance number.

Table 4.6: *Results for the lifting-surface optimisation with different propellers.*

J	0.6				
K_T	0.09363				
Propeller	4381	4382	4383	4497	4498
Skew	0^0	36^0	72^0	36^0	72^0
Indu.-rake	no	yes	yes	no	no
K_Q	0.01091	0.01087	0.01082	0.01086	0.01081
η	0.81961	0.82286	0.82661	0.82314	0.82736
η/η_{4381}	-	1.00397	1.00854	1.00431	1.00946

J	0.8				
K_T	0.16645				
Propeller	4381	4382	4383	4497	4498
Skew	0^0	36^0	72^0	36^0	72^0
Indu.-rake	no	yes	yes	no	no
K_Q	0.02655	0.02641	0.02623	0.02639	0.02619
η	0.79810	0.80252	0.80786	0.80305	0.80935
η/η_{4381}	-	1.00554	1.01222	1.00620	1.01410

J	1.0				
K_T	0.26008				
Propeller	4381	4382	4383	4497	4498
Skew	0^0	36^0	72^0	36^0	72^0
Indu.-rake	no	yes	yes	no	no
K_Q	0.05371	0.05330	0.05279	0.05324	0.05263
η	0.77074	0.77658	0.78409	0.77743	0.78654
η/η_{4381}	-	1.00758	1.01732	1.00868	1.02050

J	1.2				
K_T	0.37453				
Propeller	4381	4382	4383	4497	4498
Skew	0^0	36^0	72^0	36^0	72^0
Indu.-rake	no	yes	yes	no	no
K_Q	0.09709	0.09610	0.09476	0.09594	0.09431
η	0.73673	0.74436	0.75486	0.74560	0.75848
η/η_{4381}	-	1.01036	1.02461	1.01204	1.02952

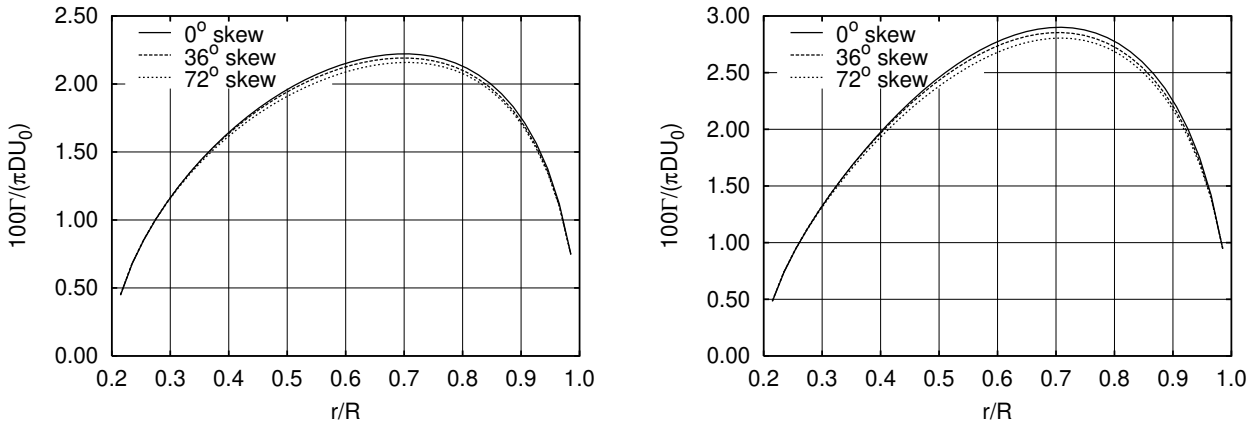

Radial distribution of circulation.

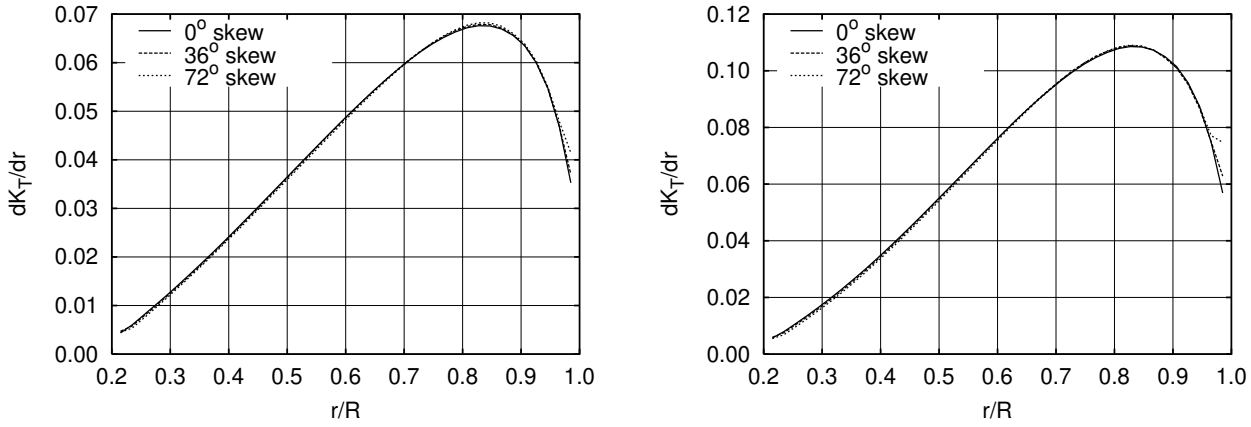

Radial distribution of thrust.

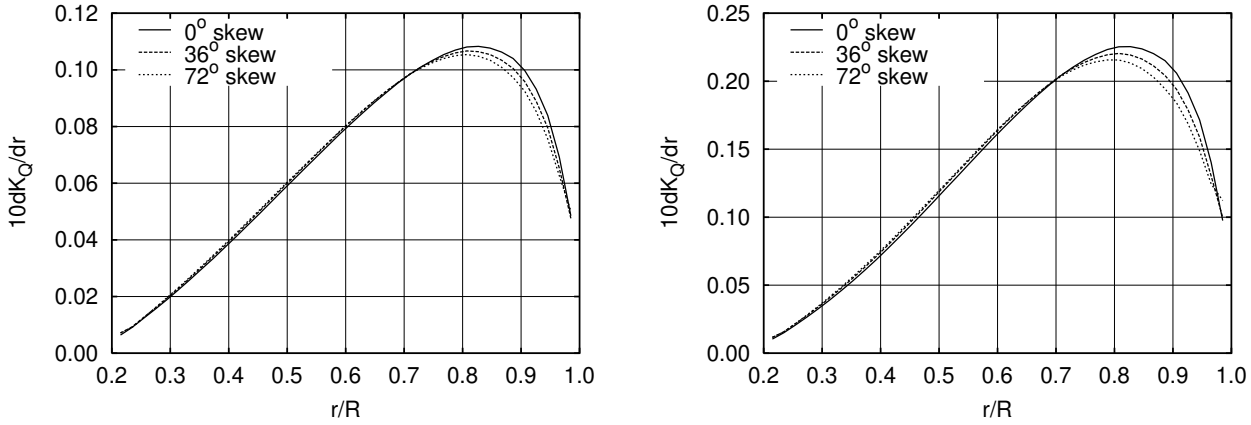

Radial distribution of torque.

Figure 4.10: *Comparison between results for the reference propeller, DC4381, the propeller with* 36^o *skew and skew-induced rake, DC4382, and the propeller with* 72^o *skew and skew-induced rake, DC4383. Left* $J = 0.8$*, right* $J = 1.0$*.*

Figure 4.10 shows the distributions of circulation, thrust and torque for the reference propeller, DC4381, and the two propellers with both skew and skew-induced rake, i.e. DC4382 and DC4383. The results are only given for $J = 0.8$ and $J = 1.0$ but the results are similar for the other two advance numbers. From the figure it is seen that the maximum value of the circulation is decreasing with increasing skew. Hence, the shape of the propeller has an influence, though small, on the optimum distribution of circulation. The distribution of thrust is almost the same for all three propellers. The skewed propellers have a slightly heavier tip loading whereas the thrust is lower on the inner part of the blade ($r/R < 0.7$), resulting in the same total thrust for all three propellers. The torque on the inner part of the blade ($r/R < 0.7$) is a little higher for the skewed propellers but on the outer part of the blade the torque is lower, which results in the lower total torque for the skewed propellers. For the skewed propellers it is observed that the outermost point has a relatively higher value, which is believed to be caused by the poor panel shape at the tip of the skewed propellers. A comparison of the tip geometry for the reference propeller and the propeller with 72° skew and skew-induced rake is shown in Figure 4.11.

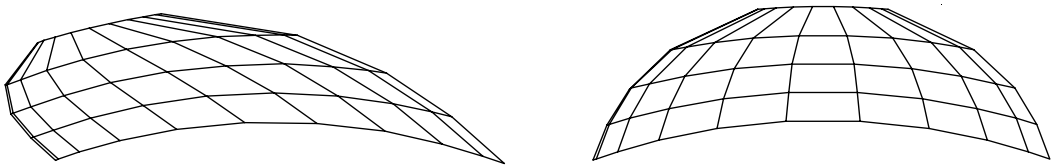

Figure 4.11: *Left:Tip geometry for the propeller with* 72^o *skew and skew-induced rake, DC4383. Right: Tip geometry for the reference propeller, DC4381. The grids are made for* $J = 0.889$ *and* $M_{sp} \times N_{ch} = 20 \times 10$.

Figures 4.12 and 4.13 present a comparison of the results for the skewed propellers with and without skew-induced rake, the results for the reference propeller are also given. The figures show that the results for the circulation and the thrust distributions are almost identical for the skewed propellers with and without skew-induced rake. For the torque there are small differences. The propellers without skew-induced rake have a higher value on the inner part of the blade, for $r/R < 0.7$, but a lower value on the outer part, which results in the slightly lower total torque for the propellers without skew-induced rake. As the distribution of circulation and the efficiency for the propellers with and without skew-induced rake are almost identical the results are in accordance with Munk's displacement theorem.

The reasons for the higher efficiencies of the skewed propellers are not known in detail and should be further investigated, but an indication of the reasons is given in the following. As previously shown, see Equations (4.26) and (4.27), the largest contributions to the thrust and the torque are from the trailing edge. Thus some insight into why the skewed propellers have higher efficiencies can be gained by combining the total axial and tangential velocities at the trailing edge with the optimum distribution of circulation. For the skewed propellers the total tangential velocity is higher on the outer part of the blade and smaller on the inner

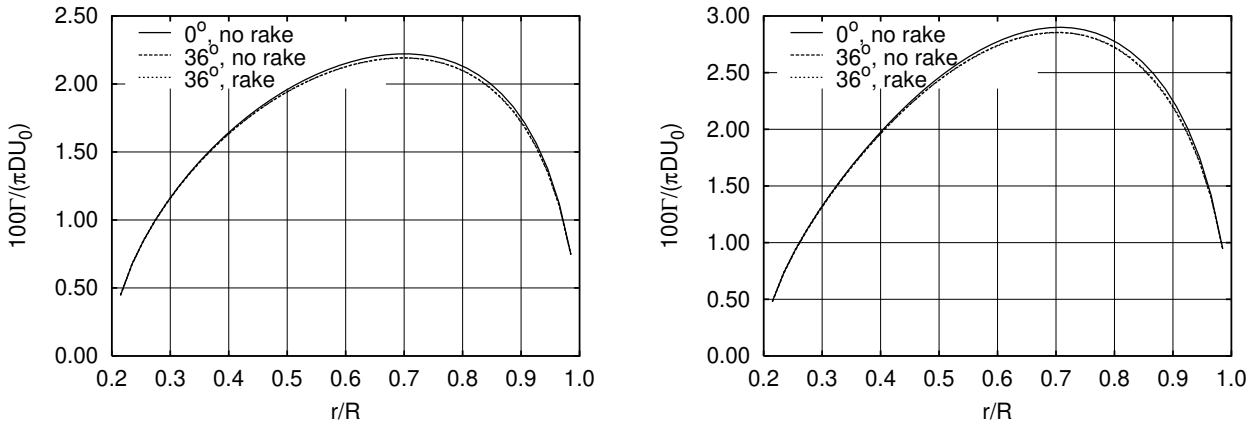

Radial distribution of circulation.

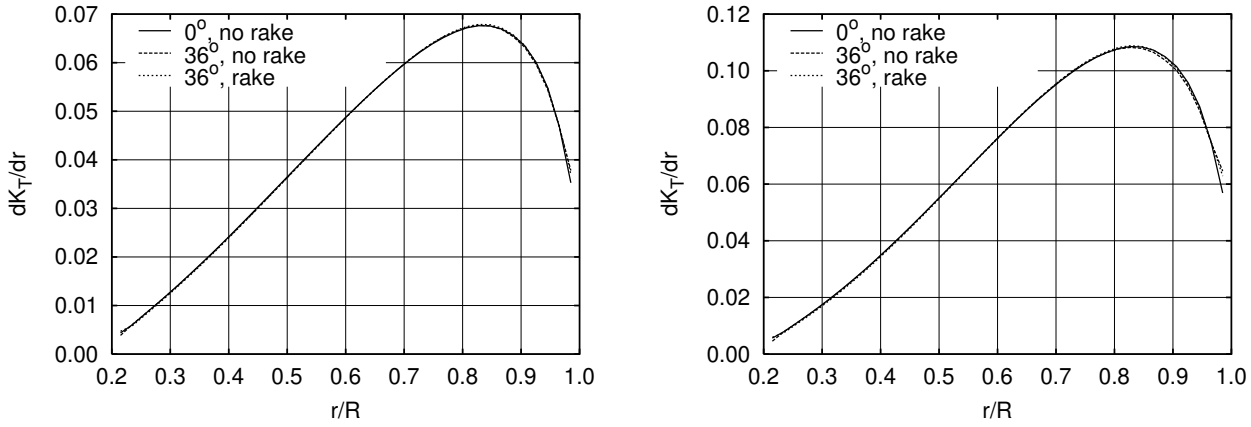

Radial distribution of thrust.

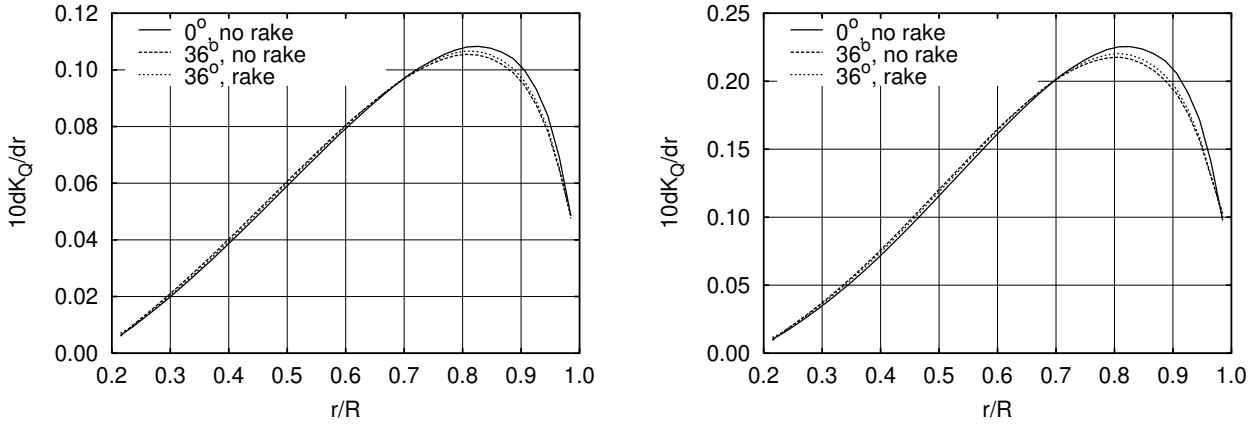

Radial distribution of torque.

Figure 4.12: *Comparison between results for the reference propeller, DC4381, and the two propellers with 36° skew, DC4382 which has skew-induced rake and DC4497 which has no rake. Left $J = 0.8$, right $J = 1.0$.*

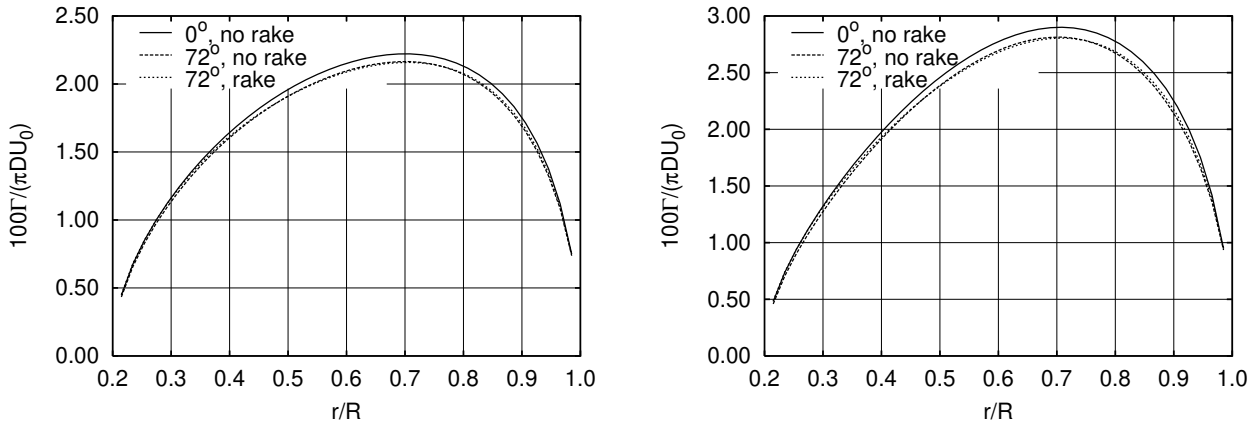

Radial distribution of circulation.

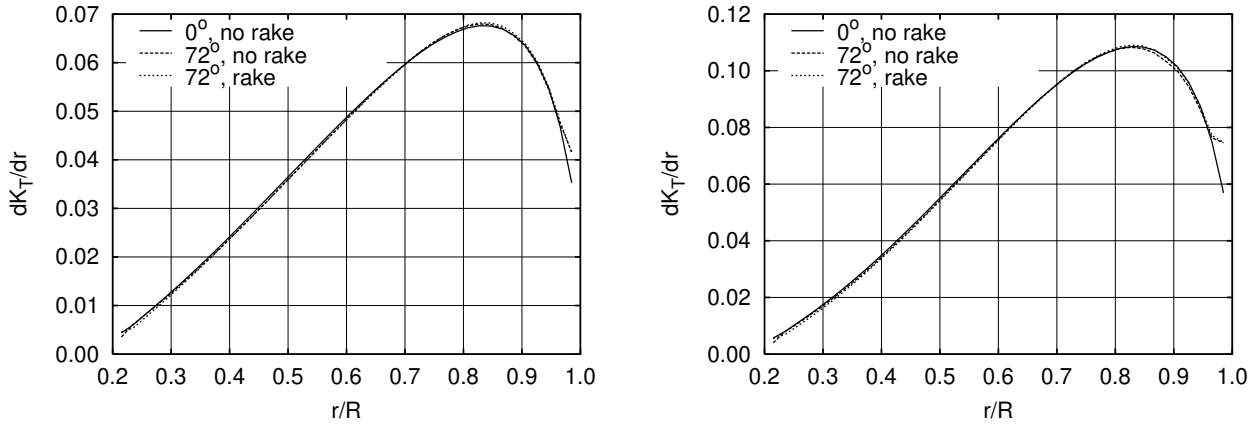

Radial distribution of thrust.

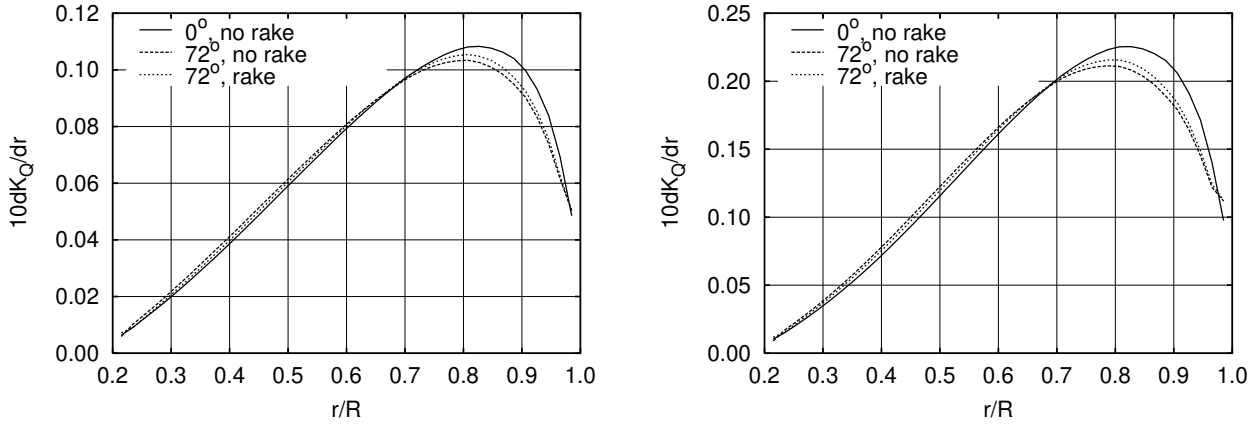

Radial distribution of torque.

Figure 4.13: *Comparison between results for the reference propeller, DC4381, and the two propellers with 72° skew, DC4383 which has skew-induced rake and DC4498 which has no rake. Left $J = 0.8$, right $J = 1.0$.*

part compared to the velocities for the propeller without skew and rake. As the circulation for the skewed propellers is lower on the outer part this results in the almost identical distribution of thrust for all the propellers, as can be seen in Figures 4.10, 4.12 and 4.13. For the skewed propellers the total axial velocity is lower on the outer part of the blade and higher on the inner part. Combined with the distribution of circulation this results in the shape of the torque distribution shown in Figures 4.10, 4.12 and 4.13, where the torque for the skewed propellers is a little higher on the inner part and lower on the outer part, resulting in the lower torque for the skewed propellers. From this comparison of propellers with and without skew it seems that skew has a favourable influence on the total axial and tangential velocities on the blades.

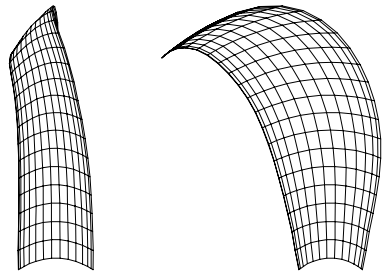

Figure 4.14: *Final grid for the Kappel propeller K1. For* $J = 0.7472$, $M_{sp} \times N_{ch} = 20 \times 14$.

4.8.1 Optimisation of the Kappel Propeller K1

The Kappel propeller K1, see Figure 4.14 for an outline, is optimised by the lifting-surface method with the following input parameters:

$$Z = 6, \quad R = 3.727\,m, \quad U_s = 11.57\,{}^{\mathrm{m}}/_{\mathrm{s}} \quad J = 0.7472$$

The propeller is optimised for a radially varying wake, with a variation for both the axial and the radial velocity component. The wake alignment procedure is included in the optimisation.

The optimisation of the Kappel propeller is normally done by the procedure outlined in Andersen (1997). By this method the force calculation is restricted to the midchord line of the propeller whereas the induced velocities at the line are calculated from both the trailers and the bound circulation, which is distributed along a part of the trailers.

Table 4.7 shows a comparison of the optimised torque coefficient and the efficiency for the two methods along with the input parameters for the optimisation. The results from the lifting-line optimisation are kindly provided by J.J. Kappel. The obtained values are almost identical for the two methods. Figure 4.15 shows a comparison of the optimised distributions of circulation. From the figure it is seen that the shapes of the distributions are almost identical. However, the distribution from the lifting-surface optimisation is a little lower on the outer part of the blade and a little higher at the root. A comparison of the distributions

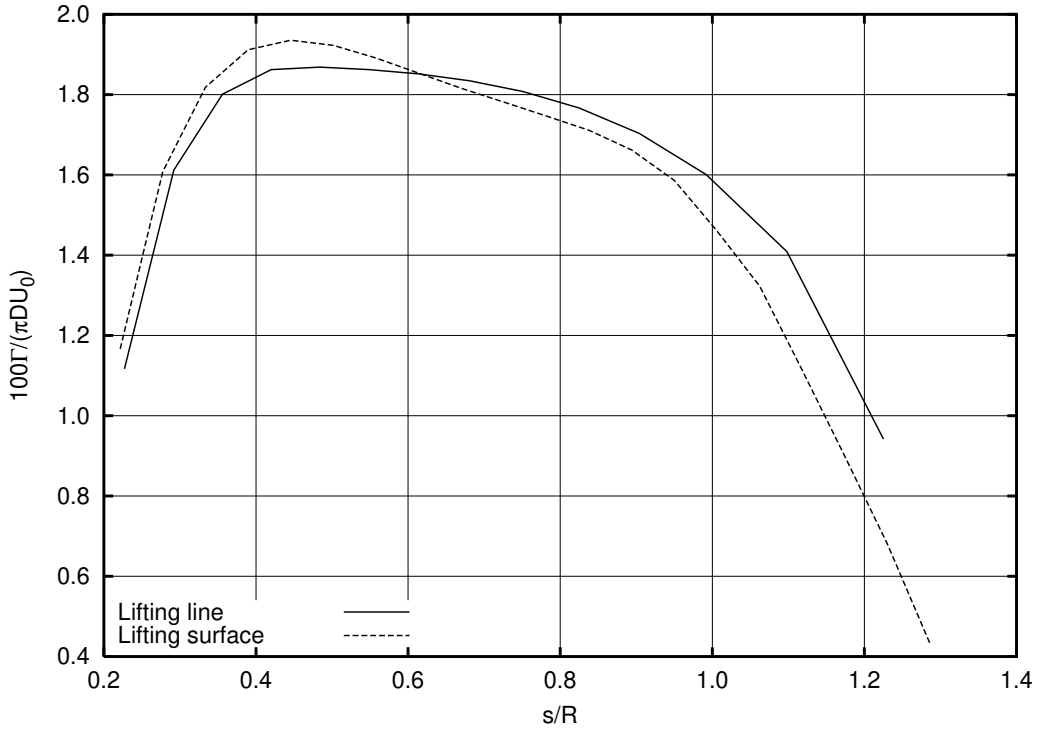

Radial distribution of circulation.

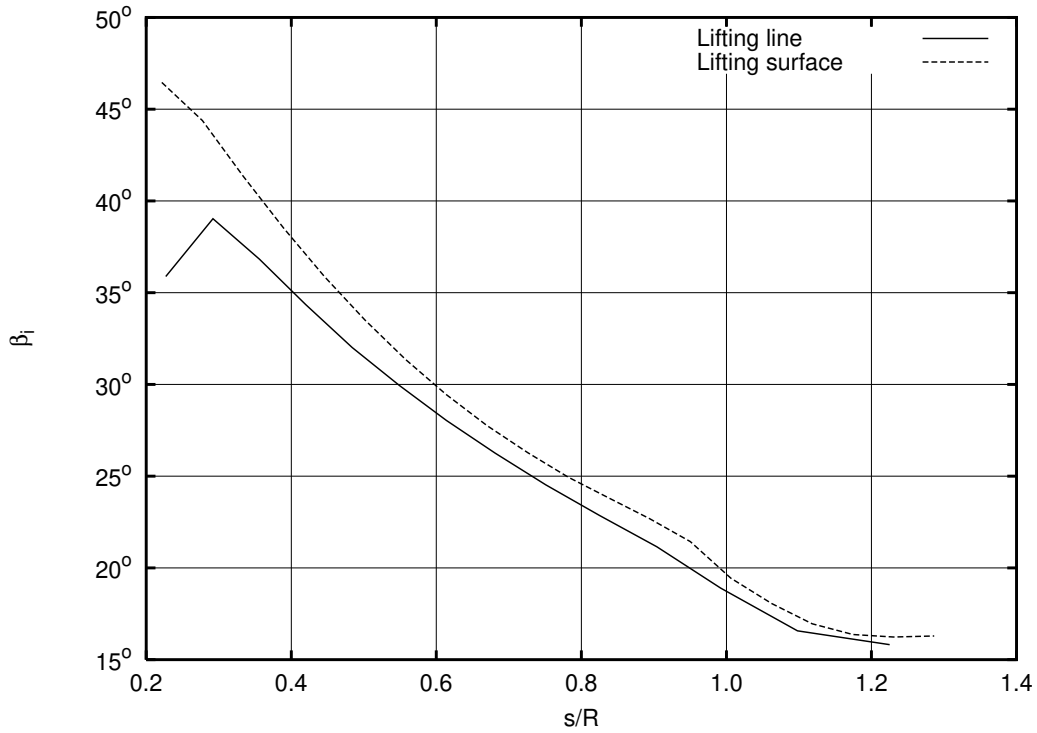

Radial distribution of pitch angle.

Figure 4.15: *Comparison between results for a lifting-line and a lifting-surface optimisation for the Kappel propeller K1.*

of the final pitch angle for the trailers is also shown in the figure. This comparison shows that the pitch angle for the lifting-surface optimisation is higher along the entire blade.

Table 4.7: *Results for the optimisation of the Kappel propeller K1 with a lifting-line optimisation and a lifting-surface optimisation.*

	J	U_s	U_A	C_{Th}	K_T	$10K_Q$	η
Lifting line	0.7472	11.57 $^{\mathrm{m}}/_{\mathrm{s}}$	9.280 $^{\mathrm{m}}/_{\mathrm{s}}$	1.0254	0.2248	0.3409	0.7842
Lifting surface	0.7472	11.57 $^{\mathrm{m}}/_{\mathrm{s}}$	9.274 $^{\mathrm{m}}/_{\mathrm{s}}$	1.0258	0.2249	0.3425	0.7810

4.9 Summary

The results from the lifting-surface optimisations show that the method converges with increasing number of panels, even for relatively high thrust loadings. The calculations show furthermore that the influence of the chordwise pressure distribution is negligible according to Munk's displacement theorem (von Kármán and Burgers, 1963). Even though the entire blade is included in the optimisation it becomes clear that with the used vortex-lattice method the larger part of the thrust and torque comes from the sides of the horseshoe vortices along the trailing edges, where the onset flow and the induced velocities are fully included, see Equations (4.26) and (4.27). This is also in agreement with Munk's theorem. The comparison between lifting-line and lifting-surface optimisations for the reference propeller shows that the distribution of thrust is almost identical for the two methods, whereas the distributions of circulation and torque differ, see Figure 4.9. This results in a higher efficiency for the propeller optimised by the lifting-surface optimisation. The details about this effect are not known and should be further investigated. The comparison for the DTNSRDC propellers shows that the distribution of thrust is almost identical for all the propellers, whereas the distributions of circulation and torque differ, see Figures 4.10, 4.12 and 4.13. From the comparison it is furthermore seen that skew increases the efficiency and the efficiency can be further improved by removing the skew-induced rake. Even though the details for this effect are not known some insight is obtained by comparing the combination of the distribution of circulation and the total velocities at the trailing edge for the different propellers. This comparison shows that skew has a favourable influence on the induced velocities at the trailing edge. Combined with the distribution of circulation for the skewed propellers the result is the higher efficiencies for these propellers. A further investigation is necessary in order to describe fully why skewed propellers have a higher efficiency, but similar findings are reported in Mishima and Kinnas (1997). It is noticeable that the distributions of thrust are almost identical for both the lifting-line and the lifting-surface optimisation for the five DTNSRDC propellers, see Figures 4.9, 4.10, 4.12 and 4.13. This indicates that, at least for linear theory, the method used for the optimisation has no influence on the optimum distribution of thrust. Furthermore, this optimum distribution is independent of the propeller geometry.

But the calculations also show that the distributions of circulation and torque are dependent on the propeller geometry. The lifting-surface method was also used to optimise a Kappel propeller in a radially varying inflow by application of the wake alignment procedure. The comparison with results from the normal optimisation procedure for the Kappel propellers shows a good agreement for the optimised torque coefficient and a reasonable agreement for the distribution of circulation. The comparison of the pitch angles for the trailers shows that the angles for the lifting-surface optimisation are higher. This indicates that the induced velocities are higher for the lifting-surface optimisation.

Chapter 5

Actuator Disk Theory

The actuator disk model is used to analyse given propellers. Thus, both the geometry and the distribution of loading are known in advance and the aim is to find the induced velocities and the pressure. The theory is based on a solution of the Euler equations where the propeller is modelled as a propeller with an infinite number of blades, i.e. an actuator disk. Wu (1962) solved, as one of the first, the equations for a heavily loaded disk in uniform inflow with the slipstream contraction included and with arbitrary distribution of loading, however, without including numerical results. Later Hough and Ordway (1965) gave closed-form solutions for the linear actuator disk in uniform inflow. For the linear theory the slipstream contraction is neglected. Conway (1995) and Conway (1998) confirmed these derivations and included numerical results both for the linear and the non-linear disk. All these solutions are based on an axially and tangentially applied force only, but as the aim is to treat Kappel propellers the Euler equations are solved including a radially applied force. Furthermore, it is desired that the computational time should be short and the model should be simple, therefore the present solution of the Euler equations is restricted to the linear equations. A radially varying inflow can be included in the Euler equations as in Goodman (1979) or Breslin and Andersen (1995), who treat the linear equations. Due to the poor results obtained by the linear shear theory in Breslin and Andersen (1995), it is decided that only the uniform inflow should be treated in this thesis.

5.1 Modified actuator disk theory

In the actuator disk theory the propeller concerned is replaced by an infinitely thin circular disk, see Figure 5.1. The disk is rotating with the angular velocity of the propeller, ω, and over the disk there is a pressure jump, Δp. The pressure jump and the normal to the disk are positive from the pressure to the suction side of the disk, see Figure 5.2. As Kappel propellers are treated the disk is not planar but has a curvature and the arc length parameter s is used to describe the surface, hence the coordinates describing the disk surface are all functions of

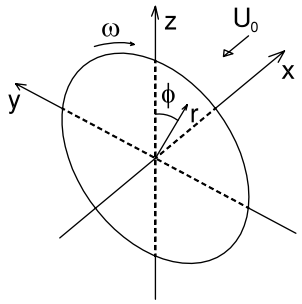

Figure 5.1: *Coordinate system for the actuator disk.*

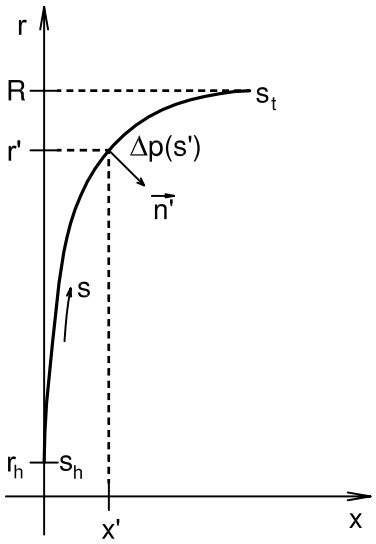

Figure 5.2: *Side view of the actuator disk.*

s. Normally, the tip of the Kappel propellers is allowed to bend towards the hub, but this is not possible in the actuator disk theory. Therefore, the radius must be monotone increasing with s, so that the radius of the tip coincides with the propeller radius. Figure 5.2 shows a side view of a curved disk.

The induced velocities and the pressure from the disk can be obtained by solving the continuity equation, see Equation (2.1), and the Euler equations, see Equation (2.2). As the flow will be axi-symmetric a cylindrical coordinate system (x, r, ϕ) is used. For this coordinate system x is positive upstream, r is positive from the hub to the tip and ϕ is positive clockwise when it is viewed in the positive x-direction, see Figure 5.1.

The continuity equation in cylindrical coordinates is

$$\frac{\partial u'_a}{\partial x} + \frac{1}{r}\frac{\partial u'_t}{\partial \phi} + \frac{\partial u'_r}{\partial r} + \frac{u'_r}{r} = 0 \tag{5.1}$$

The steady Euler equations in cylindrical coordinates are

$$\begin{aligned}(u'_a - U_0)\frac{\partial(u'_a - U_0)}{\partial x} + u'_r\frac{\partial(u'_a - U_0)}{\partial r} + u'_t\frac{1}{r}\frac{\partial(u'_a - U_0)}{\partial \phi} + \frac{1}{\rho}\frac{\partial p'}{\partial x} &= -\frac{1}{\rho}F'_a \\ (u'_a - U_0)\frac{\partial u'_r}{\partial x} + u'_r\frac{\partial u'_r}{\partial r} + u'_t\frac{1}{r}\frac{\partial u'_r}{\partial \phi} - \frac{1}{r}u_t'^2 + \frac{1}{\rho}\frac{\partial p'}{\partial r} &= -\frac{1}{\rho}F'_r \\ (u'_a - U_0)\frac{\partial u'_t}{\partial x} + u'_r\frac{\partial u'_t}{\partial r} + u'_t\frac{1}{r}\frac{\partial u'_t}{\partial \phi} - \frac{1}{r}u'_r u'_t + \frac{1}{\rho r}\frac{\partial p'}{\partial \phi} &= -\frac{1}{\rho}F'_t\end{aligned} \tag{5.2}$$

where the primes indicate differential quantities and F'_a, F'_r and F'_t are the axial, radial and tangential components, respectively, of the applied force over the differential path dS'. The forces originate from the pressure jump across the disk. The forces F'_a, F'_r and F'_t are defined as the forces from the fluid on the blade, hence the minus. In the Euler equations it is furthermore used that the total differential velocity from the disk is $\vec{u}' = (u'_a - U_0, u'_r, u'_t)$ as the onset flow has only an axial component.

In order to linearise the Euler equations, so the closed-form solutions can be obtained, it is assumed that the onset flow is much larger than the induced velocities, $U_0 >> u'_a, u'_r, u'_t$. This means that only lightly loaded propellers can be treated by this theory. By retaining only the linear terms of the induced velocities and the derivatives the linear Euler equations are

$$-U_0\frac{\partial u'_a}{\partial x} + \frac{1}{\rho}\frac{\partial p'}{\partial x} = -\frac{F'_a}{\rho} \tag{5.3}$$

$$-U_0\frac{\partial u'_r}{\partial x} + \frac{1}{\rho}\frac{\partial p'}{\partial r} = -\frac{F'_r}{\rho} \tag{5.4}$$

$$-U_0\frac{\partial u'_t}{\partial x} + \frac{1}{\rho r}\frac{\partial p'}{\partial \phi} = -\frac{F'_t}{\rho} \tag{5.5}$$

The forces on the right-hand side are found from the pressure jump across the disk:

$$\begin{aligned}F'_a &= \frac{\Delta p(s')}{r}n_a(s')\delta(x - x')\delta(r - r')\delta(\phi - \phi')dS' \\ F'_r &= \frac{\Delta p(s')}{r}n_r(s')\delta(x - x')\delta(r - r')\delta(\phi - \phi')dS' \\ F'_t &= \frac{\Delta p(s')}{r}n_t(s')\delta(x - x')\delta(r - r')\delta(\phi - \phi')dS'\end{aligned} \tag{5.6}$$

where Dirac's delta function, $\delta(x)$, is used, so the differential forces, F'_a, F'_r or F'_t, are applied only to the dummy point $(x', r'\phi') = (x(s'), r(s'), \phi(s'))$. $n_a(s'), n_r(s'), n_t(s')$ are the axial, radial and tangential normal force components, respectively, and dS' is the disk area element.

By operating on the linearised Euler equations with the 'continuity operator' from Equation (5.1), it is possible to get a Poisson equation for the pressure. In the continuity equation

the axial Euler Equation (5.3) is inserted instead of u'_a, the radial Euler Equation (5.4) is inserted instead of u'_r and, finally, the tangential Euler Equation (5.5) is inserted instead of u'_t. This gives

$$-U_0\frac{\partial}{\partial x}\Big(\frac{\partial u'_a}{\partial x}+\frac{1}{r}\frac{\partial u'_t}{\partial \phi}+\frac{\partial u'_r}{\partial r}+\frac{u'_r}{r}\Big)+\frac{1}{\rho}\Big(\frac{\partial^2 p'}{\partial x^2}+\frac{1}{r^2}\frac{\partial^2 p'}{\partial \phi^2}+\frac{\partial^2 p'}{\partial r^2}+\frac{1}{r}\frac{\partial p'}{\partial r}\Big)$$
$$=-\frac{1}{\rho}\Big(\frac{\partial F'_a}{\partial x}+\frac{1}{r}\frac{\partial F'_t}{\partial \phi}+\frac{\partial F'_r}{\partial r}+\frac{F'_r}{r}\Big) \quad (5.7)$$

The first term on the left side is zero according to the continuity equation, so that Equation (5.7) reduces to a Poisson equation:

$$\nabla^2 p' = -\Big(\frac{\partial F'_a}{\partial x}+\frac{1}{r}\frac{\partial F'_t}{\partial \phi}+\frac{\partial F'_r}{\partial r}+\frac{F'_r}{r}\Big)$$

whose solution is

$$p' = \frac{1}{4\pi}\int_{-\infty}^{\infty}\int_0^{\infty}\int_0^{2\pi}\frac{\frac{\partial F'_a}{\partial x''}+\frac{1}{r''}\frac{\partial F'_t}{\partial \phi''}+\frac{\partial F'_r}{\partial r''}+\frac{F'_r}{r''}}{\sqrt{(x-x'')^2+r^2+r''^2-2rr''cos(\phi-\phi'')}}r''d\phi''dr''dx'' \quad (5.8)$$

Each term of Equation (5.8) is integrated separately by inserting the forces from Equation (5.6). By setting $\mathbf{R}'' = \sqrt{(x-x'')^2+r^2+r''^2-2rr''cos(\phi-\phi'')}$ and $\mathbf{R} = \sqrt{(x-x')^2+r^2+r'^2-2rr'cos(\phi-\phi')}$ the $\partial F'_a/\partial x''$ term is reduced to

$$\int_{-\infty}^{\infty}\int_0^{\infty}\int_0^{2\pi}\frac{\partial F'_a}{\partial x''}\frac{1}{\mathbf{R}''}r''d\phi''dr''dx''$$
$$=\int_{-\infty}^{\infty}\int_0^{\infty}\int_0^{2\pi}\frac{\Delta p(s')}{r''}n_a(s')\frac{\partial}{\partial x''}\delta(x''-x')\delta(r''-r')\delta(\phi''-\phi')dS'\frac{1}{\mathbf{R}''}r''d\phi''dr''dx''$$
$$=\Delta p(s')n_a(s')dS'\int_{-\infty}^{\infty}\frac{1}{\sqrt{(x-x'')^2+r^2+r'^2-2rr'cos(\phi-\phi')}}\frac{\partial}{\partial x''}\delta(x''-x')dx''$$
$$=\Delta p(s')n_a(s')dS'\Big(-\frac{\partial}{\partial x'}\frac{1}{\mathbf{R}}\Big) \quad (5.9)$$

the $\partial F'_t/\partial \phi''$ term is reduced to

$$\int_{-\infty}^{\infty}\int_0^{\infty}\int_0^{2\pi}\frac{1}{r''}\frac{\partial F'_t}{\partial \phi''}\frac{1}{\mathbf{R}''}r''d\phi''dr''dx''$$
$$=\int_{-\infty}^{\infty}\int_0^{\infty}\int_0^{2\pi}\frac{\Delta p(s')}{r''}\frac{1}{r''}n_t(s')\delta(x''-x')\delta(r''-r')\frac{\partial}{\partial \phi''}\delta(\phi''-\phi')dS'\frac{1}{\mathbf{R}''}r''d\phi''dr''dx''$$
$$=\Delta p(s')n_t(s')\frac{1}{r'}dS'\Big(-\frac{\partial}{\partial \phi'}\frac{1}{\mathbf{R}}\Big) \quad (5.10)$$

the $\partial F_r'/\partial r''$ term is reduced to

$$\begin{aligned}
&\int_{-\infty}^{\infty}\int_{0}^{\infty}\int_{0}^{2\pi}\frac{\partial F_r'}{\partial r''}\frac{1}{\mathbf{R}''}r''d\phi''dr''dx'' \\
&=\int_{-\infty}^{\infty}\int_{0}^{\infty}\int_{0}^{2\pi}\frac{\Delta p(s')}{r''}n_r(s')\delta(x''-x')\frac{\partial}{\partial r''}\delta(r''-r')\delta(\phi''-\phi')dS'\frac{1}{\mathbf{R}''}r''d\phi''dr''dx'' \\
&\quad-\int_{-\infty}^{\infty}\int_{0}^{\infty}\int_{0}^{2\pi}\frac{\Delta p(s')}{r''^2}n_r(s')\delta(x''-x')\delta(r''-r')\delta(\phi''-\phi')dS'\frac{1}{\mathbf{R}''}r''d\phi''dr''dx'' \\
&\qquad\qquad=\Delta p(s')n_r(s')dS'\Big(-\frac{\partial}{\partial r'}\frac{1}{\mathbf{R}}\Big)-\text{SECOND TERM}
\end{aligned}\tag{5.11}$$

and finally the F_r'/r'' term is reduced to

$$\begin{aligned}
&\int_{-\infty}^{\infty}\int_{0}^{\infty}\int_{0}^{2\pi}\frac{1}{r''}F_r'\frac{1}{\mathbf{R}''}r''d\phi''dr''dx'' \\
&\qquad=\int_{-\infty}^{\infty}\int_{0}^{\infty}\int_{0}^{2\pi}\frac{\Delta p(s')}{r''^2}n_r(s')\delta(x''-x')\delta(r''-r')\delta(\phi''-\phi')dS'\frac{1}{\mathbf{R}''}r''d\phi''dr''dx''
\end{aligned}\tag{5.12}$$

This term cancels the second term of the above equation. Hence, the differential pressure is

$$p'=\frac{-1}{4\pi}\Delta p(s')\Big[n_a(s')\frac{\partial}{\partial x'}+n_r(s')\frac{\partial}{\partial r'}+n_t(s')\frac{1}{r'}\frac{\partial}{\partial\phi'}\Big]\frac{1}{\mathbf{R}}dS'\tag{5.13}$$

By an integration over the disk the total pressure is obtained:

$$p(x,r)=\frac{-1}{4\pi}\int_S\Delta p(s')\Big[n_a(s')\frac{\partial}{\partial x'}+n_r(s')\frac{\partial}{\partial r'}+n_t(s')\frac{1}{r'}\frac{\partial}{\partial\phi'}\Big]\frac{1}{\mathbf{R}}dS'\tag{5.14}$$

This integral will be solved later.

As the pressure is known it is possible to find expressions for the velocities by integrating the linear Euler equations. By integrating Equation (5.3) from infinitely upstream ($x\to\infty$) to the present point x the differential axial velocity is

$$\begin{aligned}
&-U_0(u_a'(x,r)\big|_{x\to\infty}-u_a'(x,r))+\frac{1}{\rho}(p'(x,r)\big|_{x\to\infty}-p'(x,r)) \\
&\qquad\qquad=-\frac{\Delta p(s')}{\rho r}n_a(s')\big[1-H(x-x')\big]\delta(r-r')\delta(\phi-\phi')dS'
\end{aligned}\tag{5.15}$$

where $H(x)$ is the Heaviside's step function defined by

$$H(x)=\begin{cases}0 & x<0,\\ \frac{1}{2} & x=0,\\ 1 & x>0.\end{cases}$$

The axially induced velocity vanishes far upstream of the disk, thus $u'_a(x,r) = 0$ for $x \to \infty$. As only the pressure difference is interesting the pressure is assumed to be zero far upstream, thus $p'(x,r) = 0$ for $x \to \infty$. Hence, the differentially induced axial velocity becomes

$$u'_a(x,r) = \frac{1}{\rho U_0} p'(x,r) - \frac{\Delta p(s')}{\rho U_0 r'} n_a(s') \big[1 - H(x-x')\big] \delta(r-r') \delta(\phi - \phi') dS' \quad (5.16)$$

and the total induced axial velocity is found by an integration over the disk:

$$u_a(x,r) = \frac{1}{\rho U_0} p(x,r) - \int_S \frac{\Delta p(s')}{\rho U_0 r'} n_a(s') \big[1 - H(x-x')\big] \delta(r-r') \delta(\phi - \phi') dS' \quad (5.17)$$

The integration over the disk is given by

$$\int_S ... dS' = \int_{s_h}^{s_t} \int_0^{2\pi} ... r' d\phi' ds' \quad (5.18)$$

where s_h is the arc length at the hub and s_t is the arc length at the tip.

By applying the integration the total induced axial velocity is

$$\begin{aligned} u_a(x,r) &= \frac{1}{\rho U_0} p(x,r) - \int_{s_h}^{s_t} \int_0^{2\pi} \frac{\Delta p(s') r'}{\rho U_0 r'} n_a(s') \big[1 - H(x-x')\big] \delta(r-r') \delta(\phi - \phi') d\phi' ds' \\ &= \frac{1}{\rho U_0} p(x,r) - \frac{\Delta p(s)}{\rho U_0} n_a(s) \big[1 - H(x-x')\big] \end{aligned} \quad (5.19)$$

where s corresponds to the arc length for the radius r.

Integration of Equation (5.4) gives the differentially induced radial velocity. Again the radially induced velocity vanishes far upstream ($u'_r(x,r) = 0$ for $x \to \infty$):

$$\begin{aligned} u'_r(x,r) = -\frac{1}{\rho U_0} \int_x^\infty \frac{\partial p'}{\partial r} dx'' \\ - \frac{\Delta p(s')}{\rho U_0 r'} n_r(s') \big[1 - H(x-x')\big] \delta(r-r') \delta(\phi - \phi') dS' \end{aligned} \quad (5.20)$$

An integration over the disk gives the total induced radial velocity:

$$\begin{aligned} u_r(x,r) &= -\frac{1}{\rho U_0} \int_S \int_x^\infty \frac{\partial p'}{\partial r} dx'' dS' - \int_S \frac{\Delta p(s')}{\rho U_0 r'} n_r(s') \big[1 - H(x-x')\big] \delta(r-r') \delta(\phi - \phi') dS' \\ &= -\frac{1}{\rho U_0} \int_S \int_x^\infty \frac{\partial p'}{\partial r} dx'' dS' - \frac{\Delta p(s)}{\rho U_0} n_r(s) \big[1 - H(x-x')\big] \end{aligned} \quad (5.21)$$

where the integration of the pressure will be solved later.

The differentially induced tangential velocity is found by an integration of Equation (5.5), where the rotational symmetry is applied and again the velocity far upstream is zero ($u'_t(x,r) = 0$ for $x \to \infty$), hence

$$u_t'(x,r) = -\frac{\Delta p(s')}{\rho U_0}\frac{n_t(s')}{r'}\big[1 - H(x-x')\big]\delta(r-r')\delta(\phi-\phi')dS' \tag{5.22}$$

and the total induced tangential velocity is

$$\begin{aligned} u_t(x,r) &= -\int_S \frac{\Delta p(s')}{\rho U_0}\frac{n_t(s')}{r'}\big[1 - H(x-x')\big]\delta(r-r')\delta(\phi-\phi')dS' \\ &= -\frac{\Delta p(s)}{\rho U_0} n_t(s)\big[1 - H(x-x')\big] \end{aligned} \tag{5.23}$$

In order to have the final expressions for the velocities it is necessary to find a closed-form solution for the pressure. To perform the integration over the disk for the pressure, see Equation (5.14), the $1/\mathbf{R}$ term is rewritten by use of the Legendre functions of the second kind, see e.g. Breslin and Andersen (1994):

$$\frac{1}{\mathbf{R}} = \frac{1}{\pi\sqrt{rr'}}\sum_{m=-\infty}^{\infty} Q_{|m|-\frac{1}{2}}(Z)e^{im(\phi-\phi')} \tag{5.24}$$

where

$$Z = \frac{(x-x')^2 + r^2 + r'^2}{2rr'} \tag{5.25}$$

Insert Equation (5.24) in the pressure Equation (5.14):

$$\begin{aligned} p(x,r) = \frac{-1}{4\pi}\int_{s_h}^{s_t}\int_0^{2\pi} \Delta p(s')r' \\ \Big[n_a(s')\frac{\partial}{\partial x'} + n_r(s')\frac{\partial}{\partial r'} + n_t(s')\frac{1}{r'}\frac{\partial}{\partial \phi'}\Big]\Big(\frac{1}{\pi\sqrt{rr'}}\sum_{m=-\infty}^{\infty} Q_{|m|-\frac{1}{2}}(Z)e^{im(\phi-\phi')}\Big)d\phi' ds' \end{aligned} \tag{5.26}$$

For the n_a- and n_r-terms $e^{im(\phi-\phi')}$ is the only function of ϕ'. The ϕ'-integration gives

$$\int_0^{2\pi} e^{im(\phi-\phi')}d\phi' = \begin{cases} 0 & \text{if } m \neq 0 \\ 2\pi & \text{if } m = 0 \end{cases} \tag{5.27}$$

For the n_t-term the ϕ'-integration gives

$$\int_0^{2\pi} \frac{\partial}{\partial \phi'}\frac{1}{\mathbf{R}}d\phi' = \frac{1}{\mathbf{R}(2\pi)} - \frac{1}{\mathbf{R}(0)} = 0 \tag{5.28}$$

Thus, the pressure equation is reduced to

$$\begin{aligned} p(x,r) &= \frac{-1}{2\pi}\int_{s_h}^{s_t} \Delta p(s')r'\Big[n_a'\frac{\partial}{\partial x'} + n_r'\frac{\partial}{\partial r'}\Big]\Big(\frac{1}{\sqrt{rr'}}Q_{-\frac{1}{2}}(Z)\Big)ds' \\ &= \frac{-1}{2\pi}\int_{s_h}^{s_t} \Delta p(s')r'\Big\{\frac{n_a'}{\sqrt{rr'}}\frac{\partial Q_{-\frac{1}{2}}(Z)}{\partial Z}\frac{\partial Z}{\partial x'} \\ &\quad + \frac{n_r'}{\sqrt{rr'}}\Big[-\frac{1}{2r'}Q_{-\frac{1}{2}}(Z) + \frac{\partial Q_{-\frac{1}{2}}(Z)}{\partial Z}\frac{\partial Z}{\partial r'}\Big]\Big\}ds' \end{aligned} \tag{5.29}$$

where

$$
\begin{aligned}
n'_a &= n_a(s') \\
n'_r &= n_r(s') \\
\frac{\partial Z}{\partial r'} &= \frac{2r'}{2rr'} + \big[(x-x')^2 + r^2 + r'^2\big]\frac{-1}{2rr'^2} = \frac{1}{r} - \frac{Z}{r'} \\
\frac{\partial Z}{\partial x'} &= \frac{-2(x-x')}{2rr'} = -\frac{x-x'}{rr'}
\end{aligned}
$$

Hence, the final expression for the induced pressure is

$$
\begin{aligned}
p(x,r) = \frac{1}{2\pi}\int_{s_h}^{s_t} \frac{\Delta p(s')r'}{\sqrt{rr'}}\Bigg\{ & n'_a \frac{x-x'}{rr'} Q'_{-\frac{1}{2}}(Z) \\
& - n'_r\Big[-\frac{1}{2r'}Q_{-\frac{1}{2}}(Z) + \Big(\frac{1}{r} - \frac{Z}{r'}\Big)Q'_{-\frac{1}{2}}(Z)\Big]\Bigg\} ds'
\end{aligned}
\tag{5.30}
$$

where $Q'_{-\frac{1}{2}}(Z) = \partial Q_{-\frac{1}{2}}(Z)/\partial Z$.

By inserting Equation (5.30) in Equation (5.19) the closed-form solution for the total induced axial velocity is

$$
\begin{aligned}
u_a(x,r) = \frac{1}{2\pi\rho U_0}\int_{s_h}^{s_t} \frac{\Delta p(s')r'}{\sqrt{rr'}}\Bigg\{ & n'_a \frac{x-x'}{rr'} Q'_{-\frac{1}{2}}(Z) \\
& - n'_r\Big[-\frac{1}{2r'}Q_{-\frac{1}{2}}(Z) + \Big(\frac{1}{r} - \frac{Z}{r'}\Big)Q'_{-\frac{1}{2}}(Z)\Big]\Bigg\} ds' \\
& - \frac{\Delta p(s)}{\rho U_0} n_a(s)\big[1 - H(x-x')\big]
\end{aligned}
\tag{5.31}
$$

Returning to the total induced radial velocity from Equation (5.21), the integration of the pressure is solved by inserting Equation (5.13) for p':

$$
\begin{aligned}
&\frac{-1}{\rho U_0}\int_x^\infty \int_{S'} \frac{\partial p'}{\partial r} dS' dx'' \\
&\quad = \frac{1}{\rho U_0}\int_x^\infty \int_0^{2\pi} \int_{s_h}^{s_t} \frac{\partial}{\partial r}\frac{1}{4\pi}\Delta p(s')\Big[n_a(s')\frac{\partial}{\partial x'} + n_r(s')\frac{\partial}{\partial r'} + n_t(s')\frac{1}{r'}\frac{\partial}{\partial \phi'}\Big]\frac{1}{\mathbf{R}} r' ds' d\phi' dx''
\end{aligned}
\tag{5.32}
$$

Again the $1/\mathbf{R}$ term is rewritten by the Legendre functions, see Equation (5.24), and the angular integration from Equation (5.27) is valid for the n_a- and n_r-terms also. For the n_t-term the ϕ'-integration gives the following, as the order of differentiation can be interchanged:

$$
\int_0^{2\pi} \frac{\partial}{\partial r}\Big\{\frac{\partial}{\partial \phi'}\frac{1}{\mathbf{R}}\Big\} d\phi' = \frac{\partial}{\partial r}\frac{1}{\mathbf{R}(2\pi)} - \frac{\partial}{\partial r}\frac{1}{\mathbf{R}(0)} = 0 \tag{5.33}
$$

By use of $\partial/\partial x' = -\partial/\partial x''$ the pressure integration from Equation (5.32) is

$$\begin{aligned}\frac{-1}{\rho U_0}\int_x^\infty\int_S \frac{\partial p'}{\partial r}dS'dx'' &= \frac{1}{2\pi}\int_x^\infty\int_{s_h}^{s_t}\frac{\Delta p(s')r'}{\rho U_0}\frac{\partial}{\partial r}\Big[-n_a'\frac{\partial}{\partial x''}+n_r'\frac{\partial}{\partial r'}\Big]\Big(\frac{1}{\sqrt{rr'}}Q_{-\frac{1}{2}}(Z)\Big)ds'dx'' \\ &= \frac{1}{2\pi}\int_{s_h}^{s_t}\frac{\Delta p(s')r'}{\rho U_0}\frac{\partial}{\partial r}\Big[\frac{n_a'}{\sqrt{rr'}}Q_{-\frac{1}{2}}(Z)+\int_x^\infty n_r'\frac{\partial}{\partial r'}\Big(\frac{1}{\sqrt{rr'}}Q_{-\frac{1}{2}}(Z)\Big)dx''\Big]ds'\end{aligned} \tag{5.34}$$

where it is used that $Q(Z)\to 0$ for $Z\to\infty$ in the evaluation of the first x''-integral.

In order to evaluate the last x''-integral the Legendre function is written in the following form, see e.g. Breslin and Andersen (1994):

$$\frac{1}{\sqrt{rr'}}Q_{-\frac{1}{2}}(Z) = \pi\int_0^\infty J_0(kr)J_0(kr')e^{-k|x-x'|}dk \tag{5.35}$$

where J_n is the Bessel functions of the first kind and the order n. The derivative with respect to r' is

$$\frac{\partial}{\partial r'}\frac{1}{\sqrt{rr'}}Q_{-\frac{1}{2}}(Z) = \pi\int_0^\infty -J_0(kr)J_1(kr')ke^{-k|x-x'|}dk \tag{5.36}$$

Hence, the last x''-integral is

$$\int_x^\infty n_r'\frac{\partial}{\partial r'}\Big(\frac{1}{\sqrt{rr'}}Q_{-\frac{1}{2}}(Z)\Big)dx'' = -\pi\int_x^\infty\int_0^\infty n_r'J_0(kr)J_1(kr')ke^{-k|x''-x'|}dkdx'' \tag{5.37}$$

In the above expression the term $e^{-k|x-x'|}$ is the only function of x. The x''-integration gives

$$\begin{aligned}&-\pi\int_0^\infty n_rJ_0(kr)J_1(kr')\int_x^\infty ke^{-k|x''-x'|}dx''dk \\ &= -\pi\int_0^\infty F(k)\int_x^\infty ke^{-k|x''-x'|}dx''dk \\ &= \begin{cases}-\pi\int_0^\infty F(k)\int_x^\infty ke^{-k(x''-x')}dx''dk & \text{for } x\ge x' \\ -\pi\int_0^\infty F(k)\Big[\int_x^{x'}ke^{k(x''-x')}dx''+\int_{x'}^\infty ke^{-k(x''-x')}dx''\Big]dk & \text{for } x<x'\end{cases} \\ &= \begin{cases}-\pi\int_0^\infty F(k)e^{-k(x-x')}dk & \text{for } x\ge x' \\ -\pi\int_0^\infty F(k)\Big[-e^{k(x-x')}+2\Big]dk & \text{for } x<x'\end{cases}\end{aligned} \tag{5.38}$$

Hence, the last x''-integral of Equation (5.34) is

$$\begin{aligned}&\int_x^\infty n_r'\frac{\partial}{\partial r'}\Big(\frac{1}{\sqrt{rr'}}Q_{-\frac{1}{2}}(Z)\Big)dx'' \\ &\quad= \begin{cases}-\pi n_r'\int_0^\infty J_0(kr)J_1(kr')e^{-k(x-x')}dk & \text{for } x\ge x' \\ \pi n_r'\int_0^\infty J_0(kr)J_1(kr')e^{k(x-x')}dk - 2\pi n_r'\int_0^\infty J_0(kr)J_1(kr')dk & \text{for } x<x'\end{cases}\end{aligned} \tag{5.39}$$

where the integration of the Bessel functions gives, see e.g. Abramowitz and Stegun (1972):

$$\int_0^\infty J_0(kr)J_1(kr')dk = \begin{cases} \frac{1}{r'} & \text{for } r < r' \\ \frac{1}{2r} & \text{for } r = r' \\ 0 & \text{for } r > r' \end{cases} \tag{5.40}$$

By using Equation (5.40) in Equation (5.39) the Heaviside's step function can be used to write Equation (5.39) for $x \neq x'$ as

$$\begin{aligned} &\int_x^\infty n'_r \frac{\partial}{\partial r'}\Big(\frac{1}{\sqrt{rr'}}Q_{-\frac{1}{2}}(Z)\Big)dx'' \\ &\quad = \mp\pi n'_r \int_0^\infty J_0(kr)J_1(kr')e^{-k|x-x'|}dk - \frac{2\pi n'_r}{r'}H(r'-r)H(x'-x) \text{ for } x \neq x' \end{aligned} \tag{5.41}$$

where $-$ applies for $x > x'$ and $+$ for $x < x'$. From Equation (5.39) it is seen that the function is continuous in the point $x = x'$, but with the introduction of the Heaviside's step function it is necessary to omit this point, later it will be included again.

The last integral of the right-hand side of Equation (5.34) gives

$$\begin{aligned} &\frac{\partial}{\partial r}\Big[\int_x^\infty n'_r \frac{\partial}{\partial r'}\Big(\frac{1}{\sqrt{rr'}}Q_{-\frac{1}{2}}(Z)\Big)dx''\Big] \\ &= \pm\pi n'_r \int_0^\infty J_1(kr)J_1(kr')ke^{-k|x-x'|}dk + \frac{2\pi n'_r}{r'}\delta(r'-r)H(x'-x) \\ &\qquad = \left[-\frac{\partial}{\partial x}\frac{1}{\sqrt{rr'}}Q_{\frac{1}{2}}(Z) + \frac{2\pi}{r'}\delta(r'-r)H(x'-x)\right]n'_r \quad \text{for } x \neq x' \end{aligned} \tag{5.42}$$

Hence, the pressure integration for the radial velocity is

$$
\begin{aligned}
&\frac{-1}{\rho U_0}\int_x^\infty\int_S \frac{\partial p'}{\partial r}dS'dx'' \\
&= \frac{1}{2\pi}\int_{s_h}^{s_t}\frac{\Delta p(s')r'}{\rho U_0}\left\{ n'_a\frac{\partial}{\partial r}\left[\frac{1}{\sqrt{rr'}}Q_{-\frac{1}{2}}(Z)\right]+n'_r\left[-\frac{\partial}{\partial x}\frac{1}{\sqrt{rr'}}Q_{\frac{1}{2}}(Z)+\frac{2\pi}{r'}\delta(r'-r)H(x'-x)\right]\right\}ds' \\
&= \frac{1}{2\pi}\int_{s_h}^{s_t}\frac{\Delta p(s')r'}{\rho U_0}\left\{ \frac{n'_a}{\sqrt{rr'}}\left[\frac{-1}{2r}Q_{-\frac{1}{2}}(Z)+\big(\frac{1}{r'}-\frac{Z}{r}\big)Q'_{-\frac{1}{2}}(Z)\right]\right. \\
&\quad \left. + n'_r\left[\frac{-1}{\sqrt{rr'}}\frac{x-x'}{rr'}Q'_{\frac{1}{2}}(Z)+\frac{2\pi}{r'}\delta(r'-r)H(x'-x)\right]\right\}ds' \\
&= \frac{1}{2\pi}\int_{s_h}^{s_t}\frac{\Delta p(s')r'}{\rho U_0}\left\{ \frac{n'_a}{\sqrt{rr'}}\left[\frac{-1}{2r}Q_{-\frac{1}{2}}(Z)+\big(\frac{1}{r'}-\frac{Z}{r}\big)Q'_{-\frac{1}{2}}(Z)\right]\right. \\
&\quad \left. - \frac{n'_r}{\sqrt{rr'}}\frac{x-x'}{rr'}Q'_{\frac{1}{2}}(Z)\right\}ds' + \frac{1}{2\pi}\int_{s_h}^{s_t}\frac{\Delta p(s')r'}{\rho U_0}n'_r\frac{2\pi}{r'}\delta(r'-r)H(x'-x)ds' \\
&= \frac{1}{2\pi}\int_{s_h}^{s_t}\frac{\Delta p(s')r'}{\rho U_0}\left\{ \frac{n'_a}{\sqrt{rr'}}\left[\frac{-1}{2r}Q_{-\frac{1}{2}}(Z)+\big(\frac{1}{r'}-\frac{Z}{r}\big)Q'_{-\frac{1}{2}}(Z)\right] - \frac{n'_r}{\sqrt{rr'}}\frac{x-x'}{rr'}Q'_{\frac{1}{2}}(Z)\right\}ds' \\
&\qquad + \frac{\Delta p(s)}{\rho U_0}n_r H(x'-x) \qquad (5.43)
\end{aligned}
$$

If Equation (5.43) is inserted in Equation (5.21) the closed-form solution for the total induced radial velocity is obtained:

$$
\begin{aligned}
u_r(x,r) &= \frac{-1}{\rho U_0}\int_x^\infty\int_S \frac{\partial p'}{\partial r}dS'dx'' - \frac{\Delta p(s)}{\rho U_0}n_r(s)\big[1-H(x-x')\big] \\
&= \frac{1}{2\pi\rho U_0}\int_{s_h}^{s_t}\frac{\Delta p(s')r'}{\sqrt{rr'}}\left\{ n'_a\left[\frac{-1}{2r}Q_{-\frac{1}{2}}(Z)+\big(\frac{1}{r'}-\frac{Z}{r}\big)Q'_{-\frac{1}{2}}(Z)\right] - n'_r\frac{x-x'}{rr'}Q'_{\frac{1}{2}}(Z)\right\}ds' \\
&\quad + \frac{\Delta p(s)}{\rho U_0}n_r(s)H(x'-x) - \frac{\Delta p(s)}{\rho U_0}n_r(s)\big[1-H(x-x')\big] \\
&= \frac{1}{2\pi\rho U_0}\int_{s_h}^{s_t}\frac{\Delta p(s')r'}{\sqrt{rr'}}\left\{ n'_a\left[\frac{-1}{2r}Q_{-\frac{1}{2}}(Z)+\big(\frac{1}{r'}-\frac{Z}{r}\big)Q'_{-\frac{1}{2}}(Z)\right] - n'_r\frac{x-x'}{rr'}Q'_{\frac{1}{2}}(Z)\right\}ds' \\
&\qquad (5.44)
\end{aligned}
$$

In the above solution for $u_r(x,r)$ it is seen that the Heaviside's step functions have cancelled each other and therefore the above result can be applied to all x.

In the solutions for u_a, see Equation (5.31), and u_r, see Equation (5.44), the n'_a-terms are recognised as the results from Hough and Ordway (1965), i.e. they are similar to the results for an actuator disk. The n'_r-terms are identical to the induced velocities from a duct, or more precisely a ring vortex, see e.g. Küchemann and Weber (1953). The expression for

u_t, see Equation (5.23), is seen to be similar to the results from Hough and Ordway (1965). Thus, by this modified actuator disk theory, the induced velocities and pressure from the Kappel propeller are calculated as a weighted sum of the velocities from a normal actuator disk and a duct.

5.1.1 Evaluation of the Singular Points

The Legendre functions in the expressions for the velocities are singular for $Z = 1$. This happens when the field point (x, r, ϕ) and the dummy point (x', r', ϕ') coincide as they can do on the disk only. Fortunately, the singularities are removable and therefore they cause no problems, except that the integration when the field point is on the disk requires special attention.

For $Z \approx 1$ the dominating terms in the approximation of the Legendre functions are, see e.g. Breslin and Andersen (1994):

$$\begin{aligned} Q_{n-\frac{1}{2}}(Z) &\approx -\tfrac{1}{2}\ln\left(\frac{(x-x')^2+(r-r')^2}{2rr'}\right) \\ Q'_{n-\frac{1}{2}}(Z) &\approx \frac{-rr'}{(x-x')^2+(r-r')^2} \end{aligned} \tag{5.45}$$

These approximations are inserted in the integrand for the induced pressure, see Equation (5.30), thus for $Z \approx 1$:

$$\begin{aligned} dp &= \frac{1}{2\pi}\frac{\Delta p(s')r'}{\sqrt{rr'}}\Bigg\{ n'_a \frac{x-x'}{rr'} Q'_{-\frac{1}{2}}(Z) \\ &\quad - n'_r\Big[-\frac{1}{2r'}Q_{-\frac{1}{2}}(Z) + \Big(\frac{1}{r}-\frac{Z}{r'}\Big)Q'_{-\frac{1}{2}}(Z)\Big]\Bigg\} ds' \\ &\approx \frac{1}{2\pi}\frac{\Delta p(s')r'}{\sqrt{rr'}}\Bigg\{ \frac{-(x-x')n'_a}{(x-x')^2+(r-r')^2} \\ &\quad - n'_r\Bigg[\frac{1}{4r'}\ln\left(\frac{(x-x')^2+(r-r')^2}{2rr'}\right) \\ &\quad + \left(\frac{1}{r}-\frac{1}{r'}\left(\frac{(x-x')^2+r^2+r'^2}{2rr'}\right)\right)\frac{-rr'}{(x-x')^2+(r-r')^2}\Bigg]\Bigg\} ds' \\ &= \frac{1}{2\pi}\frac{\Delta p(s')r'}{\sqrt{rr'}}\Bigg\{ \frac{-(x-x')n'_a-(r-r')n'_r}{(x-x')^2+(r-r')^2} \\ &\quad - n'_r\left[\frac{1}{4r'}\ln\left(\frac{(x-x')^2+(r-r')^2}{2rr'}\right)+\frac{1}{2r'}\right]\Bigg\} ds' \end{aligned} \tag{5.46}$$

From the above expression it is seen that the first term has a singularity for $x = x'$ and $r = r'$, this singularity will be examined later. Furthermore, it is seen that a logarithmic singularity is present, which will be treated numerically.

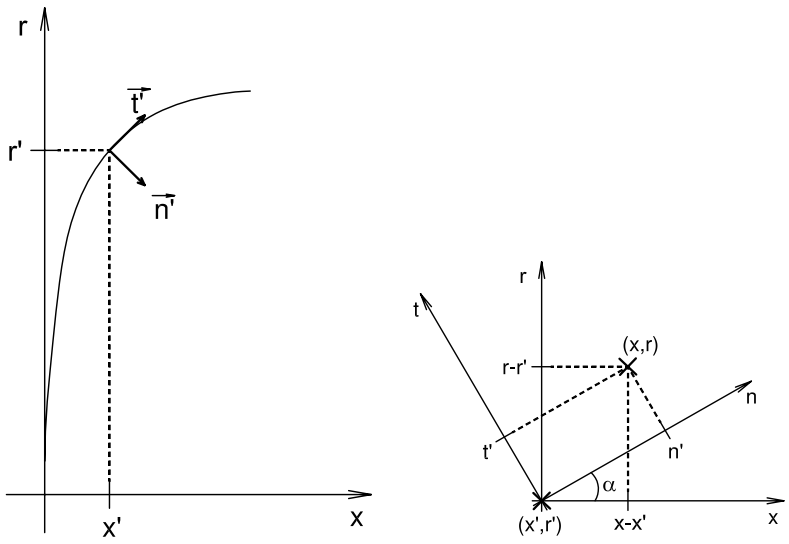

Figure 5.3: *Coordinate transformation from x, r-coordinates to n, t-coordinates.*

In order to investigate the singular term $(-(x-x')n'_a - (r-r')n'_r)/((x-x')^2 + (r-r')^2)$, the x, r-coordinate system is transformed into an n, t-system where n is the coordinate along the normal to the disk and t is the coordinate along the tangent to the disk, see Figure 5.3. The transformation is

$$\begin{aligned} n' &= (x-x')\cos\alpha + (r-r')\sin\alpha = (x-x')\frac{n'_a}{\sqrt{n'^2_a + n'^2_r}} + (r-r')\frac{n'_r}{\sqrt{n'^2_a + n'^2_r}} \\ t' &= -(x-x')\sin\alpha + (r-r')\cos\alpha = -(x-x')\frac{n'_r}{\sqrt{n'^2_a + n'^2_r}} + (r-r')\frac{n'_a}{\sqrt{n'^2_a + n'^2_r}} \end{aligned} \tag{5.47}$$

where n'_a and n'_r are the axial and radial components of the normal, respectively, at point (x', r'). Inserting the above in Equation (5.46) gives

$$\begin{aligned} dp \approx \frac{1}{2\pi}\frac{\Delta p(s')r'}{\sqrt{rr'}} \Bigg\{ & \frac{-n'\sqrt{n'^2_a + n'^2_r}}{n'^2 + t'^2} \\ & - n'_r \left[\frac{1}{4r'} \ln\left(\frac{(x-x')^2 + (r-r')^2}{2rr'} \right) + \frac{1}{2r'} \right] \Bigg\} ds' \end{aligned} \tag{5.48}$$

The $-n'\sqrt{n'^2_a + n'^2_r}/(n'^2 + t'^2)$ term corresponds to the expression for the tangential velocity for a planar distribution of vorticity. The result is $\mp\Delta p/2$ for $n \to 0_\pm$.

In a region close to s' the n, t-coordinates are approximated by a second order polynomial:

$$\begin{aligned} n' &= n_1(s-s') + n_2(s-s')^2 \\ t' &= t_1(s-s') + t_2(s-s')^2 \end{aligned} \tag{5.49}$$

Hence

$$\begin{aligned}\frac{-n'\sqrt{n'^2_a+n'^2_r}}{n'^2+t'^2} &= \frac{[-n_1(s-s')-n_2(s-s')^2]\sqrt{n'^2_a+n'^2_r}}{[n_1(s-s')+n_2(s-s')^2]^2+[t_1(s-s')+t_2(s-s')^2]^2} \\ &= \frac{[-n_1(s-s')-n_2(s-s')^2]\sqrt{n'^2_a+n'^2_r}}{(s-s')^2(n_1^2+t_1^2)\left[1+2\frac{n_1n_2+t_1t_2}{n_1^2+t_1^2}(s-s')+\frac{n_2^2+t_2^2}{n_1^2+t_1^2}(s-s')^2\right]}\end{aligned} \tag{5.50}$$

The term in the square brackets in the denominator is expanded in a Taylor series as $(1+x)^{-1}=1-x+x^2+\mathcal{O}(x^3)$:

$$\begin{aligned}&\left[1+2\frac{n_1n_2+t_1t_2}{n_1^2+t_1^2}(s-s')+\frac{n_2^2+t_2^2}{n_1^2+t_1^2}(s-s')^2\right]^{-1} \\ &=1-2\frac{n_1n_2+t_1t_2}{n_1^2+t_1^2}(s-s')-\frac{n_2^2+t_2^2}{n_1^2+t_1^2}(s-s')^2+4\left(\frac{n_1n_2+t_1t_2}{n_1^2+t_1^2}\right)^2(s-s')^2+\mathcal{O}\big((s-s')^3\big)\end{aligned} \tag{5.51}$$

Insert the expansion in Equation (5.50) and neglect terms of $(s-s')$ with orders higher than or equal to one:

$$\frac{-n'\sqrt{n'^2_a+n'^2_r}}{n'^2+t'^2} \approx \frac{\sqrt{n'^2_a+n'^2_r}}{n'^2_1+t'^2_1}\left[\frac{-n_1}{(s-s')}+2n_1\frac{n_1n_2+t_1t_2}{n_1^2+t_1^2}-n_2\right] \tag{5.52}$$

where it is seen that a Cauchy singularity is present for $s\to s'$.

For the radial velocity a similar analysis of the integrand of Equation (5.44) results in

$$\begin{aligned}du_r &\approx \frac{1}{2\pi\rho U_0}\frac{\Delta p(s')r'}{\sqrt{rr'}}\left\{n'_a\left[\frac{1}{4r}\ln\left(\frac{(x-x')^2+(r-r')^2}{2rr'}\right)+\frac{1}{2r}\right]\right. \\ &\quad\left.+\frac{-(r-r')n'_a+(x-x')n'_r}{(x-x')^2+(r-r')^2}\right\}ds' \\ &= \frac{1}{2\pi\rho U_0}\frac{\Delta p(s')r'}{\sqrt{rr'}}\left\{n'_a\left[\frac{1}{4r}\ln\left(\frac{(x-x')^2+(r-r')^2}{2rr'}\right)+\frac{1}{2r}\right]\right. \\ &\quad\left.+\frac{-t'\sqrt{n'^2_a+n'^2_r}}{n'^2+t'^2}\right\}ds'\end{aligned} \tag{5.53}$$

The $-t'\sqrt{n'^2_a+n'^2_r}/(n'^2+t'^2)$ term corresponds to the integrand for the normal velocity for a planar distribution of vorticity.

The approximation from Equation (5.49) is used again, hence the $-t'\sqrt{n'^2_a+n'^2_r}/(n'^2+t'^2)$ term can be approximated by

$$\frac{-t'\sqrt{n'^2_a+n'^2_r}}{n'^2+t'^2} \approx \frac{\sqrt{n'^2_a+n'^2_r}}{n'^2_1+t'^2_1}\left[\frac{-t_1}{(s-s')}+2t_1\frac{n_1n_2+t_1t_2}{n_1^2+t_1^2}-t_2\right] \tag{5.54}$$

Again it is seen that a Cauchy singularity is present for $s \rightarrow s'$.

The numerical evaluation of the integrals in the expressions for the velocities and the pressure, see Equations (5.31), (5.44) and (5.30), is performed using Simpson's method. When the point (x, r) is not on the disk it is straightforward to calculate the velocities. If (x, r) is on the disk it is necessary to introduce the above approximations, the axial velocity is used as an example. The integrand for the axial velocity is calculated at a number of points from the hub to the tip, by use of Equation (5.31). In the entire interval the singular logarithmic term from Equation (5.46) is subtracted. The integral of the logarithmic term is then calculated numerically by an IMSL-routine (Visual Numerics, Inc., 1997). In a small region close to the singularity point (x', r') the Cauchy term given by Equation (5.52) is subtracted. The remaining part of the integrand, i.e. the original integrand minus the logarithmic term and minus the Cauchy term, is a smooth function which is integrated by Simpson's method. The integral with the Cauchy singularity is calculated by an IMSL-routine. The sum of the three integral components, i.e. the logarithmic term, the Cauchy term and the remaining part, is the total axial velocity. A similar approach is adopted for the radial velocity. The evaluation of the induced tangential velocity causes no problems, as there are no singularities or even need of an integration, see Equation (5.23). The computer program is designated xdisk.

5.1.2 Input Geometry

In order to calculate the induced velocities it is necessary to find the normal to the blade surface. As described in Section 4.2 the reference surface for a propeller in a rolled-off coordinate system, $(x, r, r\phi)$, is described by the vector

$$\vec{\mathcal{R}}(s,t) = \left\{ \begin{array}{c} x_m(s) + tc(s)\cos\beta_v(s)\sin\beta_h(s) \\ r_m(s) + tc(s)\sin\beta_v(s) \\ -r_m(s)\phi_m(s) + tc(s)\cos\beta_v(s)\cos\beta_h(s) \end{array} \right\} \tag{5.55}$$

The Cartesian coordinates for the blade surface are

$$(x, y, z) = (x, -r\sin(\phi), r\cos(\phi)) \tag{5.56}$$

As the propeller concerned is approximated by the actuator disk the normals in the calculations are assumed to be equal to the normal for the blade on the midchord line, which is given by

$$\vec{n} = \left.\frac{\vec{N}}{|\vec{N}|}\right|_{t=0} \tag{5.57}$$

where

$$\vec{N} = \frac{\partial\vec{\mathcal{R}}}{\partial s} \times \frac{\partial\vec{\mathcal{R}}}{\partial t} \tag{5.58}$$

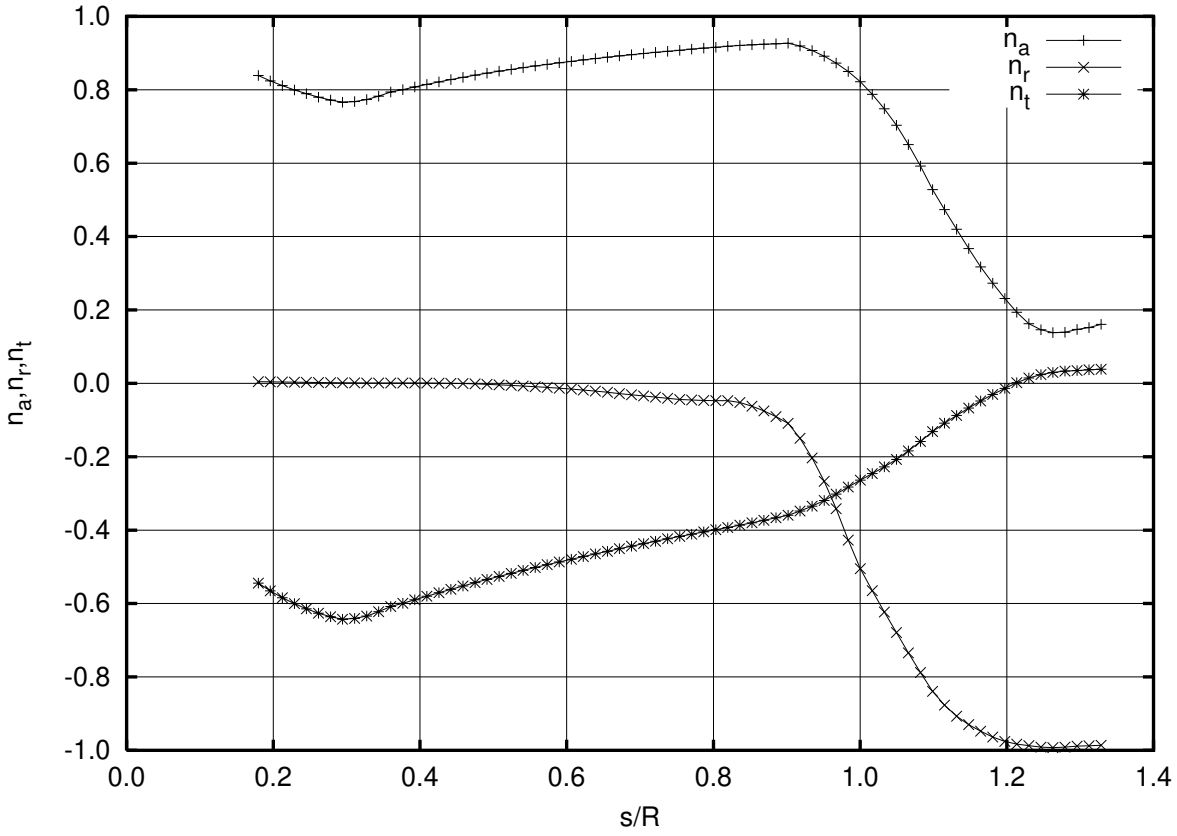

Figure 5.4: *Normals for the Kappel propeller K1.*

and

$$\frac{\partial \vec{\mathcal{R}}}{\partial s} = \begin{Bmatrix} \frac{\partial x_m}{\partial s} + \frac{\partial}{\partial s}\big[c\cos\beta_v \sin\beta_h\big]t \\ \frac{\partial r_m}{\partial s} + \frac{\partial}{\partial s}\big[c\sin\beta_v\big]t \\ -\frac{\partial r_m}{\partial s}\phi_m - r_m\frac{\partial \phi_m}{\partial s} + \frac{\partial}{\partial s}\big[c\cos\beta_v\cos\beta_h\big]t \end{Bmatrix} \tag{5.59}$$

$$\frac{\partial \vec{\mathcal{R}}}{\partial t} = \begin{Bmatrix} c\cos\beta_v\sin\beta_h \\ c\sin\beta_v \\ c\cos\beta_v\cos\beta_h \end{Bmatrix} \tag{5.60}$$

Thus

$$\vec{N}\big|_{t=0} = \begin{Bmatrix} \cos\beta_v\cos\beta_h\frac{\partial r_m}{\partial s} + \sin\beta_v\big[\frac{\partial r_m}{\partial s}\phi_m + r_m\frac{\partial \phi_m}{\partial s}\big] \\ -\cos\beta_v\sin\beta_h\big[\frac{\partial r_m}{\partial s}\phi_m + r_m\frac{\partial \phi_m}{\partial s}\big] - \cos\beta_v\cos\beta_h\frac{\partial x_m}{\partial s} \\ \sin\beta_v\frac{\partial x_m}{\partial s} - \cos\beta_v\sin\beta_h\frac{\partial r_m}{\partial s} \end{Bmatrix} c \tag{5.61}$$

In order to calculate the normals in xdisk a number of geometrical data is given as input functions of s. The given input data is the radius, chord length, rake, skew, horizontal and vertical pitch angle. Furthermore, the derivatives of the radius ($\partial r_m/\partial s$), the rake ($\partial x_m/\partial s$) and the skew ($r_m \partial \phi_m/\partial s$) with respect to s are given. Figure 5.4 shows the normals for the Kappel propeller K1.

5.1.3 Input Pressure Distribution

The pressure distribution $\Delta p(s)$ is determined either from the radial distribution of thrust

$$\begin{aligned} dT(s) &= 2\pi r(s)\Delta p(s) n_a(s) ds \\ \Delta p(s) &= \frac{1}{2\pi r(s) n_a(s)} \frac{dT(s)}{ds} \end{aligned} \tag{5.62}$$

or from the radial distribution of circulation for the blades. When the distribution of circulation is known the force is found by the Kutta-Joukowsky law:

$$d\vec{F} = \rho \vec{U}(s) \times d\vec{\Gamma}(s) = \rho \Gamma(s) \vec{U}(s) \times \vec{t}(s) ds \tag{5.63}$$

where $\vec{U}$ is the total velocity and $\vec{t}(s)$ is the tangent to the midchord line:

$$\vec{t}(s) = \left. \frac{\partial \vec{\mathcal{R}}/\partial s}{|\partial \vec{\mathcal{R}}/\partial s|} \right|_{t=0} \tag{5.64}$$

where $\partial \vec{\mathcal{R}}/\partial s$ is given in Equation (5.59). The thrust is the x-component of the force:

$$dT(s) = \left(d\vec{F}\right)_x = \rho \Gamma(s) ds (U_r t_t - U_t t_r) \tag{5.65}$$

where U_r and U_t are the radial and tangential components, respectively, of the total velocity. In accordance with linear theory the induced velocities are omitted, hence only the tangential onset flow is left and the thrust is

$$dT(s) = \rho \Gamma(s) \omega r(s) t_r(s) ds \tag{5.66}$$

Therefore, the pressure jump is

$$\begin{aligned} \rho \Gamma(s) \omega r(s) t_r(s) ds &= 2\pi r \Delta p(s) n_a(s) ds \\ \Delta p(s) &= \frac{\rho \omega}{2\pi} \frac{\Gamma(s) t_r(s)}{n_a} \end{aligned} \tag{5.67}$$

where $t_r(s)$ is the radial component of the tangent from Equation (5.64).

5.1.4 Validation of xdisk

As the velocities for the modified actuator disk theory correspond to the sum of the velocities for a normal actuator disk and the velocities from a duct, the numerical results from xdisk are compared to results for the actuator disk given by Hough and Ordway (1965) and for the duct given by Küchemann and Weber (1953).

The distribution of circulation for the duct is given by (Küchemann and Weber, 1953):

$$\Gamma = C\sqrt{1-(1-2s)^2} \tag{5.68}$$

and for the propeller the circulation is (Hough and Ordway, 1965):

$$\Gamma = Cs\sqrt{1-s} \tag{5.69}$$

The results for the calculations performed by xdisk and the results given by Küchemann and Weber (1953) and Hough and Ordway (1965) are shown in Figure 5.5.

As can be seen from the figure, the correlation between the results from the literature and the present program is good. There are no numerical results at or close to the leading and trailing edges of the duct as they cannot be calculated by the used numerical method.

5.2 Results for the DTNSRDC Propellers

The induced velocities from two propellers from the DTNSRDC propeller series have been calculated by xdisk. The two propellers are the reference propeller, i.e. DC4381, and the propeller with 72° skew and skew-induced rake, i.e. DC4383. An outline of the propellers is seen in Figure 4.4. The input parameters are

$$Z = 5, \quad R = 3.0m, \quad \hat{r}_h = 0.2, \quad U_0 = 10.0\,{}^{\mathrm{m}}/_{\mathrm{s}}, \quad J = 0.889, \quad C_{Th} = 0.662.$$

The input pressure distribution to xdisk is found either from the distribution of thrust and Equation (5.62) or from the distribution of circulation and Equation (5.67). The distributions of thrust and circulation are found by xlift, by use of linear theory.

Figures 5.6 and 5.7 show the induced velocities for the two propellers at the propeller plane and far downstream of it. The input load distributions are also given. From the figures it is seen that the input load distributions are almost identical for the two propellers, whereas there are larger differences in the axial velocities at the propeller plane. This is caused by the different geometry of the two propellers. As propeller DC4381 has no skew or rake the radial component of the normal is zero. Hence, the duct term in the expressions for the axial

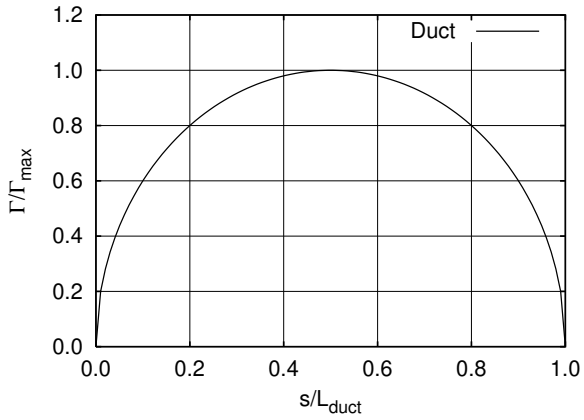

Circulation for duct.

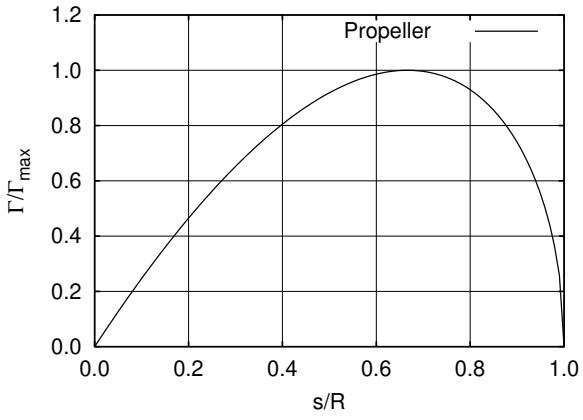

Circulation for propeller.

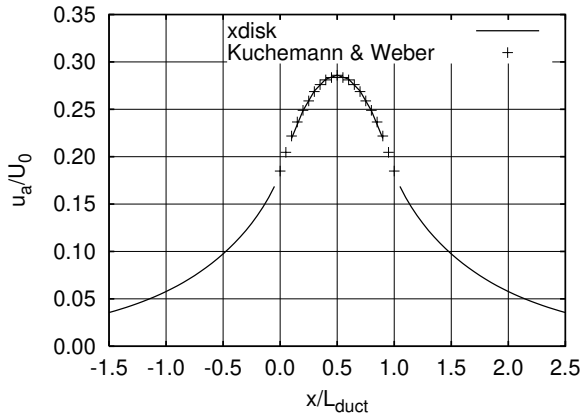

u_a *for duct.*

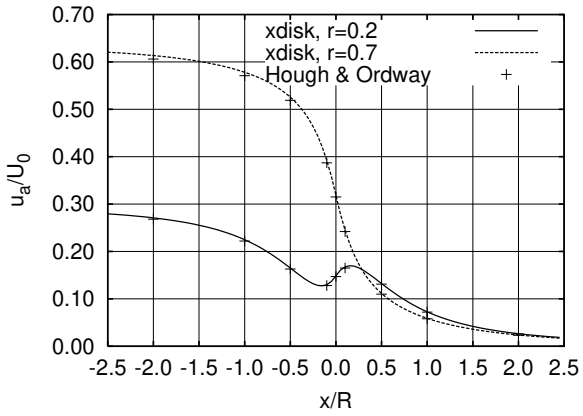

u_a *for propeller.*

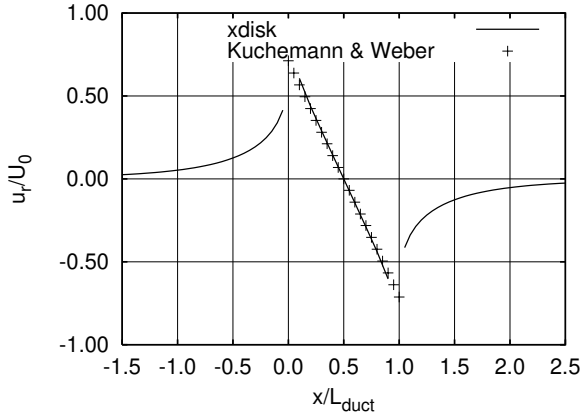

u_r *for duct.*

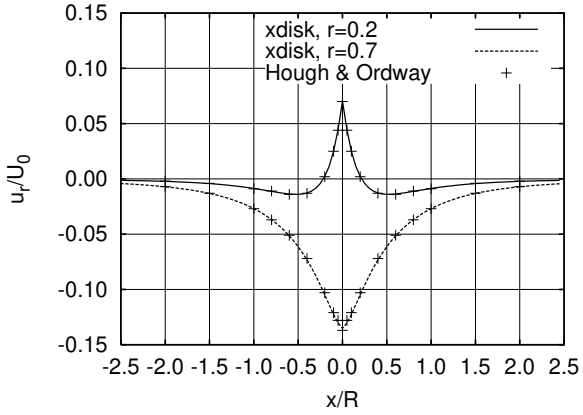

u_r *for propeller.*

Figure 5.5: *Comparison of u_a and u_r for* xdisk *and analytical results. The results for the duct are from Küchemann & Weber (1953) and the propeller results are from Hough & Ordway (1965).*

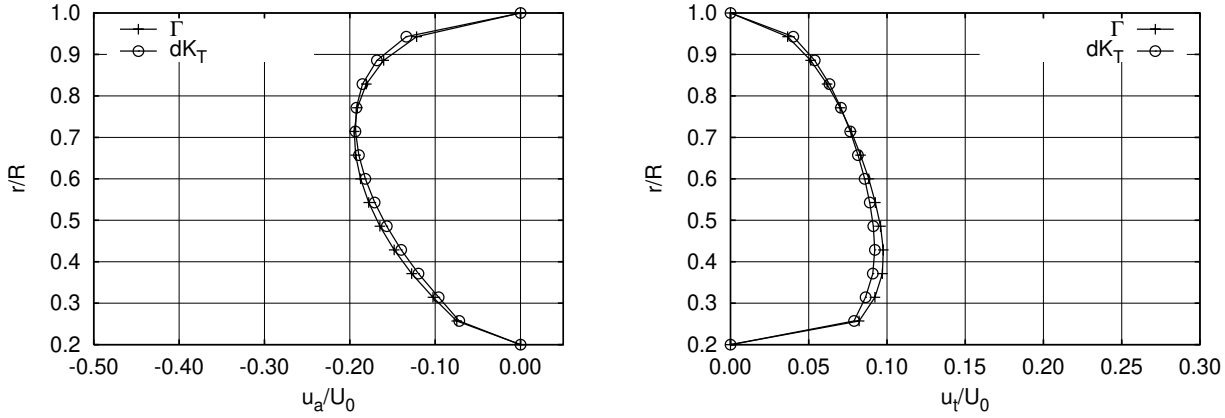

u_a and u_t at the propeller plane.

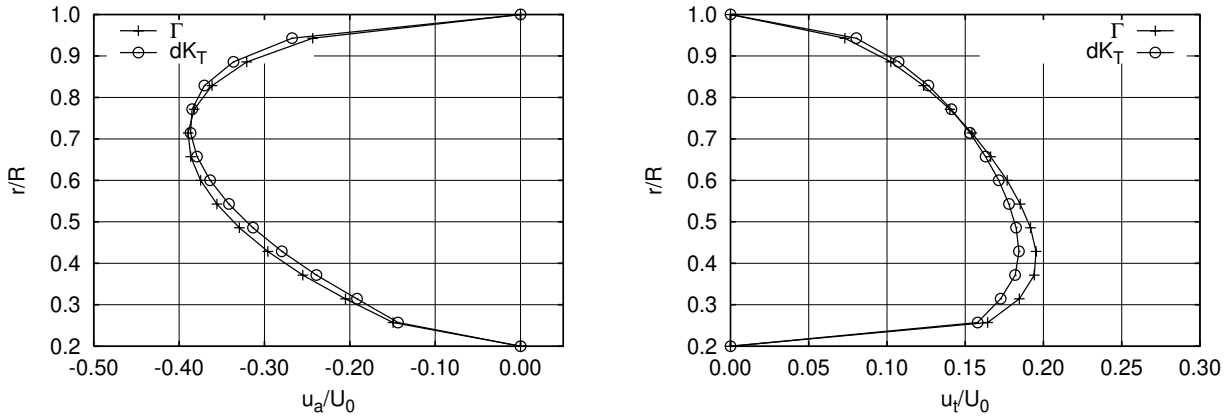

u_a and u_t far downstream of the propeller.

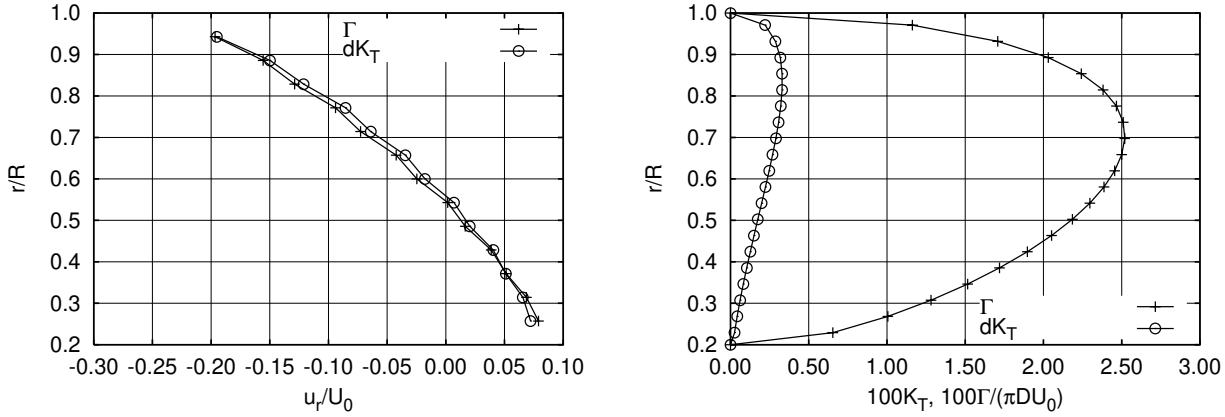

u_r at the propeller plane *Input load distributions*

Figure 5.6: *Comparison of the induced velocities with the input distribution of pressure based on either the distribution of circulation or the distribution of thrust. The calculations are made with the propeller without skew or skew-induced rake, i.e. DC4381. $Z = 5$, $R = 3.0m$, $\hat{r}_h = 0.2$, $U_0 = 10.0^m/_s$, $J = 0.889$ and $C_{Th} = 0.662$.*

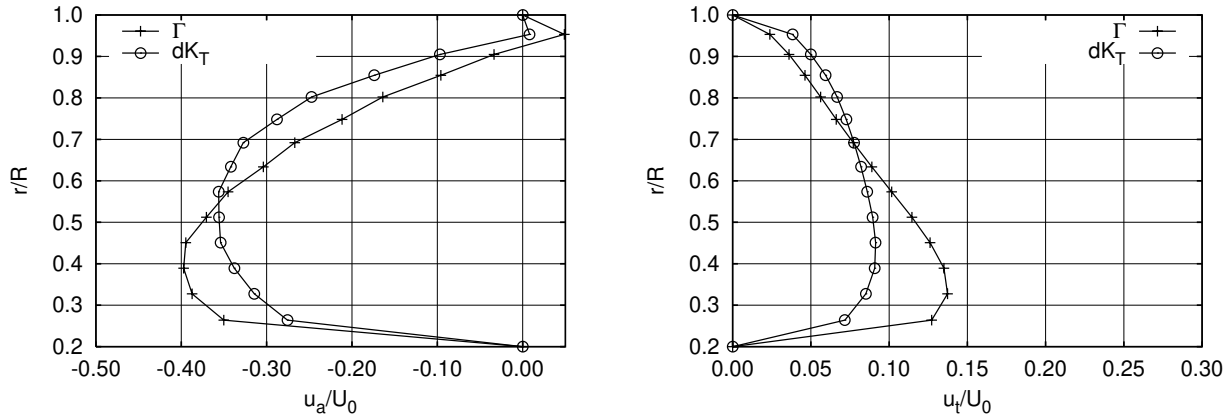

u_a *and* u_t *at the propeller plane.*

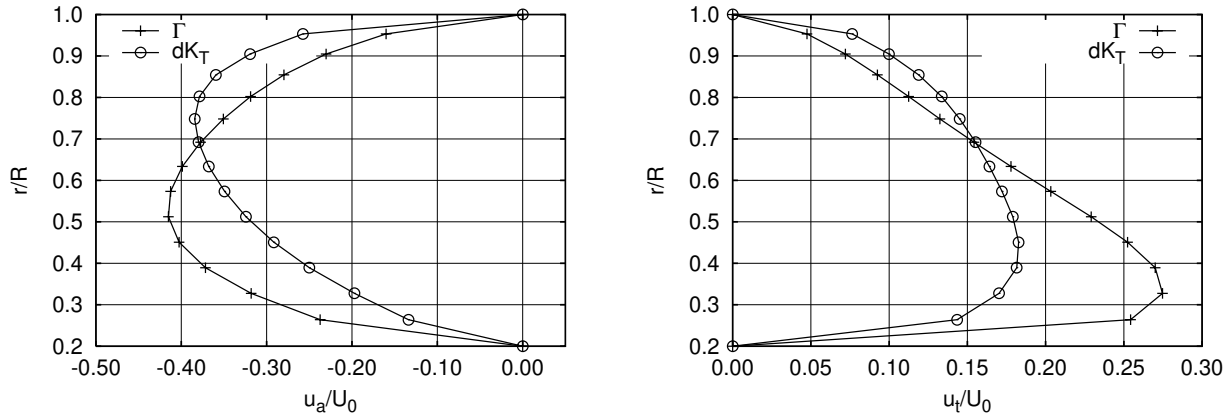

u_a *and* u_t *far downstream of the propeller.*

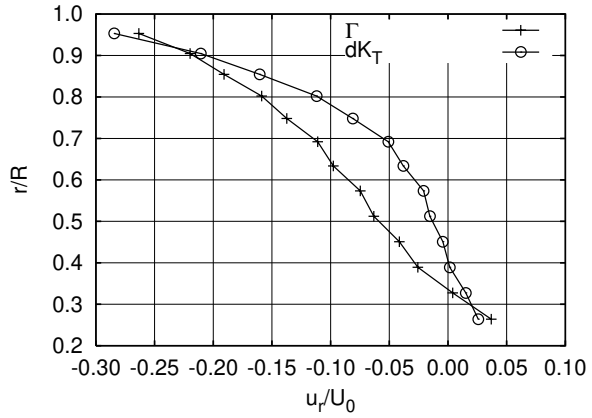

u_r *at the propeller plane*

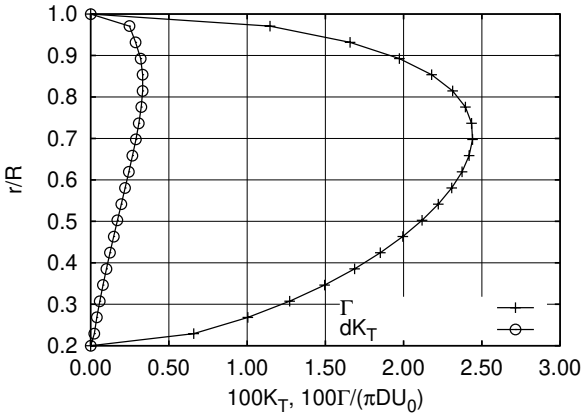

Input load distributions

Figure 5.7: *Comparison of the induced velocities with the input distribution of pressure based on either the distribution of circulation or the distribution of thrust. The calculations are made with the propeller with* 72^o *skew and skew-induced rake, i.e. DC4383.* $Z = 5$, $R = 3.0m$, $\hat{r}_h = 0.2$, $U_0 = 10.0^m/_s$, $J = 0.889$ *and* $C_{Th} = 0.662$.

and radial velocities, see Equations (5.31) and (5.44), is zero and the expressions correspond to the expressions for an actuator disk. Therefore, the axial velocities far downstream are twice as big as the velocities at the propeller plane, see Figure 5.6. Due to the skew and the skew-induced rake, propeller DC4383 has a radial normal component, hence there will be a contribution from the duct term in the axial and radial velocities. Furthermore, the disk will have an extension in the axial direction. From Figure 5.7 it is seen that this has a relatively large influence on the axial velocities, as the velocities at the propeller plane are almost as high as far downstream. A comparison of the axially induced velocities far downstream for the two propellers shows that the velocities from DC4381 are almost identical to the velocities from DC4383, when the input pressure distribution is based on the distribution of thrust for DC4383. This is because the influence from the integral term in Equation (5.31) vanishes downstream and because the distributions of thrust for the two propellers are almost identical. For the radial velocity the difference between the results for DC4381 and DC4383 is small, but the induced velocities for the DC4383 propeller are a little higher and the velocities are negative over a larger part of the blade. The wrinkled shape of the radial velocities is caused by the used numerical procedures. The tangential velocities are for both propellers twice as high far downstream as at the propeller plane. This is as they should be according to the expression for the tangential velocity, see Equation (5.23). A comparison of the tangential velocities for the two propellers shows that the velocities from DC4381 and DC4383 are almost identical, when the input pressure distribution is based on the distribution of thrust. This is because the pitch distributions for the two propellers are identical and the distributions of thrust are almost identical.

It is furthermore seen in Figure 5.6 that for propeller DC4381 the influence from the input load distribution on the velocities is small. For propeller DC4383 the results depend on the input load distribution, see Figure 5.7. The figure shows that the axial and tangential velocities calculated by the input pressure distribution on the basis of the distribution of circulation are higher and the maximum value is located closer to the hub. It is believed that these differences are caused by neglect of the induced velocities in the calculation of the input pressure distribution based on a given distribution of circulation, see Section 5.1.3. The effect of the induced tangential velocity has been investigated by calculating the tangential velocities by use of Lord Kelvin's theorem, see Section 2.1. But the effect was negligible. Hence, the differences may be caused by neglect of the radially induced velocity.

5.3 Results for a Kappel Propeller

The velocities for the Kappel propeller K1 have been calculated by xdisk for

$$Z = 6, \quad R = 3.727m, \quad U_0 = 9.28 \text{m/s}, \quad J = 0.7472, \quad C_{Th} = 1.0126.$$

The calculations are performed with both the distribution of thrust, dK_T, and the distribution of circulation, Γ, as input. The two different distributions of loadings are presented in Figure 5.8. These distributions correspond to the optimum distribution in a wake. The

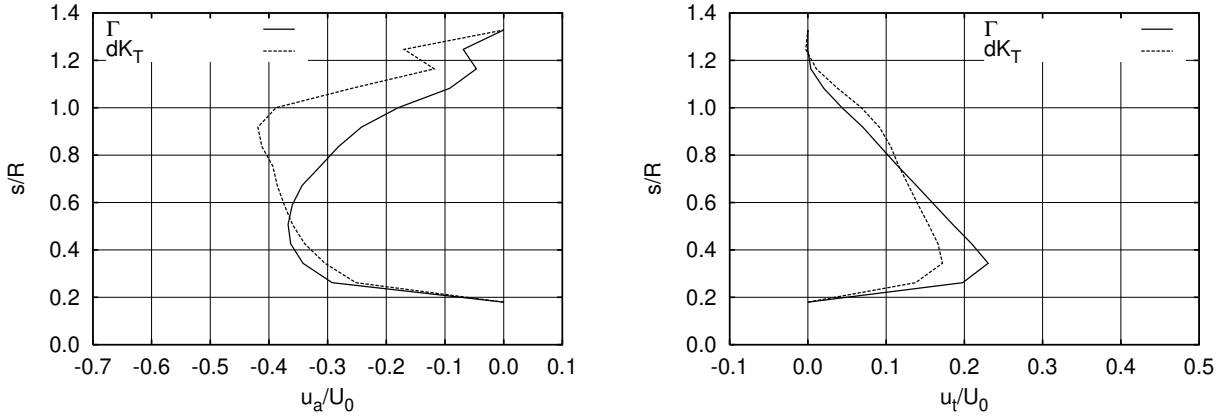

u_a *and* u_t *at the propeller plane.*

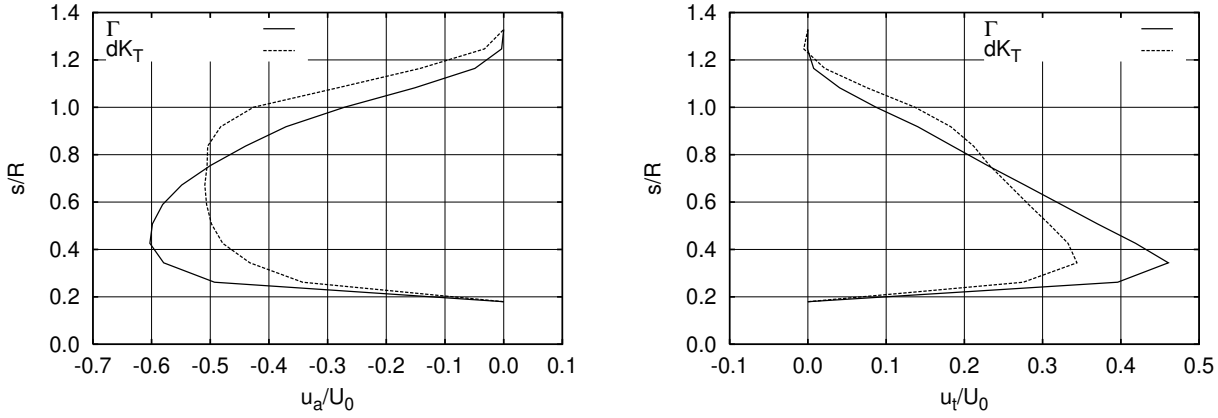

u_a *and* u_t *far downstream of the propeller.*

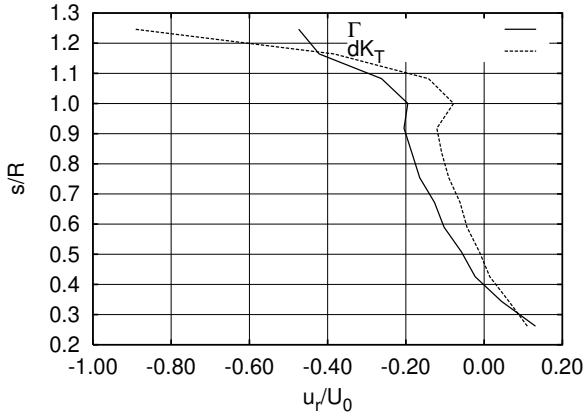

u_r at the propeller plane

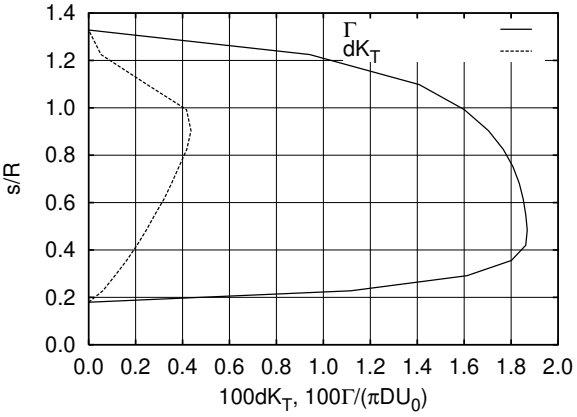

Input load distributions

Figure 5.8: *The induced velocities and input load distributions for the Kappel propeller K1, with* $Z = 6$, $R = 3.727m$, $U_0 = 9.28^{m}/_{s}$, $J = 0.7472$ *and* $C_{Th} = 1.0126$.

calculated velocities are also shown in this figure. The normal distribution for the propeller is given in Figure 5.4. From the figure it is seen that also the results for the Kappel propeller depend on the input distribution of loading. This is again caused by the neglect of the induced velocities in the expression for the input pressure distribution, see Equation (5.67), when the distribution of circulation is used as input. As for DC4383 the maximum induced velocities are higher when the circulation is used as input, except for the axial velocities at the propeller plane and the radial velocities. The induced tangential velocities show that the loading is moved toward the tip when dK_T is used as input. This results in the higher axial and radial velocities on the outer part of the blade when the thrust is used as input. As for the propeller DC4383 the induced axial velocities at the propeller plane are relatively high and are almost as high as the velocities downstream.

5.4 Summary

In this chapter the linear Euler equations are solved including all three components of the applied force. The solution of the equations is the sum of the solution for the general actuator disk, see e.g. Hough and Ordway (1965), and the solution for a duct, see e.g. Küchemann and Weber (1953). The expressions for the axial and radial velocities contain removable singularities when the velocities are calculated on the disk. The agreement between the present results obtained by xdisk and the results from Hough and Ordway (1965) and Küchemann and Weber (1953) is good, which proves that the singularities are removed satisfactorily. The results for the two DTNSRDC propellers, DC4381, i.e. the reference propeller, and DC4383, i.e. the propeller with 72° skew and skew-induced rake, and the Kappel propeller K1 turn out to depend on which parameter is used as input load distribution. The results indicate that neglect of the induced velocities in the calculation of the pressure jump when the circulation is given as input may be too rough an approximation. The results also show that the induced axial velocities at the propeller plane for DC4383 and K1 are almost as high as far downstream. If this is a physical effect should be further investigated but it is believed that the relatively high velocities are caused by the linearisation of the Euler equations. Thus, linear theory may be too coarse an approximation when propellers with skew and unconventional geometry are analysed.

Chapter 6

Energy Coefficients

Normally, the propeller efficiency is used to compare different propellers. This method, however, gives no details about the reasons why one propeller is superior to another. A better insight into the differences between propellers can be achieved by comparing the different energy losses for the propellers. Propulsion is always connected with a loss of energy. This loss can be divided into three main components, i.e. the axial loss, the rotational loss and the frictional loss. The axial loss is inevitable as it is the increased axial momentum of the fluid which results in the propeller thrust. In order for the propeller to be as efficient as possible the rotational and frictional losses should be minimised, and it is clear that the highest possible efficiency is obtained for a propeller with no slipstream rotation and no frictional loss. This maximum efficiency, which is only theoretically achievable, corresponds to the ideal efficiency.

Glauert (1963) was one of the first to examine the energy loss of the propeller. He calculates the propeller efficiency as a product of three efficiencies related to the three energy losses. The momentum theory for propellers is used to calculate the efficiencies. Glover (1987) gave the energy losses for a conventional propeller for different thrust loadings, the results are reproduced in Table 1.1. However, the method by which these results were obtained is not described. Andersen et al. (1992) made a comparison of a conventional and a Kappel propeller designed for the open water condition. The propellers are designed for the same thrust loading of $C_{Th} = 1.5$, with the same diameter, number of blades and expanded blade area ratio in order to make a comparison valid. The advance ratio of both propellers is $J = 0.62$. The frictional forces were not included in the optimisation of the radial distribution of loading. The comparison is based on four partial efficiencies related to the losses caused by slipstream contraction, rotation and inhomogeneity of the slipstream, induced drag and viscous effects. The obtained results are reproduced in Table 6.1. From the table it is seen that all four efficiencies were improved by applying a tip-fin. The total efficiency is improved by approximately 3.1 per cent by applying the tip-fin. Unfortunately, it is not described in detail how the partial efficiencies were obtained. The derivation of the energy coefficients is, however, treated thoroughly by Dyne (1993) and Dyne (1995). In Dyne (1993) the open

Table 6.1: *Energy coefficients for a conventional and a Kappel propeller from Andersen et al. (1992). Both propellers are designed for the open water condition, with the same diameter, the same expanded blade area ratio and* $Z = 4$, $J = 0.62$ *and* $C_{Th} = 1.5$. *The total propeller efficiency is* $\eta = \eta_a\eta_b\eta_c\eta_d\eta_{ideal}$.

Origin	Partial efficiency	Kappel propeller	Conventional propeller
Slipstream contraction	η_a	0.971	0.967
Rotation and inhomogeneity	η_b	0.964	0.957
Induced drag	η_c	0.948	0.939
Viscosity	η_d	0.906	0.896
Ideal efficiency	η_{ideal}	0.799	0.799
Total efficiency	η	0.642	0.623

water efficiency is calculated as a sum of four energy coefficients related to the axial loss, the rotational loss, the frictional loss and finally a loss due to the finite number of blades for the propeller. These coefficients will be used in the following to compare different propellers.

It should be remembered that the following coefficients are related to the energy loss for the propeller only. The propeller-hull interaction, which is important to the total propulsive efficiency, is not considered. Furthermore, there is no information about the unsteady properties, such as cavitation and vibrations, in the energy coefficients.

6.1 Derivation of the Energy Coefficients

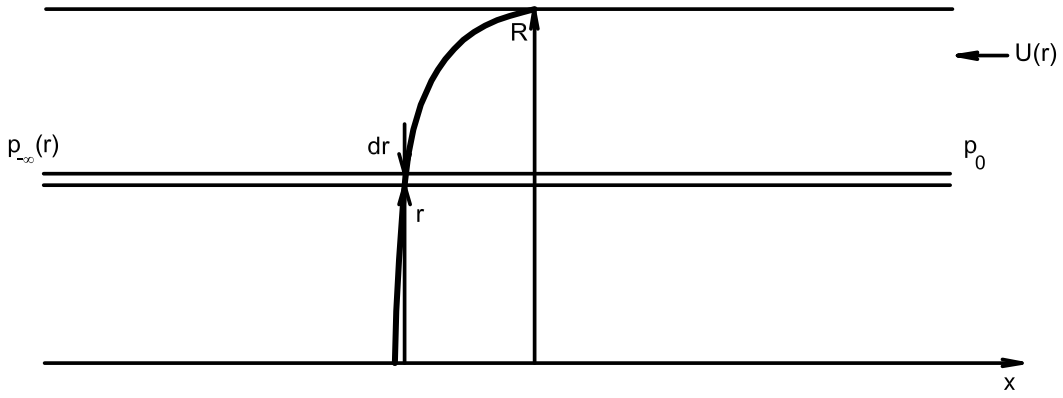

Figure 6.1: *Stream tube for the derivation of the energy coefficients.*

The derivation of the energy coefficients follows the outline in Dyne (1993), but as the present coefficients are extended to include a radially varying onset flow the derivation is described in detail.

In the derivation of the coefficients the usual assumptions about a potential flow are applied and the propeller is modelled as an actuator disk. As the slipstream contraction is ignored the coefficients are only valid for lightly and moderately loaded propellers. If the propeller is modelled as an actuator disk the inviscid part of the thrust is given by an integration over the disk of the pressure jump, $\Delta p(r)$, across it and the inviscid part of the torque is found from the ideal delivered power P_D, which is given by an integration over the disk of the product of the volume flow per time unit and the increase in total head, ΔH, over the disk, hence

$$T_\infty = 2\pi \int_{r_h}^{R} \Delta p(r) r dr - \Delta T_{fr} \tag{6.1}$$

$$Q_\infty = -\frac{P_D}{2\pi n} + \Delta Q_{fr} = \frac{-1}{n} \int_{r_h}^{R} \Delta H(r) \big[u_{a,0}(r) - U(r)\big] r dr + \Delta Q_{fr} \tag{6.2}$$

where ΔT_{fr} and ΔQ_{fr} are the contributions due to friction. The torque is assumed to be positive for a right-hand propeller. The subscript ∞ indicates that the value is related to the disk.

If it is assumed that the total head is preserved ahead of and behind the disk, the $\Delta p(r)$ and $\Delta H(r)$ can be found by applying the Bernoulli equation, see Equation (2.7), ahead of and abaft the disk to the stream tube shown in Figure 6.1. In front of the disk the Bernoulli equation is

$$p_0 + \tfrac{1}{2}\rho U^2(r) = p_+(r) + \tfrac{1}{2}\rho \Big\{ \big[u_{a,0+}(r) - U(r)\big]^2 + u_{r,0+}^2(r) \Big\} \tag{6.3}$$

and behind the disk it is

$$p_-(r) + \tfrac{1}{2}\rho \Big\{ \big[u_{a,0-}(r) - U(r)\big]^2 + u_{r,0-}^2(r) + u_{t,0-}^2(r) \Big\} = p_{-\infty}(r) + \tfrac{1}{2}\rho \Big\{ \big[u_{a,-\infty}(r) - U(r)\big]^2 + u_{t,-\infty}^2(r) \Big\} \tag{6.4}$$

The pressure jump across the disk is defined as

$$\Delta p(r) = p_-(r) - p_+(r) \Leftrightarrow p_-(r) = \Delta p(r) + p_+(r)$$

Insert this in Equation (6.4):

$$\Delta p(r) = p_{-\infty}(r) - p_+(r) + \tfrac{1}{2}\rho \Big\{ \big[u_{a,-\infty}(r) - U(r)\big]^2 + u_{t,-\infty}^2(r) - \big[u_{a,0-}(r) - U(r)\big]^2 - u_{r,0-}^2(r) - u_{t,0-}^2(r) \Big\}$$

Equation (6.3) gives an expression for $p_+(r)$, which is inserted in the above equation:

$$\begin{aligned}
\Delta p(r) &= p_{-\infty}(r) - p_0(r) + \tfrac{1}{2}\rho\Big\{\big[u_{a,-\infty}(r) - U(r)\big]^2 + u^2_{t,-\infty}(r) - \big[u_{a,0-}(r) - U(r)\big]^2 \\
&\quad -u^2_{r,0-}(r) - u^2_{t,0-}(r) + \big[u_{a,0+}(r) - U(r)\big]^2 + u^2_{r,0+}(r) - U^2(r)\Big\} \\
\Delta p(r) &= p_{-\infty}(r) - p_0 + \tfrac{1}{2}\rho\Big\{-2U(r)u_{a,-\infty}(r) + u^2_{a,-\infty}(r) \\
&\quad +u^2_{t,-\infty}(r) - u^2_{t,0-}(r)\Big\} \qquad (6.5)
\end{aligned}$$

where it is used that u_a and u_r are continuous through the disk.

The increase in total head is found by subtracting the left side of Equation (6.3) from the right side of Equation (6.4):

$$\begin{aligned}
\Delta H(r) &= p_{-\infty}(r) - p_0 + \tfrac{1}{2}\rho\Big\{-2U(r)u_{a,-\infty}(r) + u^2_{a,-\infty}(r) + u^2_{t,-\infty}(r)\Big\} \\
\Delta H(r) &= \Delta p(r) + \tfrac{1}{2}\rho u^2_{t,0-}(r) \qquad (6.6)
\end{aligned}$$

Due to the rotation of the slipstream the pressure in the stream tube far downstream will be lower than the undisturbed pressure. As the pressure must balance the centrifugal force on the stream tube, the pressure infinitely downstream is

$$p_{-\infty}(r) = p_0 - \rho\int_r^R \frac{u^2_{t,-\infty}(r)}{r}dr$$

The above derivations make it possible to calculate the thrust and torque if the axial and tangential velocities are known on the disk and infinitely downstream of it.

The efficiency for the propeller is given by

$$\eta = \frac{U_A T}{\omega Q}$$

If Equation (6.1) is inserted for the thrust, the efficiency for a propeller with an infinite number of blades is

$$\eta_\infty = \frac{(1-w)U_s 2\pi\int_{r_h}^R \Delta p(r) r dr - (1-w)U_s\Delta T_{fr}}{2\pi n Q_\infty} \qquad (6.7)$$

where w is the wake fraction. In order to derive the energy coefficients, an expression for the inviscid part of the thrust, the Δp integration in Equation (6.1), is found from the equation for the torque, see Equation (6.2), where ΔH is expressed by Equation (6.6). By adding and

subtracting the ship speed, U_s, in the volume flow term, $[u_{a,0}(r) - U(r)]$, the inviscid part of the thrust can be expressed as

$$\begin{aligned}
&2\pi U_s \int_{r_h}^{R} \Delta p(r) r dr \\
&= 2\pi n Q_\infty + \rho U_s^3 R^2 \pi \int_{\hat{r}_h}^{1} \left[1 - \frac{U(\hat{r})}{U_s} + \frac{u_{a,0}(\hat{r})}{U_s}\right]\left[-2\frac{U(\hat{r})}{U_s}\frac{u_{a,-\infty}(\hat{r})}{U_s} + \left(\frac{u_{a,-\infty}(\hat{r})}{U_s}\right)^2\right]\hat{r}d\hat{r} \\
&+ \rho U_s^3 R^2 \pi \int_{\hat{r}_h}^{1} \left\{\left[\frac{u_{a,0}(\hat{r})}{U_s} - \frac{U(\hat{r})}{U_s}\right]\left[\Delta C_{prot}(\hat{r}) + \left(\frac{u_{t,-\infty}(\hat{r})}{U_s}\right)^2\right] + \Delta C_{prot}(\hat{r})\right\}\hat{r}d\hat{r} \\
&- 2\pi n \Delta Q_{fr}
\end{aligned} \tag{6.8}$$

where

$$\Delta C_{prot}(\hat{r}) = -2\int_{\hat{r}}^{1} \left(\frac{u_{t,-\infty}(\hat{r})}{U_s}\right)^2 \frac{1}{\hat{r}} d\hat{r} \tag{6.9}$$

It is furthermore used that $u_{t,-\infty}(r) = u_{t,0-}(r)$ for an actuator disk. If Equation (6.8) is inserted in Equation (6.7) the efficiency for the actuator disk can be expressed as

$$\eta_\infty = (1-w)\{1 - AXL + AXG - ROTL - FRL\}$$

where the energy coefficients are defined as

$$AXL = -\frac{\rho U_s^3 R^2}{2nQ_\infty} \int_{\hat{r}_h}^{1} \frac{u_{a,0}(\hat{r})}{U_s}\left[-2\frac{U(\hat{r})}{U_s}\frac{u_{a,-\infty}(\hat{r})}{U_s} + \left(\frac{u_{a,-\infty}(\hat{r})}{U_s}\right)^2\right]\hat{r}d\hat{r} \tag{6.10}$$

$$AXG = \frac{\rho U_s^3 R^2}{2nQ_\infty} \int_{\hat{r}_h}^{1} \left[1 - \frac{U(\hat{r})}{U_s}\right]\left[-2\frac{U(\hat{r})}{U_s}\frac{u_{a,-\infty}(\hat{r})}{U_s} + \left(\frac{u_{a,-\infty}(\hat{r})}{U_s}\right)^2\right]\hat{r}d\hat{r} \tag{6.11}$$

$$\begin{aligned}
ROTL = &-\frac{\rho U_s^3 R^2}{2nQ_\infty} \int_{\hat{r}_h}^{1} \left\{\left[\frac{u_{a,0}(\hat{r})}{U_s} - \frac{U(\hat{r})}{U_s}\right]\right. \\
&\left.\left[\Delta C_{prot}(\hat{r}) + \left(\frac{u_{t,-\infty}(\hat{r})}{U_s}\right)^2\right] + \Delta C_{prot}(\hat{r})\right\}\hat{r}d\hat{r}
\end{aligned} \tag{6.12}$$

$$FRL = \frac{\Delta Q_{fr}}{Q_\infty} + \frac{U_s \Delta T_{fr}}{2\pi n Q_\infty} \tag{6.13}$$

AXL is the loss of energy due to the induced axial velocities. If it is used that $u_{a,0}(r) = \frac{1}{2}u_{a,-\infty}(r)$, which is true for the normal actuator disk, the axial loss can be expressed as

$$AXL = -\frac{\rho U_s^3 R^2}{2nQ_\infty} \int_{\hat{r}_h}^{1} \left(\frac{u_{a,-\infty}(\hat{r})}{U_s}\right)^2 \left[\frac{u_{a,0}(\hat{r})}{U_s} - \frac{U(\hat{r})}{U_s}\right]\hat{r}d\hat{r}$$

Thus, it is seen that the AXL is related to the kinetic energy left in the slipstream due to the action of the propeller. AXG is the axial gain, where the term gain is used as AXG

increases the efficiency. The AXG is zero for a propeller in uniform inflow. $ROTL$ is the loss of energy due to the rotation of the slipstream. It is seen that the term

$$-\frac{\rho U_s^3 R^2}{2nQ_\infty}\int_{\hat{r}_h}^1\left[\frac{u_{a,0}(\hat{r})}{U_s}-\frac{U(\hat{r})}{U_s}\right]\left(\frac{u_{t,-\infty}(\hat{r})}{U_s}\right)^2\hat{r}d\hat{r}$$

corresponds to the lost kinetic energy due to the rotation of the slipstream. The terms including ΔC_{prot} are the losses due to the lower pressure in the slipstream. FRL is the frictional loss.

For the same thrust the necessary torque will be higher for a propeller with a finite number of blades than for the actuator disk. This additional loss is included through the finite blade number loss

$$FBNL = \eta_\infty\left(1-\frac{Q_\infty}{Q_Z}\right) \tag{6.14}$$

where Q_Z is the torque for a propeller with a finite number of blades. Hence, the efficiency for a propeller with a finite number of blades is

$$\eta = (1-w)\{1-AXL+AXG-ROTL-FRL\}-FBNL$$

For a propeller in uniform inflow the above coefficients reduce to the ones obtained by Dyne (1993).

In calculations of the energy coefficients it is necessary to know the averaged induced axial and tangential velocities at the propeller plane and infinitely abaft it. These velocities are either calculated by xdisk, see Chapter 5, or found from xlift, as will be explained in Section 6.3. Before the energy coefficients can be calculated it is necessary that the thrust for the actuator disk, T_∞, is equal to the given propeller thrust, T, for a propeller with a finite number of blades. The thrust T_∞ is calculated by the averaged induced velocities, see Equations (6.1) and (6.5), and in order to achieve $T_\infty = T$ it is normally necessary that the induced velocities are scaled. Here this is done by a constant factor along the radii.

6.2 Validation of the Energy Coefficients

For validation of the energy coefficients, the AXL and $ROTL$, see Equations (6.10) and (6.12), are compared to the two corresponding coefficients proposed by Glauert (1963). He derives a coefficient related to the axial loss of energy and another related to the rotational loss in a way similar to that for the above coefficients. The derivation of these two coefficients is outlined after the calculations of the AXL and $ROTL$.

6.2.1 The AXL and $ROTL$ Coefficients

For the validation the propeller is modelled as an actuator disk with uniform onset flow for which Hough and Ordway (1965) give closed-form solutions for the induced velocities:

$$\frac{u_{a,0}(\hat{r})}{U_0} = \frac{-Z\omega}{4\pi U_0^2}\,\Gamma(\hat{r}) \qquad \frac{u_{a,-\infty}(\hat{r})}{U_0} = \frac{-Z\omega}{2\pi U_0^2}\,\Gamma(\hat{r})$$
$$\frac{u_{t,0}(\hat{r})}{U_0} = \frac{Z}{4\pi U_0 R}\,\frac{\Gamma(\hat{r})}{\hat{r}} \qquad \frac{u_{t,-\infty}(\hat{r})}{U_0} = \frac{Z}{2\pi U_0 R}\,\frac{\Gamma(\hat{r})}{\hat{r}}$$

where a representative distribution of circulation is

$$\Gamma(\hat{r}) = U_0 R A(\hat{r} - \hat{r}_h)\sqrt{1-\hat{r}} \tag{6.15}$$

where A is a constant which depends on the C_{Th}.

By means of the induced velocities given by the above equations it is possible to derive analytical expressions for the AXL and $ROTL$ coefficients. These calculations are algebraically straightforward to perform but the final expressions are very long and therefore only the results will be given here. The complete expressions are given in Appendix A.

The efficiency and energy coefficients are calculated for three different thrust loadings, $C_{Th} =$ 0.1, 0.2 and 0.5, with the following input parameters:

$$Z = 5, \quad U_0 = 12.0\ {}^{\mathrm{m}}\!/_{\mathrm{s}}, \quad R = 3.0\ \mathrm{m}, \quad \hat{r}_h = 0.2, \quad J = 1.596.$$

The low thrust loadings are used as the velocities are derived for linear theory. The results are shown in Table 6.2. From the table it is seen that the axial loss AXL corresponds to the ideal efficiency. This implies that the magnitude of AXL is right since the ideal efficiency is the efficiency of a disk with only an axial loss. As the slipstream rotation is included in the derivation of the coefficients, it is expected that this loss is higher than the loss for an ideal propeller. From the table this is seen to be true. Furthermore, it is proved that the highest loss of energy is the axial loss, which is almost twice the rotational loss.

6.2.2 Glauert's Coefficients

According to Glauert (1963) the thrust and torque for an actuator disk are given by

$$\begin{aligned} T_\infty &= 4\pi\rho\omega^2 R^4 \int_{\hat{r}_h}^1 (1-a')a'\hat{r}^3 d\hat{r} \\ Q_\infty &= 4\pi\rho U_0\omega R^4 \int_{\hat{r}_h}^1 (1+a)a'\hat{r}^3 d\hat{r} \end{aligned} \tag{6.16}$$

Table 6.2: *Comparison of AXL and ROTL with Glauert's coefficients.* $\eta_{Dyne} = 1 - AXL - ROTL$, $\eta_{Glauert} = \eta_1\eta_2$ *and* $\eta_{ideal} = 2/(1+\sqrt{1+C_{Th}})$.

C_{Th}	AXL	$ROTL$	η_{Dyne}	η_1	η_2	$\eta_{Glauert}$	η_{ideal}
0.100	0.02764	0.01619	0.9562	0.9764	0.9798	0.9567	0.9762
0.200	0.05307	0.03053	0.9164	0.9530	0.9589	0.9138	0.9545
0.500	0.11851	0.06493	0.8166	0.8839	0.8905	0.7871	0.8990

where a and a' are the so called interference factors for the axial and tangential velocities, respectively, given by

$$a = \frac{|u_{a,0}|}{U_0}$$
$$a' = \frac{J}{\pi}\frac{u_{t,0}}{U_0}\frac{1}{\hat{r}}$$

Glauert (1963) assumes that the pressure far downstream is equal to the free-stream pressure p_0. Thus, the pressure difference in the slipstream due to the rotation has been neglected.

The efficiency without friction is

$$\eta_\infty = \frac{U_0 T_\infty}{\omega Q_\infty} = \frac{4\pi\rho U_0\omega^2 R^4 \int_{\hat{r}_h}^1 (1-a')a'\hat{r}^3 d\hat{r}}{4\pi\rho U_0\omega^2 R^4 \int_{\hat{r}_h}^1 (1+a)a'\hat{r}^3 d\hat{r}} \approx \frac{1-a'}{1+a}$$

where the last approximation follows because it is assumed that the interference factors (a and a') are constants over the radius. Hence, the efficiency can be expressed as a product of two efficiencies:

$$\eta_\infty = \eta_1\eta_2$$

where

$$\eta_1 = \frac{1}{1+a}$$
$$\eta_2 = 1 - a' \tag{6.17}$$

The η_1 is related to the loss of energy from the induced axial velocity in the slipstream and the η_2 is related to the energy loss caused by the induced tangential velocity in the slipstream.

η_1 and η_2 have been calculated by the same input parameters and for the same thrust loadings as before. In calculations of the efficiencies, η_1 and η_2, the values used for a and a' correspond to the averaged values over the disk, see Appendix A. The results are presented in Table 6.2. The table shows that the η_1 is approximately equal to the ideal efficiency and

the agreement with the AXL coefficient is good. It is furthermore seen that the agreement between the two methods for the rotational loss is good for the two lowest thrust loadings, but for $C_{Th} = 0.5$ there is a difference of approximately four per cent, which is due to the different approximations applied in the two methods.

As the agreement between the results from Glover (1987), see Table 1.1, and Table 6.2 is reasonable, it is concluded that using the present energy coefficients is a reliable way of estimating the loss components for a propeller. In Sections 6.4 and 6.5 the coefficients will be used for a study of the efficiency for different propellers.

6.3 Averaged Velocities from xlift

The lifting-surface optimisation program xlift is used to calculate the energy coefficients. Therefore, the averaged induced velocities at the propeller plane and infinitely downstream of it should be calculated by this program.

The averaged velocity is given by

$$\bar{u}_j(r) = \frac{1}{n-1} \sum_{i=1}^{n-1} u_{j,i}(r) \tag{6.18}$$

where j is either the axial or the tangential component and $u_{j,i}(r)$ is the induced velocity at $n-1$ points along an arc with the radius r. The arc is located between two following blades either at the propeller plane or infinitely downstream. The space between the two blades is divided into n equal intervals, but the velocities are only calculated at $n-1$ points. This is because the two points on the blades have been neglected in order to avoid numerical problems.

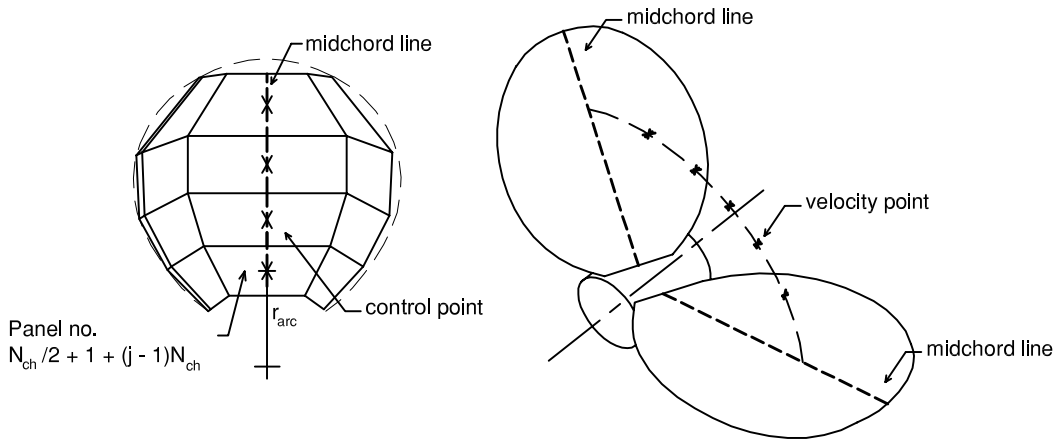

Figure 6.2: *Example of a midchord line and the location of the points on the arc between the blades where the velocity is calculated.*

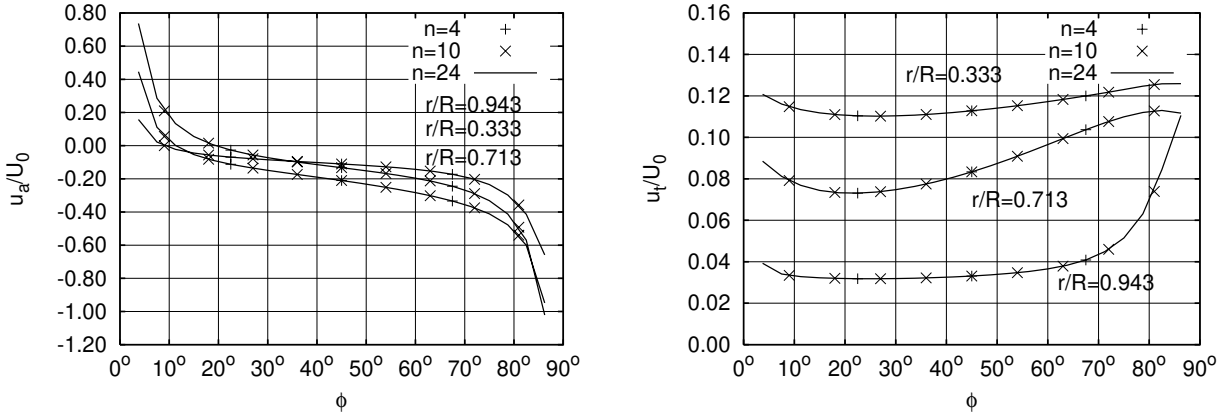

Velocity between two blades for three different radii.

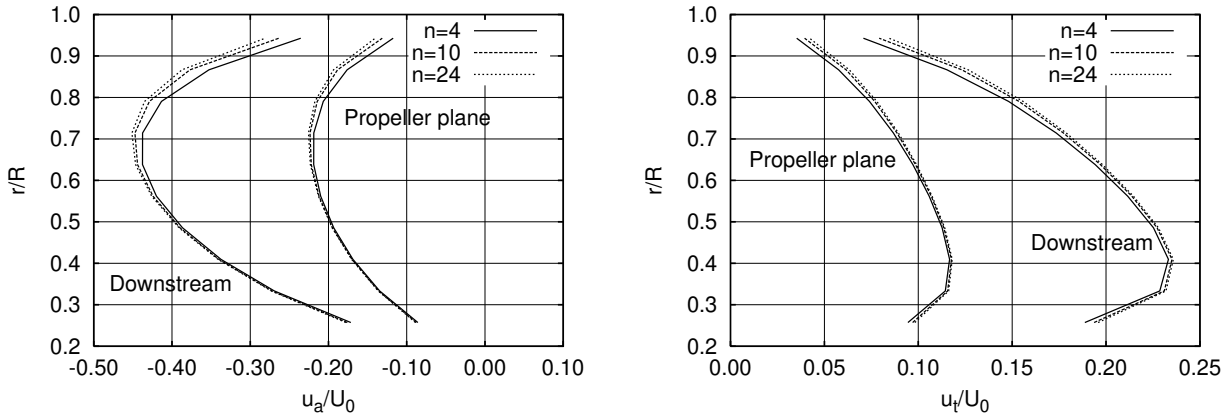

Averaged velocities at the propeller plane.

Figure 6.3: *Comparison of results for different numbers of n. For a lifting line with* $Z = 4,\ R = 3m,\ U_0 = 10.0\ ^m/_s,\ T = 959.712\,kN,\ \omega = 11.7795,\ M_{sp} = 10,\ N_{ch} = 4,\ c = 0.001\,m.$

The propeller plane is here defined as the plane spanned by a rotation of the midchord line around the propeller axis. If the number of panels is even the midchord line is given by the control point at panel number $N_{ch}/2 + 1 + (j-1)N_{ch}$, where $j = 1, 2, ..., M_{sp}$. See the example in Figure 6.2. The radius of the arc is the radius of the control point of that panel.

In order to find a usable value for the number of intervals between the blades, n, the averaged velocities are calculated for three different numbers of n for a propeller with a small constant chord length, so that it is similar to a lifting line, by means of the following input parameters:

$$Z = 4, R = 3m, U_0 = 10.0^{\mathrm{m}}/_{\mathrm{s}},\ T = 959.712kN,\ \omega = 11.7795,\ M_{sp} = 10,\ N_{ch} = 4,\ c = 0.001m$$

Figure 6.3 shows the variation of the induced velocities between two blades and the averaged velocities along the radii for different numbers of n. From the figure it is seen that the results for the induced velocities between the blades are almost identical for the different numbers of n. Furthermore, it is seen that the difference between the results for the radial variation

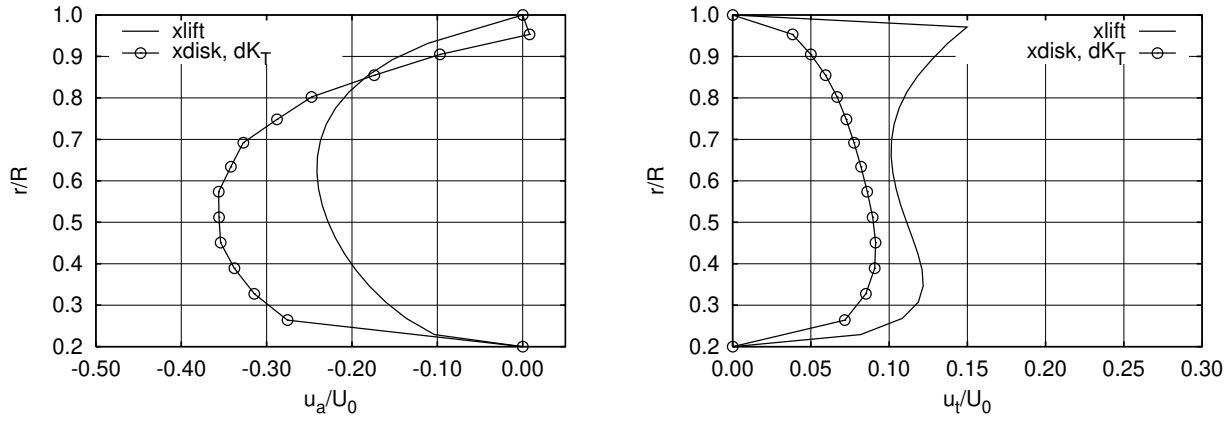

u_a and u_t at the propeller plane.

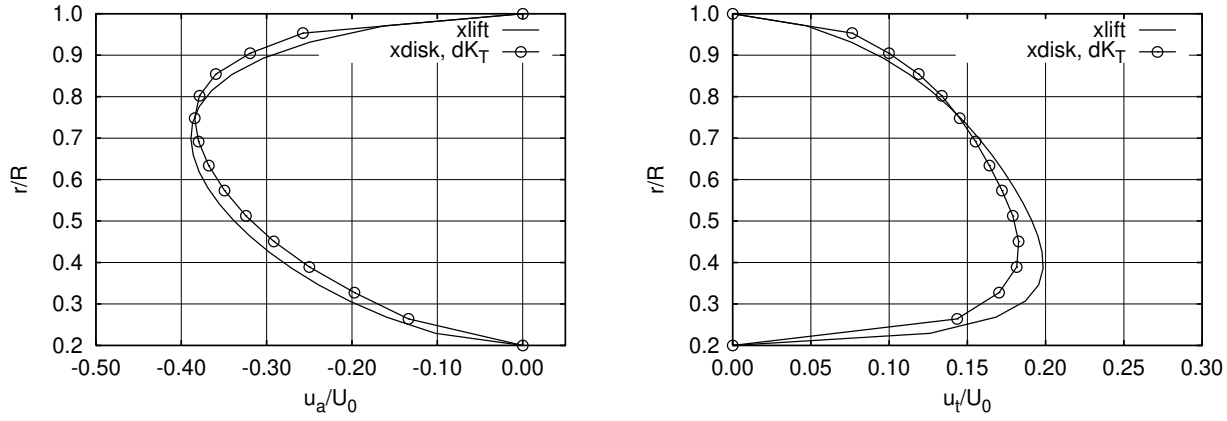

u_a and u_t far downstream.

Figure 6.4: *Comparison of velocities obtained by xlift and xdisk for the DTNSRDC propeller with 72^0 skew and skew-induced rake, i.e. DC4383. For $Z = 5$, $R = 3.0m$, $\hat{r}_h = 0.2$, $U_0 = 10.0^m/_s$, $J = 0.889$ and $C_{Th} = 0.662$.*

of the averaged velocities is reasonably small along most of the blade, but at the tip there are some differences. However, the overall shapes of the averaged velocities are almost the same. Therefore, n is chosen to be small in order to lower the computational time and will in further calculations be equal to ten. This can be done without lack of accuracy as the velocities are corrected, as explained on page 100, in calculations of the energy coefficients.

Figure 6.4 shows a comparison of the averaged induced velocities obtained by xlift and xdisk for the DTNSRDC propeller with 72^0 skew and skew-induced rake, i.e. propeller DC4383. The input parameters are

$$Z = 5, \quad R = 3.0m, \quad \hat{r}_h = 0.2, \quad U_0 = 10.0^{\mathrm{m}}/_{\mathrm{s}}, \quad J = 0.889, \quad C_{Th} = 0.662.$$

The input pressure distribution in xdisk is based on the distribution of thrust obtained by xlift by application of linear theory, which is seen in Figure 5.7.

The figure shows that the agreement between the two methods is reasonably good far downstream, but there are some differences as regards the propeller plane. For the axial velocities at the propeller plane the results from xdisk are a bit higher. Which of the two methods predicts the most realistic results should be further investigated but it is believed that the velocities predicted by xlift are the most realistic ones, as the difference between the results for the propeller plane and far downstream is larger. The figure shows that the tangential velocities at the propeller plane predicted by xlift have an unusual shape. It is seen that the tangential velocities are increasing on the outer part of the blade and the maximum value is reached at the point closest to the tip. The reason for this shape is not known in detail and should be further investigated. But an examination of the induced velocities from the trailers and from the blade separately shows that the trailers cause the higher velocities at the tip. The tangential velocity at the propeller plane is not used for the calculation of the energy coefficients and therefore the remarkable shape does not influence the coefficients. It should be noted that the agreement between results from xdisk and xlift is good for the reference propeller, i.e. DC4381, as can be seen in Figures 6.6 and 6.7.

6.3.1 Comparison of Results from xlift and xdisk

In order to compare the results from xlift and xdisk the energy coefficients have been calculated by xlift and xdisk for the same distribution of loading and propeller geometry. xlift is used to find the distribution of loading for a propeller geometry and this loading is then used, together with the propeller geometry, as input to xdisk.

For the comparison xlift is used to find the optimum distribution of circulation for a propeller in uniform inflow without rake and skew and with a very small constant chord length. Thus, the propeller is comparable with a lifting line. The calculations are done for three thrust loadings, $C_{Th} = 0.1$, 0.2 and 0.5, with the following parameters:

$$Z = 5, \quad R = 3.0m, \quad \hat{r}_h = 0.2, \quad U_0 = 12.0^{\mathrm{m}}/_{\mathrm{s}}, \quad J = 1.596, \quad c = 0.001m.$$

The distribution of circulation determined by xlift is given as input to xdisk and the energy coefficients are calculated, see Appendix A for the input distributions of circulation. For the calculation of the normals in xdisk the blade pitch angle is assumed to be equal to the pitch angle of the onset flow. As the onset flow is uniform the AXG will be zero. The calculation of the $FBNL$ is based on the torque for the propeller with a finite blade number obtained from the optimisation by xlift, see Table 6.3.

Figure 6.5 shows a comparison of the velocities, from xlift and xdisk , which are used to calculate the energy coefficients. The velocities from xlift correspond to the averaged velocities calculated as explained in Section 6.3. The energy coefficients are listed in Table 6.4.

Table 6.3: *Torque coefficient for the propeller with finite blade number from xlift and ideal efficiency for* $Z = 5$, $R = 3.0\,m$, $\hat{r}_h = 0.2$, $U_0 = 12.0\,{}^{m}/_{s}$, $J = 1.596$ *and* $c = 0.001\,m$.

C_{Th}	$10K_{Q,Z}$	η_{ideal}
0.1	0.2706	0.9762
0.2	0.5772	0.9545
0.5	1.7840	0.8990

Table 6.4: *Comparison of energy coefficients for xlift and xdisk for* $Z = 5$, $R = 3.0m$, $\hat{r}_h = 0.2$, $U_0 = 12.0\,{}^{m}/_{s}$, $J = 1.596$ *and* $c = 0.001\,m$.

	C_{Th}	$K_{T,\infty}$	$10K_{Q,\infty}$	η_∞	AXL	$ROTL$	$FBNL$	η
xdisk	0.1	0.1000	0.2664	0.9539	0.02803	0.01803	0.01459	0.9394
xlift		0.1001	0.2665	0.9539	0.02781	0.01830	0.01443	0.9395
xdisk	0.2	0.2001	0.5568	0.9127	0.05389	0.03343	0.03215	0.8805
xlift		0.2001	0.5570	0.9126	0.05348	0.03397	0.03194	0.8806
xdisk	0.5	0.5001	1.5655	0.8115	0.12085	0.06763	0.09927	0.7123
xlift		0.5003	1.5666	0.8112	0.11990	0.06891	0.09885	0.7123

From the figure it is seen that there is good agreement between the velocities from xlift and xdisk. Thus, there is also good agreement for the energy coefficients, see Table 6.4. The differences are below two per cent for all the coefficients. The agreement with the axial and the rotational losses from Glover (1987), see Table 1.1, is again satisfactory.

6.4 Energy Coefficients for the DTNSRDC Propeller Series

The energy coefficients for the propellers from the DTNSRDC propeller series used in Chapter 4 are calculated both by xdisk and xlift. An outline of the propellers is given in Figure 4.4. xlift is used to find the optimum distribution of loading for the propellers and the optimised torque for the propeller with the finite number of blades is used as reference for the $FBNL$. The results for the optimum distribution of loading and the torque from xlift are given to xdisk as input together with the geometry of the propeller. The input parameters for the optimisation by xlift are

$$Z = 5, \quad R = 3.0m, \quad \hat{r}_h = 0.2, \quad U_0 = 10.0{}^{\mathrm{m}}/_{\mathrm{s}}, \quad J = 0.889, \quad C_{Th} = 0.662.$$

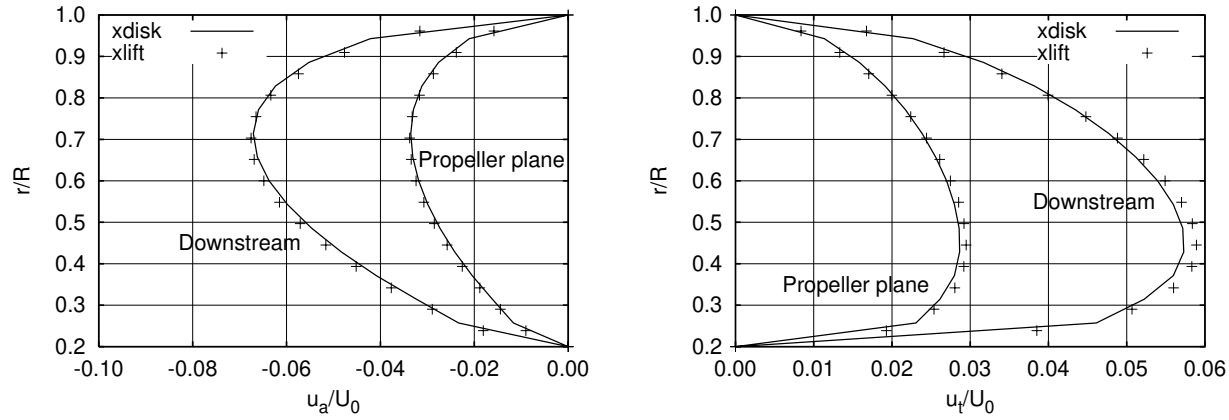

$C_{Th} = 0.1$

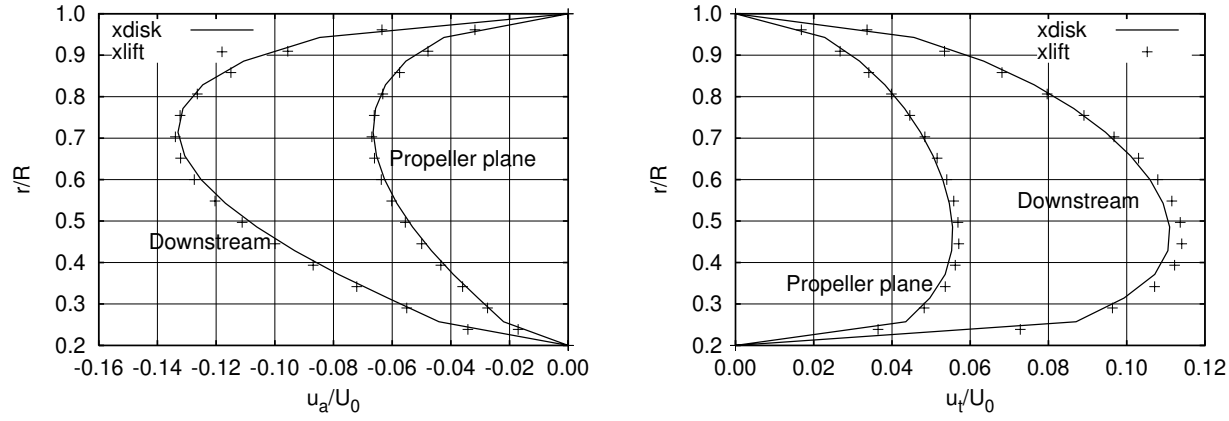

$C_{Th} = 0.2$

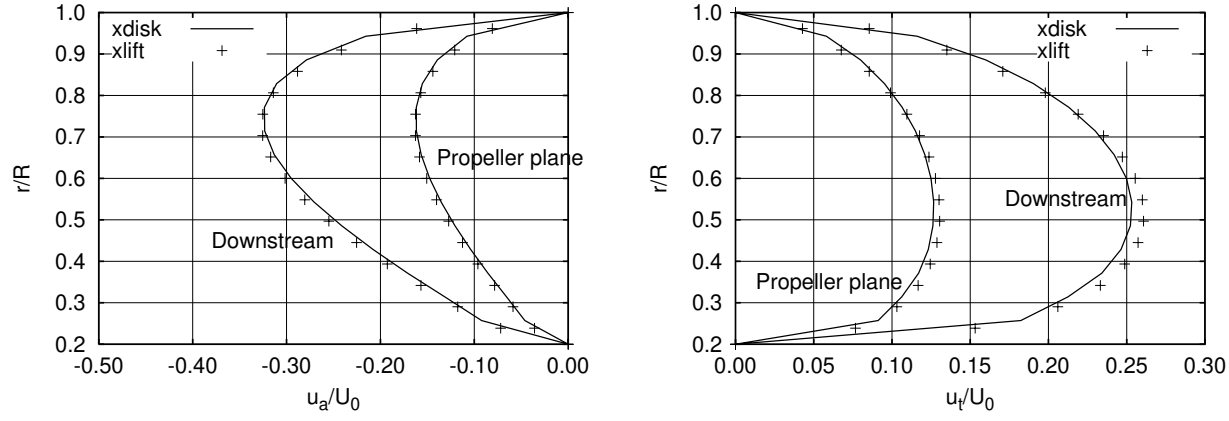

$C_{Th} = 0.5$

Figure 6.5: *Comparison of velocities for* xlift *and* xdisk*. For a lifting line with* $Z = 5$, $R = 3.0\,m$, $\hat{r}_h = 0.2$, $U_0 = 12.0\,{}^{m}/_{s}$, $J = 1.596$, $c = 0.001\,m$.

Table 6.5: *Energy coefficients for the DTNSRDC propellers calculated by* xlift*. For* $Z = 5,\ R = 3.0m,\ \hat{r}_h = 0.2,\ U_0 = 10.0^m/_s,\ J = 0.889,\ C_{Th} = 0.662$ *and* $\eta_{ideal} = 0.874$*.*

Prop.	Skew	Skew-indu. rake	AXL	$ROTL$	$FBNL$	η_∞	η
DC4381	0°	no	0.15062	0.02700	0.03547	0.8224	0.7869
DC4382	36°	yes	0.15699	0.02684	0.02395	0.8162	0.7922
DC4383	72°	yes	0.16652	0.02648	0.00804	0.8070	0.7990
DC4497	36°	no	0.16172	0.02665	0.01866	0.8116	0.7930
DC4498	72°	no	0.17298	0.02615	-0.00005	0.8009	0.8009

Table 6.6: *Energy coefficients for the DTNSRDC propellers calculated by* xdisk*. For* $Z = 5,\ R = 3.0m,\ \hat{r}_h = 0.2,\ U_0 = 10.0^m/_s,\ J = 0.889,\ C_{Th} = 0.662$ *and* $\eta_{ideal} = 0.874$*.*

Prop.	Skew	Skew-indu. rake	AXL	$ROTL$	$FBNL$	η_∞	η
DC4381.ci	0°	no	0.14447	0.02712	0.04151	0.8284	0.7869
DC4381.kt			0.14429	0.02600	0.04281	0.8297	0.7869
DC4382.ci	36°	yes	0.16524	0.03020	0.01235	0.8046	0.7922
DC4382.kt			0.16457	0.02490	0.01831	0.8105	0.7922
DC4383.ci	72°	yes	0.20129	0.03291	-0.03316	0.7658	0.7990
DC4383.kt			0.20240	0.02336	-0.02472	0.7742	0.7990
DC4497.ci	36°	no	0.17182	0.03058	0.00463	0.7976	0.7930
DC4497.kt			0.16949	0.02483	0.01271	0.8057	0.7930
DC4498.ci	72°	no	0.21753	0.03441	-0.05286	0.7481	0.8009
DC4498.kt			0.21068	0.02308	-0.03468	0.7662	0.8009

The energy coefficients obtained by xlift are given in Table 6.5 and the energy coefficients from xdisk in Table 6.6. The input loading distribution to xdisk is both the distribution of circulation and the distribution of thrust obtained by xlift. The velocities used by xlift and xdisk for the calculations of the coefficients are shown in Figures 6.6 to 6.9.

From the figures it is seen that the velocities from xdisk depend on which parameter (Γ or dK_T) is used as input for the distribution of loading. This phenomenon was discussed at some length in Chapter 5. The only exception is the propeller without rake or skew, i.e. propeller DC4381, where the agreement between the results is reasonable. The results with a given distribution of circulation move the location of the maximum velocity closer to the hub and increase the maximum value. This is true for both u_a and u_t. The difference between

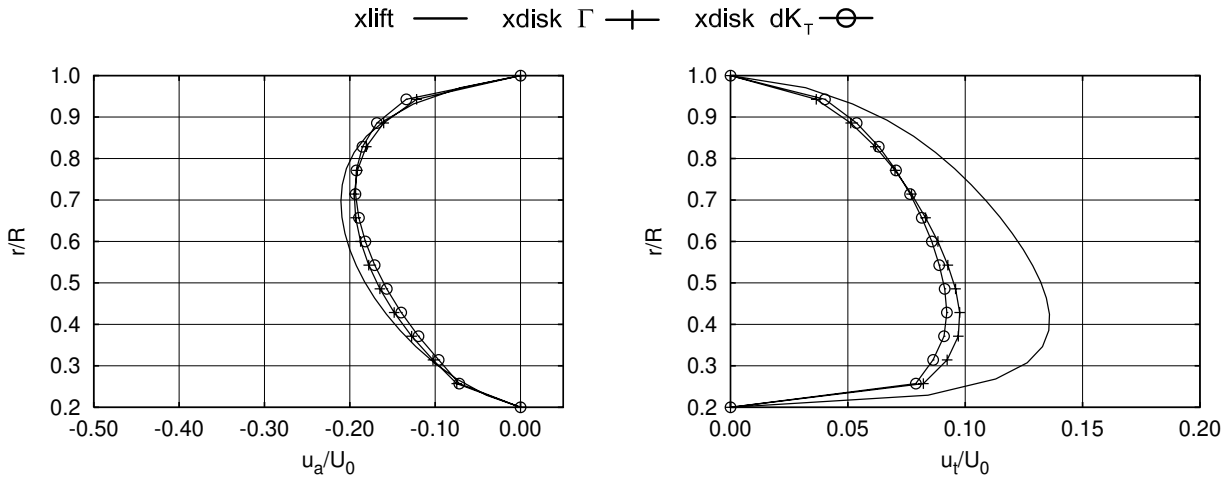

Propeller DC4381, no skew or rake

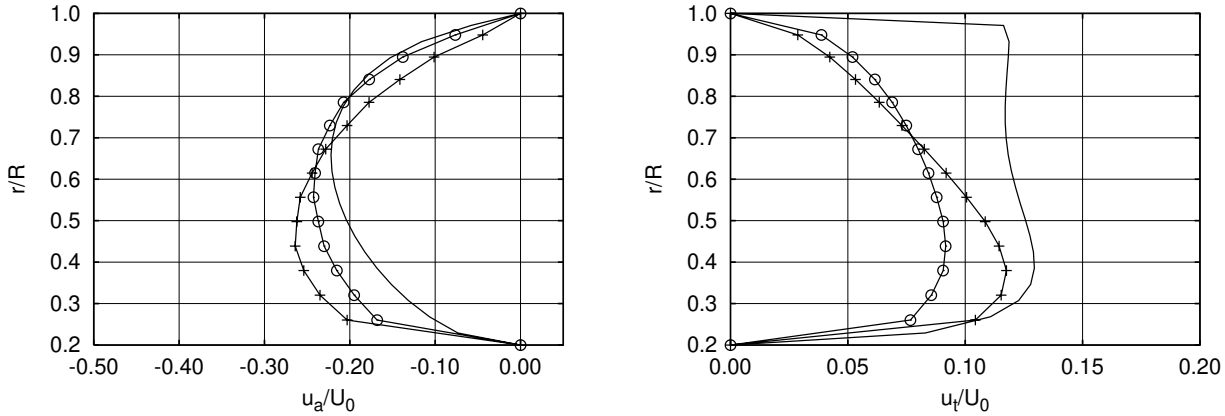

Propeller DC4382, 36^o skew and skew-induced rake

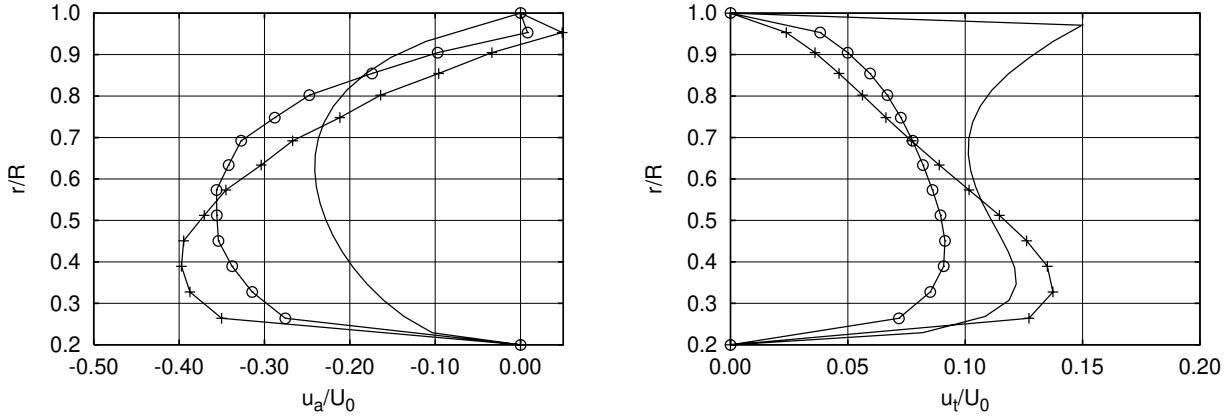

Propeller DC4383, 72^o skew and skew-induced rake

Figure 6.6: *Comparison of velocities at the propeller plane for* xlift *and* xdisk *for the DTNSRDC propeller series. For* $Z = 5$, $R = 3.0m$, $\hat{r}_h = 0.2$, $U_0 = 10.0^m/_s$, $J = 0.889$ *and* $C_{Th} = 0.662$.

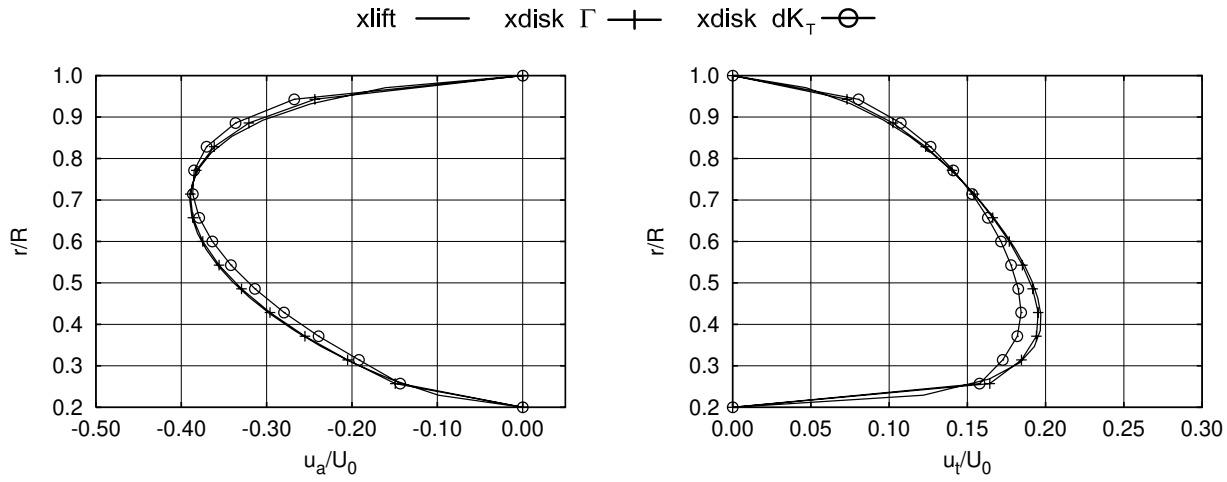

Propeller DC4381, no skew or rake

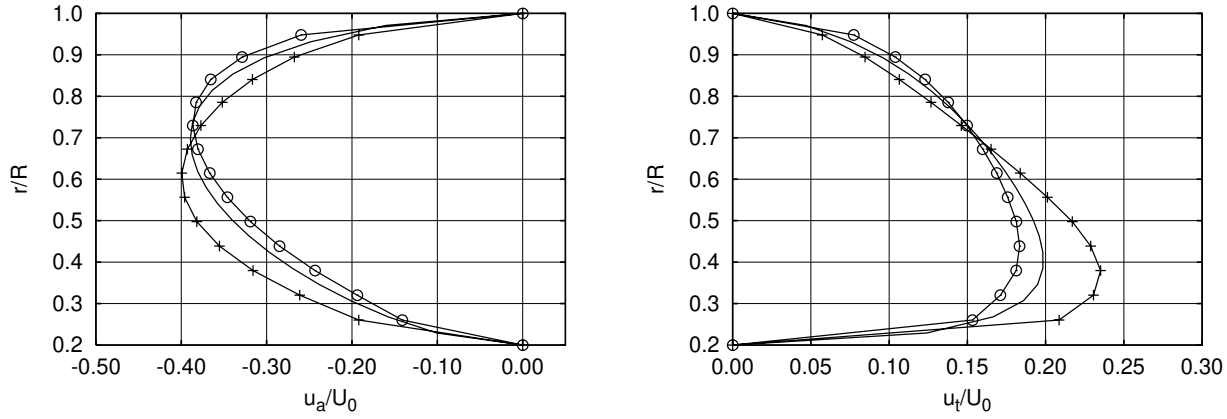

Propeller DC4382, 36^o skew and skew-induced rake

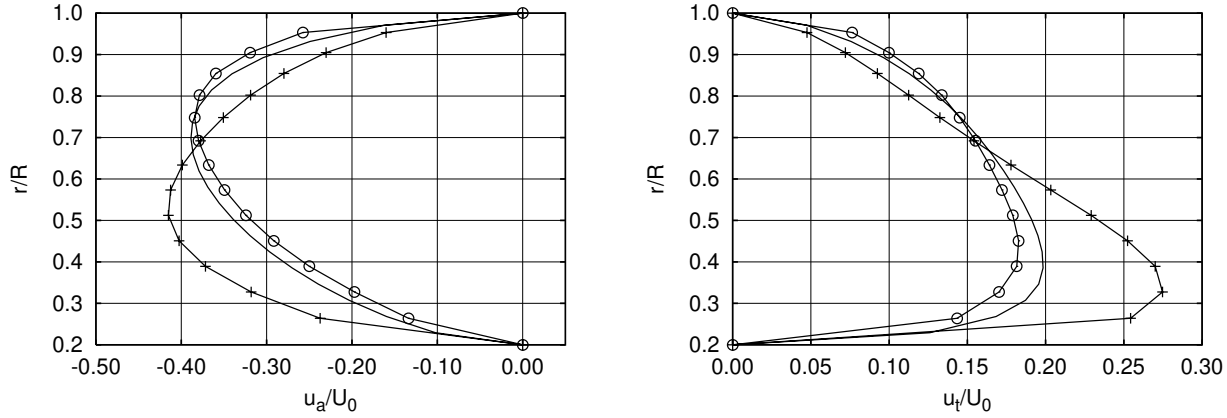

Propeller DC4383, 72^o skew and skew-induced rake

Figure 6.7: *Comparison of velocities far downstream for* **xlift** *and* **xdisk** *for the DTNSRDC propeller series. For* $Z = 5,\ R = 3.0m,\ \hat{r}_h = 0.2,\ U_0 = 10.0^m/_s,\ J = 0.889$ *and* $C_{Th} = 0.662$.

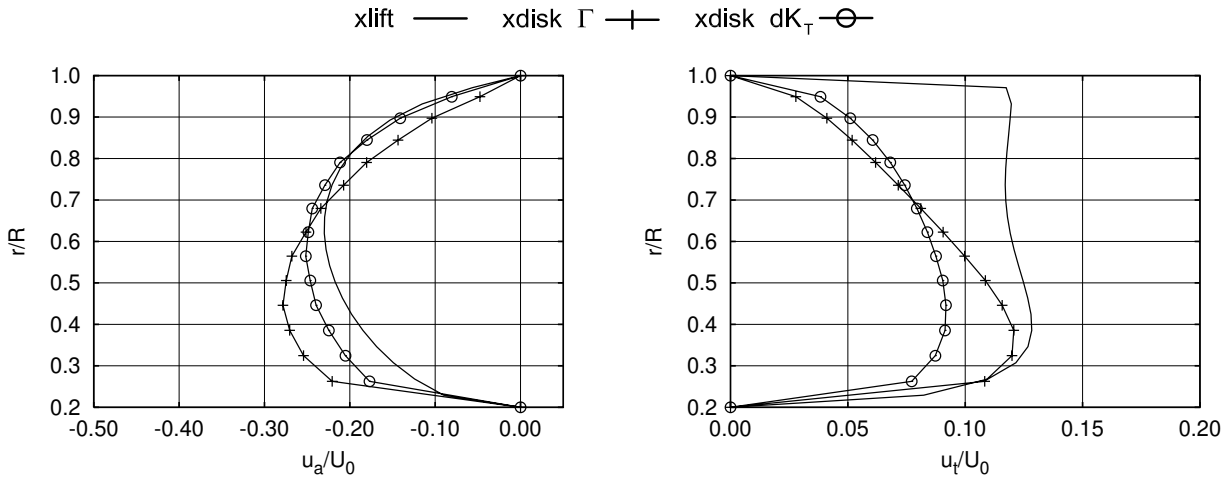

Propeller DC4497, 36^o skew and no skew-induced rake

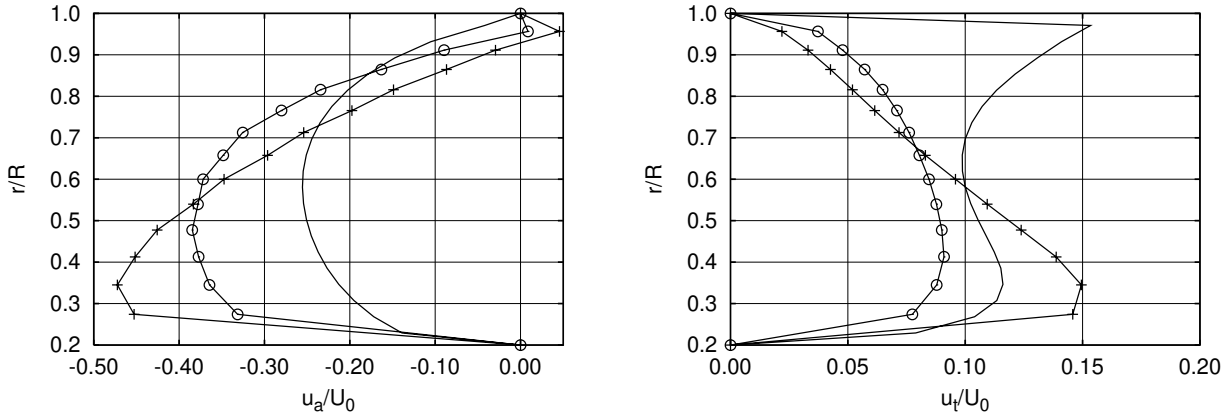

Propeller DC4498, 72^o skew and no skew-induced rake

Figure 6.8: *Comparison of velocities at the propeller plane for* xlift *and* xdisk *for the DTNSRDC propeller series. For* $Z = 5$, $R = 3.0m$, $\hat{r}_h = 0.2$, $U_0 = 10.0^m/_s$, $J = 0.889$ *and* $C_{Th} = 0.662$.

using the thrust or the circulation as input is increasing with increasing skew, whereas the skew-induced rake has a minor influence.

From the comparison of the velocities from xlift and xdisk , see also Section 6.3, it is observed that the agreement is reasonable for the axial velocities at the propeller plane for the propeller without skew or skew-induced rake, i.e. DC4381. For the two propellers with 36^o skew, i.e. DC4382 and DC4497, the magnitude of the maximum velocity agrees well but the shape of the axial velocity distributions at the propeller plane differs. For the propellers with 72^o skew, i.e. DC4383 and DC4498, the differences in both shape and magnitude are large for the axial velocities at the propeller plane. For the axially induced velocities far downstream

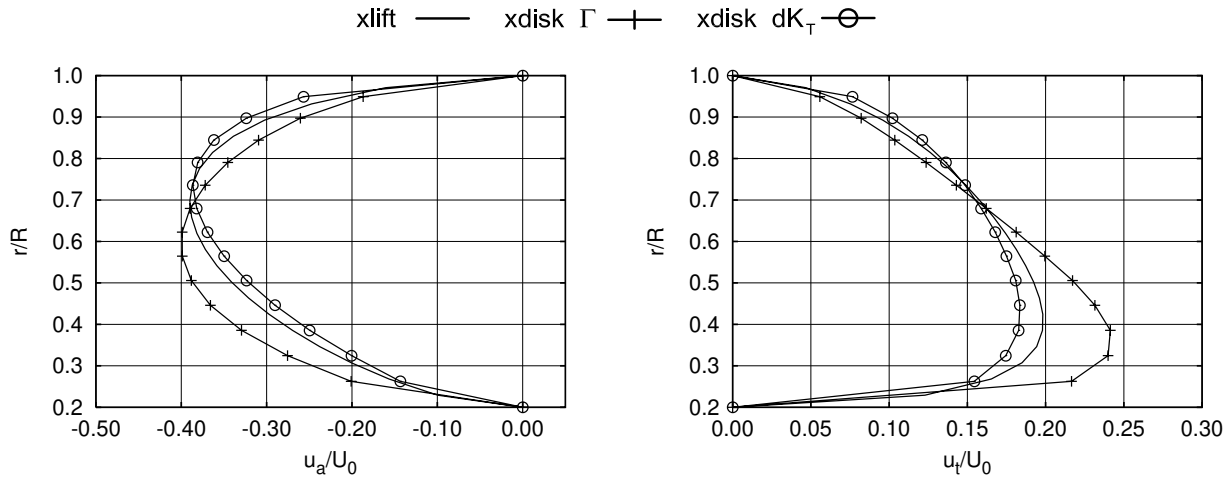

Propeller DC4497, 36^o skew and no skew-induced rake

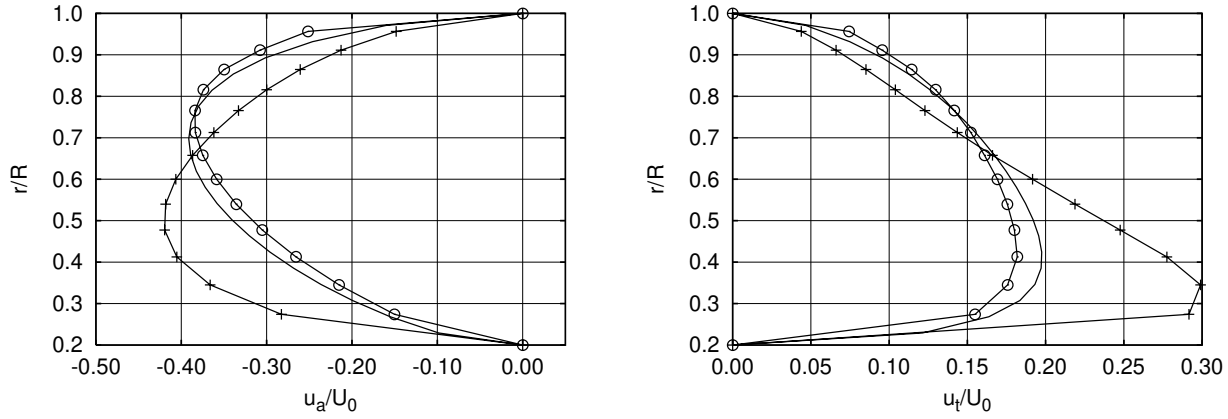

Propeller DC4498, 72^o skew and no skew-induced rake

Figure 6.9: *Comparison of velocities far downstream for* xlift *and* xdisk *for the DTNSRDC propeller series. For* $Z = 5,\ R = 3.0m,\ \hat{r}_h = 0.2,\ U_0 = 10.0^m/_s,\ J = 0.889$ *and* $C_{Th} = 0.662$.

the agreement is reasonable for all propellers, and the agreement is especially good between the velocities calculated by xlift and xdisk with the distribution of loading given as dK_T. For the tangential velocity at the propeller plane the magnitude of the velocities is similar for both xlift and xdisk , but there are large differences in the shape of the velocity distributions for all five propellers, this effect was discussed in Section 6.3. As the tangential velocity at the propeller plane is not used in the calculations of the energy coefficients these differences have no influence on the coefficients. Far downstream the agreement between xdisk and xlift is good for the propeller without skew and skew-induced rake, i.e. DC4381. For the skewed and raked propellers the agreement between the tangential velocities for xlift and xdisk based on dK_T is reasonable, whereas the velocity from xdisk based on the distribution of circulation differs.

Due to the differences in the calculated velocities the obtained energy coefficients differ as well. At first a few comments on the coefficients obtained by xlift should be made. The coefficients are listed in Table 6.5. The table reveals that when the efficiency for the propeller with the finite number of blades, η, is increasing the efficiency for the propeller with an infinite number of blades, η_∞, is decreasing. This results in a small negative $FBNL$ for the propeller with 72° skew and no skew-induced rake, i.e. propeller DC4498. The decrease of η_∞ is due to an increased AXL with increasing skew. The decrease of η_∞ is only slightly reduced by the decrease in $ROTL$ with increasing skew. The effect of removing the skew-induced rake is a further increase for the AXL and a smaller decrease for the $ROTL$.

The results from xdisk are listed in Table 6.6. Again it is seen that η_∞ is decreasing when η is increasing. This is also caused by an increase in the AXL with increasing skew. The results from xdisk show that the $ROTL$ is both increasing and decreasing but the variation in the $ROTL$ is not big enough to influence the decrease of η_∞ with increasing skew. Again the removal of the skew-induced rake enhances this tendency. Due to the higher axial velocities at the propeller plane the AXL calculated by xdisk is higher than the coefficients from xlift. The only exception is propeller DC4381, where the xdisk coefficients are slightly lower. For the $ROTL$ the results from xdisk are both higher and lower than the xlift coefficients. When the velocities are calculated by the distribution of circulation the $ROTL$ is higher, and when the velocities are calculated by the distribution of dK_T the $ROTL$ is lower. This results in an up to seven per cent lower η_∞ for the xdisk calculations and a negative $FBNL$ for the two propellers with 72° skew, i.e. propeller DC4383 and DC4498.

From Glover (1987), see Table 1.1, the axial loss is approximately 0.163 and the rotational loss is approximately 0.066 for a thrust loading of 0.662. Hence, the agreement for the axial loss is reasonable for the xlift results, whereas the results from xdisk differ more and the rotational loss predicted by xlift and xdisk is considerably lower.

6.5 Energy Coefficients for the Kappel Propeller Series

In order to investigate how the linear actuator disk method performs for the Kappel propellers, xdisk is used to calculate the energy coefficients for the three wake adapted Kappel propellers K1, K2 and K3 in *open water* with the following input parameters:

$$Z = 6, \quad R = 3.727m, \quad \hat{r}_h = 0.185, \quad U_A = 9.28^{\mathrm{m}}/_{\mathrm{s}}, \quad J = 0.7472.$$

The rest of the input parameters are taken from the optimisation of the propellers, which are provided by J.J. Kappel. The coefficients can only be obtained for open water as a uniform inflow is assumed in xdisk.

Table 6.7 presents the calculated energy coefficients and Figure 6.10 the induced velocities used for the calculations of the coefficients. From the figure it is seen that K2 and K3 have the same differences in the induced velocities calculated by the distribution of circulation or

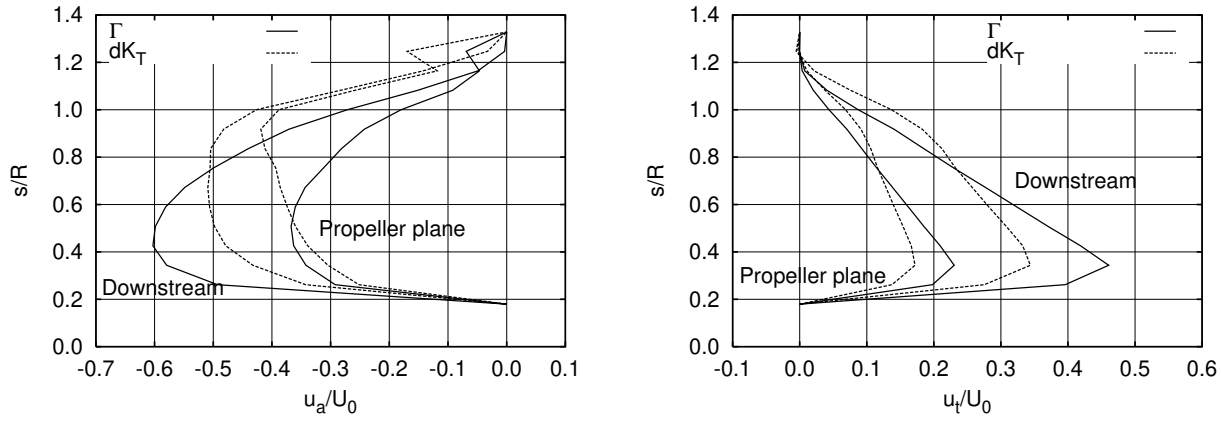

K1, $C_{Th} = 1.0126$

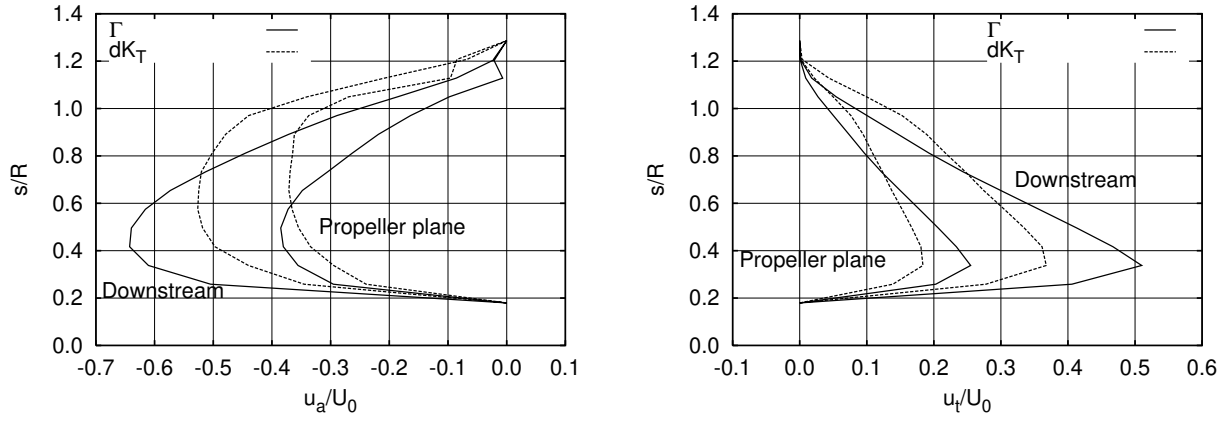

K2, $C_{Th} = 1.0127$

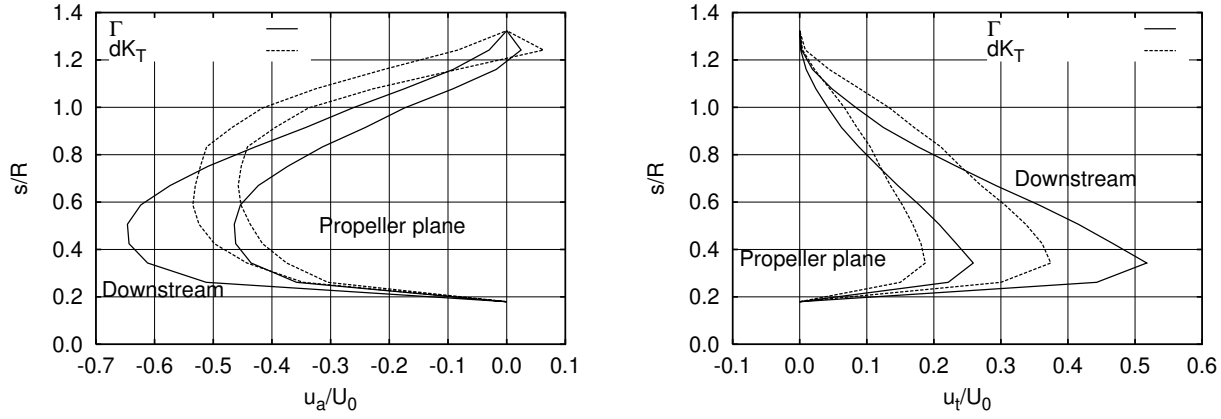

K3, $C_{Th} = 1.0039$

Figure 6.10: *Comparison of velocities for* xdisk *for the Kappel propellers.* $Z = 6$, $R = 3.727m$, $\hat{r}_h = 0.185$, $U_A = 9.28^{m}/_{s}$ *and* $J = 0.7472$.

Table 6.7: *Energy coefficients for the Kappel propellers calculated by* xdisk. $Z = 6$, $R = 3.727m$, $\hat{r}_h = 0.185$, $U_A = 9.28^m/_s$ *and* $J = 0.7472$.

Prop.	$K_{T,\infty}$	$10K_{Q,\infty}$	AXL	$ROTL$	FRL	$FBNL$	η_∞	η
K1.ci	0.22201	0.4031	0.22118	0.05079	0.07304	-0.06500	0.6550	0.7200
K1.kt	0.22201	0.4137	0.25179	0.03891	0.07116	-0.08185	0.6381	0.7200
K2.ci	0.22203	0.4031	0.22113	0.05705	0.06684	-0.05811	0.6550	0.7131
K2.kt	0.22203	0.4042	0.23755	0.04262	0.06666	-0.05992	0.6532	0.7131
K3.ci	0.22010	0.4225	0.25659	0.05719	0.06677	-0.10293	0.6195	0.7224
K3.kt	0.22010	0.4201	0.26799	0.04175	0.06716	-0.09929	0.6231	0.7224

the distribution of thrust, as was observed for K1 in Section 5.3. The table shows that for the Kappel propellers, as for the DTNSRDC propellers, the efficiency for the propeller with an infinite number of blades, η_∞, is decreasing when the efficiency for the propeller with finite blade number, η, is increasing. This influences the $FBNL$, which is seen to have a relatively large negative value for all three propellers. Hence, it seems that the used method does not perform very well for the Kappel propellers. This is believed to be mainly due to the use of xdisk to obtain the induced velocities.

6.6 Summary

The energy coefficients proposed by Dyne (1993) have been extended to include a radial variation in the axial onset flow. A comparison between the AXL and $ROTL$ coefficients and the corresponding coefficients proposed by Glauert (1963) shows a satisfactory agreement between the results when the propeller is modelled as an actuator disk in uniform onset flow. The optimisation program xlift and the modified actuator disk program xdisk have been used to calculate the energy coefficients for different propellers. A comparison of the coefficients obtained by xdisk and xlift shows good results when the propeller in xlift is modelled as a lifting line. A comparison of the coefficients for the five DTNSRDC propellers obtained by xlift and xdisk gives more questionable results. The major concern is that the efficiency for the propeller with an infinite number of blades, η_∞, is decreasing while the efficiency for the propeller with a finite blade number, η, is increasing for increasing skew. The decrease of η_∞ is mainly due to increased AXL whereas the changes in $ROTL$ have a minor effect. Furthermore, there is a difference of up to seven per cent between the η_∞ obtained by xdisk and xlift. An inspection of the induced velocities calculated by xlift shows that the axially induced velocity at the propeller plane is increasing with increasing skew, whereas the induced velocity downstream is almost equal for all the propellers. This will increase the AXL and thus reduce the efficiency η_∞. If this is a physical effect for the propellers with skew or a consequence of the used numerical model should be further examined. An inspection of

the induced axial velocities at the propeller plane calculated by xdisk shows that an increase in skew results in a high increase in the velocity, so that the velocities for the propellers with 72° skew are almost of the same magnitude as the velocity far abaft the propeller. This indicates that xdisk may be too simple a method to calculate the velocities for propellers with skew and skew-induced rake. xdisk is also used to calculate the open water energy coefficients for three Kappel propellers originally designed for a ship wake. Here the results show a relatively large negative $FBNL$ and again η_∞ is decreasing while η is increasing. Again it is believed that xdisk is too simple a method to calculate the averaged velocities for the Kappel propellers and a better method should be found before usable coefficients can be obtained.

This page is intentionally left blank.

Chapter 7

Conclusions

The present study includes an extension of the classic theory for obtaining the radial distribution of thrust which gives the highest efficiency for the propeller. This problem is formulated as a variational problem where the applied torque is minimised for a given thrust. In classic theory the problem is solved by an integral approach, which results in the Betz (1927) or the Lerbs (1952) optimum criteria for the distribution of circulation. In classic theory linearisation and application of the Munk displacement theorem (von Kármán and Burgers, 1963) are necessary in order to solve the problem, and the propeller is modelled by a lifting line. If the problem is instead solved for a discrete distribution of circulation, Kerwin et al. (1986) and Coney (1992) showed that the variational problem can be solved directly. For sufficiently low thrust loading the results obtained by the discrete method fulfil the classic optimum criteria. The discrete method is used in the present study and, as an extension to the model, the contribution from the entire blade is included as the vortex-lattice method is used to model the propeller. In the vortex-lattice method the propeller blade is replaced by a lattice of quadrilateral panels with constant circulation and the shed horseshoe vortices follow regular helices.

The method is first validated for a hydrofoil with elliptic planform in uniform inflow. According to Munk's displacement theorem (von Kármán and Burgers, 1963) it is necessary to impose constraints on the chordwise distribution of circulation in order to solve the variational problem. The obtained results are in good agreement with the analytical result obtained by Prandtl for a lifting-line model of the hydrofoil. The optimisation for the hydrofoil is made with the trailers and the grid aligned parallel to the onset flow in accordance with linear theory. Thus, the contribution to the lift will be concentrated at the trailing edge on the side which combines the two trailers in the shed horseshoe vortex, as the contributions from the panels will cancel. The drag calculation will, however depend on the entire blade as the blade and the trailers will induce a varying vertical velocity on the blade. The contribution to the drag from each panel is the difference in induced velocity on the two sides of the panel which are perpendicular to the onset flow. This difference will be small and again the largest contribution to the drag comes from the trailing edge where the induced velocity is fully included.

Subsequently, the method is applied to propellers. A validation of the developed computer program xlift shows that the method converges for increasing number of panels, even for high thrust loadings and propellers with high skew and skew-induced rake. The validation was made by linear theory. For both the thrust and the torque calculations it is shown that the contributions from the onset flow vanish at the panels and only contribute at the trailing edge, where also the contribution from the induced velocity is fully included. The contributions from the panels are only due to the difference in induced velocity on the panel sides, which will be small. This explains why the shape of the chordwise distribution of circulation only has a small influence on the optimisation, which is in accordance with Munk's displacement theorem (von Kármán and Burgers, 1963).

The reason for including the entire blade in the model is that the induced velocities, which are used in the calculations of the thrust and the torque, depend on the distribution of circulation on the entire blade and the geometry of the blade. Therefore, it is possible to examine which effect the propeller geometry has on the optimisation. Five propellers from the DTNSRDC propeller series have been optimised for the same design point. The calculations show that the efficiency is increased for increasing skew. This effect is also noted by Mishima and Kinnas (1997). The efficiency is further increased if the skew-induced rake is removed. The radial distributions of circulation, thrust and torque have been compared for the five propellers and this comparison shows that the distributions of thrust are almost identical for all five propellers whereas the distributions of circulation and torque differ. It is interesting that the distributions of thrust are identical for all five propellers, as it shows that the optimum distribution of thrust is not influenced by the propeller geometry. The reason for the higher efficiency for the skewed propellers is not known in detail and should be further investigated. But an examination of the total velocity at the trailing edge proves that the axial velocity is lower on the outer part of the blade and higher on the inner part for the skewed propellers, whereas the tangential velocity is higher on the outer part and lower on the inner part. This in combination with the radial distribution of circulation results in the same distribution of thrust for all the propellers and a lower distribution of torque on the outer part of the blade for the skewed propellers.

As a last example of the capabilities of the present method a Kappel propeller is optimised in a radially varying wake, where both the axial and the radial components of the onset flow are specified. A simple wake alignment procedure similar to the method for the moderately loaded lifting line is applied. The agreement for the optimised torque coefficient is very good for the present method and the normal optimisation method for the Kappel propellers. The differences for the obtained distribution of circulation and for the final pitch angle for the wake are reasonably small between the present method and the normal method for the Kappel propellers.

The other main objective of this thesis is the comparison of the performances of different propellers by use of energy coefficients. The energy coefficients proposed by Dyne (1993) have been extended to include a radially varying axial onset flow. Thus, it is possible to calculate the efficiency for a propeller as a sum of five energy coefficients related to the axial loss, the rotational loss, the frictional loss and a finite blade number loss. If the propeller

is located in a wake the fifth coefficient is included, which is an axial gain. The axial and the rotational losses have been compared to the two corresponding coefficients derived by Glauert (1963) for a simple propeller and the agreement is satisfactory.

In order to calculate the energy coefficients it is necessary to know the averaged axially induced velocity at the propeller plane and the averaged axial and tangential velocities far downstream of it. These velocities are found by two methods. One is xlift. The other is a modified actuator disk model of the propeller based on the linear Euler equations with specification of all three force components. The radial force component has been included in order to be able to calculate the induced velocities from propellers with skew and rake and with unconventional geometries, such as the Kappel propellers. By solving the linear Euler equations in cylindrical coordinates it is possible to obtain closed-form solutions for the pressure and the induced velocities for a propeller in open water. This makes the calculation of the induced velocities very fast. The obtained solutions for the velocities and the pressure correspond to the weighted sum of the velocities from a linear actuator disk and a duct.

An examination of the induced velocities from the five DTNSRDC propellers and the three Kappel propellers calculated by xdisk proves that the results are influenced by the parameter given as input to the pressure distribution. Comparison of the induced axial and tangential velocities far downstream calculated by xdisk and xlift shows reasonable agreement between the results if the thrust is used as input to the pressure distribution in xdisk. This indicates that neglect of the induced velocities in the calculation of the input pressure distribution, when the circulation is used as input, is to coarse an approximation. At the propeller plane there are larger differences between the results obtained by xlift and xdisk. For both methods the axial velocity is increasing with increasing skew and a removal of the skew-induced rake enhances this pattern. The axial velocities at the propeller plane for the propellers with 72^{o} skew calculated by xdisk are almost as high as the velocities far downstream. If this is realistic should be further investigated but it is believed that the results from xdisk are to high. For the Kappel propellers xdisk also predicts relatively high velocities at the propeller plane. Hence, it seems that the linear theory is too coarse an approximation to predict the induced velocities from propellers with skew and skew-induced rake and with unconventional geometries, such as the Kappel propellers. The tangential velocities at the propeller plane calculated by xlift have an unusual shape as the velocity is increasing toward the tip. The reason for this remarkable shape is not known in detail and should be further examined. But an investigation of the velocities from the blade and the trailers separately shows that the increasing velocity is caused by the trailers. As the tangential velocity at the propeller plane is not used in the calculation of the energy coefficients these results will not influence the coefficients.

The open water energy coefficients for the five DTNSRDC propellers have been calculated both by xdisk and xlift. Unfortunately, the efficiency for a propeller with an infinite number of blades calculated by the energy coefficients does not follow the efficiency found by the optimisation. By the optimisation the efficiency is increasing with increasing skew, whereas the efficiency for a propeller with an infinite number of blades based on the coefficients is decreasing with increasing skew. The reason is that for both xlift and xdisk the induced axial

velocity at the propeller plane is increasing with increasing skew, whereas the axial velocities far downstream are almost identical for all five propellers. This results in an increased AXL and thus a decrease in the efficiency. The $ROTL$ calculated by xlift is decreasing whereas the $ROTL$ calculated by xdisk is both increasing and decreasing depending on the given input loading distribution. The decrease in the $ROTL$ is relatively small and therefore the efficiency is decreasing. As mentioned above, it should be further investigated if the predicted averaged velocities at the propeller plane are accurate. The open water energy coefficients have been calculated by xdisk for the three Kappel propellers. Again the results are questionable as the $FBNL$ is relatively high and negative. The reasons for this should be further investigated but two reasons which influence the results can be mentioned. One is that the Kappel propellers are designed for a wake whereas the coefficients are obtained in open water. Another reason is the predicted velocities from xdisk, which have been shown to be questionable.

References

Abbott, I. H. and von Doenhoff, A. E. (1959), *Theory of Wing Sections*, Dover Publications, New York.

Abramowitz, M. and Stegun, I. A. (1972), *Handbook of Mathematical Functions*, Dover Publications, New York.

Andersen, P. (1997), A Comparative Study of Conventional and Tip-Fin Propeller Performance, in *Proc. Twenty-First Symposium on Naval Hydrodynamics*, pp. 930–945, National Academy Press, Washington, D.C.

Andersen, P. (1999), Tip-Modified Propellers, *Oceanic Engineering International*, 3(1):1–11.

Andersen, P., Andersen, S. V., Bodger, L., Friesch, J. and Kappel, J. J. (2000), Cavitation Considerations in the Design of Kappel Propellers, in Atlar, M., Clarke, D. and Glover, E. (editors), *NCT'50 International Conference on Propeller Cavitation*, pp. 159–174, Penshaw Press, Sunderland, UK.

Andersen, P., Kappel, J. J. and Schwanecke, H. (1992), On Development of Tip-Fin Propellers, *Jahrbuch der Schiffbautechnischen Gesellschaft*, 89:203–209.

Andersen, S. V. (1988), *Numerical Treatment of the Design-Analysis Problem of Ship Propellers using Vortex Lattice Methods*, PhD thesis, Dept. of Ocean Eng., DTU, Lyngby, Denmark.

Betz, A. (1927), Schraubenpropeller mit geringstem Energieverlust, *Vier Abhandlungen zur Hydrodynamik und Aerodynamik*, pp. 68–92.

Breslin, J. P. and Andersen, P. (1994), *Hydrodynamics of Ship Propellers*, Cambridge Ocean Technology Series 3, Cambridge University Press, Cambridge, UK.

Breslin, J. P. and Andersen, P. (1995), Effects of Wake Shear on Duct Camber, Technical Report 514, DCAMM, Technical University of Denmark, Lyngby.

Caponnetto, M. (2000), Optimisation and Design of Contra-Rotating Propellers, in *Proc. Propeller/Shafting 2000 Symposium*, pp. 3.1–3.9, SNAME, Jersey City, N.J.

Coney, W. B. (1992), Optimum Circulation Distributions for a Class of Marine Propulsors, *Journal of Ship Research*, 36(3):210–222.

Conway, J. T. (1995), Analytical solutions for the actuator disk with variable radial distribution of load, *Journal of Fluid Mechanics*, 297:327–355.

Conway, J. T. (1998), Exact actuator disk solutions for non-uniform heavily loading and slipstream contraction, *Journal of Fluid Mechanics*, 365:235–267.

Dyne, G. (1993), On the Efficiency of a Propeller in Uniform Flow, in *Trans. RINA*, volume 136, pp. 105–129, RINA, London.

Dyne, G. (1995), The Principles of Propulsion Optimization, in *Trans. RINA*, volume 137, pp. 189–208, RINA, London.

Glauert, H. (1963), Airplane Propellers, in Durand, W. F. (editor), *Aerodynamic Theory*, volume III and IV, Dover Publications, Inc., New York.

Glover, E. J. (1987), Propulsive Devices for Improved Propulsive Efficiency, in *Trans. Institute of Marine Engineers*, volume 99, pp. 23–29, The Institute of Marine Engineers, London.

Goodman, T. R. (1979), Momentum Theory of a Propeller in a Shear Flow, *Journal of Ship Research*, 23(4):242–252.

Greely, D. S. and Kerwin, J. E. (1982), Numerical Methods for Propeller Design and Analysis in Steady Flow, *Trans. SNAME*, 90:415–53.

Hoshino, T. (1989), Hydrodynamic Analysis of Propellers in Steady Flow Using a Surface Panel Method, *Journal of The Society of Naval Architects of Japan*, 166:79–92.

Hough, G. R. and Ordway, D. E. (1965), The Generalized Actuator Disk, in Shaw, W. A. (editor), *Developments in Theoretical and Applied Mechanics*, volume 2, pp. 317–336, Pergamon Press, Oxford.

ITTC (1990), Report of the Propulsor Committee, in *Proc. 19th International Towing Tank Conference*, volume 1, pp. 109–160, Canal de Experiencias Hidrodinamicas, El Pardo.

James, R. M. (1972), On the Remarkable Accuracy of the Vortex Lattice Method, *Computer Methods in Applied Mechanics and Engineering*, 1:59–79.

de Jong, K. (1991), *On the Optimization and the Design of Ship Screw Propellers with and without End Plates*, doctoral thesis, Dept. of Mathematics, Unv. of Groningen, Groningen.

Karim, M., Ikehata, M., Suzuki, K. and Kai, H. (2001), Application of Micro-Generic Algorithm (μGA) to the Optimal Design of Lifting Bodies, *J. Kansai Soc. of Naval Architects, Japan*, 235:1–8.

von Kármán, T. and Burgers, J. M. (1963), General Aerodynamic Theory–Perfect Fluids, in Durand, W. F. (editor), *Aerodynamic Theory*, volume I and II, Dover Publications, Inc., New York.

Kerwin, J. E., Coney, W. B. and Hsin, C.-Y. (1986), Optimum Circulation Distribution for Single and Multi-Component Propulsors, in Messalle, R. F. (editor), *Proc. of Twenty-First American Towing Tank Conference*, pp. 53–62, National Academy Press, Washington, D.C.

Kerwin, J. E., Keenan, D. P., Black, S. D. and Diggs, J. G. (1994), A Coupled Viscous/Potential Flow Design Method for Wake-Adapted, Multi-Stage, Ducted Propulsors Using Generalized Geometry, *Trans. SNAME*, 102:23–56.

Kerwin, J. E. and Lee, C.-S. (1978), Prediction of Steady and Unsteady Marine Propeller Performance by Numerical Lifting-Surface Theory, *Trans. SNAME*, 86:218–53.

Kinnas, S. A. and Fine, N. (1994), A Nonlinear Boundary Element Method for the Analysis of Unsteady Propeller Sheet Cavitation, in *Proc. Nineteenth Symposium on Naval Hydrodynamics*, pp. 717–737, National Academy Press, Washington, D.C.

Kinnas, S. A., Griffin, P. E., Choi, J.-K. and Kosal, E. M. (1998), Automated Design of Propulsor Blades for High-Speed Ocean Vehicle Applications, *Trans. SNAME*, 106:213–240.

Küchemann, D. and Weber, J. (1953), *Aerodynamics of Propulsion*, McGraw-Hill Book Company, Inc., New York.

Lan, C. E. (1974), A Quasi-Vortex-Lattice Method in Thin Wing Theory, *Journal of Aicraft*, 11(9):518–527.

Lerbs, H. W. (1952), Moderately Loaded Propellers with a Finite Number of Blades and an Arbitrary Distribution of Circulation, *Trans. SNAME*, 60:73–123.

Mishima, S. and Kinnas, S. A. (1997), Application of a Numerical Optimization Technique to the Design of Cavitating Propellers in Nonuniform Flow, *Journal of Ship Research*, 41(2):93–107.

Newman, J. N. (1978), *Marine Hydrodynamics*, MIT Press, Massachusetts.

Sparenberg, J. A. (1984), *Elements of hydrodynamic propulsion*, Mechanics of fluids and transport processes, Martinus Nijhoff Publishers, The Hague.

Streckwall, H. (1994), Application of a Vortex-Lattice Method to Ship Propellers, *Schiffstechnik*, Bd. 41:31–43.

Su, Y. and Ikehata, M. (1999), A Numerical Design Method of Marine Propellers Using Surface Panel Method, *J. Kansai Soc. of Naval Architects, Japan*, 231:21–28.

Visual Numerics, Inc. (1997), *IMSL Math/Library, Volumes 1 and 2*, Visual Numerics, Inc., Houston.

Waterloo Maple, Inc. (2001), *Maple 6.02a*, Waterloo Maple, Inc., Waterloo.

Wu, T. Y. (1962), Flow Through a Heavily Loaded Actuator Disc, *Schiffstechnik*, 9(47):134–138.

Yim, B. (1976), Optimum Propellers with Cavity-Drag and Frictional-Drag Effects, *Journal of Ship Research*, 20(2):118–123.

Appendix A

Energy Coefficients

This appendix contains the analytical expressions for the Dyne coefficients and the Glauert (1963) coefficients shown in Table 6.2. The energy coefficients are calculated for three different thrust loadings $C_{Th} = 0.1$, $C_{Th} = 0.2$ and $C_{Th} = 0.5$ with

$$Z = 5, \quad U_0 = 12.0\,{}^{\mathrm{m}}/_{\mathrm{s}}, \quad R = 3.0\text{ m}, \quad \hat{r}_h = 0.2, \quad J = 1.596$$

The propeller is modelled as an actuator disk where the induced velocities are given by (Hough and Ordway, 1965):

$$\frac{u_{a,0}(\hat{r})}{U_0} = \frac{-Z\omega}{4\pi U_0^2}\,\Gamma(\hat{r}) \qquad \frac{u_{a,-\infty}(\hat{r})}{U_0} = \frac{-Z\omega}{2\pi U_0^2}\,\Gamma(\hat{r}) \tag{A.1}$$

$$\frac{u_{t,0}(\hat{r})}{U_0} = \frac{Z}{4\pi U_0 R}\,\frac{\Gamma(\hat{r})}{\hat{r}} \qquad \frac{u_{t,-\infty}(\hat{r})}{U_0} = \frac{Z}{2\pi U_0 R}\,\frac{\Gamma(\hat{r})}{\hat{r}} \tag{A.2}$$

where the circulation is

$$\Gamma(\hat{r}) = U_0 R A(\hat{r} - \hat{r}_h)\sqrt{1-\hat{r}} \tag{A.3}$$

and where A is a constant which depends on the C_{Th}.

By means of the above expressions it is possible to determine the energy coefficients analytically. The mathematical program Maple (Waterloo Maple, Inc., 2001) has been used to solve the integrals.

A.1 Present Coefficients

The analytical solutions for the present energy coefficients from Equations (6.10) and (6.12) are given in the following.

Table A.1: *A for the present coefficients.*

C_{Th}	A
0.100	0.1571
0.200	0.3100
0.500	0.7471

The thrust is given by

$$
\begin{aligned}
T &= 2\pi \int_{r_h}^{R} \Delta p(r) r dr = 2\pi \int_{r_h}^{R} \Big(p_{-\infty}(r) - p_0 + \tfrac{1}{2}\rho \Big(\{ -2U_0 u_{a,-\infty}(r) + u_{a,-\infty}^2(r) \} \Big) \Big) r dr \\
&= \pi \rho U_0^2 R^2 \int_{\hat{r}_h}^{1} \left[-2 \int_{\hat{r}_{-\infty}}^{1} \Big(\frac{u_{t,-\infty}(\hat{r}_{-\infty})}{U_0} \Big)^2 \frac{d\hat{r}}{\hat{r}} - 2 \frac{u_{a,-\infty}(\hat{r})}{U_0} + \Big(\frac{u_{a,-\infty}(\hat{r})}{U_0} \Big)^2 \right] \hat{r} d\hat{r} \\
&= \frac{\rho R^2 Z A}{1680\,\pi} \Big(\Big(700\,\hat{r}_h{}^3 + 210\,\hat{r}_h^4 - 70 + 420\,\hat{r}_h - 840\,\hat{r}_h^3 \ln(\hat{r}_h) - 420\,\ln(1+\sqrt{1-\hat{r}_h}) \\
&\quad -420\,\ln(|\sqrt{1-\hat{r}_h}-1|) + 420\,\ln(\hat{r}_h) + 420\,\hat{r}_h^2 \ln(1+\sqrt{1-\hat{r}_h}) \\
&\quad -840\,\hat{r}_h\,\ln(1+\sqrt{1-\hat{r}_h}) - 420\,\ln(\hat{r}_h)\hat{r}_h^2 + 840\,\hat{r}_h\,\ln(\hat{r}_h) \\
&\quad +420\,\hat{r}_h^2 \ln(|\sqrt{1-\hat{r}_h}-1|) - 840\,\hat{r}_h\,\ln(|\sqrt{1-\hat{r}_h}-1|) \\
&\quad -1260\,\hat{r}_h^2 \Big) Z A {U_0}^2 + \Big(192\,\hat{r}_h^3 + 256 - 320\,\hat{r}_h - 128\,\hat{r}_h^2 \Big) \sqrt{1-\hat{r}_h} \pi\,\omega\,R U_0 \\
&\quad +Z A \omega^2 R^2 \left(21 + 70\,\hat{r}_h^2 - 70\,\hat{r}_h + 14\,\hat{r}_h^5 - 35\,\hat{r}_h^4 \right) \Big)
\end{aligned}
$$

where A, as the only unknown, is determined so that the thrust corresponds to the three specified thrust loadings. The results are shown in Table A.1.

The torque is given by

$$
\begin{aligned}
Q &= \frac{-1}{n}\int_{r_h}^{R}\Delta H(r)\big[u_{a,0}(r)-U(r)\big]r\,dr \\
&= \frac{-1}{n}\int_{r_h}^{R}\Big(p_{-\infty}(r)-p_0+\tfrac{1}{2}\rho\big\{-2U(r)u_{a,-\infty}(r)+u_{a,-\infty}^2(r)+u_{t,-\infty}^2(r)\big\}\Big)\big[u_{a,0}(r)-U(r)\big]r\,dr \\
&= \frac{-\rho U_0^3R^2}{2n}\int_{\hat r_h}^{1}\Big(-2\int_{\hat r_{-\infty}}^{1}\Big(\frac{u_{t,-\infty}(\hat r_{-\infty})}{U_0}\Big)^2\frac{d\hat r}{\hat r} \\
&\quad -2\frac{U(\hat r)}{U_0}\frac{u_{a,-\infty}(\hat r)}{U_0}+\Big(\frac{u_{a,-\infty}(\hat r)}{U_0}\Big)^2+\Big(\frac{u_{t,-\infty}(\hat r)}{U_0}\Big)^2\Big)\left[\frac{u_{a,0}(\hat r)}{U_0}-\frac{U(\hat r)}{U_0}\right]\hat r\,d\hat r \\
&= \frac{R^2\rho\,ZA}{25225200\pi^3 n}\ \Big(-8400\,Z^2A^2\omega^3R^3\sqrt{1-\hat r_h}\hat r_h^6 \\
&\quad -\Big(-28560\,Z^2A^2\omega^3R^3\sqrt{1-\hat r_h}-210210\,ZA\omega^2R^2\pi\ U_0+90090\ {U_0}^2Z^2A^2\omega\,R\sqrt{1-\hat r_h}\Big)\hat r_h^5 \\
&\quad -\Big(307164\ {U_0}^2Z^2A^2\omega\,R\sqrt{1-\hat r_h}+16800\,Z^2A^2\omega^3R^3\sqrt{1-\hat r_h}+525525\,ZA\omega^2R^2\pi\ U_0 \\
&\quad -360360\ {U_0}^2Z^2A^2\omega\,R\sqrt{1-\hat r_h}\ln(\hat r_h)-1576575\ {U_0}^3ZA\pi\Big)\hat r_h^4 \\
&\quad -\Big(-6306300\ {U_0}^3ZA\pi+50400\,Z^2A^2\omega^3R^3\sqrt{1-\hat r_h}+60060\ {U_0}^2Z^2A^2\omega\,R\sqrt{1-\hat r_h}\ln(\hat r_h) \\
&\quad +6306300\ {U_0}^3ZA\ln(\hat r_h)\pi-1441440\ {U_0}^2\omega\,R\sqrt{1-\hat r_h}\pi^2-801944\ {U_0}^2Z^2A^2\omega\,R\sqrt{1-\hat r_h}\Big)\hat r_h^3 \\
&\quad -\Big(-92400\,Z^2A^2\omega^3R^3\sqrt{1-\hat r_h}+840840\ {U_0}^2Z^2A^2\omega\,R\ln(1+\sqrt{1-\hat r_h})+7882875\ {U_0}^3ZA\pi \\
&\quad -840840\ {U_0}^2Z^2A^2\omega\,R\ln(|\sqrt{1-\hat r_h}-1|)+3153150\ {U_0}^3ZA\ln(\hat r_h)\pi \\
&\quad +960960\ {U_0}^2\omega\,R\sqrt{1-\hat r_h}\pi^2-1154868\ {U_0}^2Z^2A^2\omega\,R\sqrt{1-\hat r_h} \\
&\quad +720720\ {U_0}^2Z^2A^2\omega\,R\sqrt{1-\hat r_h}\ln(\hat r_h)-1051050\,ZA\omega^2R^2\pi\ U_0\Big)\hat r_h^2 \\
&\quad -\Big(153582\ {U_0}^2Z^2A^2\omega\,R\sqrt{1-\hat r_h}+58800\,Z^2A^2\omega^3R^3\sqrt{1-\hat r_h} \\
&\quad -6306300\ {U_0}^3ZA\ln(|\sqrt{1-\hat r_h}-1|)\pi+6306300\ {U_0}^3ZA\ln(\hat r_h)\pi \\
&\quad +60060\ {U_0}^2Z^2A^2\omega\,R\ln(|\sqrt{1-\hat r_h}-1|)+1051050\,ZA\omega^2R^2\pi\ U_0 \\
&\quad -6306300\ {U_0}^3ZA\ln(1+\sqrt{1-\hat r_h})\pi-60060\ {U_0}^2Z^2A^2\omega\,R\ln(1+\sqrt{1-\hat r_h}) \\
&\quad -180180\ {U_0}^2Z^2A^2\omega\,R\sqrt{1-\hat r_h}\ln(\hat r_h)+2402400\ {U_0}^2\omega\,R\sqrt{1-\hat r_h}\pi^2\Big)\hat r_h \\
&\quad +1921920\ {U_0}^2\omega\,R\sqrt{1-\hat r_h}\pi^2+240240\ {U_0}^2Z^2A^2\omega\,R\ln(1+\sqrt{1-\hat r_h}) \\
&\quad -324896\ {U_0}^2Z^2A^2\omega\,R\sqrt{1-\hat r_h}-3153150\ {U_0}^3ZA\ln(\hat r_h)\pi \\
&\quad -240240\ {U_0}^2Z^2A^2\omega\,R\ln(|\sqrt{1-\hat r_h}-1|)+315315\,ZA\omega^2R^2\pi\ U_0 \\
&\quad +13440\,Z^2A^2\omega^3R^3\sqrt{1-\hat r_h}+3153150\ {U_0}^3ZA\ln(|\sqrt{1-\hat r_h}-1|)\pi \\
&\quad +240240\ {U_0}^2Z^2A^2\omega\,R\sqrt{1-\hat r_h}\ln(\hat r_h)+3153150\ {U_0}^3ZA\ln(1+\sqrt{1-\hat r_h})\pi\Big)
\end{aligned}
$$

The energy coefficients are

$$
\begin{aligned}
AXL &= -\frac{\rho U_s^3 R^2}{2nQ}\int_{\hat{r}_h}^{1}\frac{u_{a,0}(\hat{r})}{U_s}\left[-2\frac{U(\hat{r})}{U_s}\frac{u_{a,-\infty}(\hat{r})}{U_s}+\left(\frac{u_{a,-\infty}(\hat{r})}{U_s}\right)^2\right]\hat{r}d\hat{r}\\
&= -\frac{\rho\, R^4 Z^2\omega A^2}{240240\,\pi^2\,Q}\left(\left(-10010\,\hat{r}_h^2-3003+5005\,\hat{r}_h^4-2002\,\hat{r}_h^5+10010\,\hat{r}_h\right)\pi\;U_0\right.\\
&\quad\left.+\;RZ\omega\,A\sqrt{1-\hat{r}_h}\left(-256-1760\,\hat{r}_h^2+960\,\hat{r}_h^3+320\,\hat{r}_h^4-544\,\hat{r}_h^5+160\,\hat{r}_h^6+1120\,\hat{r}_h\right)\right)
\end{aligned}
$$

$$
\begin{aligned}
ROTL &= -\frac{\rho U_s^3 R^2}{2nQ}\int_{\hat{r}_h}^{1}\left\{\left[\frac{u_{a,0}(\hat{r})}{U_s}-\frac{U(\hat{r})}{U_s}\right]\left[\Delta C_{prot}(\hat{r})+\left(\frac{u_{t,-\infty}(\hat{r})}{U_s}\right)^2\right]+\Delta C_{prot}(\hat{r})\right\}\hat{r}d\hat{r}\\
&= -\frac{\rho\, R^2 Z^2 A^2\, {U_0}^2}{88200\,\omega\,Q\,\pi^2}\left(\left(-3675+22050\,\hat{r}_h^2\ln(|\sqrt{1-\hat{r}_h}-1|)-7350\,\hat{r}_h^3-11025\,\hat{r}_h^2\right.\right.\\
&\quad\left.+22050\,\hat{r}_h^2\ln(1+\sqrt{1-\hat{r}_h})+22050\,\hat{r}_h\right)\pi\;U_0+Z\omega\,RA\left(2272\sqrt{1-\hat{r}_h}\right.\\
&\quad+2148\sqrt{1-\hat{r}_h}\hat{r}_h^4+1074\sqrt{1-\hat{r}_h}\hat{r}_h+630\sqrt{1-\hat{r}_h}\hat{r}_h^5-2520\,\hat{r}_h^4\sqrt{1-\hat{r}_h}\ln(\hat{r}_h)\\
&\quad-1680\sqrt{1-\hat{r}_h}\ln(\hat{r}_h)-5608\sqrt{1-\hat{r}_h}\hat{r}_h^3-8076\sqrt{1-\hat{r}_h}\hat{r}_h^2\\
&\quad-1260\sqrt{1-\hat{r}_h}\ln(\hat{r}_h)\hat{r}_h+1680\,\ln(|\sqrt{1-\hat{r}_h}-1|)+5040\,\hat{r}_h^2\sqrt{1-\hat{r}_h}\ln(\hat{r}_h)\\
&\quad+420\,\hat{r}_h^3\sqrt{1-\hat{r}_h}\ln(\hat{r}_h)+420\,\hat{r}_h\,\ln(|\sqrt{1-\hat{r}_h}-1|)\\
&\quad-1680\,\ln(1+\sqrt{1-\hat{r}_h})-420\,\hat{r}_h\,\ln(1+\sqrt{1-\hat{r}_h})+5880\,\hat{r}_h^2\ln(1+\sqrt{1-\hat{r}_h})\\
&\quad\left.\left.-5880\,\hat{r}_h^2\ln(|\sqrt{1-\hat{r}_h}-1|)\right)\right)
\end{aligned}
$$

where

$$
\begin{aligned}
\Delta C_{prot}(\hat{r}) &= -2\int_{\hat{r}_{-\infty}}^{1}\left(\frac{u_{t,-\infty}(\hat{r})}{U_0}\right)^2\frac{1}{\hat{r}}d\hat{r}\\
&= \frac{Z^2A^2}{4\pi^2}\left(-2\,\hat{r}+2\,\ln(\hat{r})\,(2\,\hat{r}_h+1)+\frac{4\,\hat{r}_h+2\,\hat{r}_h^2}{\hat{r}}-\frac{\hat{r}_h^2}{\hat{r}^2}+2-\hat{r}_h^2-4\,\hat{r}_h\right)
\end{aligned}
$$

A.2 Glauert's Coefficients

With reference to Equation (6.17), the coefficients are given by

$$
\begin{aligned}
\eta_1 &= \frac{1}{1+\bar{a}}\\
\eta_2 &= 1-\bar{a}'
\end{aligned}
$$

Table A.2: *A and the averaged interference factors for Glauert's coefficients.*

C_{Th}	A	$\bar{a}$	$\bar{a}'$
0.100	0.1620	0.0242	0.0202
0.200	0.3301	0.0493	0.0411
0.500	0.8794	0.1313	0.1095

where $\bar{a}$ and $\bar{a}'$ are the averaged interference factors over the disk for the axial and the tangential velocities, respectively, given by

$$\begin{aligned}
\bar{a} &= \frac{1}{1-\hat{r}_h}\int_{\hat{r}_h}^{1} a(\hat{r})d\hat{r} = \frac{1}{1-\hat{r}_h}\int_{\hat{r}_h}^{1}\frac{|u_{a,0}|(\hat{r})}{U_0}d\hat{r} = \frac{\omega\, RZ}{15\,\pi\, U_0}\,(1-\hat{r}_h)^{3/2}\,A \\
\bar{a}' &= \frac{1}{1-\hat{r}_h}\int_{\hat{r}_h}^{1} a'(\hat{r})d\hat{r} = \frac{1}{1-\hat{r}_h}\int_{\hat{r}_h}^{1}\frac{J}{\pi}\frac{u_{t,0}(\hat{r})}{U_0}\frac{d\hat{r}}{\hat{r}} \\
&= -\frac{JZ}{4\pi^2}\,\frac{\left(3\sqrt{1-\hat{r}_h} - \tanh^{-1}(\sqrt{1-\hat{r}_h})(2+\hat{r}_h)\right)}{(1-\hat{r}_h)}A
\end{aligned}$$

where the only unknown is the coefficient A, which is determined from the thrust. The trust is given by

$$\begin{aligned}
T &= 4\pi\rho\omega^2R^4\int_{\hat{r}_h}^{1}(1-a')a'\hat{r}^3d\hat{r} \\
&= 4\pi\rho\omega^2R^4\int_{\hat{r}_h}^{1}(1-\frac{J}{\pi}\frac{u_{t,0}(\hat{r})}{U_0}\frac{1}{\hat{r}})\frac{J}{\pi}\frac{u_{t,0}(\hat{r})}{U_0}\hat{r}^2d\hat{r} \\
&= -\frac{\rho\,\omega^2R^4JZ}{840}\left(\frac{ZJ\,(35-210\,\hat{r}_h+105\,\hat{r}_h^2\,(1-2\,\ln(\hat{r}_h))+70\,\hat{r}_h^3)\,A}{\pi^3}\right. \\
&\quad \left.+\frac{112\,(1-\hat{r}_h)^{5/2}\,(1-3\hat{r}_h)-240\,(1-\hat{r}_h)^{7/2}}{\pi}\right)A
\end{aligned} \tag{A.4}$$

By specifying a required thrust A can be found. Table A.2 gives the A-values and the averaged interference factors for the three thrust loadings.

A.3 Comparison of Results from xlift and xdisk

As the U_0 and the rotational speed are kept constant for the three thrust loadings the input geometry to xdisk is the same in all three cases.

The input distribution of circulation from xlift:

	$100\Gamma/(\pi DU_0)$		
s/R	$C_{Th} = 0.1$	$C_{Th} = 0.2$	$C_{Th} = 0.5$
0.20000	0.00000	0.00000	0.00000
0.23871	0.18486	0.36149	0.85049
0.29032	0.29106	0.57281	1.37170
0.34194	0.37808	0.74894	1.82701
0.39355	0.45366	0.90445	2.24803
0.44516	0.51956	1.04224	2.63852
0.49677	0.57597	1.16212	2.99445
0.54839	0.62249	1.26274	3.30866
0.60000	0.65835	1.34205	3.57207
0.65161	0.68239	1.39730	3.77365
0.70323	0.69296	1.42471	3.89966
0.75484	0.68767	1.41899	3.93210
0.80645	0.66286	1.37229	3.84571
0.85806	0.61259	1.27196	3.60129
0.90968	0.52567	1.09438	3.12757
0.96129	0.37414	0.78077	2.25033
1.00000	0.00000	0.00000	0.00000

Appendix B

Induced Velocities from the Singularities

B.1 Biot-Savart

The induced velocity, $\vec{u}$, at the point $\vec{x}$, from a vortex along a panel side, is calculated by the law of Biot-Savart:

$$\vec{u}(\vec{x}) = \frac{\Gamma}{4\pi} \int_0^{s_k} \frac{d\vec{\xi} \times \vec{R}}{|\vec{R}|^3} \tag{B.1}$$

where Γ is the circulation of the panel side and $d\vec{\xi}$ is a length element along the panel side of the length s_k. $\vec{R}$ is the vector from the vortex line element, $d\vec{\xi}$, to the point $\vec{x}$, see Figure 3.4.

As the panel sides are straight lines the solution of the integral is

$$\begin{aligned} \vec{u}(\vec{x}) &= \frac{\Gamma}{4\pi} \frac{\vec{a} \times \vec{c}}{|\vec{a} \times \vec{c}|} \frac{1}{d} [\cos\alpha + \cos\beta] \\ &= \frac{\Gamma}{4\pi} \frac{\vec{a} \times \vec{c}}{|\vec{a} \times \vec{c}|} \frac{1}{d} \left[\frac{a-e}{b} + \frac{e}{c} \right] \end{aligned} \tag{B.2}$$

The explanation of the parameters is given in Figure B.1. The vector $(\vec{a} \times \vec{c})/|\vec{a} \times \vec{c}|$ corresponds to a unit vector giving the direction of the induced velocity. The expressions for the lengths are

$$\begin{aligned} a &= |\vec{a}| = \sqrt{(x_2 - x_1) + (y_2 - y_1) + (z_2 - z_1)} \\ b &= \sqrt{(x_2 - x) + (y_2 - y) + (z_2 - z)} \\ c &= \sqrt{(x_1 - x) + (y_1 - y) + (z_1 - z)} \\ d &= \sqrt{c^2 - e^2} \\ e &= |\vec{e}| = \frac{a^2 + c^2 - b^2}{2a} \end{aligned}$$

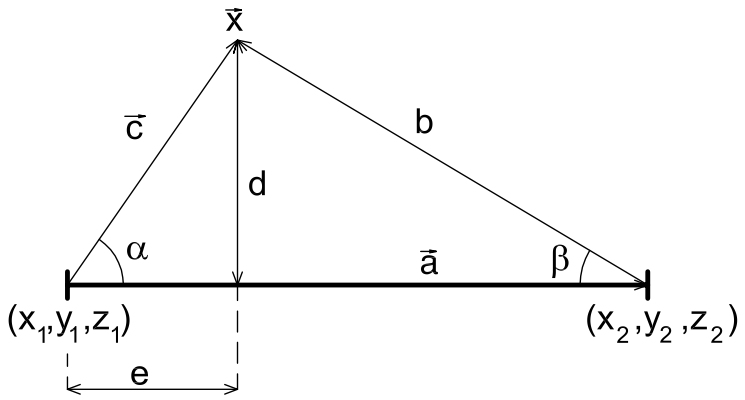

Figure B.1: *Parameters used for the numerical evaluation of the induced velocity from a straight vortex.*

Equation (B.2) is used for the numerical evaluation of the induced velocity from a panel side. If the point is on the panel side the velocity is set to zero.

B.2 Induced Velocities from the Trailers

de Jong (1991) derives a very efficient way to calculate the induced velocity from an infinitely long helix-shaped vortex in cylindrical coordinates. The induced velocity from the vortex is calculated by the Biot-Savart law and it is assumed that the pitch and the radius of the helix are constants. By a series expansion of the Biot-Savart law the velocity is calculated as a sum of cosine and sine integrals. These integrals are efficiently calculated numerically.

The same method is used to calculate the induced velocity but, in contrast to de Jong, from a semi-infinitely long helix-shaped vortex in Cartesian coordinates. These expressions are used for the calculation of the induced velocity for the shed vortices.

The helix-shaped vortex is described by

$$\vec{s} = (x, -r\sin(P'x + \phi), r\cos(P'x + \phi)) \tag{B.3}$$

where r is the radius of the helix, P' is related to the pitch P by $P' = 2\pi/P$ and ϕ is the phase angle. The vortex starts infinitely downstream and ends at point x_{TE}, which corresponds to the x-coordinate for the trailing edge of the blade.

The induced velocity from the vortex, with a unit circulation, is

$$\vec{u} = \frac{1}{4\pi}\int_{helix}\frac{d\vec{s}\times\vec{R}}{|\vec{R}|^3} \tag{B.4}$$

where

$$\vec{R} = \begin{pmatrix} x - x' \\ y - y' \\ z - z' \end{pmatrix} = \begin{pmatrix} x - x' \\ y + r' \sin(P'x' + \phi) \\ z - r' \cos(P'x' + \phi) \end{pmatrix} \tag{B.5}$$

and $d\vec{s}$ is obtained from the expression for the helix, see Equation (B.3):

$$d\vec{s} = (1, -P'r' \cos(P'x' + \phi), -P'r' \sin(P'x' + \phi))dx' \tag{B.6}$$

The vector product is

$$\begin{aligned} d\vec{s} \times \vec{R} &= \begin{pmatrix} P'r'^2 + yP'r' \sin(P'x' + \phi) - zP'r' \cos(P'x' + \phi) \\ r' \cos(P'x' + \phi) - z + (x' - x)P'r' \sin(P'x' + \phi) \\ r' \sin(P'x' + \phi) + y - (x' - x)P'r' \cos(P'x' + \phi) \end{pmatrix} dx' \\ &= \begin{pmatrix} A(x') \\ B(x') + (x' - x)C(x') \\ D(x') + (x' - x)E(x') \end{pmatrix} \end{aligned} \tag{B.7}$$

and the denominator of Equation (B.4) is

$$\begin{aligned} |\vec{R}|^3 &= [(x - x')^2 + (y + r' \sin(P'x' + \phi))^2 + (z - r' \cos(P'x' + \phi))^2]^{3/2} \\ &= [(x - x')^2 + F(x')]^{3/2} \end{aligned} \tag{B.8}$$

Hence, the x-component of the velocity is

$$\begin{aligned} u_x(\vec{x}) &= \frac{1}{4\pi} \int_{-\infty}^{x_{TE}} \frac{A(x')dx'}{[(x - x')^2 + F(x')]^{3/2}} \\ &= \frac{1}{4\pi} \int_{-\infty}^{-l} + \int_{-l}^{x_{TE}} \frac{A(x')dx'}{[(x - x')^2 + F(x')]^{3/2}} \\ &= u'_x(\vec{x}) + u''_x(\vec{x}) \end{aligned} \tag{B.9}$$

where l is sufficiently large to justify a series expansion of the denominator, so that the integral can be solved. $u''_x(\vec{x})$ is the part of the velocity induced by the vortex located between the trailing edge and the point $x = -l$. $u''_x(\vec{x})$ is calculated by approximating the regular helix shape by straight line segments, then Equation (B.2) can be used to calculate the velocity.

The series expansion for the denominator is

$$\begin{aligned} [(x - x')^2 + F(x')]^{-3/2} &= \left[(x - x')^2\right]^{-3/2} \left[1 + \frac{F(x')}{(x - x')^2}\right]^{-3/2} \\ &= |x - x'|^{-3} \left[1 - \frac{3}{2} \frac{F(x')}{(x - x')^2} + \mathcal{O}(x'^{-4})\right] \end{aligned} \tag{B.10}$$

The absolute value can be removed as $x > x'$ always. Hence, if only the two first terms are retained, the expansion becomes

$$[(x-x')^2 + F(x')]^{-3/2} \approx \frac{1}{(x-x')^3} - \frac{3}{2}\frac{F(x')}{(x-x')^5} \tag{B.11}$$

Thus, $u'_x(\vec{x})$ is approximated by

$$u'_x(\vec{x}) \approx \frac{1}{4\pi}\int_{-\infty}^{-l}\left[\frac{A(x')}{(x-x')^3} - \frac{3}{2}\frac{A(x')F(x')}{(x-x')^5}\right]dx' \tag{B.12}$$

By inserting $A(x')$ from Equation (B.7) and $F(x')$ from Equation (B.8) the velocity is

$$\begin{aligned}
u'_x(\vec{x}) &\approx \frac{1}{4\pi}\int_{l}^{\infty}\left[\frac{A(-x')}{(x'+x)^3} - \frac{3}{2}\frac{A(-x')F(x')}{(x'+x)^5}\right]dx' \\
&= \frac{1}{4\pi}\Bigg[c_0 + [c_1\cos\phi - c_2\sin\phi]\int_{P'l}^{\infty}\frac{\cos x'}{(x'+\tilde{x})^3}dx' \\
&\quad +[c_1\sin\phi + c_2\cos\phi]\int_{P'l}^{\infty}\frac{\sin x'}{(x'+\tilde{x})^3}dx' \\
&\quad +[c_3\cos\phi - c_4\sin\phi]\int_{P'l}^{\infty}\frac{\cos x'}{(x'+\tilde{x})^5}dx' \\
&\quad +[c_3\sin\phi + c_4\cos\phi]\int_{P'l}^{\infty}\frac{\sin x'}{(x'+\tilde{x})^5}dx' \\
&\quad +[c_5\cos^2\phi + c_6\sin^2\phi]\int_{P'l}^{\infty}\frac{\cos^2 x'}{(x'+\tilde{x})^5}dx' \\
&\quad +[c_5\sin^2\phi + c_6\cos^2\phi]\int_{P'l}^{\infty}\frac{\sin^2 x'}{(x'+\tilde{x})^5}dx' \\
&\quad +[8(c_5-c_6)\sin 2\phi + c_7\cos 2\phi]\int_{2P'l}^{\infty}\frac{\sin x'}{(x'+2\tilde{x})^5}dx' \\
&\quad -c_7\sin 2\phi\int_{2P'l}^{\infty}\frac{\cos x'}{(x'+2\tilde{x})^5}dx'\Bigg]
\end{aligned}$$

where $\tilde{x} = P'x$. The limits of the integral are changed so that the expressions for the cosine

and the sine integrals derived in de Jong (1991) can be used. The constants are

$$
\begin{aligned}
c_0 &= \frac{-P'^3 r^2}{2(P'l+\tilde{x})^2} + \frac{3}{8}\frac{P'^5 r^2\,(y^2+z^2+r^2)}{(P'l+\tilde{x})^4} \\
c_1 &= P'^3 rz \\
c_2 &= P'^3 ry \\
c_3 &= -\frac{3}{2}P'^5 rz\left(y^2+z^2+3r^2\right) \\
c_4 &= -\frac{3}{2}P'^5 ry\left(y^2+z^2+3r^2\right) \\
c_5 &= 3P'^5 r^2 z^2 \\
c_6 &= 3P'^5 r^2 y^2 \\
c_7 &= 48P'^5 r^2 yz
\end{aligned}
$$

By use of a similar procedure for $u_y(\vec{x})$, this velocity component yields

$$
\begin{aligned}
u'_y(\vec{x}) &\approx \frac{1}{4\pi}\int_l^\infty \left[-\frac{C(-x')}{(x'+x)^2} + \frac{B(-x')}{(x'+x)^3} + \frac{3}{2}\frac{C(-x')F(x')}{(x'+x)^4} - \frac{3}{2}\frac{B(-x')F(x')}{(x'+x)^5}\right]dx' \\
&= \frac{1}{4\pi}\Bigg[d_0 + d_1\cos\phi\int_{P'l}^\infty \frac{\sin x'}{(x'+\tilde{x})^2}dx' - d_1\sin\phi\int_{P'l}^\infty \frac{\cos x'}{(x'+\tilde{x})^2}dx' \\
&\quad + d_1\sin\phi\int_{P'l}^\infty \frac{\sin x'}{(x'+\tilde{x})^3}dx' + d_1\cos\phi\int_{P'l}^\infty \frac{\cos x'}{(x'+\tilde{x})^3}dx' \\
&\quad - d_3\sin\phi\int_{P'l}^\infty \frac{\cos x'}{(x'+\tilde{x})^4}dx' + d_3\cos\phi\int_{P'l}^\infty \frac{\sin x'}{(x'+\tilde{x})^4}dx' \\
&\quad + d_5\cos^2\phi\int_{P'l}^\infty \frac{\sin^2 x'}{(x'+\tilde{x})^4}dx' + d_5\sin^2\phi\int_{P'l}^\infty \frac{\cos^2 x'}{(x'+\tilde{x})^4}dx' \\
&\quad + [d_4\cos 2\phi - \tfrac{1}{2}d_7\sin 2\phi]\int_{2P'l}^\infty \frac{\sin x'}{(x'+2\tilde{x})^4}dx' \\
&\quad - d_4\sin 2\phi\int_{2P'l}^\infty \frac{\cos x'}{(x'+2\tilde{x})^4}dx' \\
&\quad + [d_8\cos\phi - d_6\sin\phi]\int_{P'l}^\infty \frac{\cos x'}{(x'+\tilde{x})^5}dx' \\
&\quad + [d_8\sin\phi + d_6\cos\phi]\int_{P'l}^\infty \frac{\sin x'}{(x'+\tilde{x})^5}dx' \\
&\quad + \tfrac{1}{4}d_4\cos^2\phi\int_{P'l}^\infty \frac{\cos^2 x'}{(x'+\tilde{x})^5}dx' + \tfrac{1}{4}d_4\sin^2\phi\int_{P'l}^\infty \frac{\sin^2 x'}{(x'+\tilde{x})^5}dx' \\
&\quad + [2d_4\sin 2\phi + 8d_5\cos 2\phi]\int_{2P'l}^\infty \frac{\sin x'}{(x'+2\tilde{x})^5}dx' \\
&\quad - d_7\sin 2\phi\int_{2P'l}^\infty \frac{\cos x'}{(x'+2\tilde{x})^5}dx'\Bigg]
\end{aligned}
$$

where the constants are

$$\begin{aligned}
d_0 &= \frac{P'^2 z}{2(P'l+\tilde{x})^2} - \frac{3}{8}\frac{P'^4 z\,(y^2+z^2+r^2)}{(P'l+\tilde{x})^4} \\
d_1 &= -P'^2 r \\
d_3 &= \frac{3}{2}P'^4 r\left(y^2+z^2+r^2\right) \\
d_4 &= -12P'^4 r^2 z \\
d_5 &= -3P'^4 r^2 y \\
d_6 &= 3P'^4 r y z \\
d_7 &= -24P'^4 r^2 y \\
d_8 &= \frac{3}{2}P'^4 r\left(y^2+3z^2+r^2\right)
\end{aligned}$$

and the $u_z(\vec{x})$ velocity component is

$$\begin{aligned}
u_z(\vec{x}) &\approx \frac{1}{4\pi}\int_l^\infty \left[-\frac{E(-x')}{(x'+x)^2} + \frac{D(-x')}{(x'+x)^3} + \frac{3}{2}\frac{E(-x')F(x')}{(x'+x)^4} - \frac{3}{2}\frac{D(-x')F(x')}{(x'+x)^5}\right]dx' \\
&= \frac{1}{4\pi}\Bigg[e_0 + e_1\sin\phi\int_{P'l}^\infty \frac{\sin x'}{(x'+\tilde{x})^2}dx' + e_1\cos\phi\int_{P'l}^\infty \frac{\cos x'}{(x'+\tilde{x})^2}dx' \\
&\quad -e_1\cos\phi\int_{P'l}^\infty \frac{\sin x'}{(x'+\tilde{x})^3}dx' + e_1\sin\phi\int_{P'l}^\infty \frac{\cos x'}{(x'+\tilde{x})^3}dx' \\
&\quad +e_3\cos\phi\int_{P'l}^\infty \frac{\cos x'}{(x'+\tilde{x})^4}dx' + e_3\sin\phi\int_{P'l}^\infty \frac{\sin x'}{(x'+\tilde{x})^4}dx' \\
&\quad +e_5\sin^2\phi\int_{P'l}^\infty \frac{\sin^2 x'}{(x'+\tilde{x})^4}dx' + e_5\cos^2\phi\int_{P'l}^\infty \frac{\cos^2 x'}{(x'+\tilde{x})^4}dx' \\
&\quad +[e_4\cos 2\phi - \tfrac{1}{2}e_8\sin 2\phi]\int_{2P'l}^\infty \frac{\sin x'}{(x'+2\tilde{x})^4}dx' \\
&\quad -e_4\sin 2\phi\int_{2P'l}^\infty \frac{\cos x'}{(x'+2\tilde{x})^4}dx' \\
&\quad +[e_6\cos\phi - e_7\sin\phi]\int_{P'l}^\infty \frac{\cos x'}{(x'+\tilde{x})^5}dx' \\
&\quad +[e_6\sin\phi + e_7\cos\phi]\int_{P'l}^\infty \frac{\sin x'}{(x'+\tilde{x})^5}dx' \\
&\quad +e_9\sin^2\phi\int_{P'l}^\infty \frac{\cos^2 x'}{(x'+\tilde{x})^5}dx' + e_9\cos^2\phi\int_{P'l}^\infty \frac{\sin^2 x'}{(x'+\tilde{x})^5}dx' \\
&\quad +[2e_4\sin 2\phi + e_8\cos 2\phi]\int_{2P'l}^\infty \frac{\sin x'}{(x'+2\tilde{x})^5}dx' \\
&\quad -e_8\sin 2\phi\int_{2P'l}^\infty \frac{\cos x'}{(x'+2\tilde{x})^5}dx'\Bigg]
\end{aligned}$$

where the constants are

$$
\begin{aligned}
e_0 &= \frac{-P'^2 y}{2(P'l+\tilde{x})^2} + \frac{3}{8}\frac{P'^4 y\,(y^2+z^2+r^2)}{(P'l+\tilde{x})^4} \\
e_1 &= -P'^2 r \\
e_3 &= \frac{3}{2}P'^4 r\left(y^2+z^2+r^2\right) \\
e_4 &= -12P'^4 r^2 y \\
e_5 &= -3P'^4 r^2 z \\
e_6 &= -3P'^4 r y z \\
e_7 &= -\frac{3}{2}P'^4 r\left(3y^2+z^2+r^2\right) \\
e_8 &= 24P'^4 r^2 z \\
e_9 &= 3P'^4 r^2 y
\end{aligned}
$$

For the present calculations $l = 4D$.

This page is intentionally left blank.

Appendix C

NACA Mean Line

The expression for the NACA rooftop mean lines (Abbott and von Doenhoff, 1959):

$$\frac{z_f}{c} = \frac{C_{Li}}{2\pi(\mathbf{a}+1)}\left\{\frac{1}{1-\mathbf{a}}\left[\tfrac{1}{2}(\mathbf{a}-\tfrac{1}{2}+t)\ln|\mathbf{a}-\tfrac{1}{2}+t| - \tfrac{1}{2}(\tfrac{1}{2}+t)^2\ln(\tfrac{1}{2}+t) + \tfrac{1}{4}(\tfrac{1}{2}+t)^2 - \tfrac{1}{4}(\mathbf{a}-\tfrac{1}{2}+t)^2\right] - (\tfrac{1}{2}-t)\ln(\tfrac{1}{2}-t) + g - h(\tfrac{1}{2}-t)\right\}$$

where

$$g = \frac{-1}{1-\mathbf{a}}\left[\mathbf{a}^2(\tfrac{1}{2}\ln\mathbf{a} - \tfrac{1}{4}) + \tfrac{1}{4}\right]$$

$$h = \frac{1}{1-\mathbf{a}}\left[\tfrac{1}{2}(1-\mathbf{a})^2\ln(1-\mathbf{a}) - \tfrac{1}{4}(1-\mathbf{a})^2\right] + g$$

and C_{Li} is the ideal lift coefficient.

This page is intentionally left blank.

PhD Theses
Department of Naval Architecture and Offshore Engineering
Technical University of Denmark · Kgs. Lyngby

1961 Strøm-Tejsen, J.
Damage Stability Calculations on the Computer DASK.

1963 Silovic, V.
A Five Hole Spherical Pilot Tube for three Dimensional Wake Measurements.

1964 Chomchuenchit, V.
Determination of the Weight Distribution of Ship Models.

1965 Chislett, M.S.
A Planar Motion Mechanism.

1965 Nicordhanon, P.
A Phase Changer in the HyA Planar Motion Mechanism and Calculation of Phase Angle.

1966 Jensen, B.
Anvendelse af statistiske metoder til kontrol af forskellige eksisterende tilnærmelsesformler og udarbejdelse af nye til bestemmelse af skibes tonnage og stabilitet.

1968 Aage, C.
Eksperimentel og beregningsmæssig bestemmelse af vindkræfter på skibe.

1972 Prytz, K.
Datamatorienterede studier af planende bådes fremdrivningsforhold.

1977 Hee, J.M.
Store sideportes indflydelse på langskibs styrke.

1977 Madsen, N.F.
Vibrations in Ships.

1978 Andersen, P.
Bølgeinducerede bevægelser og belastninger for skib på lægt vand.

1978 Römeling, J.U.
Buling af afstivede pladepaneler.

1978 Sørensen, H.H.
Sammenkobling af rotations-symmetriske og generelle tre-dimensionale konstruktioner i elementmetode-beregninger.

1980 Fabian, O.
Elastic-Plastic Collapse of Long Tubes under Combined Bending and Pressure Load.

1980 Petersen, M.J.
Ship Collisions.

1981 Gong, J.
A Rational Approach to Automatic Design of Ship Sections.

1982 Nielsen, K.
Bølgeenergimaskiner.

1984 Nielsen, N.J.R.
Structural Optimization of Ship Structures.

1984 Liebst, J.
Torsion of Container Ships.

1985 Gjersøe-Fog, N.
Mathematical Definition of Ship Hull Surfaces using B-splines.

1985 Jensen, P.S.
Stationære skibsbølger.

1986 Nedergaard, H.
Collapse of Offshore Platforms.

1986 Yan, J.-Q.
3-D Analysis of Pipelines during Laying.

1987 Holt-Madsen, A.
A Quadratic Theory for the Fatigue Life Estimation of Offshore Structures.

1989 Andersen, S.V.
Numerical Treatment of the Design-Analysis Problem of Ship Propellers using Vortex Lattice Methods.

1989 Rasmussen, J.
Structural Design of Sandwich Structures.

1990 Baatrup, J.
Structural Analysis of Marine Structures.

1990 Wedel-Heinen, J.
Vibration Analysis of Imperfect Elements in Marine Structures.

1991 Almlund, J.
Life Cycle Model for Offshore Installations for Use in Prospect Evaluation.

1991 Back-Pedersen, A.
Analysis of Slender Marine Structures.

1992 Bendiksen, E.
Hull Girder Collapse.

1992 Petersen, J.B.
Non-Linear Strip Theories for Ship Response in Waves.

1992 Schalck, S.
Ship Design Using B-spline Patches.

1993 Kierkegaard, H.
Ship Collisions with Icebergs.

1994 Pedersen, B.
A Free-Surface Analysis of a Two-Dimensional Moving Surface-Piercing Body.

1994 Hansen, P.F.
Reliability Analysis of a Midship Section.

1994 Michelsen, J.
A Free-Form Geometric Modelling Approach with Ship Design Applications.

1995 Hansen, A.M.
Reliability Methods for the Longitudinal Strength of Ships.

1995 Branner, K.
Capacity and Lifetime of Foam Core Sandwich Structures.

1995 Schack, C.
Skrogudvikling af hurtiggående færger med henblik på sødygtighed og lav modstand.

1997 Simonsen, B.C.
Mechanics of Ship Grounding.

1997 Olesen, N.A.
Turbulent Flow past Ship Hulls.

1997 Riber, H.J.
Response Analysis of Dynamically Loaded Composite Panels.

1998 Andersen, M.R.
Fatigue Crack Initiation and Growth in Ship Structures.

1998 Nielsen, L.P.
Structural Capacity of the Hull Girder.

1999 Zhang, S.
The Mechanics of Ship Collisions.

1999 Birk-Sørensen, M.
Simulation of Welding Distortions of Ship Sections.

1999 Jensen, K.
Analysis and Documentation of Ancient Ships.

2000 Wang, Z.
Hydroelastic Analysis of High-Speed Ships.

2000 Petersen, T.
Wave Load Prediction—a Design Tool.

2000 Banke, L.
Flexible Pipe End Fitting.

2000 Simonsen, C.D.
Rudder, Propeller and Hull Interaction by RANS.

2000 Clausen, H.B.
Plate Forming by Line Heating.

2000 Krishnaswamy, P.
Flow Modelling for Partially Cavitating Hydrofoils.

2000 Andersen, L.F.
Residual Stresses and Deformations in Steel Structures.

2000 Friis-Hansen, A.
Bayesian Networks as a Decision Support Tool in Marine Applications.

2001 Lützen, M.
Ship Collision Damage.

2001 Olsen, A.S.
Optimisation of Propellers Using the Vortex-Lattice Method.

Maritim Teknik

**Institut for Mekanik,
Energi og Konstruktion**

**Danmarks Tekniske
Universitet**

Studentertorvet, Bygning 101E
DK-2800 Kongens Lyngby
Danmark
Phone + 45 4525 1360
Fax + 45 4588 4325
info.mt@mek.dtu.dk
www.mek.dtu.dk

ISBN 87-89502-58-2